

**Development and Modeling of a Lab-scale Integrated Copper-Chlorine
Cycle for Hydrogen Production**

by

Aida Farsi

A thesis submitted to the
School of Graduate and Postdoctoral Studies in partial
fulfillment of the requirements for the degree of

Doctor of Philosophy in Mechanical Engineering

Faculty of Engineering and Applied Science
University of Ontario Institute of Technology (Ontario Tech University)

Oshawa, Ontario, Canada

August 2020

© Aida Farsi, 2020

THESIS EXAMINATION INFORMATION

Submitted by: **Aida Farsi**

Doctor of Philosophy in Mechanical Engineering

Thesis title: **Development and Modeling of an Lab-scale Integrated Copper-Chlorine Cycle for Hydrogen Production**

An oral defense of this thesis took place on August 2020 in front of the following examining committee:

Examining Committee:

Chair of Examining Committee	Dr. Haoxiang Lang
Research Supervisor	Dr. Ibrahim Dincer
Research Co-supervisor	Dr. Greg Naterer
Examining Committee Member	Dr. Dipal Patel
Examining Committee Member	Dr. Martin Agelin-Chaab
University Examiner	Dr. Liliana Trevani
External Examiner	Dr. İnci Eroğlu (Middle East Technical University, Chemical Engineering Department, Ankara, Turkey)

The above committee determined that the thesis is acceptable in form and content and that a satisfactory knowledge of the field covered by the thesis was demonstrated by the candidate during an oral examination. A signed copy of the Certificate of Approval is available from the School of Graduate and Postdoctoral Studies.

ABSTRACT

Hydrogen is one of the most important energy carriers, clean fuels, and storage media in the upcoming future. Hydrogen production through the thermochemical copper-chlorine (Cu-Cl) cycle is one of the most promising methods of nuclear hydrogen production on a large scale. Researchers at the University of Ontario Institute of Technology (UOIT) have designed and developed a lab-scale integrated Cu-Cl cycle for producing hydrogen. This study aims to develop the thermodynamic, hydrodynamic, electrochemical, and heat and mass transfer models for the experimental Cu-Cl cycle to evaluate the performance of the cycle and its components. Also, an exergoeconomic and optimization study is performed for a more cost-effective approach and revealing optimal design conditions. The results of this study will be useful as a benchmark for the lab-scale Cu-Cl cycle performance assessment accounting for actual large-scale implementation.

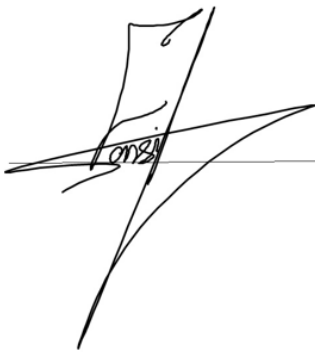
In practical operation of the Cu-Cl cycle, besides the main steps of hydrolysis, thermolysis, electrolysis and drying, the depleted anolyte (consumed anolyte at the electrolyzer) needs to be recycled to be concentrated sufficiently for the electrochemical process. Recycling of the oxidized anolyte through the separation processes is achieved by distillation of anolyte, drying unit, separation cell, pressure swing distillation unit (PSDU), and CuCl_2 concentrator. The overall exergy efficiency of the integrated lab-scale Cu-Cl cycle is found to be 33.4%. The estimated cost of produced hydrogen from the scaled-up facilities with a capacity of 1000 kg/day H_2 is about 3.91 \$/kg H_2 . In the hydrolysis reactor, with an increase of St/Cu ratio (from 5 to 17 and 30), the maximum exergetic efficiency of the system occurs at the lower reactor operating temperature (from 450°C to 388°C and 380°C, respectively). From the hydrodynamic study of $\text{CuCl}/\text{HCl}(\text{aq})$ electrolyzer, the cells close to the anolyte or catholyte input ports possess a higher voltage efficiency than other cells for the X-shape bipolar modules, resulting in less decomposition potential. In the PSDU, both heat and mass transfer model results predict the same values for the low and high pressure packing column height of 1.7 m and 2 m, respectively.

Keywords: hydrogen production; thermochemical copper chlorine cycle; energy and exergy efficiencies; multi-objective optimization.

AUTHOR'S DECLARATION

I hereby declare that this thesis consists of original work of which I have authored. This is a true copy of the thesis, including any required final revisions, as accepted by my examiners.

I authorize the University of Ontario Institute of Technology (Ontario Tech University) to lend this thesis to other institutions or individuals for the purpose of scholarly research. I further authorize University of Ontario Institute of Technology (Ontario Tech University) to reproduce this thesis by photocopying or by other means, in total or in part, at the request of other institutions or individuals for the purpose of scholarly research. I understand that my thesis will be made electronically available to the public.

A handwritten signature in black ink, appearing to read 'Aida Farsi', written over a horizontal line.

Aida Farsi

STATEMENT OF CONTRIBUTIONS

Part of the contents described in this thesis have been published as follows.

- Farsi, A., Dincer, I., & Naterer, G. F. (2020). Second law analysis of CuCl_2 hydrolysis reaction in the Cu–Cl thermochemical cycle of hydrogen production. *Energy*, 117721.
- Farsi, A., Zamfirescu, C., Dincer, I., & Naterer, G. F. (2020). Electrochemical Transport in CuCl/HCl (aq) Electrolyzer Cells and Stack of the Cu–Cl Cycle. *Journal of The Electrochemical Society*, 167(4), 044515.
- Farsi, A., Kayhan, Ö., Zamfirescu, C., Dincer, I., & Naterer, G. F. (2019). Kinetic and hydrodynamic analyses of chemically reacting gas-particle flow in cupric chloride hydrolysis for the Cu-Cl cycle. *International Journal of Hydrogen Energy*, 44(49), 26783-26793.
- Farsi, A., Zamfirescu, C., Dincer, I., & Naterer, G. F. (2019). Thermodynamic assessment of a lab-scale experimental copper-chlorine cycle for sustainable hydrogen production. *International Journal of Hydrogen Energy*, 44(33), 17595-17610.
- Farsi, A., Kayhan, Ö., Zamfirescu, C., Dincer, I., & Naterer, G. F. (2019). Azeotropic pressure swing distillation of hydrochloric-water for hydrogen production in the CuCl cycle: Thermodynamic and design methods. *International Journal of Hydrogen Energy*, 44(16), 7969-7982.
- Farsi, A., Kayhan, Ö., Zamfirescu, C., Dincer, I., & Naterer, G. F. (2019). Thermodynamic model of pressure swing distillation for a high pressure process of hydrochloric/water separation and hydrogen production. *International Journal of Hydrogen Energy*, 44(7), 3481-3491.

I performed the majority of the synthesis, testing of membrane materials, and writing of the manuscripts.

ACKNOWLEDGEMENTS

First of all, I would like to express my gratitude to my supervisor, Prof. Dr. Ibrahim Dincer, and my co-supervisor, Prof. Dr. Greg Naterer for their truthful guidance, unlimited and continuous support throughout my PhD thesis. This PhD thesis would not be possible without their courage, motivation, supervision, patience, understanding, and support.

I gratefully acknowledge the help and support of Dr. Calin Zamfirescu in critical times. Furthermore, I am thankful to my co-authors, Dr. Oznur Kayhan and Mr. Ghassan Chehade for the help provided at the Clean Energy Research Laboratory. I would like to extend my appreciation to my committee members, Dr. Martin Agelin-Chaab and Dr. Dipal Patel, Dr. Liliana Trevani and Dr. İnci Eroğlu for their valuable feedbacks and comments in improving this thesis. I also would like to thank all my colleagues at Clean Energy Research Laboratory (CERL) and ACE 3030B for their support.

I express my utmost appreciation and thankfulness for my father and mother, Hossain Farsi and Nahid Shayegan, for their love, support, guidance and prayers. They always believed and trusted me and has made countless sacrifices to help me get to this point. In addition, I am thankful to my sister and brother, Alice and Adel for their motivation, kindness and support.

Last but not least, special thanks and love to my beloved fiancé, Alireza Fakhraey for believing in me and supporting me every day. He has stood by me through all difficulties, my absences, and my impatience.

TABLE OF CONTENTS

ABSTRACT	ii
AUTHOR’S DECLARATION	iii
STATEMENT OF CONTRIBUTIONS.....	iv
ACKNOWLEDGEMENTS	v
TABLE OF CONTENTS	vi
LIST OF TABLES	ix
LIST OF FIGURES	xi
NOMENCLATURE	xvi
Chapter 1. Introduction	1
1.1. Thermochemical Cycle for Hydrogen Production	1
1.2. Copper-Chlorine Thermochemical Decomposition Cycle for H ₂ Production	3
1.3. Hydrolysis Reactor of Copper Chloride Decomposition	10
1.4. Thermolysis Reactor for Oxygen Production.....	14
1.5. Electrochemical Process of Hydrogen Production.....	17
1.6. Pressure Swing Distillation of Azeotropic Mixture	22
1.7. Dehydration Process of Cupric Chloride.....	25
1.8. Heat Recovery Prospects within the Cu-Cl Cycle	27
1.9. Cost, Exergoeconomic and Life Cycle Assessments (LCA).....	29
1.10. Motivation	33
1.11. Objectives.....	35
Chapter 2 . Literature Review	38
2.1. Overview of the Cu-Cl Thermochemical Cycle.....	38
2.2. CuCl ₂ /HCl (aq) Electrolyzer	41
2.3. Hydrolysis Reaction	44
2.4. Thermolysis Reaction.....	48
2.5. Pressure Swing Distillation Unit of Anolyte.....	50
2.6. Dehydration Process of CuCl ₂ (aq)	52
Chapter 3 . Experimental Apparatus and Procedure	54
3.1. Experimental Demonstration of the Lab-scale.....	54

3.3. Lab-scale CuCl_2 Hydrolysis Reactor Operation.....	62
3.4. $\text{CuCl}_2/\text{HCl}(\text{aq})$ Electrolyzer Stack.....	68
Chapter 4 . Analysis and Optimization.....	73
4.1. Thermodynamic Analysis of the Lab-scale Integrated Cu-Cl Cycle	73
4.2. Hydrolysis Reaction Analysis	85
4.2.1. Thermodynamic modeling of Hydrolysis Reaction.....	85
4.2.2. Hydrodynamic Model of the Hydrolysis Unit.....	88
4.2.3. Shrinking Core Model for the Hydrolysis Reaction	91
4.3. $\text{CuCl}/\text{HCl}(\text{aq})$ Electrolyzer Formulation	95
4.3.1. Electrochemical Formulation.....	95
4.3.2. Gibbs Free Energy Minimization (GEM).....	96
4.3.3. Kinetic Study of Electrochemical Cell	99
4.4.4. Hydrodynamic Model of $\text{CuCl}/\text{HCl}(\text{aq})$ Electrolyzer Stack	102
4.4. Pressure Swing Distillation Analysis	105
4.4.1. Thermodynamic Model of PSDU	105
4.4.2. Packing Column Height of PSDU	108
4.4.3. Mass Transfer Model of PSDU	108
4.4.4. Heat Transfer Model of PSDU	110
4.5. Exergoeconomic Study of Integrated Cu-Cl Cycle.....	113
4.5.1. SPECO Formulation	116
4.5.2. Scale-up Analysis	120
4.6. Optimization Study	123
Chapter 5 . Results and Discussion	128
5.1. Lab-scale Integrated Cu-Cl Cycle Simulation Results.....	128
5.2. Sensitivity Analysis Results	134
5.3. Hydrolysis Reaction Results	139
5.4. $\text{CuCl}/\text{HCl}(\text{aq})$ Electrolyzer Unit Results.....	147
5.5. Pressure Swing Distillation Unit Results	156
5.5.1. Thermodynamic Results of PSDU	156
5.5.2. Packing Column Height.....	169
5.6. Exergoeconomic Study Results.....	171
5.6.1. Scale-up Study Results	178

5.7. Optimization Study Results.....	181
Chapter 6 . Conclusions and Recommendations.....	193
6.1. Conclusions	193
6.2. Recommendations	195
References	197
Appendix.....	209

LIST OF TABLES

Table 1.1. Alternative thermochemical cycles recommended by ANL[5], [6].....	2
Table 1.2 . Different types of hybrid copper–chlorine thermochemical cycles	6
Table 1.3. List of laboratories and institutions investigated different types of Cu-Cl cycles.....	9
Table 1.4. List of desirable reaction and probable side reactions in the hydrolysis reactor.	12
Table 1.5. Detailed presentation of various design configurations of hydrolysis reactor proposed in the literature.	15
Table 1.6. List of elementary reactions for the copper oxychloride thermal decomposition	17
Table 1.7. Electrochemical unit categories based on membrane type and reaction in cathode side.....	19
Table 1.8. Various types of membranes investigated at different institutions with the membrane measured proton conductivity and permeability to CuCl ₂ [36], [37].....	20
Table 1.9. Main types of copper chloride solution drying methods and process illustrations [7], [45]	26
Table 1.10. Energy inputs and outputs for five-step Cu-Cl cycle.....	29
Table 1.11. Heat recovery methods from molten cuprous chloride within the copper chlorine cycle suggested by [51].....	30
Table 2.1. List of laboratories and institutions investigated different types of Cu-Cl cycles.....	41
Table 2.2. Summary of electrode development of CuCl/HCl (aq) electrolyzer for anodic and cathodic reactions.....	43
Table 2.3. Overview of reactor design parameters for main hydrolysis experiments developed at various institutions.....	47
Table 3.1. Technical specifications of different components at PSDU	62
Table 3.2 .Case studies for anolyte and catholyte concentrations in CuCl/HCl (aq) electrolyzer.....	72
Table 4.1. Typical variable ranges in the Cu-Cl thermochemical cycle.	79
Table 4.2. Integrated Cu-Cl thermochemical water decomposition cycle initial and design parameters [20].	80
Table 4.3. The material properties and correlations applied in Aspen Plus simulation model of proposed integrated Cu-Cl cycle [20], [71], [144], [145].....	81
Table 4.4. Exergy efficiency and exergy destruction rate definition for the proposed integrated Cu-Cl cycle components.	83
Table 4.5. Parameters for kinetic study of CuCl/HCl(aq) electrolyzer [39], [92], [93]..	101
Table 4.6. DURATHERM450 thermal properties [171]	107
Table 4.7. List of material costs (\$ CAD) within the lab-scale experimental Cu-Cl cycle.	115
Table 4.8. Cost of experimental units (\$ CAD) in the lab-scale integrated Cu-Cl cycle	116

Table 4.9. Cost balance equation (CBE) and auxiliary F and P rules for the system components	120
Table 4.10. Economic factors in the cost analysis	122
Table 4.11. Properties and parameters of the NN and GA to optimize the lab-scale integrated Cu-Cl cycle	125
Table 5.1. Hydrolysis reaction design parameters used for verification purpose.	128
Table 5.2. Thermo-physical properties of the chemical species in the copper chloride (CuCl ₂) decomposition reactor (T _{dryer} =125°C; reactor pressure of 1 atm; Ar/N ₂ =0).	129
Table 5.3. Initial input and assessed thermodynamic properties of the integrated Cu-Cl cycle's state points	130
Table 5.4. Overall hydrogen production rate, temperature, pressure, energy and exergy efficiencies and exergy destruction of the proposed integrated four-step Cu-Cl cycle. .	132
Table 5.5 . Equilibrium concentrations (mol/l) of anolyte speciation from GEM at standard temperature and pressure conditions (2M CuCl and 10M HCl(aq)) verified by [95], [96]	148
Table 5.6 . Variations in thermodynamic properties through the cathode and anode half-reactions for anode conversion degrees of 5% at the standard state (temperature of 25 °C, pressure of 1 atm and concentration of 1 M) verified by [39]. [95], [96].....	148
Table 5.7. Summarize physical constants, empirical equations used in the calculations of saturation pressures, binary interaction parameters and chemical equilibrium constant parameters used in developed HCl(aq) PSD model simulation in Aspen Plus [187]–[189].	157
Table 5.8. Aspen Plus data flowsheet for the low pressure side	158
Table 5.9. Aspen Plus data flowsheet for the high pressure side.....	158
Table 5.10 . Heat transfer parameters and related height of each section for the low pressure column	171
Table 5.11. Heat transfer parameters and related height of each section for the high pressure column	171
Table 5.12. Direct and indirect depreciable capital costs based on Hydrogen Analysis (H2A) Production model [180].	179
Table 5.13. Fixed operating costs of the Cu-Cl plant using a Hydrogen Analysis (H2A) Production model [180]	179
Table 5.14. Direct capital costs of units in a 1000 kg/day Cu-Cl cycle plant using a Hydrogen Analysis (H2A) Production model [180].	180
Table 5.15. Training results of the ANN based on Bayesian regularization for different numbers of hidden layers	182
Table 5.16. Design input parameters and objective functions for three different points on the Pareto frontier of Figure 10b.....	185

LIST OF FIGURES

Figure 1.1(a). Five different Cu-Cl cycle configurations and the electrolysis process comparison for producing hydrogen based on the equivalent required electrical power [8]	8
(b) Cost comparison of systems I, III and III for H ₂ production capacity (data from [9])..	4
Figure 1.2. Schematic diagram representation of the simplified Cu-Cl cycle.	8
Figure 1.3. Main domains of hydrogen production research at UOIT	10
Figure 1.4. (a) Schematic diagram of the lab-scale integrated Cu-Cl cycle at UOIT	11
Figure 1.5. Polarization curve for anode half-reaction with a double side coated electrodes, total active area of 2 cm ² and 100 mmol/L cuprous chloride solution, prepared by UOIT; Polyfit is applied for data extracted from [35].	21
Figure 1.6. Polarization curve for the full cell electrochemical unit; AECL data extracted from [40] and PSU data extracted from [11]	22
Figure 1.7. Txy diagram of HCl-water mixture at 1 and 4 atm. (b) Concentration diagram of HCl-water at 1 and 4 atm.....	24
Figure 1.8. Flowsheet for pressure swing distillation	25
Figure 1.9. Experimental system at UOIT for low-temperature spray drying of hydrated CuCl ₂	26
Figure 1.10. T-S diagram representing ideal heat pump and power systems integrated with a five-step copper chlorine cycle (modified from Refs. [7],[50]).....	28
Figure 1.11. Breakdown cost components percentage for a hybrid Cu-Cl plant is represented; data from Orhan et al. [54].	31
Figure 1.12. Global warming potential (GWP) eco-indicator for different hydrogen production methods; data from [60], [61].	32
Figure 2.1. (a) Partial pressure of oxygen and equilibrium constant at the thermally decomposition of the reaction of copper oxychloride (b) Equilibrium molar fractions of species in the thermolysis reactor; data from [113]; (Polyfit is applied for data).....	49
Figure 2.2. Schematic view with remarks representing the thermolysis test loop at UOIT; adapted from [112].	50
Figure 2.3. Effect of inlet air velocity (T=30°C and 10 g moisture per kg dry air) on predicted drying time at different droplet diameters and pressures; [50]; (smoothing cubic splines is used)	53
Figure 3.1. Schematic diagram representing the main parts of a lab-scale copper-chlorine thermochemical cycle for hydrogen production	55
Figure 3.2 . Lab scale of integrated four-step Cu-Cl cycle at UOIT.....	57
Figure 3.3. Schematic diagram of the lab-scale integrated Cu-Cl cycle at UOIT	58
Figure 3.4. Process flow diagram of HCl(aq) pressure swing distillation	60
Figure 3.5. Sketch of the laboratory atmospheric distillation unit of HCl (aq) at UOIT ..	61
Figure 3.6. Schematic diagram representing the cupric chloride hydrolysis reactor	67
Figure 3.7. (a) Schematic diagram representing the lab-scale integrated Cu-Cl cycle built at CERL in UOIT. (b) Anolyte loop for the lab-scale CuCl/HCl(aq) electrolyzer stack operating at room temperature and 1atm	70

Figure 3.8. Schematic diagram of Z-type manifold configuration of CuCl/HCl(aq) electrolyzer stack (anolyte and catholyte distribution flow pattern).....	71
Figure 3.9. Photograph of CuCl/HCl (aq) electrochemical cell at UOIT (a) stack with 10 MEA (b) disassembled stack (c) Ti/Pt Nafion 117 membrane (d) Ti electrode.	71
Figure 4.1. Flowsheet of the modeling methodology used to assess the performance of the lab-scale integrated Cu-Cl cycle.	73
Figure 4.2. Aspen Plus flowsheet diagram of the integrated four-step Cu-Cl cycle	74
Figure 4.3. Schematic diagram of the anolyte recycle loop in the integrated Cu-Cl cycle.	84
Figure 4.4. Aspen Plus flowsheet of hydrolysis reaction including CuCl ₂ conversion into Cu ₂ OCl ₂ , gas/solid product separation and CuCl ₂ decomposition into CuCl and Cl ₂	86
Figure 4.5. Schematic of a control mass with radius of R(t) at time t= t and radius of R(t + dt) at t+dt.....	88
Figure 4.6 (a). Schematic diagram representing the cupric chloride hydrolysis reactor, (b) Flow velocity distributions estimated in the boundary layer over an isothermal vertical surface [141] and [142].....	89
Figure 4.7. Representation of reacting particle with time.....	92
Figure 4.8. Reacting particle representation when rate-controlling resistance is diffusion through the ash layer.....	93
Figure 4.9. (a) Schematic of the CuCl/HCl(aq) electrolyzer stack containing 10 MEAs (left side modified from Hall et al. (19)) and (b) anolyte and catholyte flow patterns in the bipolar modules of manifolds.	104
Figure 4.10. Detailed schematic of streams at the column's trays, re-boiler and reflux condenser	108
Figure 4.11. Column heating materials; electric thermal tube for the low pressure side (left column) and DURATHERM450 thermal oil for the high pressure side (right column) and their relative heat transfer sections	111
Figure 4.12. (a) Schematic diagram of an energy system representing fuel, products and (b) the structure shown in (a) where all streams are exergy flows.	119
Figure 4.13. Schematic of large-scale thermochemical Cu-Cl cycle for hydrogen production	122
Figure 4.14. Schematic diagram of the Artificial Neural Network to analyze relationships between the inputs and outputs of the lab-scale integrated Cu-Cl cycle.	126
Figure 5.1. Concentration of Cu ₂ OCl ₂ in the solid products as a function of steam to copper chloride ratio and comparison with Ref. [26]	129
Figure 5.2. Unit thermal energy supplied or released per mole of produced hydrogen at different elements of integrated Cu-Cl cycle	133
Figure 5.3. Unit exergy rate per mole of produced hydrogen at different integrated Cu-Cl cycle's components	133
Figure 5.4. Exergy efficiency associated with each of the components of the proposed four-step integrated Cu-Cl cycle	134
Figure 5.5. Variation of exergy efficiency with the change of hydrolysis reactor temperature at different St/Cu molar ratio	136

Figure 5.6. Variation of exergy efficiency with the change of thermolysis reactor temperature at different St/Cu molar ratios.....	137
Figure 5.7. Variation of exergy efficiency with changes in the PSDU temperature at different St/Cu molar ratios	137
Figure 5.8. Variation of exergy efficiency with changes in the HCl/CuCl (aq) electrolyzer stack temperature at different St/Cu molar ratios	138
Figure 5.9. Variation of exergy efficiency with changes in the average temperature of the anolyte recovery separators unit at different St/Cu molar ratios	139
Figure 5.10(a). Exergy efficiency variation with changes in the steam to copper chloride molar ratio at different hydrolysis reaction temperatures, (b) Effect of the temperature gradient between the hot and cold sides of the hydrolysis reactor at different steam concentration ratios.	140
Figure 5.11. Effects of particle size on the terminal velocity of solid particles at different hydrolysis reaction temperatures	142
Figure 5.12. Variation of terminal velocity with cupric chloride (aqueous) volumetric flow rate at different hydrolysis temperatures	143
Figure 5.13. Variation of solid conversion with time at different particle sizes for diffusion control.....	144
Figure 5.14. Variation of solid conversion with time at different particle sizes in the kinetic control reaction.....	144
Figure 5.15(a). Variation of solid conversion with time at different hydrolysis temperatures in the diffusion control reaction, (b). Variation of solid conversion with time at different hydrolysis temperatures in the kinetic control reaction.....	145
Figure 5.16. Variation of solid conversion with time at different steam/solid fractions in the diffusion-controlled reaction.....	146
Figure 5.17. Variation of solid conversion with time at different steam/solid fractions in the kinetic controlled reaction.....	146
Figure 5.18 . Predicted η_{anode} at a given j_{cell} for $\xi_{CuCl} = 0.0, 0.25$ and 0.5 (compared to Hall et. al. [39]).....	149
Figure 5.19 (a) Pressure distribution profile (Pa) in the MEA modules and (b) flow velocity (m/s) in the bipolar plate channels with identical cross-sectional areas along 10 MEAs series-connected.	150
Figure 5.20. Flow distribution percentage at the anodic side, cathodic side and overall cell in the CuCl//HCl(aq) electrolyzer stack at 25°C, conversion extent of 5% and current density of 0.5A/m ²	151
Figure 5.21. Cell-to cell voltage distribution and average stack voltage at different electrolyzer operating temperatures at a conversion extent of 5% and the current density of 0.5A/m ²	152
Figure 5.22. Stack and cell-to-cell performance ratio at the initial design operating condition of the CuCl/HCl(aq) electrolyzer unit.....	153
Figure 5.23. Polarization curve for CuCl electrolysis at different operating temperatures for a conversion extent of 5% (2M CuCl and 10M HCl(aq))	154

Figure 5.24. Polarization curve for CuCl/HCl(aq) electrolyzer stack at different operating temperatures and variations of hydrogen production rate as a function of current density.	155
Figure 5.25 .Voltage efficiency of cells and stack (\times) at different electrolyzer operating temperatures at conversion extent of 5% and current density of 0.5A/cm ²	155
Figure 5.26. (a) Temperature profile and the heat transfer main regions along the high pressure distillation column height. (b) HCl and water molar fraction change along the height of high pressure distillation column.	159
Figure 5.27. Effect of the reflux ratio change on the bottom and distillate molar fraction	160
Figure 5.28. Influence of the reflux ration on the distillate mole flow rate and the bottom mole flow rate	160
Figure 5.29. Variation of the bottom and distillate temperatures as a function of reflux ratio	162
Figure 5.30. Change in the bottom and distillate molar fraction over the feed temperature	162
Figure 5.31. Influence of the feed temperature on the bottom and distillate mole flow rates	163
Figure 5.32. (a) Temperature profile along the low pressure column height from the bottom to top (b) Temperature profile through the high pressure column height from the bottom to top	164
Figure 5.33. (a) Change in the HCl mole fraction from the bottom to the top of the low pressure column (b) Change in the HCl mole fraction from the bottom to the top of the high pressure column	165
Figure 5.34. Effect of varying low pressure side feed temperature and the slope of operating line on the distillate mole fraction of HCl	167
Figure 5.35. Influence of low pressure feed flow rate and the slope of operating line on the distillate HCl molar concentration	167
Figure 5.36 (a). Variations with the low pressure feed temperature and slope for the re-boiler heat duty in high and low pressure columns (b). Variations with the low pressure feed temperature and slope for the condenser heat duty in high and low pressure columns	168
Figure 5.37. (a) McCabe-Thiele graph for the HCl (aq) at 1atm (before azeotropic point) with $q=1$, $x_f=0.1$, $x_b=0.12$ and $x_d=0.001$ (b) McCabe-Thiele graph for the HCl (aq) at 4atm (after azeotropic point) with $q=1$, $x_f=0.12$, $x_b=0.096$ and $x_d=0.22$	170
Figure 5.38. Breakdown of exergy destruction rates (kW) in components of the Cu-Cl cycle	173
Figure 5.39. Breakdown of cost rates of exergy destruction (\$/h) in the Cu-Cl cycle components	173
Figure 5.40. Component related cost rates (\$/h) in the lab-scale Cu-Cl cycle	174
Figure 5.41. Breakdown of total cost rates (\$/h) in the components of the lab-scale integrated Cu-Cl cycle	174
Figure 5.42. Component exergoeconomic factors in the lab-scale Cu-Cl cycle.....	175

Figure 5.43. Effects of CuCl/HCl (aq) electrolyzer stack capital cost on the cost rates of the overall lab-scale Cu-Cl cycle	176
Figure 5.44. Effects of interest rate on the cost rate of the lab-scale Cu-Cl cycle.....	177
Figure 5.45. Effects of system lifetime (in years) on the cost rates of the lab-scale Cu-Cl cycle	177
Figure 5.46. Effects of annual operation time (in hours) on the cost rates of the lab-scale Cu-Cl cycle	178
Figure 5.47. Costs of hydrogen and other related costs (\$/kg) in a large-scale Cu-Cl cycle plant with a capacity of 1000 kg/dayH ₂	181
Figure 5.48. Regression plots of models for the supplied data	183
Figure 5.49 . Pareto front from multi-objective optimization results	184
Figure 5.50. Distribution of variables for the Pareto optimal front in Figure 5.49.....	188
Figure 5.51. Variation of exergy efficiency with total cost for the optimum design parameters (a) HCl/CuCl (aq) electrolyzer; (b) PSDU; (c) St/Cu molar ratio; (d) hydrolysis temperature; (e) thermolysis temperature; and (f) average temperature of anolyte recovery separations unit.....	192

NOMENCLATURE

A	heat transfer area (m^2), active area (m^2)
A_{DH}	Debye-Huckel constant
\bar{a}	average ionic radius (\AA)
a	acceleration (m/s^2)
b	molality (mol/kg)
B	heat exchanger
B_{DH}	Debye-Huckel constant
c	molarity (kg/l), cost per unit exergy ($\$/\text{kWh}$)
C	volumetric concentration (mol/m^3)
\dot{C}	cost rate ($\$/\text{h}$)
C_s	Setchenow coefficient
\dot{C}_D	cost rate of exergy destruction ($\$/\text{h}$)
C_p	specific heat ($\text{kJ}/(\text{kg} \cdot \text{K})$)
C_D	Drag coefficient
CRF	capital recovery factor
D	diameter (m), mass diffusion coefficient (m^2/s)
D_e	effective diffusivity (m^2s^{-1})
E	electrical potential (V)
Ex	specific exergy (kJ/kg , kJ/kmol)
\dot{E}_X	Exergy rate (kW)
f	friction factor, exergoeconomic factor, specific body force (N/kg)
F	Faraday's number
F_B	Buoyancy force ($\text{kg/m} \cdot \text{s}^2$)

F_D	Drag force (kg/m.s^2)
F_g	Gravity force (kg/m.s^2)
g	acceleration of gravity (m/s^2) , specific gibbs free energy (J/mol)
Gr	Grashof number
h	specific enthalpy (kJ/kg), heat transfer coefficient ($\text{kW/m}^2\text{K}$)
h_{ow}	weir over height, means $h_{ow} = \text{level} - h_w$ (m)
h_f	heat of formation (kJ/kg)
i (I)	current (A)
I_e	ionic strength of electrolyte
J	current density (A/m^2)
j	mass diffusion flux with respect to mass-average velocity ($\text{kg/m}^2\text{s}$)
k_0	reaction rate constant
k''	chemical reaction rate constant (m/s)
L	furnace height (m)
LHV	Lower heating value (kJ/kg)
l_w	weir length
\dot{m}	mass flow rate (kg/h)
M	molar mass (kg/mol)
Nu	Nusselt number
n	mass diffusion flux with respect to stationary coordinates ($\text{kg/m}^2 \text{ s}$)
Pr	Prandtl number
P	pressure (kPa)
P_i^{vap}	vapor pressure of ith component (kPa)
P_n	pressure at nth tray (kPa)
\dot{Q}	heat transfer rate (kW)

Q	molar flux ($\text{mol}/\text{m}^2\cdot\text{s}$), heat (J)
R	universal gas constant ($\text{J}/\text{mol}\cdot\text{K}$)
R_{PEM}	membrane resistance (Ω)
Re	Reynolds number
RR	reflux ratio
r_i	chemical species production rate (kg/s)
R,r	radial coordinate, reaction rate, radius of solid particle (m)
R_p	reaction source ($\text{mol}/\text{m}^3\cdot\text{s}$)
Ra	Rayleigh number
r_c	radius of unreacted core (m)
r_A	rate of reaction ($\text{mol}/\text{m}^2\cdot\text{s}$)
s	specific entropy ($\text{kJ}/\text{mol}\cdot\text{K}$)
T	temperature ($^{\circ}\text{C}$, K)
t	time (s)
u	velocity (m/s)
U	overall heat transfer coefficient ($\text{kW}/\text{m}^2\cdot\text{K}$)
V	vapor molar fraction
v	velocity (m/s); specific volume (m^3)
v_{st}	steam velocity (m/s)
v_{tr}	terminal velocity (m/s)
v_{int}	initial velocity (m/s)
V_s	solid particle volume (m^3)
\dot{V}_{CuCl_2}	cupric chloride volumetric flow rate (m^3/s)
\dot{W}	work rate (kW)
X	liquid molar fraction; equilibrium conversion of solid

Y	vapor molar fraction
$y_{n,i}^*$	concentration at equilibrium
$y_{i,n}$	vapor mole fraction of ith component and nth tray
$y_{n,i}$	vapor mole fraction of ith component leaving tray n
$y_{n-1,i}$	vapor mole fraction of the ith component leaving tray (n-1)
\dot{Z}	cost rate of owning and operating the system (\$/h)
z	charge
Z	capital investment

Acronym

ADB	anolyte depleted buffer
ADA	atmospheric distillation unit of anolyte
AECL	atomic energy of Canada limited
AMV	anolyte make-up vessel
ANO	anode buffer
AEM	anion exchange membrane
ANL	argonne national laboratory
CAT	cathode buffer
CEA	commisariat á energy atomique át aux energies alternatives
CEM	cation exchange membrane
CERL	clean energy research laboratory
Cu-Cl	copper-chlorine
CNL	Canadian nuclear laboratories
DC	dissolution cell of CuCl in HCl(aq)
DEC	decanter of CuCl
GIF	generation IV international forum

GSP	graphite separator plate
GWP	global warming potential
HClCon	HCl(aq) concentrator
HPC	high pressure column
HYD	hydrolysis
IGT	institute of gas technology
LGS	liquid-gas separator
LPC	low pressure column
LCA	life cycle assessment
MP	melting point (K)
NBP	normal boiling point (K)
NCLI	national chemical laboratory for industry (Tokyo)
NTU	number of heat transfer units
N/A	not applicable
PSDU	pressure swing distillation unit
PSU	Pennsylvania State University
QUE	quench
RO	reverse osmosis
RDE	rotating disc electrode
SEM	scanning electron microscopy
Sepu	separation unit
St	steam
StCon	steam concentrator
SCE	saturated calomel reference electrode
Thrm	thermolysis

UOIT University of Ontario Institute of Technology

VLE vapor liquid equilibrium

Greek letters

α_i activity of each species

α transfer coefficient

Λ pre-exponential

β thermal expansion coefficient

λ thermal conductivity (W/mK); chemical affinity (kJ/kg)

μ fluid viscosity (kg/m/s (cP)); chemical potential (kJ/mol)

ρ density (kg/m³)

v specific volume (m³/kg)

η overpotential (V)

ε voltage efficiency

σ membrane ionic conductivity (S.cm⁻¹); porosity

η_{en} energy efficiency

Ψ exergy efficiency, potential exergy (kJ/mol)

τ_r complete conversion of solid particle using reaction control, s

τ_g complete conversion of solid particle using diffusion control, s

δ^2 ratio of diffusion to reaction resistance

ξ^v friction coefficient

φ specific potential on a species due to any present conservative forces (kJ/kg)

ω reaction rate (kg/m³s)

Subscripts/superscripts

b bubble point; boundary where heat transfer occurs

ch chemical

D	distillate
F	feed
FFE	falling film evaporation
FC	free convection
g	gas
L	liquid
MF	mist flow
PB	pool boiling
s	solid
v	vapor

Chapter 1. Introduction

1.1. Thermochemical Cycle for Hydrogen Production

It is widely accepted that hydrogen is a promising next-generation fuel. It is recognized as a carbon-free source which is the main contributor to global climate change issues. Hydrogen has the merit of being both an energy carrier and an energy storage medium, which results in higher efficiency for power plants to be run at full capacity and storing the excess energy in the form of hydrogen. Besides a large need for hydrogen in industrial sectors and petroleum products, it has also attracted the attention of automakers, and for trains, ships, and other transportation applications which consume hydrogen [1]. Only a small minority of hydrogen is currently produced with clean methods, while, most of the current systems like reforming processes utilize fossil fuels to produce hydrogen with a considerable amount of carbon dioxide emissions. This is attracting attention toward sustainable large-scale technologies for hydrogen production at low cost and without emitting carbon dioxide.

International energy agency, Japan [2] addressed the status of worldwide hydrogen production. It is reported that the majority of hydrogen is produced from carbon-based fuels of natural gas (71.27%), coal (27.26%) and oil (0.73%), while only less than 1% of hydrogen is produced from a renewable source. Amongst the clean hydrogen production methods (zero-carbon dioxide emission processes), the thermochemical water decomposition cycle is regarded as a promising alternative large-scale hydrogen production technology. Development and scaling-up such cycles in a sustainable means can drastically enhance hydrogen economy and sustainable energy development.

Thermochemical water splitting cycle (TWSC) uses both thermal energy and electrical energy to produce hydrogen through a sequence of thermo-chemical and electrochemical reactions in which the power consumption is substantially less than commercial water electrolysis process. Except water which is decomposed into the hydrogen and oxygen, all other intermediate chemical species are recycled in a closed-loop cycle [1], [3]. Over 200 cycles for thermochemical water splitting have been surveyed in the literature [4], however, a few types have been identified through theoretical and experimental investigations that proved the scientifically and economical feasibility of such systems. Among these feasible

types, the copper-chlorine (Cu-Cl) cycle is an efficient low-temperature type of water-splitting process for producing hydrogen [3]. Other thermochemical hydrogen production systems are also presented in Table 1.1 .

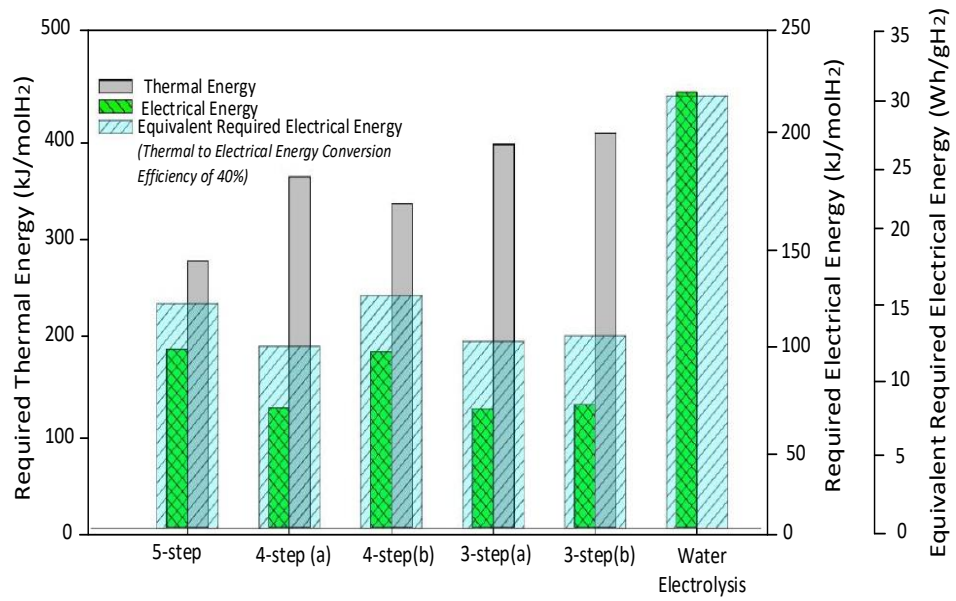
Table 1.1. Alternative thermochemical cycles recommended by ANL[5], [6]

No	Type	Reactions	Temperature	Efficiency	Maturity
1	Hybrid Sulfur	$\text{H}_2\text{SO}_4 \rightarrow \text{SO}_2 + \text{H}_2\text{O} + \frac{1}{2} \text{O}_2(\text{g})$	900°C	40%	High
		$2\text{H}_2\text{O} + \text{SO}_2 \rightarrow \text{H}_2\text{SO}_4 + \text{H}_2$	100-120°C		
2	Hybrid sulfur ammonia	$\text{SO}_2 + 2\text{NH}_3 + \text{H}_2\text{O} \rightarrow \text{NH}_4 + 2\text{SO}_3$	25°C	20-50%	Medium
		$\text{NH}_4 + 2\text{SO}_3 + \text{H}_2\text{O} \rightarrow \text{NH}_4 + 2\text{SO}_4 + \text{H}_2$	75°C		
		$\text{NH}_4 + 2\text{SO}_4 + \text{K}_2\text{SO}_4 \rightarrow 2\text{NH}_3 + \text{K}_2\text{S}_2\text{O}_7 + \text{H}_2\text{O}$	400°C		
		$\text{K}_2\text{S}_2\text{O}_7 \rightarrow \text{SO}_3 + \text{K}_2\text{SO}_4$	550°C		
		$\text{SO}_3 \rightarrow \text{SO}_2 + \frac{1}{2} \text{O}_2$	850°C		
3	Sulfur Iodine	$\text{I}_2 + \text{SO}_2 + 2\text{H}_2\text{O} \rightarrow 2\text{HI} + \text{H}_2\text{SO}_4$	<120°C	42%	High
		$\text{H}_2\text{SO}_4 \rightarrow \text{SO}_2 + \text{H}_2\text{O} + \frac{1}{2} \text{O}_2(\text{g})$	>800°C		
		$2\text{HI} \rightarrow \text{I}_2(\text{g}) + \text{H}_2(\text{g})$	450°C		
4	Vanadium Chlorine	$2\text{VCl}_2 + 2\text{HCl} \rightarrow 2\text{VCl}_3 + \text{H}_2$	120°C	30-47%	Low
		$4\text{VCl}_3 \rightarrow 2\text{VCl}_4 + 2\text{VCl}_2$	760°C		
		$2\text{VCl}_4 \rightarrow 2\text{VCl}_3 + \text{Cl}_2$	200°C		
5	Iron Chlorine	$\text{Cl}_2 + \text{H}_2\text{O} \rightarrow 2\text{HCl} + \text{O}_2$	850-925°C		
		$3\text{FeCl}_2 + 4\text{H}_2\text{O} \rightarrow \text{Fe}_3\text{O}_4 + 6\text{HCl} + \text{H}_2$	450-750°C	15-35%	Medium
		$\text{Fe}_3\text{O}_4 + 8\text{HCl} \rightarrow \text{FeCl}_2 + 2\text{FeCl}_3 + 4\text{H}_2\text{O}$	100-125°C		
		$2\text{FeCl}_3 \rightarrow 2\text{FeCl}_2 + \text{Cl}_2$	300°C		
		$\text{Cl}_2 + \text{H}_2\text{O} \rightarrow 2\text{HCl} + \frac{1}{2} \text{O}_2$	800°C		

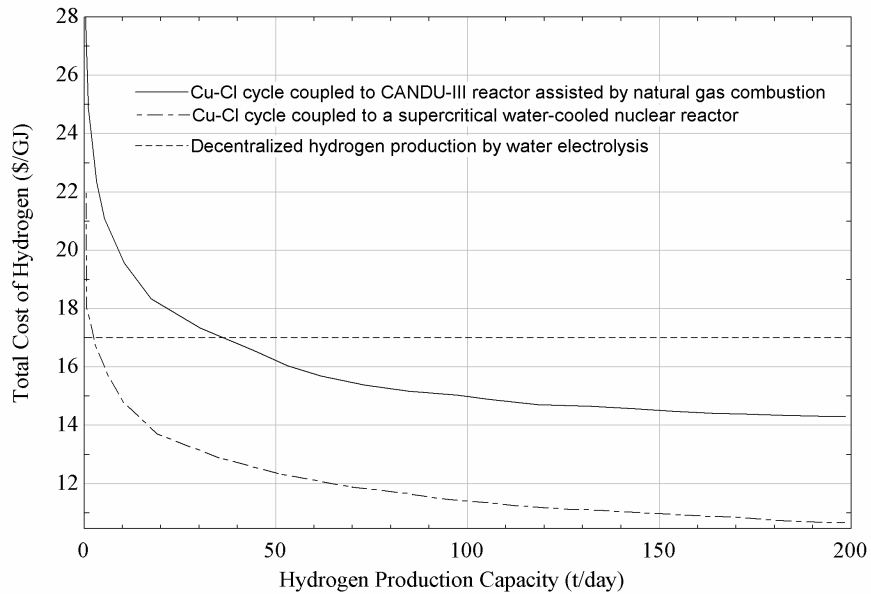
The Cu-Cl cycle is one of the most promising types of thermochemical cycles that operate in a relatively low-temperature range (450°C-550°C) which provides opportunities for efficient integration of such cycle with energy systems in particular nuclear power stations. Nuclear hydrogen production can potentially make nuclear power plants more economically competitive through integration with high-temperature electrolysis and thermochemical cycles. Radiation from the nuclear elements and through all stages of nuclear fuel processing can be directly used to produce hydrogen from water [7]. The relatively lower operating temperature of Cu-Cl cycle leads to lower maintenance and material costs compared to the high-temperature hydrogen production thermochemical cycles. Furthermore, the other advantages of Cu-Cl cycle can be referred to the low cost of chemical species interacted in cycle and minimum instances of undesired reactions [1].

1.2. Copper-Chlorine Thermochemical Decomposition Cycle for H₂ Production

The hybrid thermochemical cycles can be categorized into five configurations which are compared in terms of the required thermal and electrical energy shown in Figure 1.2(a). Also, Figure 1.2 (b) shows the cost comparison of decentralized hydrogen production by water electrolysis, production of hydrogen by steam-methane reforming, Cu-Cl cycle coupled to a supercritical water-cooled nuclear reactor and Cu-Cl cycle coupled to CANDU-III reactor assisted by natural gas combustion. It is shown that the water electrolysis for large-scale production of hydrogen in distributed facilities is not cost-competitive relative to other technologies [10]. Water electrolysis is known as a benchmark commercial technology for hydrogen production from water. However, producing hydrogen from electrolysis is costly and provides a relatively low overall efficiency of 18–24%. A variety of thermochemical water decomposition cycles have been introduced as alternatives to water electrolysis. Some of the thermochemical cycles such as the Cu-Cl cycle can be more efficient compared to water electrolysis due to favorable thermodynamics of the cycle reactions at elevated temperatures so less electrical energy is required for producing the same amount of H₂ [11].



(a)



(b)

Figure 1.1(a). Five different Cu-Cl cycle configurations and the electrolysis process comparison for producing hydrogen based on the equivalent required electrical power [8]
 (b) Cost comparison of different hydrogen production systems (data from [9])

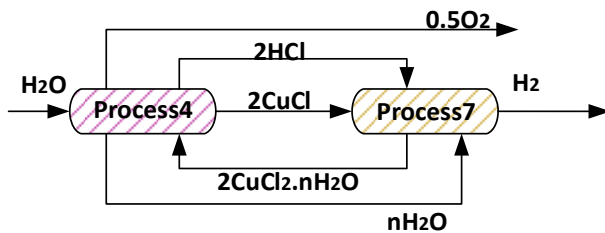
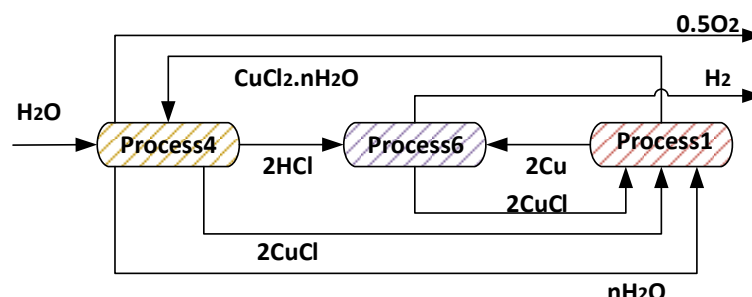
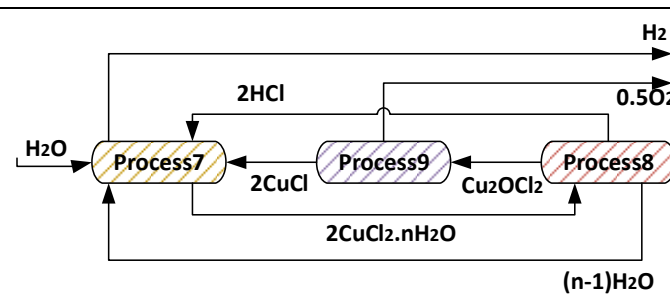
The transport and handling of solid particles within the cycle can be eliminated by reducing the number of main reactions through the combination of some steps of the Cu-Cl cycle to minimize the formation of undesirable solid particles. Improvement in the

reaction kinetics and process of mixing and handling of gaseous-liquid phases are other benefits of reducing the number of steps in the Cu-Cl cycle. Predicting the heat and mass transfer mechanisms of solid-solid or solid-fluid mixtures becomes more complex because of incomplete reactions, undesired byproducts and consequently a decrease of overall cycle efficiency [12]. On the other hand, reducing the number of steps of the Cu-Cl cycle may potentially lead to serious challenges such as higher heat grade requirements, an increase of undesirable byproduct formation, and a decrease in the production of desired products. Also, from a practical engineering perspective, a higher-grade source of heat requirement brings additional difficulties in the selection of materials for designing and constructing the reactors and heat exchangers within the Cu-Cl cycle [12].

Table 1.2 shows the schematic of operating principle of Cu-Cl cycles with their associated reactions for each step and corresponding temperatures. It is shown that for each cycle, the first step demonstrates the chemical reaction at which water is introduced. According to Table 1.2, for the cycles of Cu-Cl-2, Cu-Cl-3a, Cu-Cl-3c, Cu-Cl-4b and Cu-Cl-5, steam is introduced in the hydrolysis reactor indicating that the water is pre-heated, boiled and super-heated (in an integrated system or separately) before supplying to the hydrolysis reaction. The two cycles of Cu-Cl-3b and Cu-Cl-4a do not need steam because water is introduced in a liquid phase to the electrochemical reaction in which the complexation of cupric chloride happens.

In a Cu-Cl thermochemical cycle, without emitting any greenhouse gases or other substances to the environment, its chemical reactions form a closed internal loop that recycles all chemicals on a continuous basis. The separation and recycling of chemicals within a thermochemical cycle is of crucial importance. As shown in the diagram of Figure 1.2, hydrolysis is supplied with excess steam and thus the hydrolysis product is a weak hydrochloric acid solution. Furthermore, the electrochemical cell in the cycle consumes HCl but not water. Pressure swing distillation is therefore required to eliminate water and concentrate the acid. The strong acid flows toward the electrolysis unit to make-up the anodic electrolyte with dissolved CuCl. The removed water is directed toward a unit of operation for CuCl/ CuCl₂ separation which is based on three processes: drying, selective dissolution and decanting.

Table 1.2 . Different types of hybrid copper–chlorine thermochemical cycles

Cycle	Schematic of hybrid copper–chlorine cycle/Reactions
Cu–Cl-2 cycle (two steps)	 <p>4-Hydrolysis: $\text{H}_2\text{O}(\text{g}) + 2\text{CuCl}_2 \cdot n\text{H}_2\text{O}(\text{s}) \rightarrow 0.5\text{O}_2(\text{g}) + 2\text{HCl}(\text{g}) + 2\text{CuCl}(\text{l}) + n\text{H}_2\text{O}(\text{g})$ $T = 550^\circ\text{C}$ 7-CuCl chlorination: $2\text{CuCl}(\text{s}) + 2\text{HCl}(\text{aq}) + n\text{H}_2\text{O}(\text{l}) \rightarrow \text{H}_2(\text{g}) + 2\text{CuCl}_2 \cdot n\text{H}_2\text{O}(\text{aq})$ $T = 200^\circ\text{C}$</p>
Cu–Cl-3a cycle (three steps)	 <p>4-Hydrolysis: $\text{H}_2\text{O}(\text{g}) + 2\text{CuCl}_2 \cdot n\text{H}_2\text{O}(\text{s}) \rightarrow 0.5\text{O}_2(\text{g}) + 2\text{HCl}(\text{g}) + 2\text{CuCl}(\text{l}) + n\text{H}_2\text{O}(\text{g})$ $T = 550^\circ\text{C}$ 6-Thermolysis: $2\text{Cu}(\text{s}) + 2\text{HCl}(\text{g}) \rightarrow \text{H}_2(\text{g}) + 2\text{CuCl}(\text{l})$ $T = 450^\circ\text{C}$ 1-Disproportionation: $n\text{H}_2\text{O}(\text{l}) + 4\text{CuCl}(\text{s}) \rightarrow 2\text{Cu}(\text{s}) + 2\text{CuCl}_2 \cdot n\text{H}_2\text{O}(\text{aq})$ $T = 75^\circ\text{C}$</p>
Cu–Cl-3b cycle (three steps)	 <p>7-CuCl chlorination: $n\text{H}_2\text{O}(\text{l}) + 2\text{CuCl}(\text{s}) + 2\text{HCl}(\text{aq}) \rightarrow \text{H}_2(\text{g}) + 2\text{CuCl}_2 \cdot n\text{H}_2\text{O}(\text{aq})$ $T = 75^\circ\text{C}$ 9-Thermolysis: $\text{CuO} \cdot \text{CuCl}_2(\text{s}) \rightarrow 0.5\text{O}_2(\text{g}) + 2\text{CuCl}(\text{l})$ $T = 527^\circ\text{C}$ 8-Oxy-chlorination: $2\text{CuCl}_2 \cdot n\text{H}_2\text{O}(\text{s}) \rightarrow \text{CuO} \cdot \text{CuCl}_2(\text{s}) + 2\text{HCl}(\text{g}) + (n-1)\text{H}_2\text{O}(\text{g})$ $T = 400^\circ\text{C}$</p>

Cu-Cl-3c cycle (three steps)	
	<p>5-Cl₂ hydrolysis: $\text{H}_2\text{O}(\text{g})+\text{Cl}_2(\text{g})\rightarrow 0.5\text{O}_2(\text{g})+2\text{HCl}(\text{g})$ $T=800^\circ\text{C}$ 7-CuCl chlorination: $2\text{CuCl}(\text{s})+2\text{HCl}(\text{aq})+\text{nH}_2\text{O}(\text{l})\rightarrow\text{H}_2(\text{g})+2\text{CuCl}_2\cdot\text{nH}_2\text{O}(\text{aq})$ $T=200^\circ\text{C}$ 10-CuCl₂ thermolysis: $2\text{CuCl}_2\cdot\text{nH}_2\text{O}(\text{s})\rightarrow 2\text{CuCl}(\text{l})+\text{Cl}_2(\text{g})+\text{nH}_2\text{O}(\text{g})$ $T=500^\circ\text{C}$</p>
Cu-Cl-4a cycle	
	<p>1-Disproportionation: $\text{nH}_2\text{O}(\text{l})+4\text{CuCl}(\text{s})\rightarrow 2\text{Cu}(\text{s})+2\text{CuCl}_2\cdot\text{nH}_2\text{O}(\text{aq})$ $T=75^\circ\text{C}$ 6-Cu chlorination: $2\text{Cu}(\text{s})+2\text{HCl}(\text{g})\rightarrow\text{H}_2(\text{g})+2\text{CuCl}(\text{l})$ $T=450^\circ\text{C}$ 9-Thermolysis: $\text{CuO}\cdot\text{CuCl}_2(\text{s})\rightarrow 0.5\text{O}_2(\text{g})+2\text{CuCl}(\text{l})$ $T=527^\circ\text{C}$ 8-Oxy-chlorination: $2\text{CuCl}_2\cdot\text{nH}_2\text{O}(\text{s})\rightarrow\text{CuO}\cdot\text{CuCl}_2(\text{s})+2\text{HCl}(\text{g})+(\text{n}-1)\text{H}_2\text{O}(\text{g})$ $T=377^\circ\text{C}$</p>
Cu-Cl-4b cycle (four steps)	
	<p>3-Hydrolysis, dry: $\text{H}_2\text{O}(\text{g})+2\text{CuCl}_2(\text{s})\rightarrow\text{CuO}\cdot\text{CuCl}_2(\text{s})+2\text{HCl}(\text{g})$ $T=400^\circ\text{C}$ 7-CuCl chlorination: $2\text{CuCl}(\text{s})+2\text{HCl}(\text{aq})+\text{nH}_2\text{O}(\text{l})\rightarrow\text{H}_2(\text{g})+2\text{CuCl}_2\cdot\text{nH}_2\text{O}(\text{aq})$ $T=75^\circ\text{C}$ 9-Thermolysis: $\text{CuO}\cdot\text{CuCl}_2(\text{s})\rightarrow 0.5\text{O}_2(\text{g})+2\text{CuCl}(\text{l})$ $T=527^\circ\text{C}$ 12-Crystallization: $2\text{CuCl}_2\cdot\text{nH}_2\text{O}(\text{aq})\rightarrow 2\text{CuCl}_2(\text{s})+\text{nH}_2\text{O}(\text{l})$ $T<100^\circ\text{C}$</p>

Cu-Cl-5 cycle (five steps)	
	<p>2-Hydrolysis: $\text{H}_2\text{O}(\text{g}) + 2\text{CuCl}_2 \cdot \text{mH}_2\text{O}(\text{s}) \rightarrow \text{CuO} \cdot \text{CuCl}_2(\text{s}) + 2\text{HCl}(\text{g}) + \text{mH}_2\text{O}(\text{g})$ $T = 377^\circ\text{C}$</p> <p>6-Cu chlorination: $2\text{Cu}(\text{s}) + 2\text{HCl}(\text{g}) \rightarrow \text{H}_2(\text{g}) + 2\text{CuCl}(\text{l})$ $T = 450^\circ\text{C}$</p> <p>9-Thermolysis: $\text{CuO} \cdot \text{CuCl}_2(\text{s}) \rightarrow 0.5\text{O}_2(\text{g}) + 2\text{CuCl}(\text{l})$ $T = 527^\circ\text{C}$</p> <p>1-Disproportionation: $4\text{CuCl}(\text{s}) + \text{nH}_2\text{O}(\text{l}) \rightarrow 2\text{Cu}(\text{s}) + 2\text{CuCl}_2 \cdot \text{nH}_2\text{O}(\text{aq})$ $T = 75^\circ\text{C}$</p> <p>12-Drying(spray): $2\text{CuCl}_2 \cdot \text{nH}_2\text{O}(\text{aq}) \rightarrow 2\text{CuCl}_2 \cdot \text{mH}_2\text{O}(\text{s}) + (\text{n}-\text{m})\text{H}_2\text{O}(\text{g})$ $T < 257^\circ\text{C}$</p>

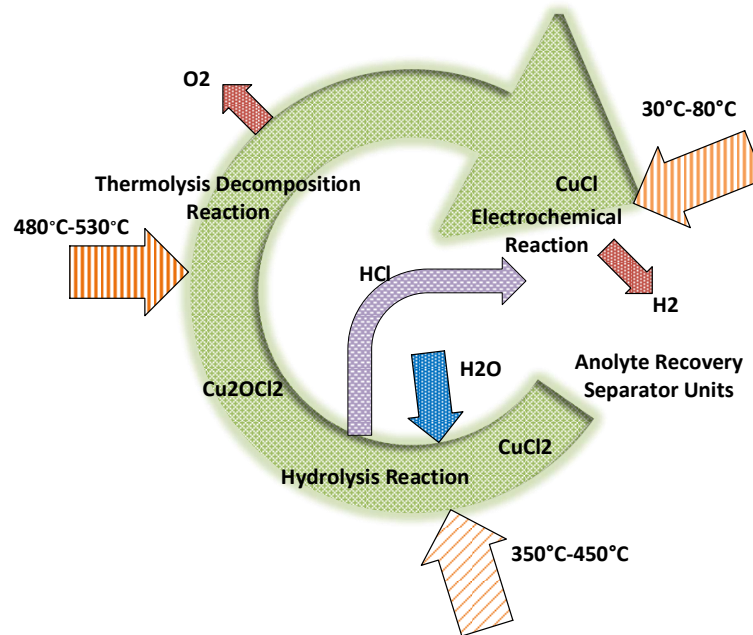


Figure 1.2. Schematic diagram representation of the simplified Cu-Cl cycle.

As mentioned before, the Cu-Cl thermochemical hydrogen producing cycle has many advantages. Besides the available chemical species, the higher overall conversion efficiency of the cation exchange membrane electrolyzer compared to conventional electrolysis and relatively low-temperature needs (less than 530°C) compared to the S-I cycle, make it have a great potential for low-grade waste heat recovery, as well as lower material maintenance costs [1]. The Argonne National Laboratory (ANL) in the USA,

Pennsylvania State University (PSU), Canadian Nuclear Laboratories (CNL) and UOIT are leading work on scaling up the copper-chlorine cycle for practical applications [8]. One of the objectives of Canadian Nuclear Laboratories (CNL) is to scale-up the technology of the Cu-Cl thermochemical cycle for linkage with its next-generation supercritical water-cooled reactor (SCW-CANDU).

Clean Energy Research Laboratory (CERL) team at UOIT is enormously investigating on copper chlorine cycle to upgrade this technology into a large-scale for industrial sectors. Numerous papers were published from this group for modeling, simulating and evaluating of the cycle and its components, experimental unit operations and scaled-up hydrogen production system. The studies conducted in the hydrogen production area at UOIT are mainly categorized into thermal, light-based and thermal hydrogen production methods as shown in Figure 1.3. The most recent approach in UOIT as the led-international team is

Table 1.3. A list of laboratories and institutions investigated different types of Cu-Cl cycles.

Cycle	T _{max} (°C)	Institutions	Other identities
Cu-Cl-2	550	NCLI, Dokyia and Kotera et al. [13]	Cu-Cl-C, in Lewis and Masin et al. [14]
Cu-Cl-3a	527	ANL, Perret et al. [15]	ANL-287 in Abanades et al.[5] Three-step cycle (UOIT) in Wang et al. [16]
Cu-Cl-3b	527	AECL and ANL. Suppiah et al. [17]	Cu-Cl-B in Lewis and Masin et al.[14] Three-step cycle (UOIT) in Naterer et al. [18]
Cu-Cl-3c	800	NCLI, Dokyia and Kotera et al. [13]	UNLV-56, in McQuillan et al.[19] Cu-Cl-D in Lewis and Masin et al.[14]
Cu-Cl-4a	527	UOIT, Wang et al. [16]	Four-step cycle (UOIT) in Wang et al.[16]
Cu-Cl-4a	480	UOIT, Farsi et al [20]	Four-step cycle (UOIT) in Farsi et al.[20]
Cu-Cl-4b	527	UOIT, Naterer et al.[18]	Four-step cycle (UOIT) in Naterer et al.[18]
Cu-Cl-5	527	IGT, Carty et al.[21]	H-5 in Carty et al.[21] ALTC-1 in Lewis et al. [17] Cu-Cl-A in Lewis and Masin et al.[14] Five-step cycle (UOIT) in Wang et al.[16]

the construction of a lab-scale integrated copper chlorine cycle. The components of the cycle were sized to correspond to 100 g per day of hydrogen production. Figure 1.4 (a) and (b) show the schematic view of the integrated lab-scale copper chlorine cycle in CERL at UOIT. Detailed descriptions of this system have been provided in previous studies [20], [22]–[25]. Furthermore, a list of institutions and alternative identification of the Cu-Cl cycle are provided in Table 1.3. There have been numerous past studies for modeling and evaluating various versions of the Cu-Cl cycle from a thermodynamic viewpoint at which the cycle is integrated with nuclear/renewable thermal-power plants.

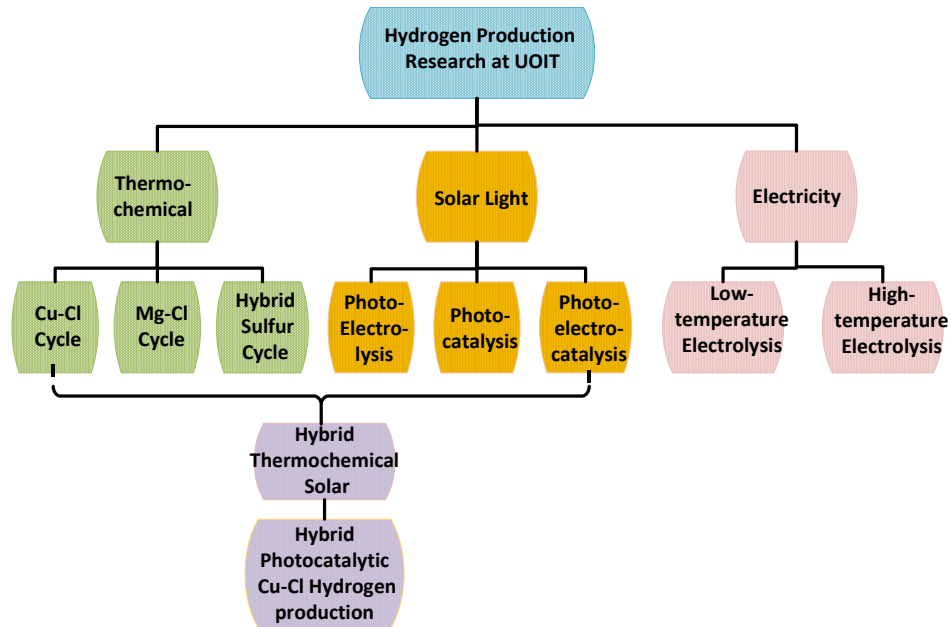
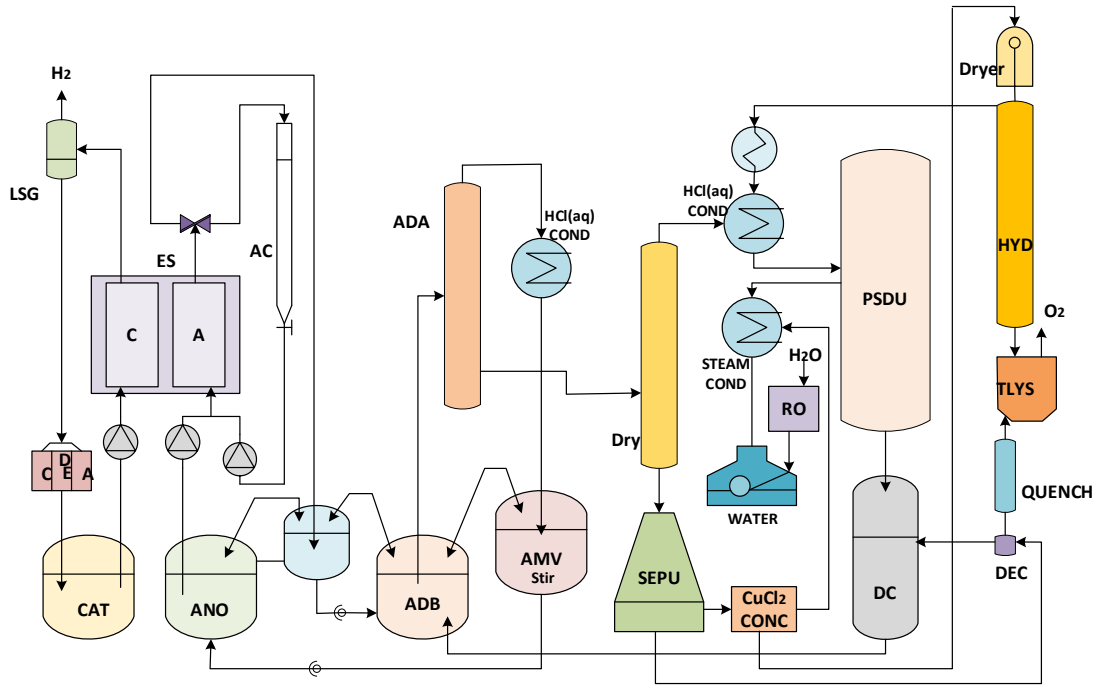


Figure 1.3. Main domains of hydrogen production research at UOIT

1.3. Hydrolysis Reactor of Copper Chloride Decomposition

Ideally, in the copper chloride decomposition (hydrolysis) reactor a moving solid CuCl_2 and steam mixture react and form Cu_2OCl_2 and hydrochloric acid. Practically, to achieve a high conversion of copper chloride into copper oxychloride, excess steam is introduced within the hydrolysis reactor. Once cupric chloride and steam are introduced in the hydrolysis reactor, some possible reactions may occur that are listed in Table 1.4. The most important undesirable reaction is the decomposition of CuCl_2 generating chlorine and cuprous chloride (reaction 2, Table 1.4).



(a)



(b)

Figure 1.4. (a) Schematic diagram of the lab-scale integrated Cu-Cl cycle at UOIT
 (b) Photograph of lab-scale integrated Cu-Cl cycle at UOIT

Although the desired products of hydrolysis reaction are hydrochloric acid and copper-oxy chloride, the decomposition of copper oxy-chloride may also occur (reaction 3 in Table 1.4) due to the high reactor temperature. The cuprous chloride produced from copper-oxy chloride decomposition can be in solid, liquid and gas phases depending on the reaction temperature. An alternative possible side reaction can be referred to tricopper trichloride ($\text{Cu}_3\text{Cl}_3(\text{g})$) generation from $\text{CuCl}(\text{g})$ directly (reaction 4, Table 1.4) that should be avoided because Cu_3Cl_3 is stable. Formation of CuCl does not lead to a problem in the hydrolysis reactor since it is the desired product of thermolysis reaction. The primary problem is associated with the molecular chlorine formation that should be recycled in the cycle. So, the reactor design parameters and sizes need to be selected and measured properly to minimize the formation of chlorine. The reverse Deacon reaction (forward reaction 5, Table 1.4) in which the side product of chlorine gas ($\text{Cl}_2(\text{g})$) consumes and produces $\text{HCl}(\text{g})$ and $\text{O}_2(\text{g})$, while the backward is Deacon reaction considered as the desirable reaction. Noteworthy, in the hydrolysis reactor oxygen agent is not desired product since it helps chlorine release process [7, 27, 27].

Table 1.4. List of desirable reactions and probable side reactions in the hydrolysis reactor.

ID	Reaction	Remarks
1	$2\text{CuCl}_2(\text{s}) + \text{H}_2\text{O}(\text{g}) \rightarrow \text{Cu}_2\text{OCl}_2(\text{s}) + 2\text{HCl}(\text{g})$	Hydrolysis desired reaction
2	$\text{CuCl}_2(\text{s}) \rightarrow \text{CuCl}(\text{s, l, g}) + 0.5\text{Cl}_2(\text{g})$	CuCl formation from CuCl_2 decomposition
3	$\text{Cu}_2\text{OCl}_2(\text{s}) \rightarrow 0.5\text{O}_2(\text{g}) + 2\text{CuCl}(\text{s, l, g})$	Decomposition of copper oxychloride
4	$3\text{CuCl}(\text{g}) \rightarrow \text{Cu}_3\text{Cl}_3(\text{g})$	Tri-copper tri-chloride formation
5	$\text{Cl}_2(\text{g}) + \text{H}_2\text{O}(\text{g}) \leftrightarrow 0.5\text{O}_2(\text{g}) + 2\text{HCl}(\text{g})$	Deacon reaction and reverse Deacon reaction

Several hydrolysis reactors were developed and investigated such as fluidized bed, packed bed, spray and falling particle reactors. Most of the examined reactors are batch type, while some of them are semi-batch reactors where the reacting solid particles remain inside reactor whereas steam and gas carriers (argon) are supplied and extracted until the experiment ends. Some reactors are flow-based reactors such as spray and falling droplet reactors at which both solid particles and fluids are continuously supplied and extracted

continuously. The reactors are sized from the small bench with the copper chloride sample weight of tens of grams, to larger-scale reactors such as the one built and tested at UOIT. The weight of copper chloride sample determines the scale of the hydrolysis reaction experiment. Various types of hydrolysis reactors were investigated and tested by institutions that are illustrated next.

In a fixed bed reactor in order to characterize the hydrolysis reaction, a thermochemistry analysis and experiment are conducted. The fixed bed reactor configuration is shown in Table 1.5. Based on the schematic of fixed bed reactor shown in Table 1.5, steam is generated in an auxiliary unit consisting of a demineralized water vessel and steam generator and then injected to the reactor. Inert gas is supplied to adjust different reaction parameters such as reducing the steam partial pressure, preheating purposes, or for the shutoff period.

X-ray diffraction (XRD) technique is used before and after each experiment to characterize the solid components. The hot gaseous products comprised of H_2O , HCl and Cl_2 are cooled and characterized by diverse methods like UV-visible spectroscopy [28] or chromatography. In the UV-visible spectroscopy technique, an alkaline solution (normally NaOH) is used to trap HCl and then pH measurements are applied to specify the HCl concentration [7].

A vertical fluidized bed hydrolysis reactor with its auxiliary components is shown in Table 1.5. Some experiments are performed on fluidized bed reactors at which the granular sample is placed on a porous media distributor then fluidized by steam and inert gas. The $\text{H}_2\text{O}/\text{CuCl}_2$ molar ratio is much larger than the stoichiometric value. However fluidized bed reactor design provides direct contact between solid CuCl_2 particles and steam results in higher reaction conversion, a large amount of steam should be circulated to fluidize and transfer heat of reaction. This requires an additional amount of energy for the cycle.

Another type of hydrolysis reactor is spray in which the atomized particles are created from a concentrated solution of CuCl_2 (aq) and sprayed in a high-temperature zone filled with steam. The schematic view of this reactor is shown in Table 1.5. The droplets residence time should be designed adequately to meet the reaction temperature and efficient reaction. Operation of the hydrolysis reactor under the vacuum pressure facilitates the

endothermic chemical reaction from the thermodynamic aspect. The ANL institution was also developed and tested this kind of reactor [26], [27] in which a uniform temperature is dominated throughout the reactor by using multi-zone temperature controllers. To atomize the CuCl_2 (aq) solution, an ultrasonic nozzle was set up leading to fast vaporization of water content in the droplet and formation of small copper chloride particles. The steam was introduced through the argon gas line to increase steam concentration for attaining constant steam to copper chloride molar ratio in the reactor.

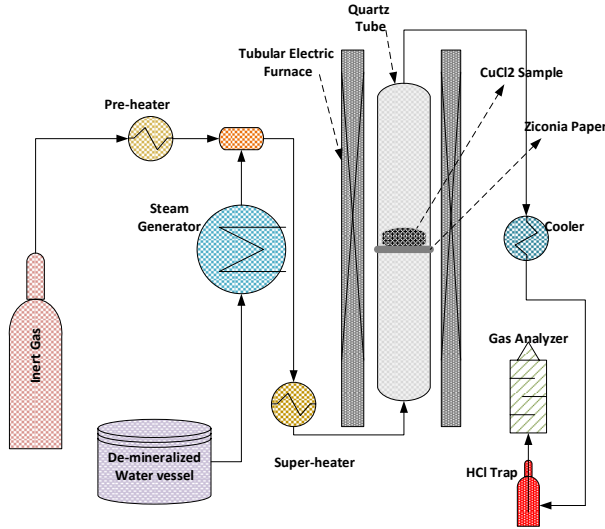
Recently researchers at UOIT presented a new thermally-driven hydrolysis reactor based on the temperature differences at two sides of the reactor (shown in Table 1.5). The solid copper chloride droplets are falling into a vertical quartz tube rather than being scattered through the spray process. Free falling particles in conjunction with the relatively slow circulation of steam (steam movement due to the natural convection) provide more reactants residence time. This reactor is under investigation of the research group at Clean Energy Research Laboratory (CERL) in UOIT [25]. A detailed description of this reactor and its working principle are provided in the next.

1.4. Thermolysis Reactor for Oxygen Production

In the thermolysis reaction, solid copper oxychloride dissociates into molten cuprous chloride and oxygen gas. In this endothermic solid conversion process, three phases of solid, liquid and gas exist, at which the molten cuprous chloride provides some heat for the copper oxychloride particles. The gaseous-phase products consist of oxygen gas and CuCl vapor (main products of reaction), hydrochloric acid gas, chlorine gas and water vapor (potential products of side reaction) leave the decomposition reactor with other solid/liquid products including undecomposed particles, molten cuprous chloride, unreacted solid copper chloride from hydrolysis reaction. The decomposition of Cu_2OCl_2 occurs through several elementary reactions listed in Table 1.6. At the temperature above 400°C , the solid Cu_2OCl_2 particles decompose and produce cupric oxide. At the high temperature range of 500°C - 600°C , one desired reaction of cupric oxide chlorination (Table 1.6 reaction number 3 or 4) and the undesired reaction of cupric chloride thermolysis (Table 1.6 reaction number 2) take place. At the temperature higher than 600°C , reaction number 6 potentially occurs

that consumes oxygen gas and produce chlorine gas. The other reactions listed in Table 1.6 could possibly occur when the reaction condition and kinetics become favorable [7].

Table 1.5. Detailed presentation of various design configurations of the hydrolysis reactor proposed in the literature.

Reactor	Configuration	Description
<p>(a) Vertical fixed bed reactor with a basket holder for studying the hydrolysis reaction. [29]</p> <p>(b) Vertical fixed bed reactor [30]</p>		<p>(a) Consisted of a quartz tube with an outer diameter of 0.50-in (13 mm) with a basket and quartz frit at the bottom. The Interam is used to hold the basket in place and Zirconia paper was set up to line the quartz basket. Crushed $\text{CuCl}_2 \cdot \text{H}_2\text{O}(\text{s})$ is deposited at the quartz glass in a fixed bed. The weight of the probe is measured before and after reaction.</p> <p>(b) $\text{CuCl}_2(\text{aq})$ was completely dehydrated in an oven at 100°C for 2 to 3 hours to form un-ball milled crystals. Tungsten carbide balls with an inert atmosphere of high purity argon are used to form ball-milled small particles. Ball-milled samples were introduced into a fixed bed quartz reactor with a length of 50cm and an outer diameter of 1.2cm and were immobilized by quartz wool. A syringe pump was used to regulate water droplets then they passed through a pre-heater to generate steam at 150°C.</p>

<p>Spray reactor enclosed in a vertical tubular furnace[26]</p>		<p>Enclosed in a vertical tubular furnace. A uniform temperature was obtained by a 91.5cm heating zone containing three separately powered parts. Thermal insulation is used at the top while the heating tape is used at the bottom to maintain a temperature at 150°C during the reaction.</p>
<p>Vertical fluidized bed reactor [7], [31]</p>		<p>A vertical quartz tube setup in an electrical furnace. A porous media distributor is used for the granular sample.</p>
<p>Natural convection loop with falling particles in the hydrolysis reactor. [25]</p>		<p>Consists of a 47in length and outer diameter of 1.5 in quartz glass placed in a tubular vertical furnace equipped with hot rasching rings/ wires to maintain the reaction temperature at 420°C. A water-cooled condenser is used to create a temperature gradient at two sides of the reactor. CuCl₂ (aq) drops from the burette placed at the top.</p>

Table 1.6. List of elementary reactions for the copper oxychloride thermal decomposition

ID	Elementary reaction	Temperature (°C)
1	Decomposition: $2\text{Cu}_2\text{OCl}_2(\text{s}) \rightarrow 2\text{CuO}(\text{s}) + \text{CuCl}_2(\text{s}) + \text{CuCl}(\text{s,l}) + 0.5\text{Cl}_2(\text{g})$	400-500
2	Thermolysis: $\text{CuCl}_2(\text{s}) \rightarrow \text{CuCl}(\text{l}) + 0.5\text{Cl}_2(\text{g})$	500-600
3	Chlorination: $\text{CuO}(\text{s}) + 0.5\text{Cl}_2(\text{g}) \rightarrow \text{CuCl}(\text{l}) + 0.5\text{O}_2(\text{g})$	500-600
4	Chlorination: $\text{CuO}(\text{s}) + \text{Cl}_2(\text{g}) \rightarrow \text{CuCl}_2(\text{l}) + 0.5\text{O}_2(\text{g})$	>480
5	Oxidation: $\text{CuCl}(\text{l}) + 0.5\text{O}_2(\text{g}) \rightarrow \text{CuO}(\text{s}) + 0.5\text{Cl}_2(\text{g})$	>550
6	Decomposition: $\text{CuO}_2\text{Cl}_2(\text{s}) \rightarrow \text{CuO}(\text{s}) + \text{CuCl}_2(\text{s})$	400-500
7	Oxidation: $2\text{CuCl}(\text{l}) + 0.5\text{O}_2(\text{g}) \rightarrow \text{CuO}_2\text{OCl}_2(\text{s})$	>550
8	Decomposition: $\text{CuO}_2\text{Cl}_2(\text{s}) \rightarrow \text{CuO}(\text{s}) + \text{CuCl}(\text{s,l}) + 0.5\text{Cl}_2(\text{g})$	>400

1.5. Electrochemical Process of Hydrogen Production

The electrochemical unit in the copper chlorine cycle is advantageous over the conventional water electrolysis method. The CuCl/HCl(aq) electrolyzer can be powered under the applied potential of roughly 0.4 V per cell, which is much less than the potential required for the conventional water electrolysis technology (1.4 V per cell). The electrochemical unit is identified based on the type of membrane and the half-cell reaction at the cathode side. The cell is categorized based on the products of the cathode (H_2 or Cu) and ions components transferred across the anode and cathode (H^+ or Cl). Table 1.7 provides the detailed schematic diagram of various types of CuCl/HCl(aq) electrolyzers with their associated anolyte/catholyte processes and anodic/cathodic half-reactions.

The most prominent alloys and materials used as electrode materials are titanium, platinum and glassy carbon. Easton et al. [32] used cyclic voltammetry at a rotating disk electrode to investigate the electrochemical kinetics for a noble metal based material for the anode electrode. They indicated that at a relatively higher pH, the difference between platinum and glassy carbon electrodes is reduced significantly. Also, they investigated ceramic carbon for the anode electrode. Two different types of membranes show promise for use in the CuCl/HCl(aq) electrolyzer as a porous polyethylene membrane (PPE) which is commercially available, inexpensive and has a maximum current density of about 0.3 A/cm² (platinum loading on cathode 2 mg/cm²). Nafion-based material with a design point of 0.5 A/cm² at 0.7 V was used in tests and the value of 0.30 A/cm² at 0.7 V was exceeded. The platinum loadings on both the cathode and anode 0.8 mg/cm² and no copper deposits

were observed in a 36 hour test with 85-100% hydrogen production efficiency. Furthermore, modifications of the MEA was made by computer painting of catalysts, fabricating different flow field patterns, controlling hydrophilic/hydrophobic properties of gas diffusion electrodes, and integrating stack and system controls [33].

Table 1.8 also illustrates different types of membranes and their associated CuCl_2 permeability tested at various institutions. At AECL some membranes were examined separately in a custom-made electrolyzer cell. Based on Naterer et al. [34], the Radel membranes (Polysulfonate membrane commercially from Solvay Advanced Polymers Radel NT 5500) tested in PSU represented more copper diffusion rate than Nafion tested at AECL. However, the permeability tests conducted by ANL demonstrated that the CuCl_2 permeability of Nafion 117 is ten times higher than the aforementioned membranes. Furthermore, new anode electrode structure and thermal spray coating with the development of advanced material improved corrosion resistance is reported in Naterer et al. [34]. In particular, an anodic ceramic carbon electrode (CCE) is investigated in the experimental tests of electrochemical reactions conducted by Easton et al. [35].

The electrochemical reaction in the copper chlorine cycle depends on the type of membrane and cycle version. The species can be transferred between cathode and anode sides through either cation exchange membrane (CEM) that passes protons or anion exchange membrane (AEM) that conducts only chlorine ions. The anode half-cell reaction is identical for all cases of cells. Hydrochloric acid must use in anolyte (and some cases catholyte) as an important agent to prevent CuCl precipitation in the electrolyte (CuCl does not dissolve in water), facilitates the formation of a hydrated CuCl in the catholyte and being either a source of Cl or protons. One of the main obstacles for long term operation of the electrochemical cell is the vulnerability of membrane to diffuse copper that oxidize this agent via the following reaction:

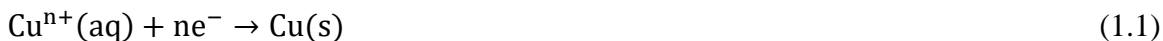


Table 1.7. Electrochemical unit categories based on membrane type and reaction in the cathode side.

Cell Type	Schematic diagram	Brief Description
Cu-H ⁺		<ul style="list-style-type: none"> • CEM (H⁺): permeable to protons. • Copper is produced at the cathode
Cu-Cl ⁻		<ul style="list-style-type: none"> • AEM (Cl⁻): permeable to chlorine ions. • Copper is produced at the cathode.
H ₂ -H ⁺		<ul style="list-style-type: none"> • CEM (H⁺): permeable to protons. • Hydrogen gas is produced at the cathode.
H ₂ -Cl ⁻		<ul style="list-style-type: none"> • AEM (Cl⁻): permeable to chlorine ions. • Hydrogen gas is produced at the cathode.

Table 1.8. Various types of membranes investigated at different institutions with the membrane measured proton conductivity and permeability to CuCl_2 [36], [37]

Membrane	Institution	Properties	Details
CEM IEC 2.0 & IEC 2.5	PSU/ANL/AECL	$\delta = 0.01 \text{ cm}$ * $\sigma = 0.038 \text{ S/cm}$ $K = 2.1 \times 10^{-8} \text{ cm}^2/\text{s}$ $\sigma / K = 18 \times 10^5 \text{ Scm}^2/\text{s}$	Cross-linked polysulfone membrane.
CM2-base	GTI/ANL	$\delta = 0.035 \text{ cm}$ $\sigma = 0.083 \text{ S/cm}$ $K = 5.8 \times 10^{-9} \text{ cm}^2/\text{s}$ $\sigma / K = 143 \times 10^5 \text{ Scm}^2/\text{s}$	Containing a double layer Nafion. To remove skin effects and improve membrane wettability, the etching process was applied to treat membranes.
GC2hydromod	GTI/ANL	$\delta = 0.003 \text{ cm}$ $\sigma = 0.0054 \text{ S/cm}$ $K = 9.4 \times 10^{-10} \text{ cm}^2/\text{s}$ $\sigma / K = 57 \times 10^5 \text{ Scm}^2/\text{s}$	Based on commercially available membranes. No heat treatment was applied before testing
NAFION 117	ANL/AECL/UOIT	$\delta = 0.020 \text{ cm}$ $\sigma = 0.0840 \text{ S/cm}$ $K = 6.4 \times 10^{-7} \text{ cm}^2/\text{s}$ $\sigma / K = 1.8 \times 10^5 \text{ Scm}^2/\text{s}$	A reference membrane trade sign for Du Pont Du Nemours.

* The conductivity values ($\sigma(\text{S/cm})$) are calculated using $\sigma = L/RA$ where L is the membrane thickness (cm), R is the membrane resistance (Ω), and A is the area of the electrode (cm^2).

This reaction should be implied because it consumes electrons supplied to the cathode for copper reduction and the crystals of solid copper block the gas transport pores and plate onto the electrode that poison the electrode surface. This may result in a drastic increase in cell over-potentials and consequently reduction in cell performance. Employing a proton-pump to control the amount of copper in catholyte to determine the effect of copper concentration on cell performance is recommended by Couborn and Easton et al. [38]. The challenge of copper precipitation is almost solved by increasing HCl concentration. Based on the experimental findings in Ref [39], however, the anode electrode does not need a catalyst for the electrochemical reaction, it requires a relatively large exposed surface area. Whereas the cathodic electrode requires catalyst (platinum-based material is commonly used).

A typical polarization graph for anodic half-reaction with a double side coated electrodes, the total active area of 2 cm^2 (two sides) and 100 mmol/L cuprous chloride

solution was presented by UOIT (shown in Figure 1.5). While the polarization graph for the full-cell electrochemical unit reported by AECl and PSU is shown in Figure 1.6. With respect to Figure 1.5, the experiment was conducted for two cases of stirred and quiescent solution of hydrochloric acid with a volumetric flow rate of 3 mol/L and 6 mol/L. Based on the obtained data shown in Figure 1.5, the half-cell potential for the current saturation is 0.4-0.5 V, while for the maximum current density (600 A/m^2), the corresponding half-cell over-potential of anodic reaction is 0.2 V. According to Figure 1.6, for the full-cell reaction experiment performed by AECl operating with the anolyte of 1M CuCl dissolved in 6 M HCl and catholyte of 6 M HCl, the corresponding current densities for the decomposition potentials of 0.57, 0.7, 0.8 and 0.9 V are 1000, 2380, 3420, and 4290 A/m^2 , respectively, which indicates the promising electrochemical reaction for obtaining high current densities at a reasonable low voltage of full-cell unit in the CuCl (aq)/HCl (aq) electrolyzer. Based on Figure 1.6 for PSU system, the corresponding current density for 0.48 V and 0.74 V is 100 A/m^2 and 1000 A/m^2 , respectively.

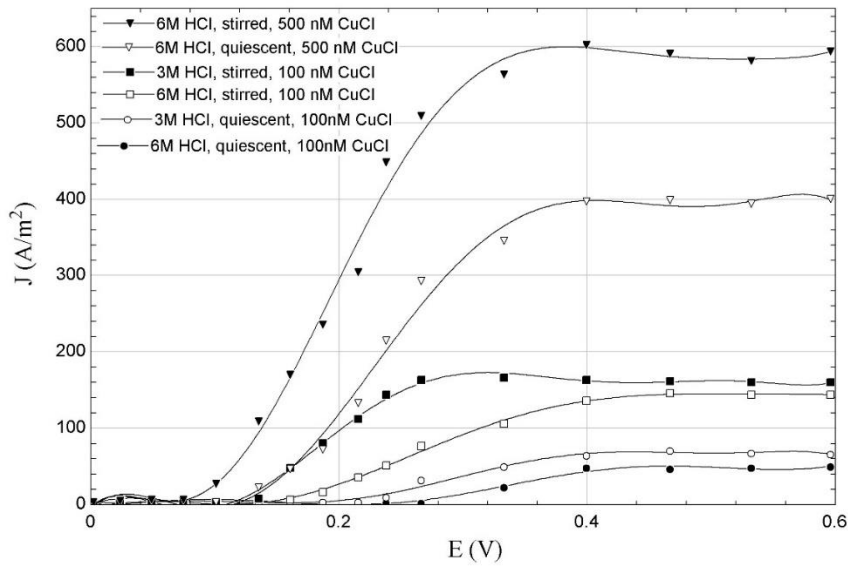


Figure 1.5. Polarization curve for anode half-reaction with a double side coated electrodes, total active area of 2 cm^2 and 100 mmol/L cuprous chloride solution, prepared by UOIT; Polyfit is applied for data extracted from [35].

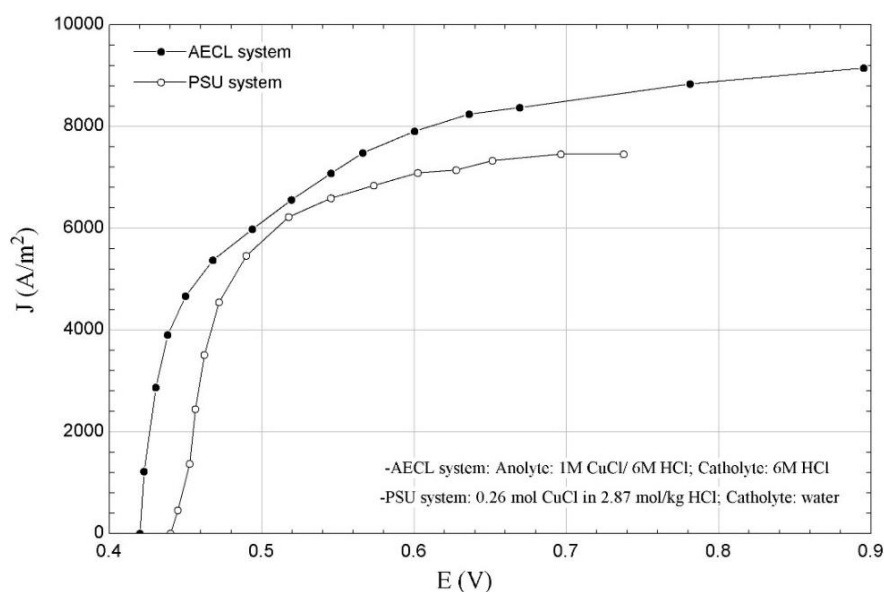


Figure 1.6. Polarization curve for the full cell electrochemical unit; AECL data extracted from [40] and PSU data extracted from [11]

1.6. Pressure Swing Distillation of Azeotropic Mixture

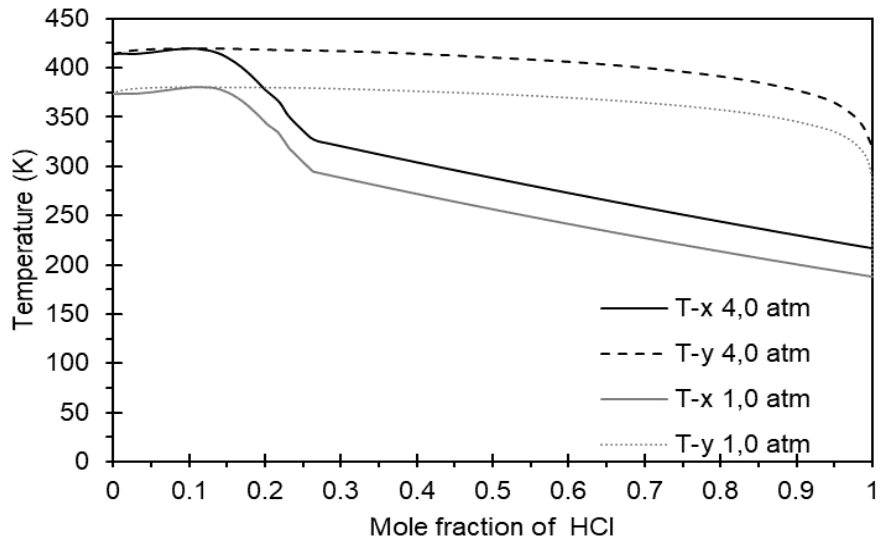
In the chemical process industry, purification of products is often obtained through separation processes. Distillation is one of the most greatly used purification processes. It is a process of vaporizing a liquid and recovering it by condensing the vapors and it depends on vapor-liquid phases' composition differences. If the mixture is in ideal or near ideal vapor-liquid equilibrium form, the conventional distillation process is used and if not a non-ideal vapor-liquid equilibrium behavior occurs and the mixture may form an azeotrope, which is a mixture that vapor and liquid phase concentrations are the same. Each azeotrope has a typical boiling point. If the boiling point of azeotrope is less than the boiling point temperatures of the components, it is referred to as minimum boiling azeotrope (positive azeotrope). If the boiling point of the azeotrope is greater than the boiling point temperatures of the components, it is referred to as maximum boiling azeotrope (negative azeotrope). Herein, special distillation processes, such as pressure swing distillation and extractive distillation, are used to separate the azeotropes [41].

Several methods are used in industry to separate azeotropic mixtures. In some methods, a third chemical component is added to the process to alter the vapor-liquid equilibrium.

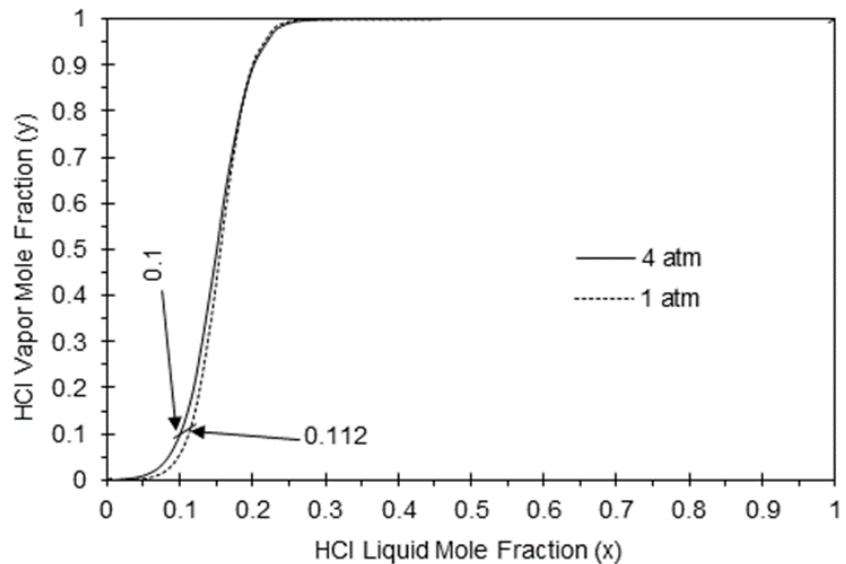
In the extractive distillation process, a higher boiling solvent is required. In the azeotropic heterogeneous distillation process, the entraining chemical component is used [41]. Another common method is pressure swing distillation (PSD) which is more environmentally benign and allows for energy savings as it does not require additional agents for the separation [42].

The principle of separation through PSD is based on a change in pressure. This specific change can alter the relative volatility of the mixture. Azeotropic composition differences between the two pressures is an important factor that demonstrates the applicability of using PSD [43]. In the PSD method, if the azeotropic composition changes significantly with pressure two columns operating at two different pressures can manage a separation. The approach is to manage the operation of one column at low pressure and the other column at higher pressure. If the azeotrope is a minimum boiling, the azeotrope will exit the top and the product stream will exit from the bottom. If the azeotrope is a maximum boiling, the azeotrope will exit from the bottom and the product stream exits from the top. The azeotrope is then fed to the second high pressure column. In high pressure column similar separation occurs with the low pressure column. Then, the azeotropic stream that exits from the bottom of high pressure column is fed back to the low pressure column [44].

Figure 1.7(a) illustrates Txy curves for the HCl-water azeotropic mixture at different pressures. At 1atm, the azeotropic composition is 11.2 mol % HCl (20.2 % by weight) and the temperature is 380 K. At 4 atm, the azeotropic composition is 10 mol % HCl (20 % by weight) and the temperature is 419 K. This small shift in the azeotropic composition is shown in Figure 1.7(b) which indicates that PSD may be attractive under those conditions. The HCl-water binary mixture at a maximum boiling azeotrope is considered in a pressure swing distillation process. The separation process is capable of concentrating HCl aqueous mixtures beyond the azeotropic composition. Figure 1.8 shows the considered pressure swing distillation system diagram, represented in a simplified manner for the purpose of this paper analysis. The system is supplied through the “Feed” port with aqueous hydrochloric acid of low concentration. There is a mixing port (device) at the input side which mixes the feed with the recycled acid. This process will enhance the concentration of the acid supplied into the lower pressure distillation column.



(a)



(b)

Figure 1.7. Txy diagram of HCl-water mixture at 1 and 4 atm. (b) Concentration diagram of HCl-water at 1 and 4 atm

An alternative to this arrangement is to provide a separate port for the recycled acid placed at optimum height on the stripping section of the column. The two alternatives may differ slightly in terms of performance in favor of the second one. Nevertheless, since our analysis purpose is to draw conclusions about the thermodynamic feasibility of the process and its performance parameter, rather than optimization, we have chosen the first configuration and modeled the mixing as an examined process.

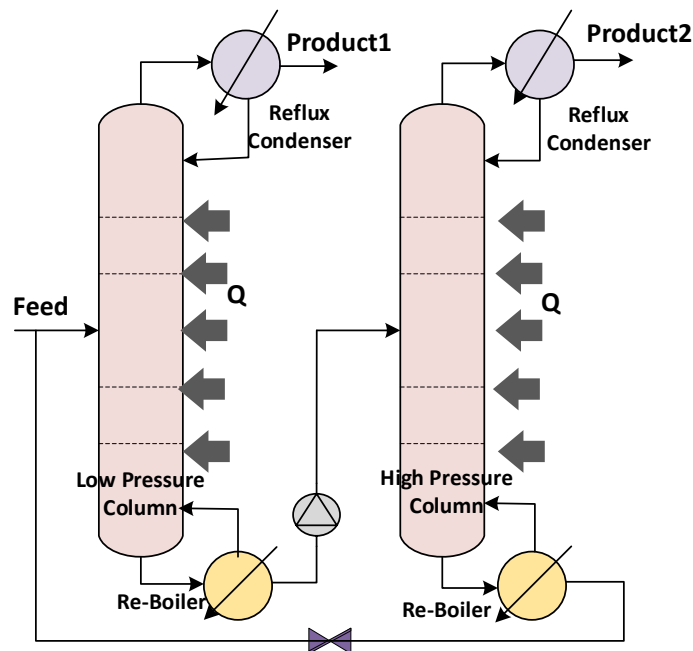


Figure 1.8. Flowsheet for pressure swing distillation

1.7. Dehydration Process of Cupric Chloride

To optimize the cupric chloride decomposition reaction, the steam to cupric chloride molar ratio should be selected reasonably. The products of electrochemical reaction-CuCl₂ diluted in HCl (aq)- are delivered into the separator units to split the depleted anolyte species including CuCl₂ diluted in HCl (aq) and unreacted cuprous chloride. In the dehydration unit of CuCl₂, water is extracted from copper chloride. Typically, per mole of cupric chloride dissolves in 8 moles of water, however, the desired steam to copper chloride molar ratio for the hydrolysis reaction is 2. With this molar ratio, CuCl₂.2H₂O crystals appear as an agglomeration of planar square cells. A slurry mixture of CuCl₂ and water is formed when the solution concentration is over the limit of solubility. The water should be fully removed from the CuCl₂ (aq) solution before entering to the hydrolysis reactor. Figure 1.9 shows the schematic of the experimental facility of low-temperature spray dryer at UOIT.

The drying methods for full elimination of water from hydrated copper chloride are illustrated in Table 1.9. In the spray drying method, the main operating parameters are atomization air pressure, atomization liquid feed rate and inlet air temperature, while the dependent parameters are powder quality, the moisture content in the product and outlet

air temperature. The crystallization method has drawn the attention due to the relatively small-size equipment that improves the economic viability of the drying process. In the crystallization process, the solid crystals precipitate from the aqueous mixture through a physicochemical liquid-solid separation technique at which the variation in the solubility conditions of solute in solvent leads the precipitation.

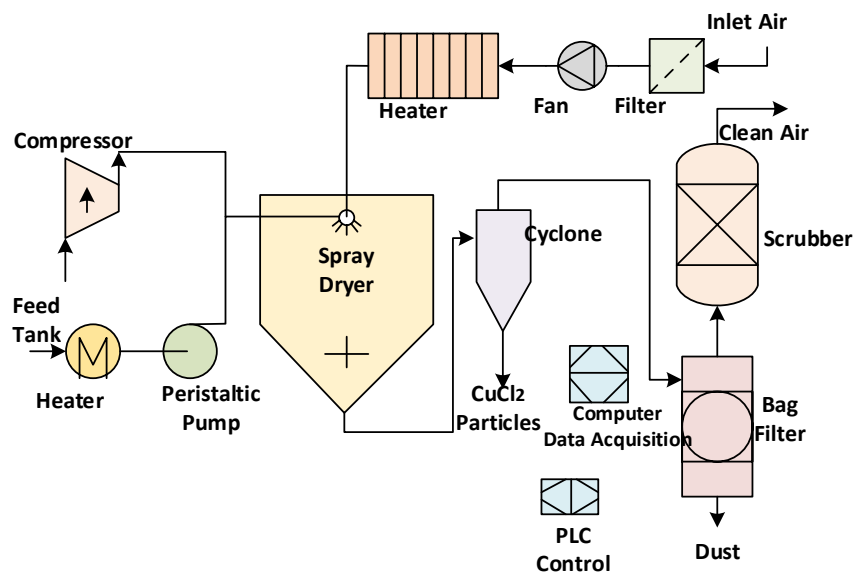


Figure 1.9. Experimental system at UOIT for low-temperature spray drying of hydrated CuCl_2

Table 1.9. Main types of copper chloride solution drying methods and process illustrations [7], [45]

Drying Method	Process description
Spray drying of copper chloride aqueous solution	The CuCl_2 (aq) droplets are sprayed into a hot air (at 80°C - 100°C) maintained in a large enough vessel.
Spray drying of cupric chloride slurry	A slurry mixture containing 3.5 moles of water per mole of cupric chloride is sprayed and water is eliminated through an evaporative heat and mass transfer.
Flash drying	The surrounding liquid of moisture suddenly becomes lower than the saturation point. This leads to a large pressure drop that changes the initial subcooled liquid to superheated liquid which results in the evaporation of moisture.
Combined flashing and spray drying	At a chamber where hot air is circulating, a slurry or aqueous solution is sprayed.
Crystallization	The solid crystals from an aqueous solution are created through the cooling process or/and concentration changes at which the solution drops below the solidification point.

1.8. Heat Recovery Prospects within the Cu-Cl Cycle

In the copper chlorine thermochemical cycle, there are many heat recovery potentials. Since the reactors and units of cycle operate at diverse temperatures, this provides opportunities to transfer heat between the endothermic and exothermic reactions via heat exchangers and to integrate heat engines and heat pumps with the cycle. Therefore, efficient thermal management of the cycle is momentous for improving the efficiency of the system significantly.

For this respect, pinch analysis may provide practical information for the required energy inputs and outputs of cycle processes and their associated levels of temperatures. The pinch diagram (temperature–enthalpy coordinate) can be expressed in terms of the temperature-entropy diagram as well (Table 1.10 and Figure 1.10). The streams indicate the thermodynamic systems interacting with surrounding through heat transfer solely. In Figure 1.10, the Heat Sink area (embraced of 9 to 13) represents the ideal (maximum) work that can be acquired from recovered heat from copper chlorine cycle. While the Heat Source area (encompassed of 1 to 8) indicates the ideal (minimum) work required by the heat pump to transfer useful heat to the copper chlorine cycle. Finding proper working fluids and processes allowing for the construction of heat engine and heat pump is one of the challenging issues for the integration of copper chlorine cycle with a thermal energy source (T_m). However, thermochemical processes such as vapor-compression or steam-methane reaction heat pump with copper chloride as working fluid has been regarded as an interesting insight to employ integrated heat pumps with Cu-Cl cycle.

Among the versions of the Cu-Cl cycle, the five-step cycle has the most heat recovery opportunities as it involves four thermal reactions. A pinch diagram of releasing and absorbing heat streams (Temperature-enthalpy profile) suggests a straightforward flow configuration for heat recovery purposes. Orhan et al. [46] evaluated the energy and exergy efficiencies of heat exchangers within the Cu-Cl cycle to improve the system performance. They calculate the heat exchanger effectiveness and the number of heat transfer units (NTU). They showed that the energy and exergy efficiencies improve with the increase of effective heat exchangers because more heat would be recovered by heat exchangers with higher effectiveness and consequently declines the demand for external heat. Al-Zareer et al. [47] analyzed thermodynamically the integrated generation IV gas-cooled fast nuclear

reactor and four-step Cu-Cl cycle for hydrogen and electricity production. They showed the improvement in system thermodynamic efficiency resulting from the applied heat exchanger network within the proposed system. Razi et al. [48] suggested six configurations of steam and heat recovery for the lab-scale integrated Cu-Cl cycle in UOIT and compared them from the net heat input, net thermal exergy, exergy destruction of heaters, heat recovery output temperature and the energy and exergy efficiencies of the cycle. Ishaq et al. [49] assessed a new tri-generation system integrated with industrial waste heat recovery and reverse osmosis desalination powered by flue gas ejected from a glass melting furnace integrated with a four-step Cu-Cl cycle.

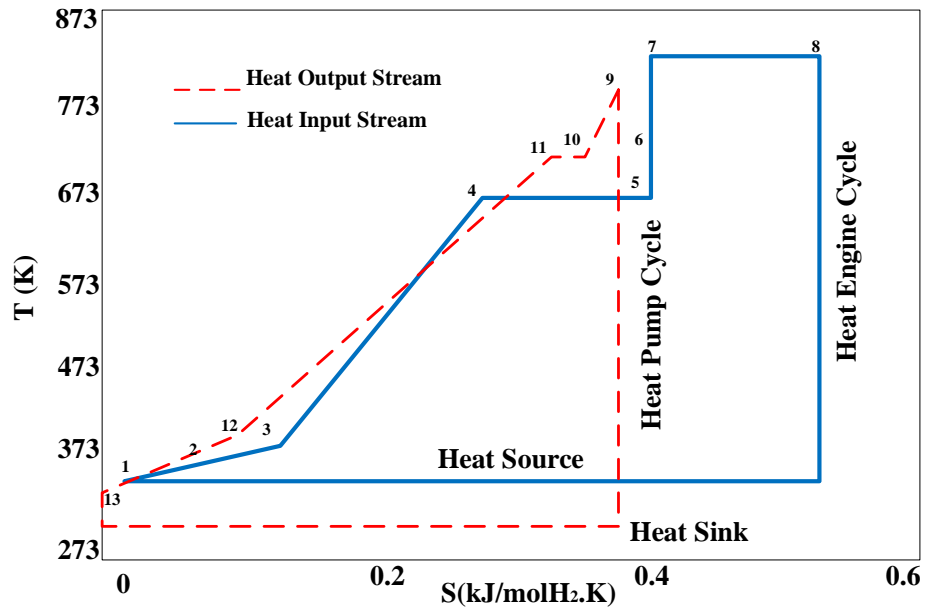


Figure 1.10. T-S diagram representing ideal heat pump and power systems integrated with a five-step copper chlorine cycle (modified from Refs. [7],[50]).

Recovering heat from the molten salt CuCl droplet formed at the oxygen production reactor is one of the challenging processes within the Cu-Cl cycle because of the interaction between droplets/particles with the gas stream as multi-phase flow. The liquid-phase CuCl droplets need to be cooled and solidified before entering into the electrochemical cell at a relatively low temperature of 50°C-80°C. Recovering heat from molten cuprous chloride follows the dynamics of high-viscosity droplet at which convective heat transfer and interactions of droplet breakup, velocity etc. are dominant. Jaber et al. [52], [53] developed

a model for the heat recovery process of molten cuprous chloride and compared the obtained numerical results with the reference data of a heat transfer problem of the droplet and air stream since there was no available experimental data for spraying of molten cuprous chloride. In Table 1.11 an overview of various heat recovery methods considered in the cooling of CuCl droplets is provided.

Table 1.10. Energy inputs and outputs for five-step Cu-Cl cycle

1-2: Electrolytic Cu(s) production step: $4\text{CuCl(s)} \rightarrow 2\text{CuCl}_2\text{(aq)} + 2\text{Cu(s)}$
2-3: Heating: $2\text{Cu(s)} + 2\text{CuCl}_2\text{(aq)} + 1.248\text{H}_2\text{O(l)}$
3-4: Heating: $\text{H}_2\text{O(g)} + 2\text{Cu(s)}; 2\text{CuCl}_2\text{(s)}$
4-5: Hydrolysis reactor: $2\text{CuCl}_2\text{(s)} + \text{H}_2\text{O(g)} \rightarrow \text{CuOCuCl}_2\text{(s)} + 2\text{HCl(g)}$
5-6: Copper particles heating: 2 mole Cu(s) per mole H ₂
7-8: Oxygen production reactor: $\text{CuOCuCl}_2\text{(s)} \rightarrow 2\text{CuCl(l)} + 0.5\text{O}_2\text{(g)}$
9-10: Cooling: $0.5\text{O}_2\text{(g)} + 2\text{CuCl(l)}$
10-11: Hydrogen production reactor: $2\text{Cu(s)} + 2\text{HCl(g)} \rightarrow 2\text{CuCl(l)} + \text{H}_2\text{(g)}$
11-12: Cooling: $\text{H}_2\text{(g)} + 0.5\text{O}_2\text{(g)} + 4\text{CuCl(l} \rightarrow \text{s)}$
12-13: Cooling: $\text{H}_2\text{(g)} + 0.5\text{O}_2\text{(g)} + 4\text{CuCl(s)} + 1.248\text{H}_2\text{O(g} \rightarrow \text{l)}$
W _{EL} : Electrical power needed to drive Cu(s) production step (1 → 2)
Q _H : Total heat input into the cycle
Q _C : Total heat rejected by the cycle
Q _L : Assumed heat losses, amounting to 5 %

1.9. Cost, Exergoeconomic and Life Cycle Assessments (LCA)

A cost analysis study was performed by Orhan [54]. It is assumed 15% annual return on investment, 10 years amortization period, 20% annual capital charge, \$800,000 per ton of hydrogen storage cost and \$300/kW electrolyzer stack. Based on the analysis findings at the capacity factor of 0.6, with the increase of production capacity (from 1 to 10 ton/day H₂), the cost of unit capacity declines in a logarithmic trend (from 3-6.8 million). Furthermore, the breakdown cost components percentage for a hybrid Cu-Cl plant is represented in Figure 1.11. A design and cost analysis for a multi-generation system included a four-step Cu-Cl cycle driven by biomass/solar is suggested by Ishaq et al. [55] in which Aspen Plus economic analyzer software was used by considering the real data available in its library. The installation cost, equipment cost and utility cost associated with the copper chlorine cycle are estimated in the software.

Table 1.11. Heat recovery methods from molten cuprous chloride within the copper chlorine cycle suggested by [51].

Type	Brief description
Drum Flaker	<ul style="list-style-type: none"> • Molten CuCl is Solidified at the outer surface of a rotating cylinder • A coolant is used to cool the inner surface. • Drum surface temperature is lower than the melting point.
Casting extruder	<ul style="list-style-type: none"> • Water as a coolant is supplied to the bottom at the outer shell (tube in a tube heat exchanger configuration) and heat is recovered to generate steam. • Molten copper chlorine enters at 530°C and leaves at 50°C. • To prevent the plugging of channel extruder is used to remove solids.
Spinning atomizer	<ul style="list-style-type: none"> • Molten cuprous chloride is introduced from a nozzle. • A centrifugal force is formed through a spinning disk. • CuCl droplets distributed around in relatively large vessels then fall, while inert gas (air) is dispersed by a perforated plate. • Heat is transferred from cuprous chloride to coolant and the generated solid particles are removed at the bottom.
Inert gas atomizer	<ul style="list-style-type: none"> • Atomization process with inert gas (air) is used to granulate cuprous chloride (a slurry of CuCl and water can be atomized as well). • Second gas (air) is used to extend particle jet (design of horizontal vessel should be in a way to avoid particles to stick at walls before solidification). • To separate the entrained CuCl solids, cyclone might be used.
Falling-through atomizer	<ul style="list-style-type: none"> • Sieve shaker is used to spray molten CuCl (due to the corrosive effect of molten salt spraying process is not easy, however, increasing the temperature of the upstream process will facilitate it). • Counter-current airflow is employed for the heat recovery process and molten CuCl solidification should be completed before reaching the bottom of the column. • Fluidized-bed can help to remove additional heat and the temperature of hot air resulting from the recovery process is 200°C.
Quenching atomizer	<ul style="list-style-type: none"> • A spray nozzle at top of vessel is used to pump molten CuCl and high injection temperature (530°C) is required for proper atomization (atomization gases are not required). Then the atomized cuprous chloride falls into a quenching water bath. • Upward stream is flowing to remove residual heat from CuCl. Some droplets are solidified during descent whereas others solidified inside the quenching water bath. • Steam is generated by heat released from quenching bath and then superheated in the area above bath.
Quenching atomizer with slurry vessel	<ul style="list-style-type: none"> • All droplets are solidified in the column instead of quenching bath (protective coating for corrosion is required inside the vessel) • After agglomerating solid particles at the bottom of the main vessel, they are delivered to the water bath for cooling process. • Flowing steam in the vessel absorbs heat of droplets and become superheated (there is no steam explosion).

Exergoeconomic study relates exergy analysis of a system into economic laws to provide instructive information on cost-effectively operation, optimization and design of a system. In fact, mass, energy, exergy and cost formulations are incorporated to form a quantitative connection between thermodynamic loss and capital cost of the examined system. For enhancing the economic feasibility of copper chlorine cycle, some studies are carried out in the content of exergoeconomic analysis. The exergo-environmental and exergoeconomic analysis of integrated system including copper chlorine cycle were addressed in Ozbilen et al. [56], and Ozcan and Dincer [57]. Moreover, Orhan et al. [58] assessed energy and exergy efficiencies of the copper chlorine cycle through the sensitivity analysis and compared the costs of Cu-Cl cycle and other energy sources as renewable energies, nuclear energy and fossil fuels. Also in a comparative study, they carried out an exergoeconomic analysis for different integrated Cu-Cl cycle configurations. They emphasized on the informative information for improving the cost-effectiveness of the copper chlorine cycle [59].

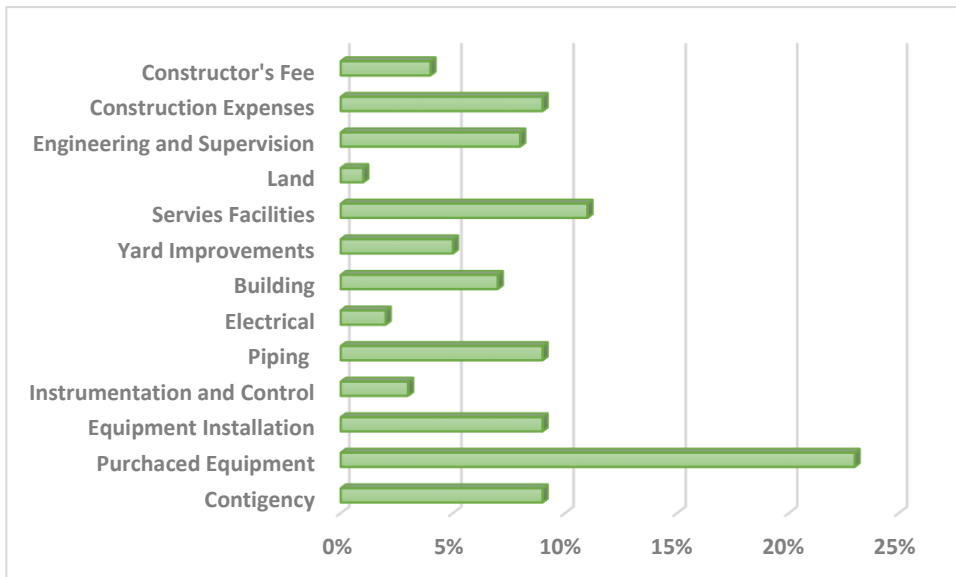


Figure 1.11. Breakdown cost components percentage for a hybrid Cu–Cl plant is represented; data from Orhan et al. [54].

In general, life cycle assessment (LCA) is a study of evaluating the environmental impacts of a product or process from all life-cycle stages (cradle-to-cradle) including production, transportation, installment, operation and disposal steps of the processes. The LCA methodology can be performed through the following phases as defining scope and

goal (boundaries and objectives); inventory information on material and energy flows (known as life cycle inventory (LCI) analysis); Evaluation of environmental impacts associated to material and energy flows (known as life cycle impact assessment); finally, improvement analysis including results, concluding remarks and recommendation and improvements.

In particular, for producing hydrogen, the type of energy in terms of process driving can be biological, photonic, electrical, thermal, or mechanical. Here, LCA study is required to assess the means of hydrogen production and selection of the best possibility. In Ozbilen et al. [60], [61], the LCA methodology is applied to assess the total environmental impact of the hydrogen production processes and to recognize environmentally crucial phases. They outlined the environmental impacts and emissions concerning standard categories which the overall system emissions are the summation of outputs of a thermochemical cycle and nuclear power sector.

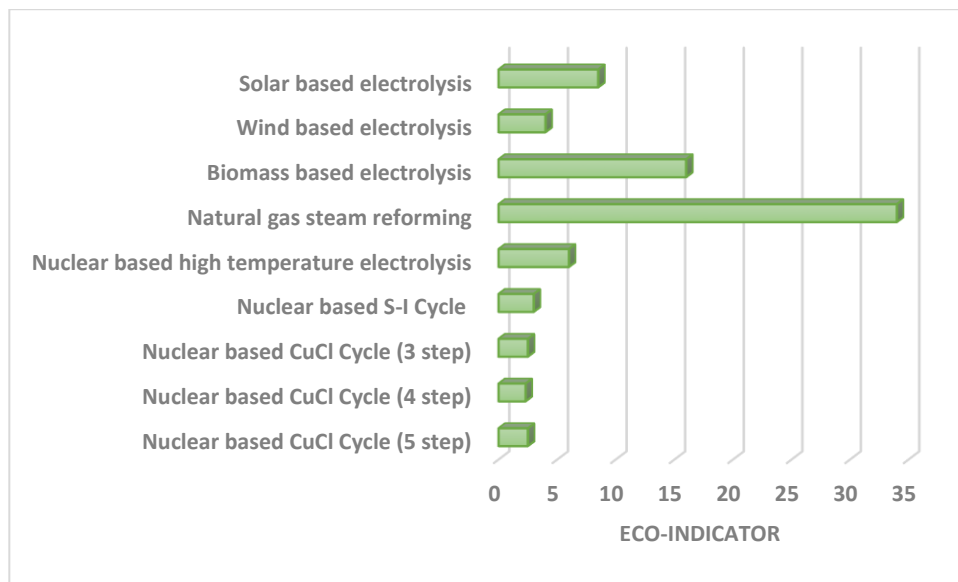


Figure 1.12. Global warming potential (GWP) eco-indicator for different hydrogen production methods; data from [60], [61].

The global warming potential (GWP) for different hydrogen production approaches is shown in Figure 1.12. It can be observed that the minimum environmental impact is associated to the four-step copper chlorine cycle compared to the three and five-step Cu-Cl cycles. The nuclear-based four-step Cu-Cl cycle is the most environmentally benign

approach of hydrogen production in terms of GWP. From Refs. [60], [61], the GWP declines drastically from 15.8 to 0.56 kg carbon dioxide- equivalent, if the required electrical energy of all processes supplied by the nuclear plant. It is shown that the highest environmental impact belongs to mining and conversion stages because of fossil fuel consumed for this process. Based on the parametric studies, the impact categories are not affected considerably by the further increment of hydrogen production capacity and lifetime.

1.10. Motivation

Hydrogen is a promising clean energy carrier and carbon-free source which does not emit greenhouse gases as fuel. In addition to a large need for hydrogen in industrial sectors and for petroleum products, it also has been noticed in the transportation sectors as a potential fuel for vehicles, trains, ships and others. Only an insignificant amount of hydrogen is produced by the clean methods, while, most of the current systems like the reforming process utilize fossil fuels to produce hydrogen with releasing a considerable amount of carbon dioxide. This growing the attention toward sustainable large-scale technologies to mitigate the adverse effect of greenhouse gases. Here, thermochemical water splitting cycle has opened a promising alternative large-scale hydrogen production method which raised wide interests and studies for more development and improvement of such a system. Thermochemical water splitting cycle is comprised of series of chemical and physical processes without emitting contaminants into the environment. Except water which is decomposed into the hydrogen and oxygen, all other intermediate chemical species are recycled in a closed-loop cycle. Although thermochemical water dissociation technology has not been commercialized as yet, numerous recent studies indicated that such technology can potentially compete with the conventional steam methane reforming process for hydrogen production [29].

Over 200 cycles for thermochemical water splitting process have been surveyed by literature, however, a few types of them have been identified through the theoretical and experimental investigations that proved the scientifically and economically feasibility of such systems. With accounting the chemical viability, availability and abundance of materials and thermodynamic feasibility, safety and simplicity, the following thermochemical cycles are found as potentially commercial significance: sulfur-iodine (S-

I), copper chlorine (Cu-Cl), magnesium-iodine (Mg-I), iron-chloride (Fe-Cl), copper-sulphate (Cu-SO₄), vanadium-chloride (V-Cl), cerium-oxide (CeO₂/Ce₂O₃), Ni-Ferrite (NiFe₂O₄), ZnO/Zn and Fe₃O₄/FeO redox reactions and hybrid chlorine [1], [5], [62], [63]. Among these feasible types, the copper-chlorine cycle is a promising low-temperature kind of water-splitting process for producing hydrogen.

Cu-Cl thermochemical hydrogen production cycle is benefiting from many advantages. Besides the available chemical species, the higher overall conversion efficiency of cation exchange membrane electrolyzer compared to the conventional electrolyzer and the relatively low-temperature need (less than 530°C) compared to sulfur-ion (S-I) cycle, make a great potential for the low-grade waste heat recovery in such cycles [1]. Argonne National Laboratory in USA, Pennsylvania State University, Canadian Nuclear laboratories (Atomic energy of Canada Limited) and UOIT are leading on scaling up the copper chlorine cycle for practical application [5- 8]. Currently, the Clean Energy Research Laboratory (CERL) team at UOIT is extensively working on a four-step Cu-Cl cycle experimentally and theoretically to develop this technology into a larger scale as industrial sectors.

Various studies are done for the whole hybrid thermochemical water decomposition cycle integrated with thermal energy sources like nuclear energy, renewable energy, hybrid nuclear-renewable energies, fossil fuels and waste heat from the industrial plants. Such studies primarily assessed the main components of the Cu-Cl cycle from the energy, exergy, exergoeconomic, exergo-environmental, optimization, and cost methods.

There is an immediate need for reducing the environmental impact of fossil fuels specifically in the transportation sector to mitigate global warming. To achieve this aim, the underlying motivation of this thesis is to demonstrate a practical lab-scale Cu-Cl cycle at UOIT for the first time and establish the large-scale feasibility of the Cu-Cl cycle for sustainable hydrogen production. The key contributions of this dissertation are summarized below.

- The lab-scale integrated Cu-Cl cycle is introduced and addressed with separate units for recovering oxidized anolyte for the first time which is not reported in past literature.

- The low and high pressure distillation columns of the PSD method to separate HCl from water are newly designed, modeled and simulated to determine the feasibility of concentrating the HCl (aq) through its azeotrope, which is not possible to manage with a conventional distillation method.
- A new design is presented for the hydrolysis reactor within the proposed Cu-Cl cycle and analyzed through a hydrodynamic study to find the residence time of the reactants. Also, the chemically reacting gas-solid reaction model based on a shrinking core method is developed to predict the conversion of copper chloride solid particles.
- The CuCl/HCl(aq) electrolyzer stack of the experimental cycle is modeled based on the electrochemical formulation to predict the decomposition potential of individual cells and overall stack. Moreover, to prevent the gas and solid accumulation and the formation of hot spots especially at elevated current densities, the anolyte/catholyte flow distribution within the MEAs is modeled based on the finite element method by Comsol multi-physics simulator software.
- The overall lab-scale integrated cycle is simulated in Aspen Plus software to evaluate the thermodynamic properties of all streams interacting within the cycle and to validate the components of the cycle.
- To evaluate the viability of the system, an exergoeconomic analysis is conducted to relate exergy with costs.
- Finally, to improve the performance of the lab-scale integrated Cu-Cl cycle, a multi-objective optimization method is used based on a genetic algorithm with the help of an artificial neural network.

1.11. Objectives

In this PhD study, an integrated lab-scale of four-step Cu-Cl water decomposition cycle for hydrogen production at UOIT will be investigated and analyzed. This raises the motivation to develop the model of different parts of the cycle for better, more efficient and more sustainable production of hydrogen as an alternative fuel and as a carbon-free energy carrier. Although some theoretical examination for simplified Cu-Cl cycles or some experimental studies on a specific part of such systems were carried out in the past, there is no previous work that practically incorporates the whole Cu-Cl cycle modules in one

unit as an integrated Cu-Cl cycle. This work is necessary to be done as a part of a larger project aiming to develop and commercialize the water splitting Cu-Cl cycle. This will provide a better understanding of the practical challenges regarding the real cycle setup and consequently try to fix and modify them. The main objectives of this study are listed as follows:

1. To develop and analyze the lab-scale of an integrated Cu-Cl cycle setup for hydrogen production
 - Analyzing the system using Aspen Plus software for the determination of mass and energy streams entering and exiting each component.
 - Modeling some systems through mathematical models that are solved using Engineering Equation Solver (EES).
2. To analyze the integrated Cu-Cl cycle energetically and exergetically
 - Performing detailed energy and exergy analyses for each of the system's components; calculating the energy and exergy efficiencies of each module, as well as determining the exergy destruction rates and ratios of all components in the integrated Cu-Cl cycle.
 - Detecting the main irreversibility sources and proposing some suggestions such as heat recovery and isolation of some parts.
 - Calculating the energy and exergy efficiencies for each component of the system and the overall performance measures.
 - Performing parametric analysis for the understanding of the cycle performance under different operational conditions with the variation of key parameters.
 - Conducting an exergoeconomic analysis to gain insight into the system cost-effectiveness subject to its cost of irreversibilities
3. To perform a kinetic and hydrodynamic study of reactors in the integrated Cu-Cl cycle:
 - Conducting a hydrodynamic study to formulate the gas-solid conversion in the hydrolysis reactor, and to study the flow distribution in the CuCl/HCl(aq) electrolyzer stack.

- Developing a kinetic model and diffusion mass transport mechanism through a shrinking core model for prediction of reactant conversion rates. Also, a kinetic model to predict the over-potentials dominated in the CuCl/HCl(aq) electrolyzer unit.
- 4. To optimize the system with respect to overall exergy efficiency and overall cost via multi-objective optimization.
 - Defining the objective functions, decision variables and constraints in accordance with cost and thermodynamic parameters.
 - Incorporating an artificial neural network in conjunction with the GA multi-objective optimization method for finding the optimal operating condition for higher efficiency, higher production and lower costs in the system.
 - Selecting the optimal solution based on the trade-off points for maximization of exergy efficiency and minimization of cost.

Chapter 2 . Literature Review

2.1. Overview of the Cu-Cl Thermochemical Cycle

Various studies were done for the whole thermal-electrical hybrid thermochemical water decomposition cycle integrated with thermal energy sources like nuclear energy, renewable energy, hybrid nuclear-renewable energies, fossil fuels, and waste heat from industrial plants. Such studies assessed the Cu-Cl cycle from the energy, exergy, exergoeconomic, exergo-environmental, optimization and cost methods [8, 64- 70]. Others focused on the specific step of the thermochemical cycle like hydrolysis, thermolysis or electrolysis units through an empirical investigation and a detailed theoretical calculation such as the heat and mass transfer analysis, kinetics of the reactions, etc. [1, 71, 72].

Ozcan and Dincer [67], [68] developed the magnesium and chlorine cycle (Mg-Cl cycle) integrated with a nuclear reactor, liquid hydrogen storage and Rankine cycle and analyzed it from the aspects of energy and exergy and exergoeconomic views. From the simulation results, they found that the Mg-Cl cycle can be potentially competitive with other types of thermochemical cycles. They reported 18.6% and 31.4% for the energy and exergy efficiencies of the analyzed system under the specific operating conditions. Orhan et al.[11, 68, 75] compared different configurations of thermochemical copper-chlorine water decomposition cycles with energy, exergy and exergoeconomic analysis and evaluated them in combination with the nuclear plant. They reported the energy and exergy efficiencies for both four-step and five-step Cu-Cl cycles integrated with the nuclear plant. Ozbilen et al. [70] examined a four-step copper-chlorine thermochemical water splitting cycle from the facets of exergo-environmental and exergoeconomic analyses. They also performed a multi-objective optimization on the proposed system to achieve the optimal operating condition.

Al-Zareer, Dincer and Rosen [8, 70, 76-78], carried out a comprehensive thermodynamic study of different Cu-Cl thermochemical cycle configurations powered by distinct energy sources as a coal gasifier, supercritical water-cooled nuclear reactor (SCWR) and solar-based system. In a comparative study, they compared the configurations from the unit thermal energy and exergy utilization in all system components, and the relevant exergy destruction, energy and exergy efficiencies for each configuration.

Through the Aspen Plus simulation model, they addressed that the integration of SCWR with the four-step Cu-Cl cycle is leading over other configurations in terms of energy and exergy efficiencies. Khalid et al. [75], [76] incorporated high-temperature electrolysis to evaluate four configurations of the Cu-Cl cycle and analyzed the systems thermodynamically. Also through an experimental investigation, they asserted the feasibility of the high-temperature electrolysis utilization. Additionally, Ishaq et al.[77], [78] addressed a thermodynamic study for recovering waste heat from the industrial application into the Cu-Cl thermochemical water decomposition cycle. Ref. [79] presented the specific exergy costing (SPECOC) method, whereas [70] applied the other costing method, exergoeconomic analysis, combined with the environmental aspect, in the form of an exergo-environmental study.

Since the Cu-Cl thermochemical water decomposition cycle for producing hydrogen comprises of several thermochemical reactions in the reactors, electrochemical reaction in the electrolyzer and several physical separation processes, many studies and experiments have been conducted for the specific part of this system. Here, CNL and UOIT have developed a demonstration Cu-Cl cycle working at a maximum temperature of 550 °C [80]. UOIT has also developed and enhanced another thermochemical Mg-Cl cycle [67], [68], [81], where the researchers enhanced the efficiency of the process by adding one step to the cycle.

Dincer and Naterer [80] performed a comprehensive overview of the theoretical and experimental advances of the thermochemical water-splitting cycle in the Clean Energy Research Laboratory (CERL) at UOIT to address the current challenges in hydrogen production processes as efficiency, cost and environmental issues, and proposed opportunities for the sustainable hydrogen production. In this survey, several novel experimental investigations on the Cu-Cl cycle were done (each element was analyzed separately). These activities are involved with the application of high-temperature electrolysis, convective spray drying experiment, XRD diffraction pattern of solid products in hydrolysis (to determine the composition of the solid products), empirical investigation of anolyte temperatures and flow rate effects on the electrolyzer performance, the unreacted hydrolysis reactants and finally the pressure effects on copper oxychloride

decomposition (thermolysis step). Wang et al. [86, 87], assessed a design viewpoint regarding the reactor scale-up in the Cu-Cl cycle to handle multiphase flow in the molten salt reactor (or themolysis step). They also compared different hydrolysis reactions in 2, 3 and 5 step Cu-Cl cycles which use reactive spray drying (combining hydrolysis reaction with spraying) instead of a separate dryer unit (as in 4-step Cu-Cl cycle). They also addressed the technical challenges of transportation of solids which can block the reactor operation. Finally, they provided new data about the design parameters, capacity required for feed materials, steam and heat supply for achieving insight about the reactor scale-up to a lab-scale capacity.

Also, Naterer et al. [1], [84] in past review papers reported the recent advances in the Cu-Cl cycle. In these surveys, they provided the recent experimental and numerical results for different steps of the copper-chlorine cycle. They indicated the collaboration of UOIT, CNL and Argonne National Laboratory through the Generation IV International Forum (GIF [85]) to scale up the Cu-Cl cycle and enable this technology to a larger scale.

A list of institutions and alternative identification of Cu-Cl cycle are provided in Table 2.1. There have been numerous past studies for modeling and evaluating various versions of Cu-Cl cycle from a thermodynamic viewpoint at which the cycle is integrated with nuclear/renewable thermal-power plant. Al-Zareer et al. [71] proposed an integrated supercritical water-cooled nuclear reactor and hybrid copper chlorine cycle. They presented a novel design for the proposed system in which steam supplied heat required in Cu-Cl cycle through heat recovery from some units. They investigated the effect of steam circulation on the energetic and exergetic performance of integrated system and outlined the significant impact of this parameter. Furthermore, a comparative thermodynamic study of the Cu-Cl cycle derived by various energy sources comprising solar, coal gasifier, supercritical water-cooled nuclear reactor (SCWR) [8]. Khalid et al. [76] investigated a new three-step Cu-Cl cycle considering the effects of reactors temperatures on the overall energy and exergy efficiencies. They also compared four different copper chlorine cycle configurations incorporated with a high-temperature electrolysis unit from the thermodynamic viewpoint. Wu et al. [86] proposed a new stand-alone 2-step Cu-Cl cycle with the $\text{CuCl}/\text{HCl}(\text{aq})$ electrolyzer for tri-generation of hydrogen, oxygen and electricity.

The power efficiency of the system is assessed in five different case studies to meet the value of at least 48%.

Table 2.1. A list of laboratories and institutions investigated different types of Cu-Cl cycles.

Cycle	T _{max} (°C)	Institutions	Other identities
Cu-Cl-2	550	NCLI, Dokyia and Kotera [13]	Cu-Cl-C, in Lewis and Masin [14]
Cu-Cl-3a	527	ANL, Perret et al [5]	ANL-287 in Abanades et al. [5] Three-step cycle (UOIT) in Wang et al. [16]
Cu-Cl-3b	527	AECL and ANL. Suppiah et al. [17]	Cu-Cl-B in Lewis and Masin [14] Three-step cycle (UOIT) in Naterer et.al [18]
Cu-Cl-3c	800	NCLI, Dokyia and Kotera [13]	UNLV-56, in McQuillan et al. [19] Cu-Cl-D in Lewis and Masin [14]
Cu-Cl-4a	527	UOIT, Wang et al. [16]	Four-step cycle (UOIT) in Wang et al. [16]
Cu-Cl-4a	480	UOIT, Farsi et al [20]	Four-step cycle (UOIT) in Farsi et al. [20]
Cu-Cl-4b	527	UOIT, Naterer et al. [18]	Four-step cycle (UOIT) in Naterer et al.[18]
Cu-Cl-5	527	IGT, Carty et al. [17]	ALTC-1 in Lewis et al. [17] Cu-Cl-A in Lewis and Masin [14] Five-step cycle (UOIT) in Wang et al.[16]

2.2. CuCl₂/HCl (aq) Electrolyzer

Since the anolyte fed into the cation exchange membrane electrolyzer creates complex speciation because of its strong ionic solution, the chemical exergy specification of an anolyte medium is required to be estimated through the correlations associated with the anolyte speciation in actual conditions. In this regard, Hall et al. [91-94] measured the thermodynamic properties of the anolyte at CuCl (aq)/HCl (aq) electrolyzer with a specific composition through the experimental open-circuit potentials (OCP) and compared them with values acquired from the prospective thermodynamic model (Gibbs energy minimization method). They showed that the speciation effect and activity coefficient has a major effect on the OCP data for the specific property determination. They also reported the values for the Gibbs energy, entropy and overall efficiency of the CuCl (aq)/HCl (aq) electrolyzer at the specific operating condition. Moreover, Zamfirescu et al. [91] the

chemical exergy for the anolyte in the cation exchange membrane electrolyzer in Cu-Cl cycle for producing hydrogen. They utilized the Gibbs energy minimization method and provided an average value of 14.09MJ/mole anolyte for the anolyte chemical exergy. Also, they compared three different cases associated with the mass flow rate of anolyte interacting with the electrolyzer and determined the best case scenario in terms of electrical power consumption by the electrolyzer. In another study, Zamfirescu, Dincer and Naterer [65] developed novel regression formulae to estimate the relevant thermophysical properties of copper compounds such as Cu_2OCl_2 , CuCl , CuO , and CuCl_2 .

Modeling of $\text{CuCl (aq)/ HCl (aq)}$ electrochemical cell through thermodynamics and kinetics provides a predictive view for effective design parameters and performance improvement of electrochemical reaction. Hall et al. [39], [91-93] from PSU group performed a thermodynamic study of $\text{CuCl (aq)/HCl (aq)}$ electrolyzer using equilibrium thermodynamics and a kinetic study of examined electrolyzer using rotating disc electrode (RDE) and scanning electron microscopy (SEM). Also, they presented a model to simulate the applied potential [39] in which the equilibrium electrode decomposition potential was estimated from the Nernst equation for anode and cathode sides that incorporates the concentration values of species ($b_{\text{CuCl}_2(\text{aq})}$, $b_{\text{CuCl}(\text{aq})}$ and $b_{\text{H}^+(\text{aq})}$ obtained from GEM), Faraday's constant ($F=96485\text{C}\cdot\text{mol}^{-1}$), molar gas constant ($R = 8.3145 \text{ J}\cdot\text{mol}^{-1}\cdot\text{K}^{-1}$) and thermodynamic temperature ($T = 298 \text{ K}$). Here, $E_{\text{eff}}^\circ = 0.656 \text{ V}$, $E^\circ = 0$. The empirical parameter of γ is the mean activity coefficient and $P_{\text{H}_2(\text{g})}$ denotes the partial pressure of produced hydrogen gas. It should be mentioned that at equilibrium condition, all anodic half-cell reactions have identical redox potential.

Various anodic half-reactions can occur depending on HCl (aq) and CuCl (aq) concentration and exciting species in the anolyte. The anode half-reactions can be predicted based on the oxidation/reduction phenomena and species concentration determination through Gibbs Energy Minimization (GEM) approach. For instance, based on 2 mol/L of CuCl (aq) and 10 mol/L HCl (aq) the most probable anode half-reactions are [92]:



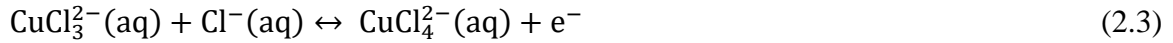


Table 2.2. Summary of electrode development of CuCl/HCl (aq) electrolyzer for anodic and cathodic reactions

Institution	Remarks	Ref
UOIT	<ul style="list-style-type: none"> • Determined better structure for anode electrode at high current densities and reduce over-potential losses using standard three-electrode including anode, saturated calomel reference electrode (SCE) and platinum wire counter electrode. • Determined the over-potential diagrams for the half-cell reaction with respect to SCE. • Demonstrated the HCl concentration effect on reaction kinetic with the impact of dissolved CuCl component. 	[35], [95]
AECL	<ul style="list-style-type: none"> • Conducted full-cell test to confirmed the high current density (>1000A/m²) in 1 mol/L CuCl dissolved in 6 mol/L HCL. • Conducted half-cell experiment with catalyst coated/uncoated graphite separator plate (GSP) and 1 mol/L CuCl/6 mol/L HCl anolyte solution. The best performance was belong to catalyst-free GSP with a saturation current density of 1,200A/m² at 0.5V polarization and 0.263V over-potential at anode side. • Development of an advanced cathodic electrode in which the cathode half-reaction was tested in a three-electrode cell with the reference electrode of SCE and counter electrode of graphite rod. 	[96]
PSU	<ul style="list-style-type: none"> • Reported the promising experimental results for water as the sole proton transferor catholyte instead of using a high concentration of HCl. • A commercial membrane electrode assembly (MEA) of HYDRion 115 and HYDRion 117 produced by Electrochem Inc was used in the full-cell water electrolysis experiment. • Conducted an electrochemical reaction test with a 5 cm² proton exchange membrane (PEM) NAFION commercial cell for water electrolysis supplied by Electrochem Inc and attached with two carbonic diffusion layers. The anolyte flow rate was changed from 30 to 68 mL/min. In contrast to AECL experiment, in PSU experiment, the oxidized anolyte (spent anolyte) is not recycled. 	[11] [39], [87]– [89], [97]
ANL	<ul style="list-style-type: none"> • Recommended Electro-winning technology using carbon electrodes at cathode side because of copper precipitation (3 to 100 μm dendritic powder). The anolyte feed port and product steam output are placed at the bottom and top of cathode compartment respectively. • Demonstrated that the copper production development from electrochemical cell of Cu-Cl cycle has been set aside because the alternative producing hydrogen performs to be more competitive. 	[17]

Odukoya and Naterer [93] from UOIT group carried out an electrochemical diffusive mass transfer and entropy generation of copper-based electrochemical cell. Also, Orhan et

al. [94] analyzed a copper production step (electrochemical reaction) from the energy and exergy aspect considering the cell temperature and reference environment temperature as two design parameters. Farsi et al. [24] developed a predictive thermodynamic, kinetic and hydrodynamic models for the lab-scale experimental CuCl (aq)/HCl(aq) electrolyzer stack. The GEM analysis and kinetic model revealed that the higher the anolyte temperature, the lower the decomposition potential and consequently the higher the stack voltage efficiency. From hydrodynamic simulation results, they showed the relatively uniform flow distribution at the examined electrolyzer compared to the common water electrolyzer in which gaseous phase reactants interacted. Also, anolyte chemical exergy calculation is addressed in Zamfirescu et al. [91] and the equilibrium thermodynamic study of CuCl (aq)/HCl (aq) electrolyzer is presented in Soltani et al. [92]. Table 2.2 presents an overview of electrode development of CuCl/HCl (aq) electrolyzer for anodic and cathodic reactions accomplished at different institutions.

2.3. Hydrolysis Reaction

Lewis et al. [29] with the collaboration of the Argonne National Laboratory and a group of universities proposed a consistent methodology in the Nuclear Hydrogen Initiative (NHI) for efficiency assessment of Cu-Cl cycles by presenting the criteria as chemical viability and thermodynamic feasibility. In this regard, they defined three levels for the efficiency calculation and showed how the efficiency changes as the process knowledge and optimization enhanced. Hence, in level 1, they considered the energy needed for the proposed cycle. In level 2, they took into account the equilibrium phase like side reactions. In level 3, they applied the more reliable actual product distribution through the experimental data. In the second part [14], they brought together the results from the universities and investigated the criteria for down selection of one or two cycles. Finally, in the third part [98], they provided a more precise evaluation of the Cu-Cl cycle. They also recognized the challenges associated with the development of different cycles like unavailable thermodynamic data which should be evaluated through accurate engineering expertise or an Aspen Plus databank.

Ferrandan et al. [26] carried out an experimental study for the hydrolysis reaction of CuCl₂ in the Cu-Cl cycle. They found that from the stoichiometry of the reaction the

steam/CuCl₂ ratio is 0.5, while from the experimental investigation, chemical and XRD analysis, the ratio of steam to CuCl₂ in the hydrolysis reactor needs to be between 23 and 30 to achieve 100% conversion of CuCl₂ at atmospheric pressure. On the other hand, they indicated that to have high process efficiency, less excess steam at the reactor is advantageous which can be obtained by reducing pressures (0.4- 0.7 atm) resulting in a significant reduction in the CuCl concentration of the solid products. The hydrolysis reactor design configuration developed by the Argonne National Laboratory uses a spray reactor to increase the contact area between CuCl₂ solid particles and steam and consequently increase the reactor performance. The atomizer design in the spray reactor is critical for obtaining a high yield of the desired product. Based on the experiments, a high yield of Cu₂OCl₂, more than 89%, can be achieved when an argon carrier gas flow was high. It was reported that the ratio of steam to CuCl₂ in the hydrolysis reactor is between 23 and 30 to achieve 100% conversion of CuCl₂ at atmospheric pressure; while from the stoichiometry of the reaction, this ratio is 0.5 [27] and [99].

Furthermore, Daggupati et al [3] and [100] studied the hydrolysis and thermolysis reactions in the Cu-Cl cycle in terms of kinetics of the reaction and chemical equilibrium conversion. They also examined the pressure, temperature and excess steam on the equilibrium conversion. Haseli et al. [101] and [102] analyzed the transport mechanism and hydrodynamic viewpoint of the hydrolysis reactor by incorporating a shrinking core model (SCM) and volumetric model (VM or uniform reaction model) and compared the reaction conversion values from these two models. They indicated that with an increase in the superficial velocity at the fluidized bed, the steam and CuCl₂ conversion ratio decreases and increases, respectively, and it increases for both reactants at the higher bed inventory. In other research [102] they applied a Gómez-Barea method to analyze the fluid-particle mass transport phenomena in the hydrolysis reactor of the Cu-Cl cycle for producing hydrogen.

A list of institutions that investigated experimentally different types of hydrolysis reactor and the associated main reactor characteristics in the laboratory scale are provided in Table 2.3. According to this list, ANL evaluated experimentally a benchtop spray hydrolysis reactor with the load of 300 g CuCl₂(s), while UOIT assessed a semi-batch

fluidized bed hydrolysis reactor operates with 2250 g of $\text{CuCl}_2(\text{s})$. Up to this time, this is the largest scale of developed hydrolysis reactor. At UOIT, a horizontal packed bed and vertical fluidized bed reactors have been investigated and scaled-up. The hydrolysis system was tested with a production capacity of 1000 times more than the lab-scale tests. The main components of a horizontal packed bed reactor and its associated characteristics are mentioned in the following. The main steam generator with a capacity of 45 kW producing superheated steam (temperature more than 500°C) and maximum mass flow rate capacity of 30kg/h. The steam flow is produced in an electric steam generator (ESG) unit and then superheated in the electric super-heater (ESH). The other ESG is used to generate supplementary saturated steam of 3 kg/h. three main condensers (quartz and Pyrex glass) with the heat transfer area of 1.2m^2 are employed to lower the temperature of reaction gas mixture and then condense it at maximum steam flow condition. The steady copper oxychloride production from solid copper chloride and steam was confirmed from the experiment. Also, it was realized that with the increase of steam to copper chloride molar ratio, reduced pressure and reactor temperature, higher conversion of CuCl_2 would be achieved. Detailed system characteristics and descriptions are provided in Ref. [103] and [36].

Modeling and simulation of hydrolysis reaction help to design of more efficient reactor and better set the operating parameters. Ferrendon et al. [2] studied and simulated a spray hydrolysis reactor and showed the high conversion of CuCl_2 (almost 100 %) at 390°C for steam to copper chloride molar ratio of 17 [26, 27, 109]. Lewis et al. [29, 102, 110], proposed a methodology for evaluating the key operating parameters, efficiencies and performance of hydrolysis reaction in the Cu-Cl cycle.

The research at UOIT for the hydrolysis reactor led to the formulation of a model of gas-solid reaction. Pope et al. [107] examined a high-temperature fluidized bed reactor for hydrolysis of steam with CuCl_2 particles. They showed an efficient reactant conversion based on the rate of chemical reactions in the fluidized bed. However, low HCl concentrations and a significant amount of excess steam lead to a slow rate of reaction. Haseli et al. [101, 102] performed a comparative study of hydrodynamic and kinetic for a fluidized bed reactor by using two methods of shrinking core model and volumetric model.

Table 2.3. Overview of reactor design parameters for main hydrolysis experiments developed at various institutions

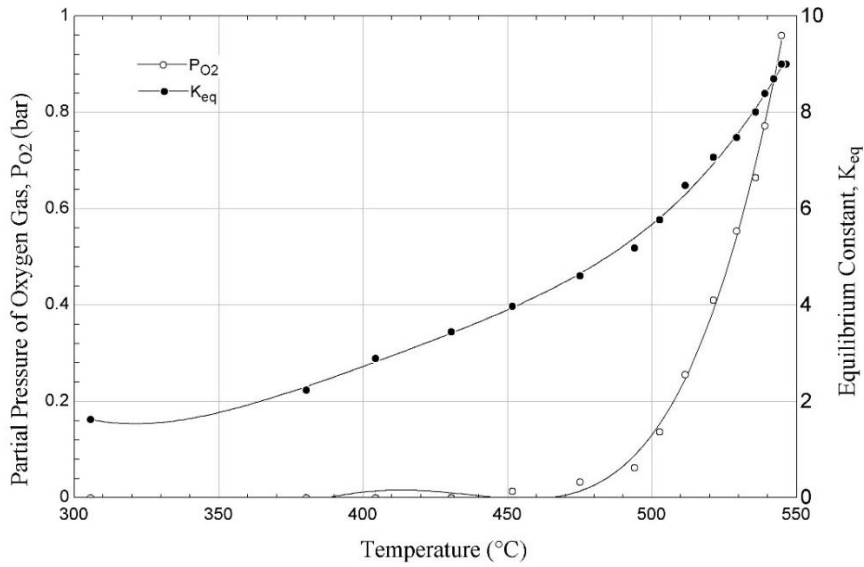
Research Group	Reactor type	Reactor detail	Ref.
ANL	Fluidized bed vertical reactor	<ul style="list-style-type: none"> • Steam to CuCl_2 molar ratio: 16 • Height quartz tube: 35.6 cm with quartz frit in the middle. • Inner diameter: 25.4 mm • Reaction sample: 1.35 g 	[104] [17]
ANL	Fixed bed horizontal reactor (tubular electric furnace)	<ul style="list-style-type: none"> • Height of glass tube: 70 cm • Outer diameter: 12.7 mm • Reaction temperature range: 300°C–350°C. 	[104] [17]
ANL	Fixed bed vertical reactor	<ul style="list-style-type: none"> • Outer diameter of quartz tube: 12.7 mm • Quartz tube with a basket and quartz frit at the bottom. • Reaction sample: 300 mg. 	[104] [17]
ANL	Continuous spray reactor (Vertical furnace)	<ul style="list-style-type: none"> • Height of Borosilicate glass: 1.3 m • Inner diameter of tube: 11.4 cm • Volume of tube: 14 L • Central port atomizer at top; co-current configuration of two ports for gas injection/extraction. • Three independent heating zones. • Sample : $\text{CuCl}_2 \cdot 2\text{H}_2\text{O}$ • Sample volumetric flow rate: 1–5 mL/h in hot steam. • Sample temperature: 400°C • Argon sweep gas volumetric flow rate: 300 mL/min. • Under vacuum, 0.25 bar. 	[27]
CEA	Fixed bed horizontal reactor (Tubular furnace)	<ul style="list-style-type: none"> • Horizontal glass reactor • Inner diameter: 10 mm • Sample weight: 860 mg crushed $\text{CuCl}_2 \cdot 2\text{H}_2\text{O}$. • Steam to CuCl_2 molar ratio: 15. • Temperature for analysis of gaseous HCl and Cl_2: 390°C. 	[27]
UOIT	Vertical fluidized bed reactor	<ul style="list-style-type: none"> • Height of reactor: 1.1 m. • Inner tube diameter: 15 cm. • Bed weight: 2.25 kg. • Ceramic porous media for distributing injected steam. • Split tubular electric furnace: 15 kW with three heating zones 	[36]

They also incorporated Gomez-Barea model to study the mass transport mechanism in CuCl_2 decomposition reactor. Daggupati et al. [3, 104, 112, 113], investigated the conversion of CuCl_2 using gas-solid reaction model under the chemical equilibrium and non-equilibrium conditions. They showed that the full conversion of copper chloride could be obtained by controlling excess steam, operating pressure and providing inert gas. Also, they analyzed the mass transport phenomena and the convective heat transfer for cupric chloride particles when reacting with the steam in the fluidized bed reactor. The equation that the study used for the time required for fully conversion of copper chloride particles through the diffusion-controlled and reaction-controlled was based on the effective diffusivity of reactant (D_e), molar density (ρ_{CuCl_2}), steam concentration ($C_{\text{H}_2\text{O}}$), particle size (R_{CuCl_2}) and reaction rate constant (k'').

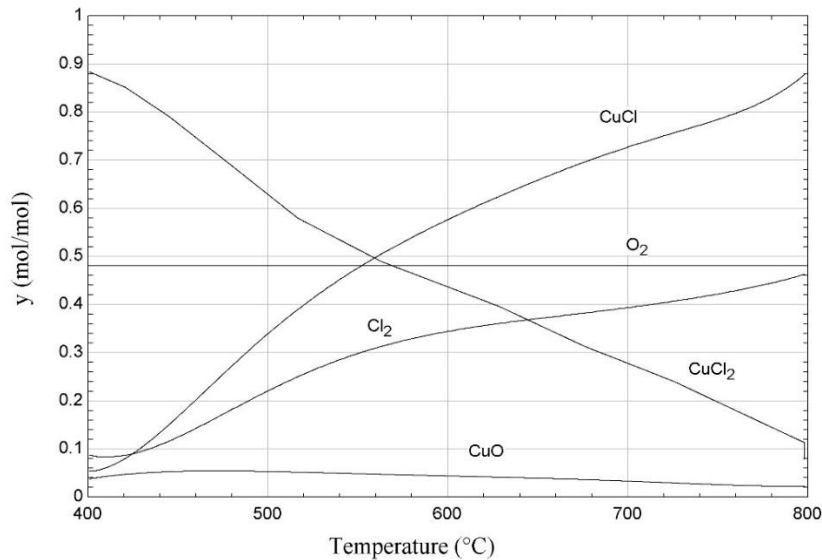
Recently, Singh and coworkers [30] performed a comprehensive experimental investigation for a fixed bed hydrolysis reactor. They applied advanced techniques such as X-ray diffraction (XRD), thermogravimetry–mass spectrometry (TG-MS), extended X-ray absorption fine structure (EXAFS) and temperature-programmed desorption (TPD) to characterize and estimate the thermal properties of chemical compounds within the hydrolysis reactor. Besides the prediction of kinetic parameters of the examined reactor, the evaluation and optimization of reaction performance were carried out, as well. They showed the propriety of ball-milled CuCl_2 over un-ball-milled one when the conversion of 97% of ball-milled CuCl_2 into CuOCuCl_2 was achieved at the specific operating condition as compared with 55% conversion of un-ball-milled CuCl_2 into CuOCuCl_2 .

2.4. Thermolysis Reaction

Marin et al. [114-116] indicated that at the equilibrium condition, the oxygen releasing increases significantly for the reaction temperature of above 427°C . They showed the change of equilibrium constant and oxygen partial pressure with the thermal decomposition temperature (see Figure 2.1). In this study, the equilibrium constant formula is applied for the thermal decomposition reaction in terms of operating pressure (a case study of 1 bar) and partial pressure of oxygen gas. Thermogravimetric tests for thermally decomposition of Cu_2OCl_2 reaction were conducted by Nixon et al. [113]. A tubular furnace in dry air at temperature between 325°C and 400°C is used to synthesize Cu_2OCl_2 from other species.



(a)



(b)

Figure 2.1. (a) Partial pressure of oxygen and equilibrium constant at the thermally decomposition of the reaction of copper oxychloride (b) Equilibrium molar fractions of species in the thermolysis reactor; data from [113]; (Polyfit is applied for data)

In this experiment, they found that the cupric chloride and cupric oxide should be formed at the first phase of thermally decomposition of copper oxychloride. This is mainly due to the importance of copper oxychloride decomposition at a temperature above 480°C that is near to the cupric chloride decomposition temperature. It is observed Figure 2.1b that at the relatively lower reaction temperature, the formation of cupric chloride with oxygen release is desired thermodynamically respecting cuprous chloride formation. The

consumption of chlorine gas is studied comprehensively in Ref. [114] in which the rate of reaction formula is employed.

At UOIT, a large scale thermolysis reactor was established with the oxygen generation capacity of $1.13 \text{ N m}^3/\text{h}$ corresponding to hydrogen production rate above 4 kg/day . This scale is 1000 times larger than the earlier proof-of-principle experimental in ANL[113]–[115]. The schematic of copper oxychloride decomposition reactor with a brief description of its supplementary units at the test loop is presented in Figure 2.2. Marin et al. [110], [112] compared the theoretical and experimental yields of Cu_2OCl_2 decomposition. The conversion percentage of Cu_2OCl_2 mixture from model results was found between 50%–80% at 527°C and 1 bar which confirmed the measured values obtained in the experiments.

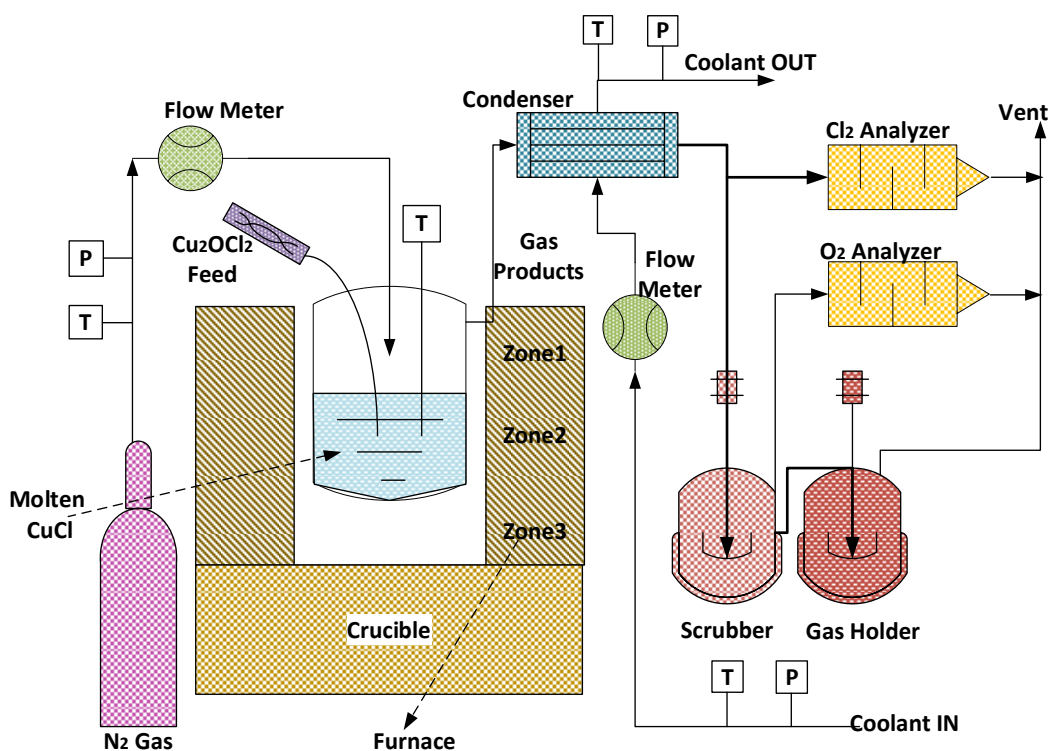


Figure 2.2. Schematic view with remarks representing the thermolysis test loop at UOIT; adapted from [112]

2.5. Pressure Swing Distillation Unit of Analyte

Some binary mixtures which have non-ideal vapor-liquid behavior produce azeotropes in some chemical processes. It is known that typical boiling azeotropes can form between two chemical components. Minimum boiling azeotrope can form when activity coefficients are

greater than unity, components are dissimilar and repulsion forces are strong. When activity coefficients are less than unity and components attract each other, maximum boiling azeotrope can form [116]. These types of mixtures can be only separated by special distillation methods, such as extractive distillation [121-124] azeotropic distillation [125-128], and pressure swing distillation (PSD) [22, 23, 129-131]. Compared to the mentioned alternative methods, the advantages of PSD process are the lack of a third solvent's being introduced, simple configuration, the possibility of heat integration application for energy savings [132-135].

PSD process is considered a special method based on an azeotropic composition by changing the system's pressure and no need to add other components. This shift in pressure can alter the relative volatilities [44]. This principle is used for separation of maximum and minimum boiling homogeneous azeotropic mixtures in PSD in two operating columns including high pressure (HPC) and low-pressure column (LPC) that are operated at two different pressures [121]. In the minimum boiling mixtures separation by the PSD, the bottom streams are pulled out as high-purity products, and the distillate streams are recycled into the other column and vice versa for the maximum boiling azeotrope [122].

Past studies have examined pressure swing distillation processes. Lei et al. [123], and Luyben [124] conducted modeling and optimization studies of PSD. Luyben [125], Yu et al. [126], and Mulia-Soto and Flores-Tlacuahuac [119] studied the design and control of heat integrated PSD systems. Hosgor et al. [116], Luyben [117], Lladosa et al. [127], Wang et al. [128] presented comparisons between extractive distillation and PSD in terms of control systems for different binary mixtures. HCl is an important fluid in the Cu-Cl cycle. Increasing the HCl concentration between the hydrolysis and electrolysis step of the cycle is necessary. Therefore, PSD will be used in this process with applications to the Cu-Cl cycle.

Recycling the oxidized anolyte (utilized HCl (aq) and CuCl₂ (aq) from the electrolyzer cell) through the sequence separation modules has importance. However, few past studies focused on such units, specifically for HCl (aq), as it has complex thermodynamic behavior. For this matter, this study will develop a thermodynamic model of a pressure swing distillation unit (PSDU) through an Aspen Plus simulation for recycling more

concentrated HCl (aq) in a Cu-Cl. Thermophysical properties of the HCl (aq) azeotropic binary mixture used electrolyte nonrandom two-liquid (eNRTL) and universal quasi-chemical (UNIQRK) as the activity coefficient models for phase equilibria description. They also analyzed the PSDU from the design viewpoint through the mass transfer mechanism utilizing the McCabe-Thiele method for a number of trays specification and the heat transfer analysis for determining the packing column height of the separation apparatus. Lescisin et al. [129] confirmed the feasibility of the separation process of HCl-water binary mixture beyond its azeotropic point by a PSD system through the simulation results and design estimation.

2.6. Dehydration Process of CuCl_2 (aq)

Several methods were employed for the dehydration process of cuprous chloride aqueous solution at different institutions. Daggupati et al. [130] from UOIT investigated the variation of tapped and bulk densities with the inlet temperature of drying air in a low-temperature spray drying. They reported that high moisture content results in a cohesive and non-flowing behavior of produced powder. [130]. Also, Daggupati et al. [130] studied the variation of the ratio of tapped density to aerated bulk density of a powder with a Sauter mean diameter of the solid particle. They concluded that the drying air inlet and outlet temperatures are the main contributors to moisture content in the droplet. In a high-temperature spray drying unit, they considered the volumetric distribution of particle mean size and proposed acceptable flowability of powder and particle size for high-temperature drying [130]. Naterer et al. [131] focused on a crystallization drying method in which a thermal bath and a chlorine ion analyzer are used). Samples of grown crystals during the experiment were collected and dimensions of the dendritic crystals observed in the range of 0.1–0.6 cm. They showed that 20 % of copper chlorine can be crystallized upon cooling from 80°C to 20°C. Ongoing research needs to be performed to decline the drying temperature requirement and enlarges the portion of solids formed. In another paper, Naterer et al. [83] developed a spray drying model in which the following assumptions are made to extract the energy balance formulation for the droplet. A continuous shrinkage for droplet with no formation of solid core, continuous growth of copper chloride crystals and constant average thermal conductivity of droplet. Negligible change in kinetic energy associated to the drying air for the movement of droplet. They showed that the nozzle

characteristics and downward movement of spray flow increase the coalescence potential and droplet size. They are the main contributors to Sauter mean diameter. Flashing effect is minor in spray/flash drying compared to the drying mechanism of evaporation. At 35°C, for droplet size less than 200 μm and low operating pressure, the drying time is less than 8s (shown in Figure 2.3). The low-temperature drying is promising for evaporative drying however it may limit the quality of product.

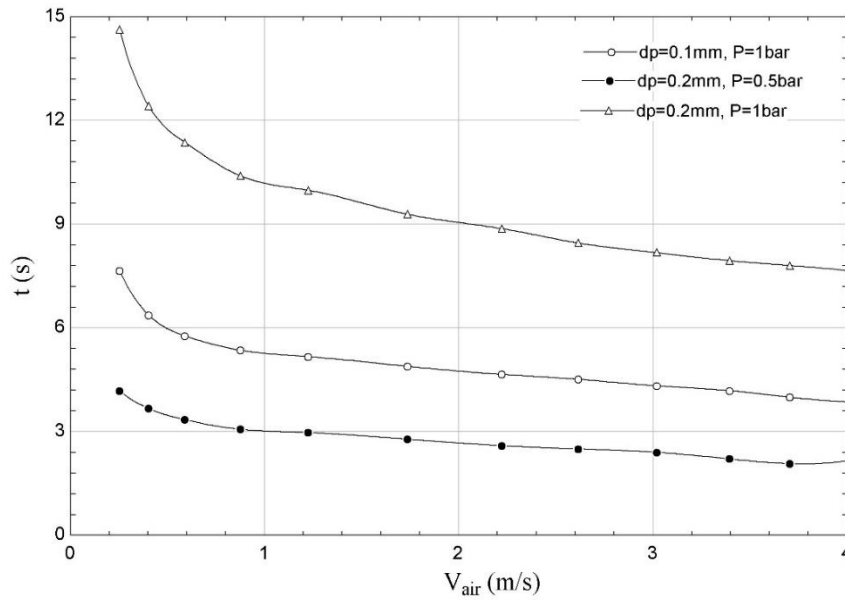


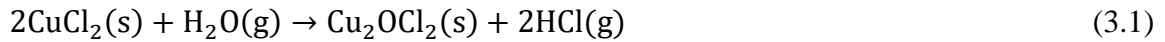
Figure 2.3. Effect of inlet air velocity ($T=30^\circ\text{C}$ and 10 g moisture per kg dry air) on predicted drying time at different droplet diameters and pressures; [50]; (smoothing cubic splines is used)

Chapter 3 . Experimental Apparatus and Procedure

3.1. Experimental Demonstration of the Lab-scale

The thermochemical decomposition of water into hydrogen and oxygen is carried out through various types of Cu-Cl cycles and all of them contribute to the identical overall chemical reactions. Figure 3.1 shows the schematic diagram representing the main parts of a lab-scale Cu-Cl thermochemical cycle for hydrogen production. The primary interactions contribute to a four-step copper-chlorine thermochemical water decomposition cycle and the relative required temperature are addressed as follows.

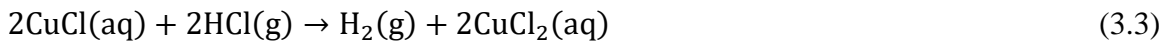
Step 1. Hydrolysis reaction: The hydrolysis reactor needs to be maintained at a temperature between 370°C and 400°C to achieve the equilibrium conversion over 90%, theoretically. At the pressure of 1 bar, the hydrolysis reaction can be expressed as:



Step 2. Copper oxychloride (Cu_2OCl_2) decomposition reaction (Thermolysis): In this step by maintaining the reaction temperature between 500°C and 530°C, and when a complete conversion of reactant to the product exists, the copper oxychloride splits into the copper chloride (CuCl) and oxygen at the atmospheric pressure.



Step 3. Electrolysis: This step comprises several sub-reactions at anode and cathode sides of the cation exchange membrane electrolyzer which ultimately yields the hydrogen and cupric chloride. The overall electrochemical reaction of the cation exchange membrane electrolyzer can be defined as follows at the temperature between 25°C and 90°C and pressure of 1 bar.



Step 4. Dryer: In the temperature range of 100°C and 130°C and atmospheric pressure, the drying process of aqueous cupric chloride occurs to end up the Cu-Cl cycle:



As mentioned before, in an actual operation condition of thermochemical and electrochemical reactions, a part of reactants do not undergo the reaction (conversion ratio less than 100%), thus, more species are interacting in a real case study compared to the theoretical case described above through the chemical equations (1) to (4). This proposal aims to investigate a real four-step integrated Cu-Cl cycle lab scale at UOIT (shown in Figure 3.2), as this is required for further research and development. The constituents interacting with diverse modules in the system should be taken into account.

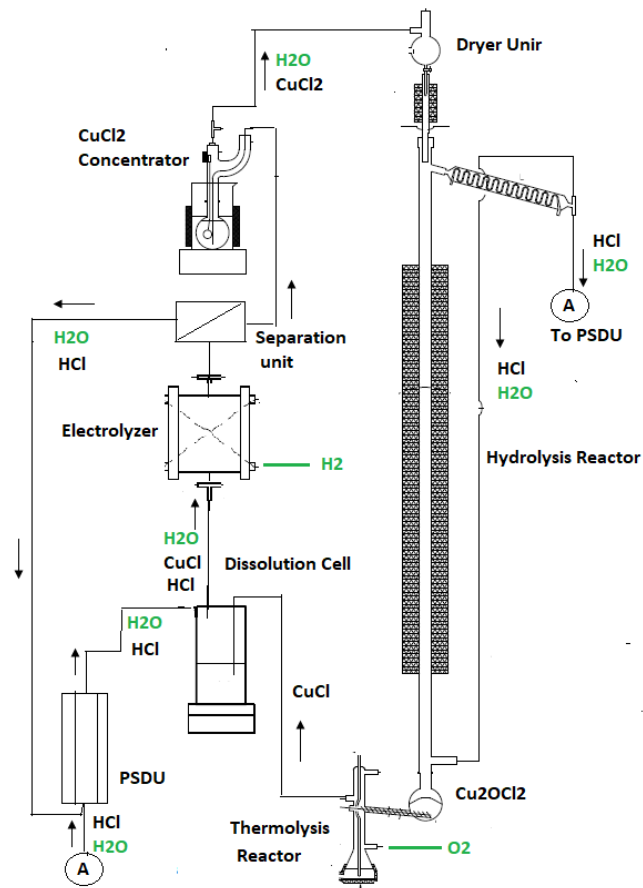


Figure 3.1. Schematic diagram representing the main parts of a lab-scale copper-chlorine thermochemical cycle for hydrogen production

A schematic view of a lab-scale integrated Cu-Cl cycle at UOIT is shown in Figure 3.3. The integrated four-step Cu-Cl cycle comprised of a dryer, hydrolysis, thermolysis, electrolysis and atmospheric distillation unit of anolyte (ADA), anolyte makeup vessel (AMV), drying unit, separation unit through selective CuCl_2 dissolution in water, CuCl_2

(aq) concentrator, stirred dissolution cell of CuCl in HCl (aq), pressure swing distillation unit (PSDU), HCl (aq) condensers, steam condensers, quench cell and decanter of CuCl.

The steam and CuCl₂ (s) are introduced into the hydrolysis reactor. With the help of Argon or Nitrogen as steam carriers, Cu₂OCl₂ (s) and HCl (g) are produced through the endothermic chemical reaction. Possible side reactions like decomposition of CuCl₂ into CuCl and Cl₂ are neglected in this study. The Cu₂OCl₂ is transferred into the thermolysis reactor where at the relatively high temperature, it is decomposed into CuCl (l) and O₂ (g). In the quench cell, CuCl₂ (l) is turned into a solid form through the phase change process using cooling water. The decanter transfers CuCl (s) into the dissolution cell (DC) where the concentrated HCl (aq) from the pressure swing distillation unit (PSDU) dissolves the CuCl particles and forms the fresh anolyte for the electrochemical reaction. At the HCl/CuCl (aq) electrolyzer, the hydrogen is produced from the electrochemical reaction of anolyte (containing CuCl and HCl (aq)) and catholyte (containing HCl (aq)). The catholyte is cleaned through the electro dialysis cell, while the depleted (oxidized) anolyte is transferred to the atmospheric distillation unit of anolyte (ADA) and the anolyte dryer unit where the salts (mixture of CuCl and CuCl₂) are separated from the HCl (aq). Separation of CuCl and CuCl₂ occurs at the separation unit where water is introduced to dissolve CuCl₂ and the undissolved CuCl is delivered back to the decanter. The dissolved CuCl₂ (aq) is concentrated at the CuCl₂ concentrator cell, then the mushy mixture is transferred to the dryer unit to completely dehydrate CuCl₂ and complete the cycle.

Since the lab-scale comprises diverse units of hydrolysis, thermolysis, electrolysis, dryer, quench cell and anolyte recycling loop through the sequence of separation processes, an experimental investigation will be conducted for each individual unit and then the whole system to achieve a better system analysis and improvement. Here, the general experimental steps for the lab-scale are summarized as follows:

- (a) Specifying the technical parameters for each module like element sizes, materials, and operation parameter limits like the stable temperature and pressure.
- (b) Testing and running each unit of the integrated cycle based on the available data to analyze the unit's performance, as well as to detect the challenges contributing to the examined unit and trying to eliminate them by some modifications.

(c) Testing and running the whole integrated cycle to examine the overall system performance. Varying some parameters at each experimental run to understand the effect of some key operating parameters on the system's outputs such as efficiencies, amount of produced hydrogen, heat duties, etc.

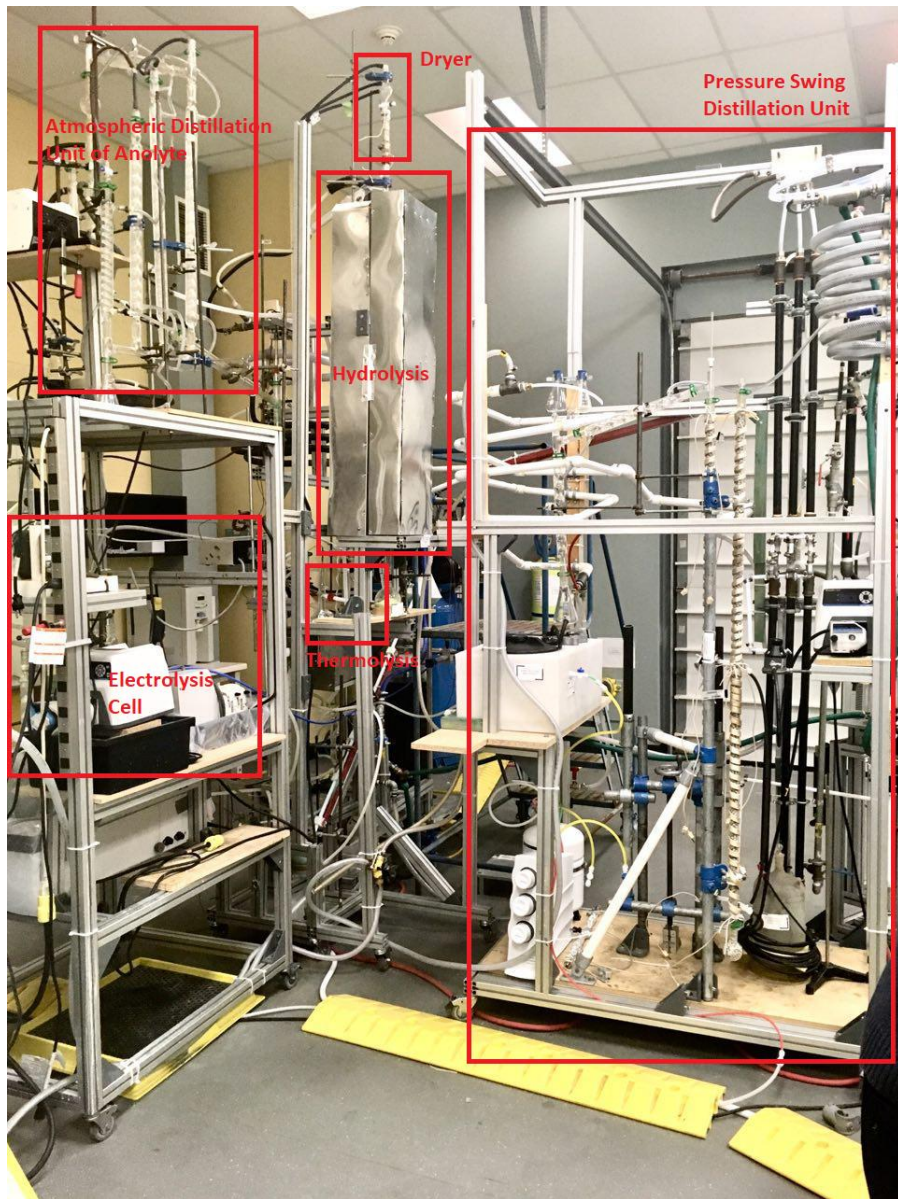


Figure 3.2 . Lab scale of integrated four-step Cu-Cl cycle at UOIT.

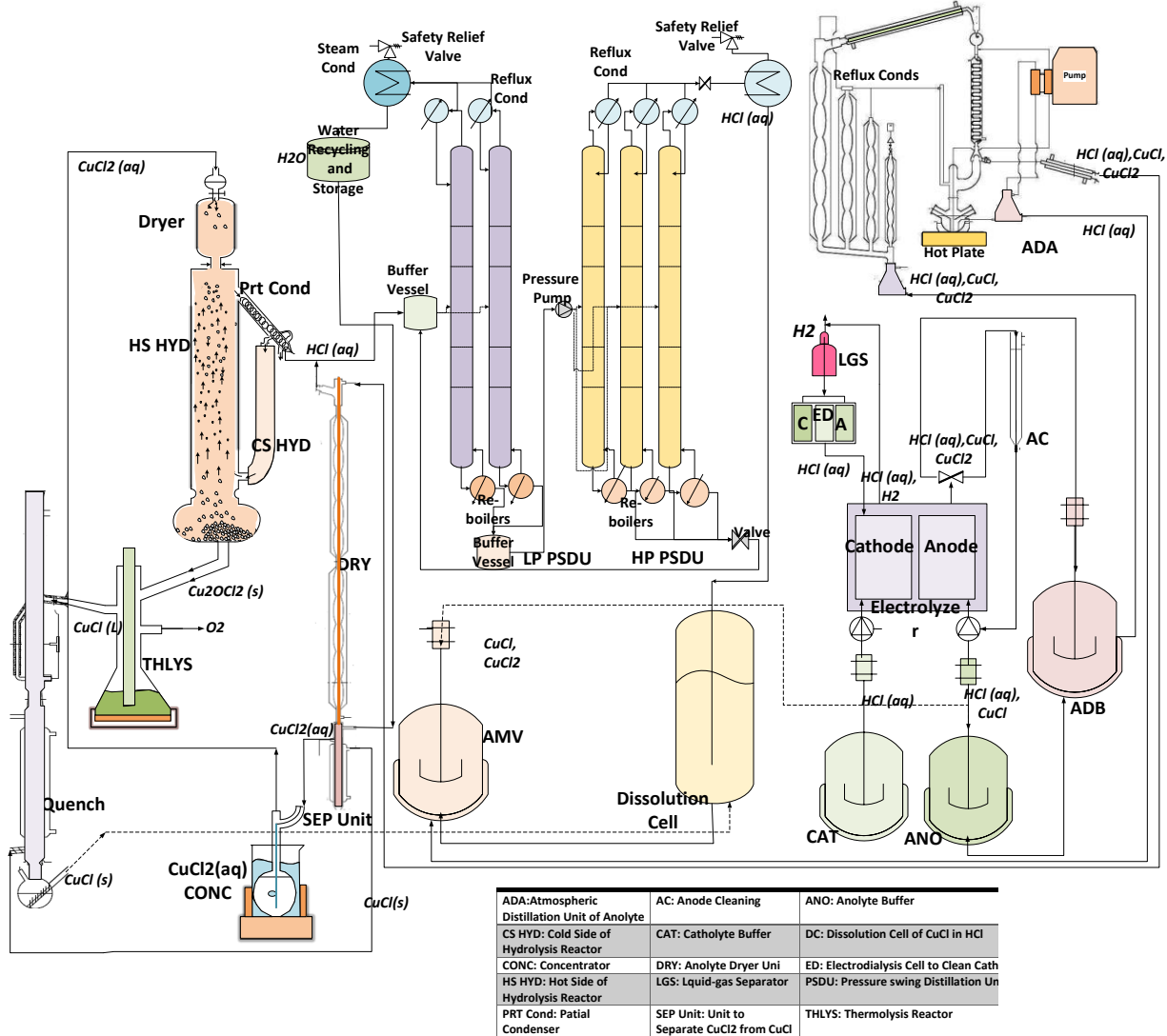


Figure 3.3. Schematic diagram of the lab-scale integrated Cu-Cl cycle at UOIT

3.2. Pressure Swing Distillation Unit Description and Experimental Procedure

In this section, a detailed pressure swing distillation unit (PSDU) description and the experimental methodology are presented as follows. Moreover, the technical specifications of different components at PSDU apparatus are tabulated in Table 3.1. The complete schematic diagram of constructed PSD process in CERL as seen in Figure 3.4 is consist of three high pressure and two low pressure columns with re-boilers, reflux condenser, buffer vessels, steam condenser, HCl (aq) condenser, safety relief valves, pump, throttling valves.

The size of columns allows to yield 100 g per day of hydrogen production, but the design of the columns is adjustable to increase capacity.

A detailed packed laboratory atmospheric distillation column in CERL is shown in Figure 3.5. The columns are designed to be integrated into a Cu-Cl cycle able to deliver over 100 g HCl (aq) per day. For the research purpose, the sizes of heat exchangers and vessels were oversized. Nevertheless, the design of the column is flexible that allows to augment capacity by adjusting some parts. The system is supplied with the low concentration HCl (aq) sourced from the hydrolysis reactor. The HCl (aq) at the supply port is in the liquid phase, as a low-concentrated HCl(aq), and it is mixed in the inlet buffer vessel with recycled low pressure HCl (aq) which comes concentrated at around 19% by weight coming from the bottom of the high pressure side. In the low pressure side (left hand side of the azeotrope point at 1atm).

The buffer vessel at the input is stirred and has a capacity of 2.5 l, which is stirred using a magnetic stirrer to mix all streams prior to feeding the columns (see Figure 3.4). The safety valve placed shown above the buffer vessel is a low pressure valve system that maintains atmospheric pressure in the vessel. This is done by placing the safety valve atop of a reflux condenser. If for any reason the pressure tends to be higher than the atmosphere at the column inlet, gas is allowed to be released in the fume hood. The valve system atop the condenser will allow air to enter the system if the pressure enters in a vacuum. The liquid is fed gravitationally in two parallel column. The system allows for adjustment of the feed low rate by placing the buffer system in on a rack system of modifiable height.

The low pressure distillation columns are made of 1 inch glass cylinder of 5 ft height and the feed is taken approximately at half height. The vapor pressure in both columns is balanced atop where the reflux section is located. Re-boilers are sat-up at columns bottom and consist of spherical vessels of 50 ml each, heated electrically. Raschig rings are placed in all columns to increase the heat transfer contact area. The top segment of the column is not insulated allowing for air cooling which forms reflux condensers of 20 cm each. A steam condenser is made of one Allihn condenser inclined at 105° and one vertical allihn condenser discharging in a liquid trap. In addition, a reflux condenser is used for steam condensing.

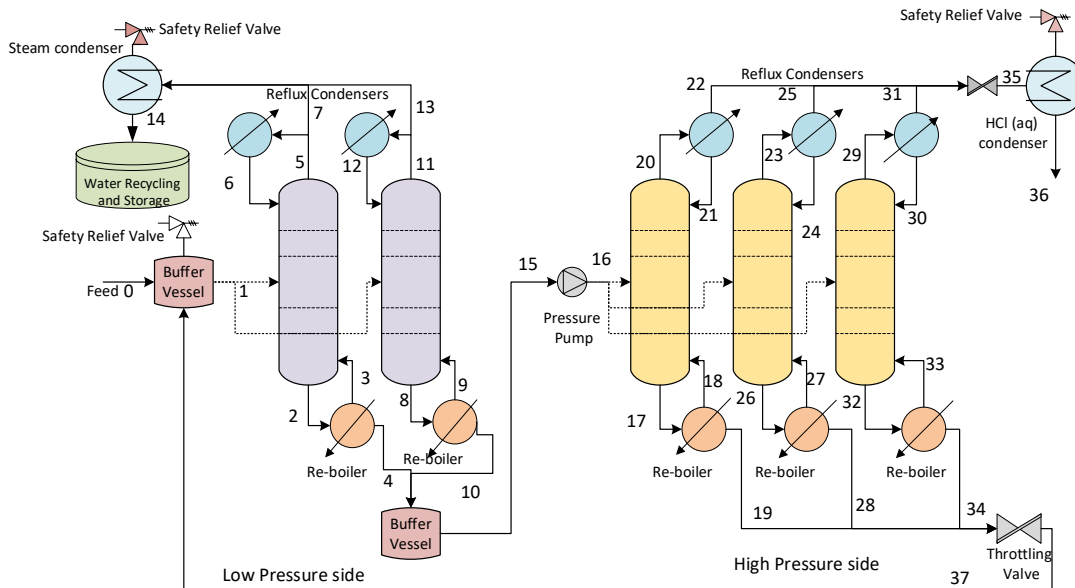


Figure 3.4. Process flow diagram of HCl(aq) pressure swing distillation

The condensed water is discharged in the water storage and recycling buffer which has a capacity of 25 liters. The buffer is maintained at a constant level by a float valve, which allows for freshwater intake provided by a reverse osmosis system. The buffer vessel discharges water to the unit of operation that separates CuCl_2 from CuCl by selective dissolution and decanting processes.

The bottoms of the low pressure distillation columns are collected in a buffer vessel with 4 l capacity. The concentration of the bottoms will correspond to the atmospheric pressure azeotrope point and is 20% by weight. The pressure pump is a Masterflex positive displacement pump of peristaltic pump capable to pressurize the hydrochloric acid solution up to 10 bar. The pump has a special neoprene tubing designed for high pressure special application. The arrangement is made such as the temperature of the pumped liquid is around 50 – 60°C and not more than 60°C for safety reasons. At point 16 at pump discharge, a pressure relief valve is placed (not shown) that discharges at 50 psi gauge. The pump discharges in three paralleled high pressure distillation columns.

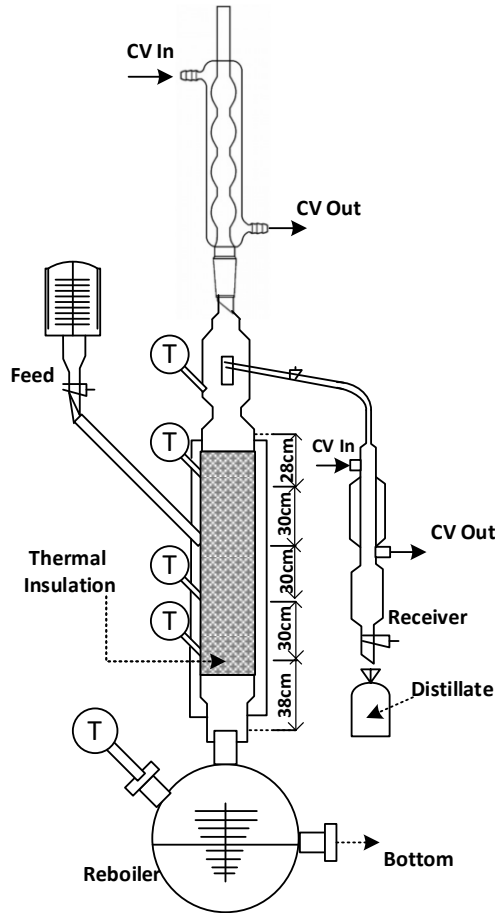


Figure 3.5. Sketch of the laboratory atmospheric distillation unit of HCl (aq) at UOIT

Each high pressure column is 7 ft tall and consists of PTF tubing of 3/8 inch internal diameter. The feed section is placed at 4 ft from the bottom. A side reflux condensation section is installed at the feed section (not shown in the figure). At columns bottom, a liquid trap is formed which has 1 ft height and is set to work as boiler due to heat addition. The high pressure columns heating is done by hot thermal fluid consisting of DURATHERM™ 450 thermal oil. The oil is heated at cca, 175°C and feed on the bottom in a tube and shell arrangement in which the distillation column is at the core and the oil flows upward through the annulus. The temperature inside the high pressure distillation column is assumed to be cca. 155°C. At the top of the column, the column is not insulated and therefore is cooled by ambient air to form a reflux condenser.

The pressure of the high pressure column is regulated by two devices, one placed atop on the vapor side, and the other at the bottom on the liquid side. The top regulator maintains

the vapor pressure in the column at the set point. The bottom regulator operated comprises a float and a throttle and opens when the liquid level in the reflux condenser becomes higher than approx. 1 ft, otherwise the throttle is closed by a popped valve. The high pressure vapors atop are throttled by the pressure regulator system. Therefore, the HCl(aq) condenser 35 – 36 operates at atmospheric pressure. The condenser is made of multiple segments including an air-cooled desuperheater, two water-cooled segments and on water-cooled reflux condenser. The concentrated HCl(aq) in 36 is diverted toward the dissolution cell of CuCl to make-up the anolyte.

3.3. Lab-scale CuCl₂ Hydrolysis Reactor Operation

Figure 3.6 shows the cupric chloride hydrolysis reactor constructed in the Clean Energy Research Laboratory (CERL) at UOIT. The setup and results are adjusted to the sizes, dimensions, parameters and design of the cupric chloride hydrolysis reactor shown in Figure 3.6. The experimental data will be used for verification of the numerical results from the modeling study. The hydrolysis unit is sized to correspond to 100 liters per hour of producing hydrogen.

Table 3.1. Technical specifications of different components at PSDU

Component	Technical specifications
	<p>1) Glass column: Maximum stable temperature: 300°C Column height: 0.9 m Tube diameter: 0.0254 m Coefficient of expansion (20 – 300°C) = $3.3 \times 10^{-6} \text{ K}^{-1}$ Density = 2.23 g/cm³ Specific heat (20°C) = 750 J/kg°C Thermal conductivity = 1.14 W/m°C Poissons Ratio (25 - 400°C) = 0.2</p> <p>2) Rusching ring Material : Ceramic Thermal conductivity: 150 W/m·K Density: 3.21 g/cm³ Melting point: 2800 °C</p>
	<p>1) DURATHERM Oil (circulating between tubes) $C_p = 2.52 \text{ (kJ/kg.K)}$ $\rho = 759 \text{ (kg/m}^3\text{)}$ $\mu = 1.045 \times 10^{-3} \text{ (kg/m.s)}$ $\lambda = 0.133 \text{ (W/m.K)}$</p>

	<p>2) PTFE tube (inner tube) Density: 2200 kg/m³ Glass temperature: 114.85 °C Melting point 326.85 °C Thermal expansion: $112 \times 10^{-6} \text{ K}^{-1}$ Thermal diffusivity: 0.124 mm²/s Young's modulus: 0.5 GPa Yield strength: 23 MPa Bulk resistivity: 1016 Ω·m Coefficient of friction: 0.05–0.10</p> <p>3) Carbon steel tube (outer tube) Thickness: 0.0016 m Diameter: 0.0254 m Length: 1.25 m Thermal conductivity: 45.3 W/m.K Heat capacity: 502.416 J/kg.K Density: 7.85 g/cm³</p>
	<p>Water Chiller: Temperature range: -80°C to +10°C Temperature stability : +/- 0.03°C Cooling capacity: 60 Hz 250 watts at -70°C \ 50 Hz 280 watts at -80°C Compressor: 2 x 1 hp Heater 1200 watts Bath volume: gallon 4.0 Liter: 15.1 Unit dimensions H x W x D inch : 47.50 x 27.375 x 17.75 H x W x D cm: 102.7 x 69.2 x 45.1 Bath opening/Bath depth W x L/D in: 7 x 5.4/9.5 W x L/D cm: 17.8 x 13.7/24.1 5.1 Pump performance 60 Hz (LPM) 10 LPM @ 0' head, 12' max GPM @ 0' head, 12' max 50 Hz (LPM) 10 LPM @ 0' head, 11' (GPM) 2.6 GPM @ 0' head, 11' max Pump: force and suction force Unit weight: lb: 336, kg :152.4</p>
	<p>Preheater 1) Erlenmeyer Flask Capacity: 250 ml Uses a No. 6.5 rubber stopper Height: 132 mm Marked to fill 50-200 ml in 25 ml increments Extra-large marking spot Corning Item: 4980-250</p>

	<p>2) Hot Plate Fisher scientific isotemp Surface Area Heating: 7.25 x 7.25 in. Top Plate Material: Ceramic Hertz:50/60Hz Dimensions (L x W x H): 13 x 8.2 x 3.8 in. (33 x 20.8 x 9.7cm) Plug Type: US style Voltage: 110-120V Stirring Range:50 to 1,500rpm Electrical Requirements: 100120V 50/60Hz Max. Temperature (Metric):450°C</p>
	<p>Pressurization Pump Type: peristaltic pump (high pressure) Model No:07528-20 3-300 RPM Power: 115-230 VAC (50-60HZ) Number of Channels1 Max Flow Rate Per Channel (mL/min)65 Min Flow Rate Per Channel (mL/min)0.75 Drive07528-20 (L/S® Precision Variable-Speed Drive) Pump Head77390-00 (L/S® PTFE-Tubing Pump Head) Tubing77390-60, 2/pk (PTFE Tubing Set, 4mm x 6mm) Tubing sizes accepted PTFE Tubing Sets Width (in)8.3 Height (in)8.5 Length (in)13.05 Width (cm)21.08 Height (cm)21.59 Length (cm)33.15</p>
	<p>Glassier bay reverse osmose: Water Pressure Limits: 40 – 100 PSI (276 – 689 kPa) Supply Water Temperature Limits: 40 – 100 °F (5 - 38 °C) Maximum Total Dissolved Solids (TDS): 2000 ppm Maximum Water Hardness @ 6.9 pH: 10 gpg Chlorine in water supply (max. ppm): 2.0 Supply water pH limits (pH): 4-10 Product (quality) water, 24 hours1: 18.4 gal (69.6 liters)</p>

The cupric chloride hydrolysis reactor is a quartz tube, where the endothermic chemical reaction occurs. The reactor is placed in a tubular vertical furnace equipped with hot rasching rings/wires for maintaining the column at 520°C. A water-cooled condenser is set up to create a temperature gradient between two sides of the reactor. During the operation, the dryer unit is supplied through the aqueous cupric chloride (CuCl_2 (aq)) from the cupric chloride concentrator module. The concentrated CuCl_2 mixture dropping from the burette is completely removed from the cupric chloride at a temperature and pressure of 120°C and 1 atm. Depending on the CuCl_2 (aq) volumetric flow rate, the size of spherical cupric chloride solid particles can be roughly quantified. Once the dried cupric chloride and steam as the reactants enter into the high-temperature furnace (520°C), a portion of the steam is drawn into the cold side (250°C).

The partial condenser between the hot and cold sides provides the temperature difference between the sides. The gaseous phase, steam and produced hydrochloric acid, are drawn into the partial condenser. Most of the HCl (aq) condenses and leaves the hydrolysis reactor and the rest of the steam (with the dropped temperature of 250°C) continues to circulate within the reactor. In this thesis, it is assumed that the amount of HCl circulating within the reactor is negligible to consider its possible effects on the reaction process. It is assumed that most of HCl is removed from the reactor in the partial condenser). However, further studies and experiments can be initiated to investigate the possible effect of HCl at the reactor. The hot and cold sides make a convection-driven flow to blow steam through a natural convection process. This eliminates the need for a blower to suspend the species while consuming electrical power.

A steam-to- CuCl_2 ratio of between 7 and 10 is required to eliminate the formation of CuCl side products in the input stream. The lower ratio is not desirable since it facilitates the formation reaction of CuCl . Decreasing the operating pressure results in an increased yield of solid product, whereas it declines the yield of CuCl side product [7]. In the vertical high-temperature furnace with a length of 1.22 m and a diameter of 1.5 in, the steam is drawn from the cold side and meets the falling solid cupric chloride particles. The solid cupric chloride particles are affected by upward buoyancy and drag forces and a downward

gravity force which gradually decelerates the particles until a constant terminal velocity is achieved. This creates enough time for reactants to be preheated and then fully converted.

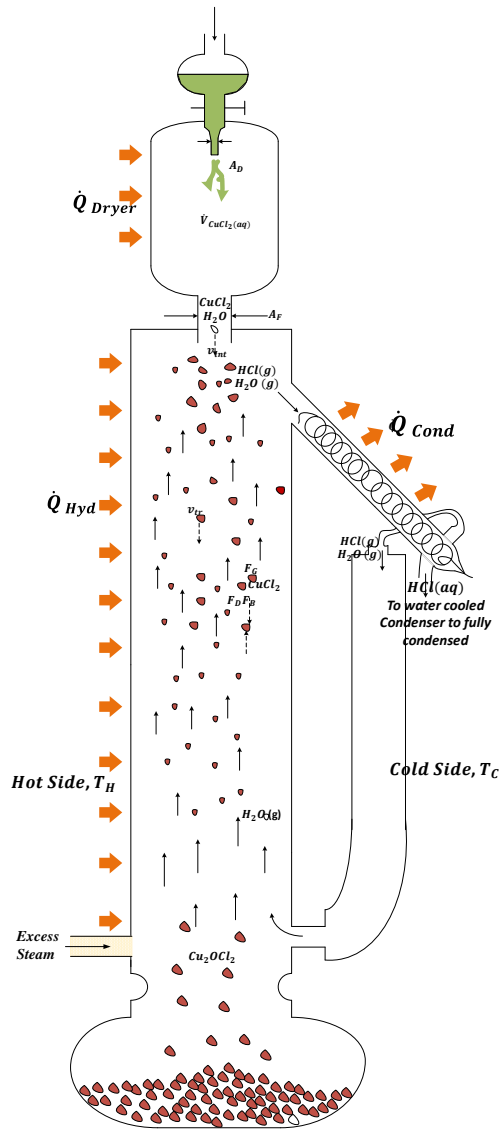


Figure 3.6. Schematic diagram representing the cupric chloride hydrolysis reactor

The residence time decreases at a lower pressure as natural convection effects decline at a lower pressure (at a lower pressure, the Grashof number is lower). Meanwhile, during the endothermic chemical reaction, it is assumed that there is no cupric chloride particle decomposition and no excess steam reaction with chlorine in the bulk phase. The gaseous hydrochloride with steam is circulating through the loop, while the resulting solid copper-

oxy-chloride particles accumulate at the bottom of the reactor. The resulting solid products are weighted and analyzed with methods such as XRD and SEM.

3.4. CuCl₂/HCl(aq) Electrolyzer Stack

Figure 3.7 (a) shows a schematic of the Cu-Cl cycle operating at low pressure (1 atm) and room temperature which can supply feed into the CuCl/HCl(aq) electrolyzer stack. Figure 3.7(b) reveals the anolyte loop in CuCl/HCl(aq) electrolyzer unit, as well. The liquid anolyte flowing through the electrolyzer couples the electrochemical part with the thermochemical units of the Cu-Cl cycle as the hydrolysis and thermolysis reactors. The anolyte as the aqueous strong solution is the fluid medium that carries chemical species like copper(I) chloride (CuCl) coming from the thermolysis reactor and copper (II) chloride (CuCl₂) which is carried from the electrolyzer into the hydrolysis reactor. Hydrogen ions (protons) as the product of CuCl₂ hydrolysis reaction (produced HCl(aq)) transferred into the electrochemical unit where finally reduced into hydrogen gas. During the electrochemical process in the electrolyzer unit, a fraction of copper (I) chloride (CuCl) is converted to copper (II) chloride (CuCl₂). Then the oxidized anolyte (consumed anolyte at the electrolyzer stack) is transferred into several separator units to separate CuCl, CuCl₂ (aq) and HCl(aq) species as necessary for the cyclic operation. A detailed description of a lab-scale integrated Cu-Cl cycle at UOIT is provided in Refs. [20], [23], [132]. In the following sections, the CuCl/HCl(aq) electrolyzer stack design and anolyte/catholyte flow configuration across the manifold and bipolar modules are described.

Figure 3.8 illustrates the anolyte and catholyte flow pattern distributions through the CuCl/HCl(aq) electrolyzer stack. It is shown that the electrolyzer stack encompasses 10 series-connected membrane electrode assemblies (MEA) with an active area of 50 cm² and a thickness of 4mm (thickness of each cell). The MEAs inside the stack contains titanium/platinum foil bipolar plates with grooves or channels for supplying anolyte or catholyte reactants through the cell. The HCl(aq) solution requires graphite coated titanium electrodes to avoid corrosive deterioration of the titanium electrodes. Moreover, the anode and cathode are separated with a Nafion 117 membrane for conducting the protons produced in the electrochemical reaction. Carbon gaskets were used as a cell sealant. The hydrodynamics of the flow inside the electrolyzer stack need geometrical optimization to

ensure a uniform flow distribution across the MEAs and to reduce the surface contact between the titanium stack parts (reduce ohmic losses).

In the Z-type manifold configuration of the electrolyzer stack, the anolyte is supplied by the anode manifold and catholyte is supplied by the cathode manifold. The anolyte is a concentrated solution of 2 M copper (I) chloride (CuCl) dissolved in 10 M hydrochloric acid feeding the stack. From the inlet port, fluid spreads through the MEAs to the anolyte outlet port by the collectors. The catholyte solution contains 10 M HCl(aq) and enters from the left side at the bottom and leaves the electrolyzer stack from the opposite side at the top. The anolyte and catholyte flow passages in the bipolar plate form an X-shape configuration which creates an effective fluid distribution inside each unit cell. Based on the electrochemical reaction stoichiometry and Faraday's law, the anolyte and catholyte volume flow rates are evaluated as 117 L/h and 104 L/h for an overall hydrogen production rate capacity of 46 L/h.

The reduction of anolyte occurs with the oxidation of Cu^{I} into Cu^{II} as chloride complexes. From the positively charged anode to the negatively charged cathode, the protons are transferred thereby reducing to hydrogen gas through the electrochemical reaction. Once the dissolved Cu^{I} or Cu^{II} diffuses into the cathode electrode, they are oxidized electrochemically to reduced metallic copper. This reaction consumes the electrons required for the reduction of copper which affects the stack efficiency. Also, the crystalized copper can block the gas diffusion permeability. Based on experimental observations [97], the presence of hydrochloric acid decreases the amount of solid copper formation at the membrane and electrode, which enhances the electrochemical performance of the electrolyzer stack.

Figure 3.9 shows a photograph of 10 membrane electrode assembly (MEA) electrolyzer stack and its components at UOIT. The titanium (Ti)/platinum (Pt) Nafion 117-based membranes with the active surface area of $7\text{cm} \times 7\text{cm}$ is placed between titanium gas diffusion layers. A titanium electrode is used to complete the electrochemical reaction. Table 3.2 shows two cases for anolyte concentration and its effect on the membrane. It can be observed that the anolyte/catholyte with a high concentration of copper compound results in copper precipitation on the membrane and decrease cell efficiency significantly.

So, the selection of proper anolyte/catholyte in which the concentration of hydrochloric acid and copper chloride are in a practical ratio would prevent the copper precipitation process.

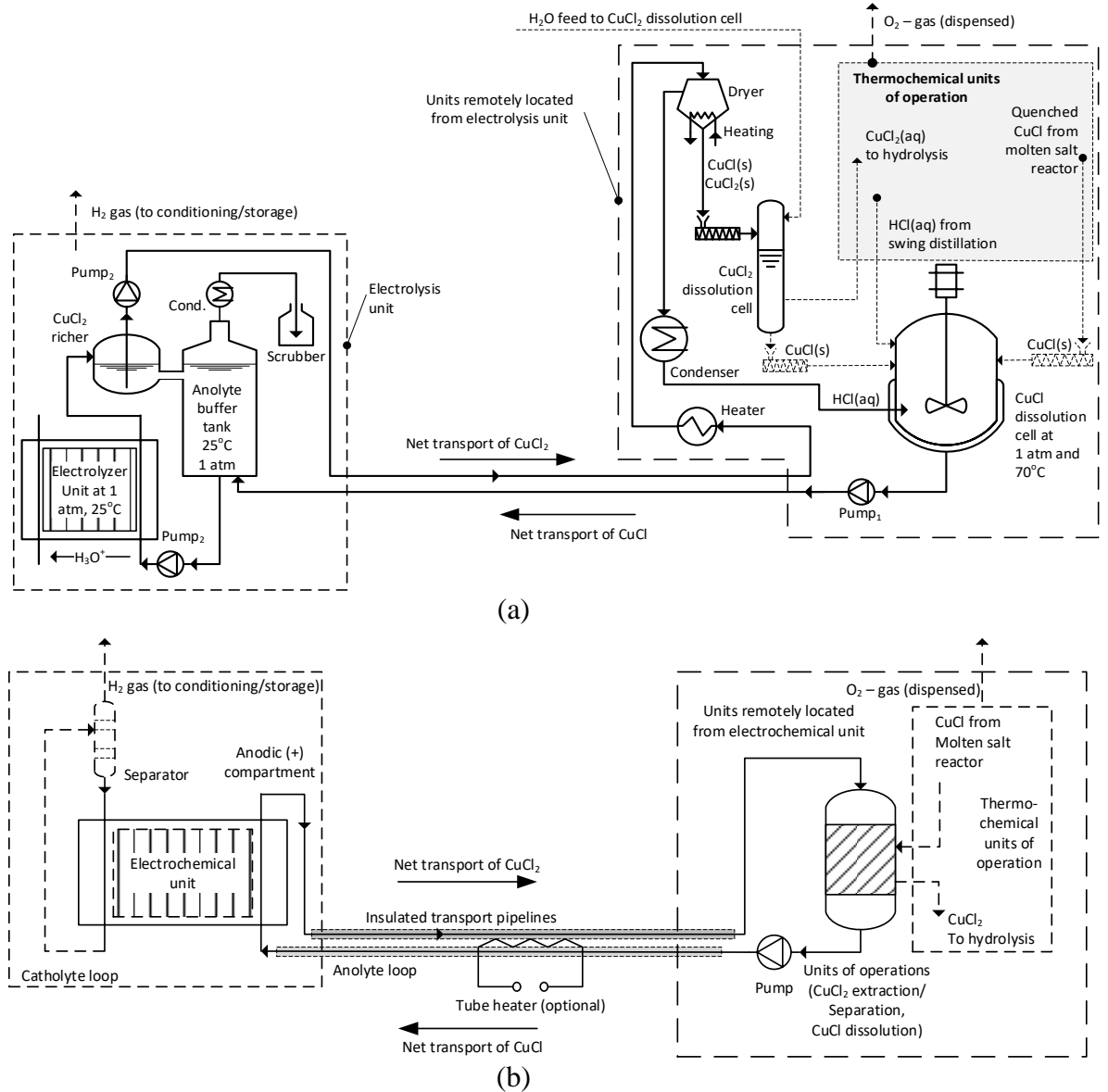


Figure 3.7. (a) Schematic diagram representing the lab-scale integrated Cu-Cl cycle built at CERL in UOIT. (b) Anolyte loop for the lab-scale CuCl/HCl(aq) electrolyzer stack operating at room temperature and 1 atm .

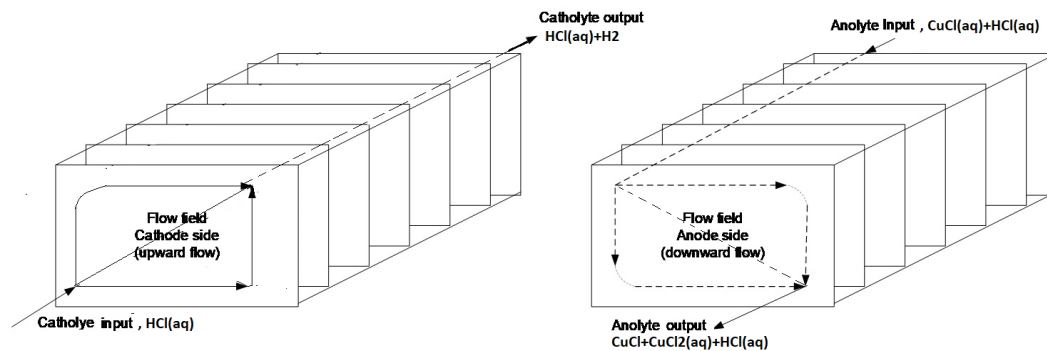


Figure 3.8. Schematic diagram of Z-type manifold configuration of CuCl/HCl(aq) electrolyzer stack (anolyte and catholyte distribution flow pattern).

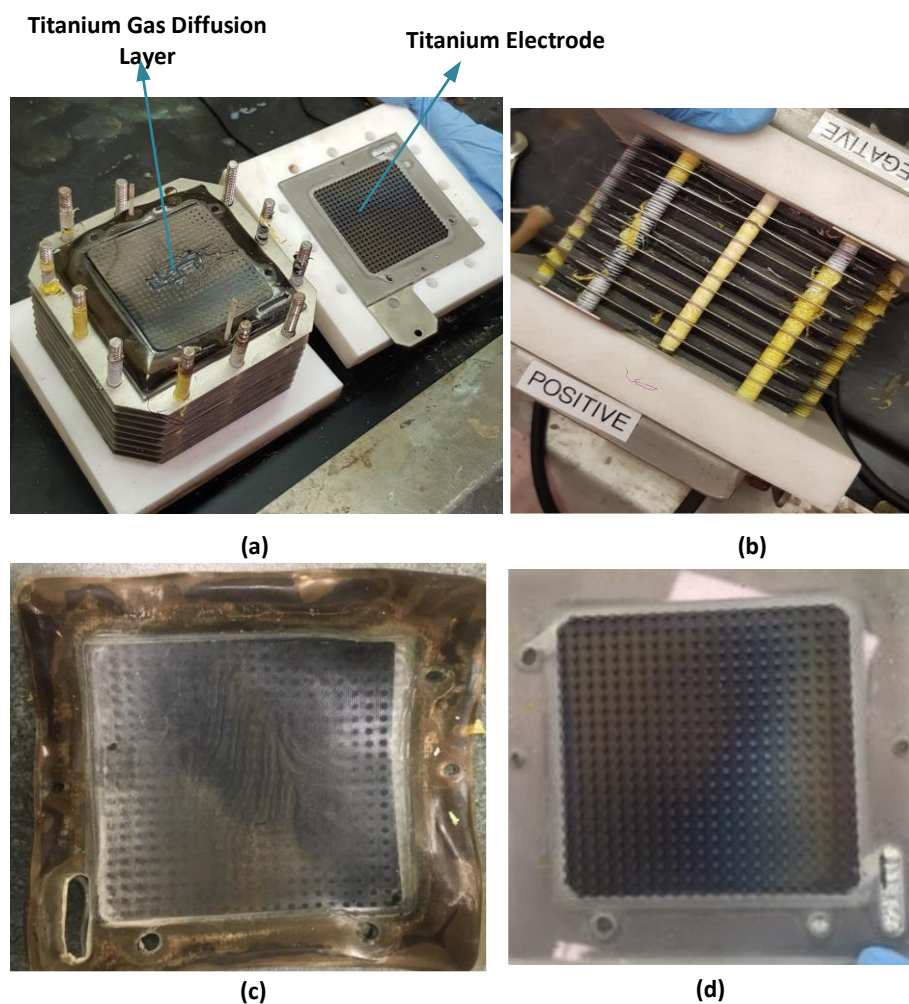
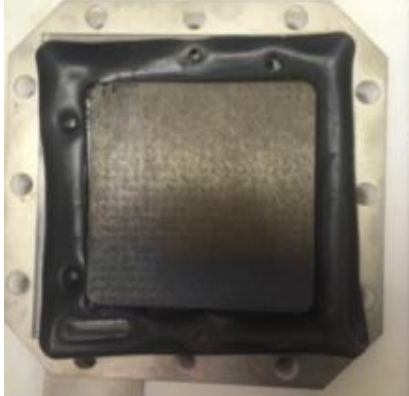


Figure 3.9. Photograph of CuCl/HCl (aq) electrochemical cell at UOIT (a) stack with 10 MEA (b) disassembled stack (c) Ti/Pt Nafion 117 membrane (d) Ti electrode.

Table 3.2 .Case studies for anolyte and catholyte concentrations in CuCl/HCl (aq) electrolyzer.

Electrolyte characteristics	Effect on Nafion 117 membrane
Anolyte : 2 mol CuCl in 7 mol of HCl (aq)	 <p data-bbox="716 751 1323 787">Copper precipitation on the membrane surface.</p>
Catholyte: 7 mole of HCl (aq)	
Anolyte : 0.2 mol CuCl in 2 mol of HCl(aq)	
Catholyte: 2 mole of HCl (aq)	

Chapter 4 . Analysis and Optimization

In this chapter, the lab-scale integrated Cu-Cl cycle performance is studied and optimized. To analyze and then optimize the examined cycle, the components of the cycle are model and simulated in Aspen Plus tool, Engineering Equation Software (EES) and Comsol Multiphysics software. Also, In order to evaluate the economic aspects of the system, exergoeconomic and scale-up analyses are performed. The primary analyses performed in this work are illustrated in the following sections as shown in Figure 4.1.

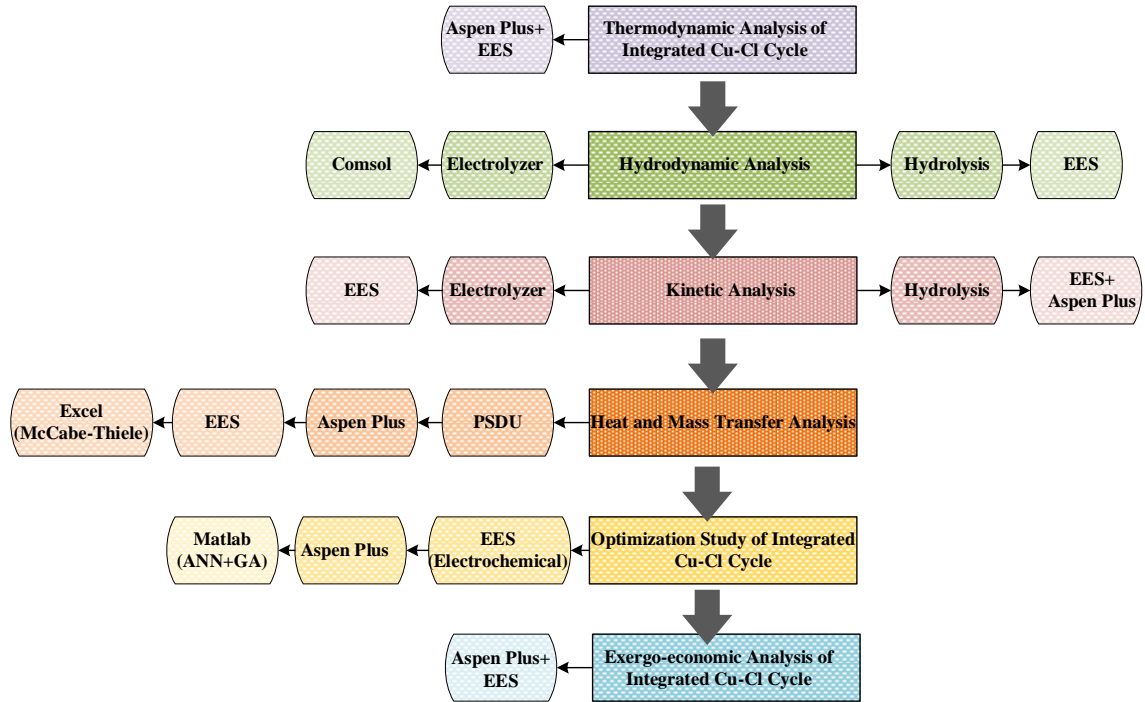


Figure 4.1. Flowsheet of the modeling methodology used to assess the performance of the lab-scale integrated Cu-Cl cycle.

4.1. Thermodynamic Analysis of the Lab-scale Integrated Cu-Cl Cycle

The Aspen Plus flowsheet of the integrated four-step Cu-Cl cycle is presented in Figure 4.2. It comprises of dryer, hydrolysis, thermolysis, electrolysis, atmospheric distillation unit of anolyte (ADA), anolyte makeup vessel (AMV), drying unit, separation unit through selective CuCl_2 dissolution in water, CuCl_2 (aq) concentrator, stirred dissolution cell of CuCl in HCl (aq), pressure swing distillation unit (PSDU), HCl (aq) condensers, steam condensers, quench cell and decanter of CuCl . The open streams (purple circles) in the

Aspen Plus flowsheet in Figure 4.2 are used to prevent excessive iteration by the software. This does not lead to any problem with the software or reliability of results. The detailed integrated cycle description is presented following.

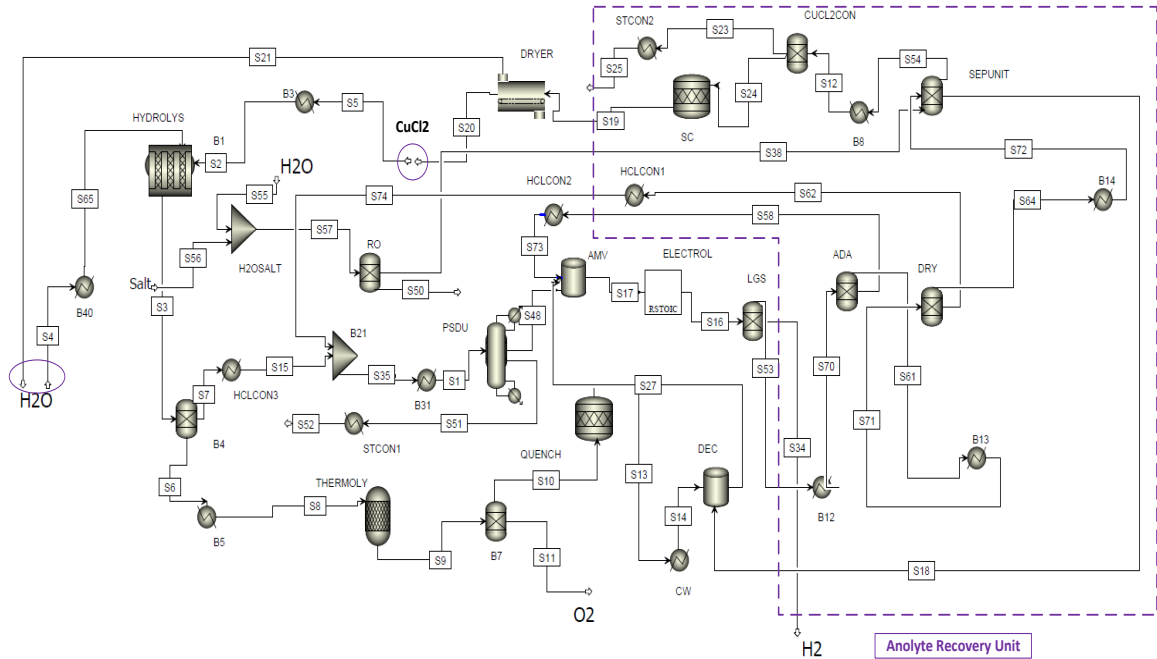


Figure 4.2. Aspen Plus flowsheet diagram of the integrated four-step Cu-Cl cycle

The anodic electrolyte comprises the slurry CuCl, CuCl₂ (aq) and concentrated HCl (aq) to form a strong anolyte at the dissolution cell (S17). This strong anolyte is sent into the anolyte makeup vessel (AMV) which is maintained at a temperature of 45°C. Through the electrochemical reaction, from the cation exchange membrane electrolyzer at the cathode side, hydrogen is produced and then separated from the other products at the liquid-gas separator (LGS) (S34). At the anode side, the oxidized anolyte as CuCl₂ (aq) and HCl (aq) leave the electrolyzer unit.

The oxidized anolyte passes through the subsequent processes recovering the electrolyte by removing water. For this regard, the oxidized anolyte is heated until 110°C by heater B12 and then enters into the atmospheric distillation unit of anolyte (ADA) (S70), where the concentrated HCl (g) and H₂O (g) partially separated from the oxidized electrolyte, then condense in the HCl (aq) condenser (S73). From the bottom of the ADA unit, the anolyte at a molality of 6 HCl with the high salt concentration moves toward the dryer anolyte unit (S61).

The HCl (aq) separated at the ADA unit mixes with the other hydrochloric binary mixture which comes from the hydrolysis, and then is fed into the pressure swing distillation unit (PSDU) (S1). At the PSDU, consider an HCl-water binary mixture at a maximum boiling azeotrope in a pressure swing distillation process. The separation process is capable of concentrating HCl aqueous mixtures beyond the azeotropic composition. The samples from the bottom product are taken at certain time intervals. The samples are analyzed by an acid-base titration method with a phenolphthalein indicator to calculate the concentration of the bottom product. Once the HCl (aq) enters the low pressure column the distillation process starts occurring, with the liquid falling down through the stripping section and the vapor rising through the reflux section. It is assumed that the low pressure column is made of a glass tube and is heated from the exterior at a constant heat flux. Two such columns are placed in parallel to conduct the low pressure distillation process. At the top part of the columns, a reflux condenser is placed, consisting of a non-insulated glass column cooled with air. A positive displacement pressure pump is used to displace the liquid from low pressure to high pressure at an appropriate flow rate, as per the operating conditions. The pump injects the HCl (aq) into the high-pressure column. At the top of the pressurized column, a non-insulated section exits for the reflux process. The high-pressure column is assumed to be heated with high temperature thermal oil circulated at a high flow rate. There are three similar high-pressure columns operating in parallel to show the pressure swing distillation system diagram [40]. Finally, the concentrated HCl (aq) (S48) from the PSDU, the CuCl from the decanter (S27) and the recycled HCl (aq) from the dry unit (S73) are delivered into the stirred dissolution cell (DC) where through the continuous stirring, a homogeneous anolyte would be formed and then stored in the stirred anolyte make-up vessel (AMV).

At the separation unit where the mushy CuCl and CuCl₂ mixture is coming from the anolyte dryer unit, more CuCl constituent will be extracted from the mushy CuCl and CuCl₂ mixture to yield the more concentrated CuCl₂ (aq). Since only CuCl₂ dissolves in the water, by falling the mushy CuCl and CuCl₂ mixture into the cold distilled water (supplied by the reverse osmosis desalination unit (RO)), the CuCl₂ dissolves in water and then goes forward to the CuCl₂ (aq) concentrator (S54). At this part, the thermal oil is used to supply heat to the aqueous mixture to partially remove water from the CuCl₂ (aq) through

the water vaporization and then condensation in the steam condenser (S25). Ultimately, at the dryer unit with a temperature of 130 °C, the rest of the concentrated mixture of CuCl_2 and H_2O is separated from each other (S20 and S21) and delivered to the hydrolysis reactor.

At the hydrolysis thermochemical reaction, CuCl_2 (s) is falling downward and H_2O (g) and HCl (g) are coming upward from the vertical furnace. Through the endothermic reaction, Cu_2OCl_2 (s), H_2O (g) and HCl (g) are formed at the temperature of 430°C. HCl (g) and H_2O (g) as the hydrolysis products move forward to the HCl (aq) condenser and then are fed into the pressure swing distillation unit (PSDU). The Cu_2OCl_2 (s) is the other hydrolysis product (S6), preheated until 530°C (by B5 heat exchanger) and then delivered to the thermolysis reactor. It decomposes into O_2 (g) and CuCl (L) moving toward the quench cell to be solidified. Again, since CuCl (l) does not dissolve in the cold water, and the liquid CuCl drops into the cold water bed which absorbs the heat released from the CuCl solidification process. Then at the decanting cell, the CuCl dense slurry is transferred to the dissolution tank (S29) where the HCl (aq) from the PSDU mixes with the CuCl (s) to form a strong aqueous electrolyte consisting hydrochloric acid, cupric chloride, cuprous chloride and water ready for the electrolyzer unit.

In order to have a successful thermodynamic analysis by means of the Aspen Plus simulation tool, implementing the standard thermodynamic properties of all possible materials, as well as adapting the proper property methods for different forms of species are required. The lab-scale integrated Cu-Cl cycle is examined in this section with an exergy analysis. In the present integrated Cu-Cl cycle, numerous design input parameters influence the cycle performance. Table 4.1 provides a detailed list of design parameters in the system. Simulation tools for considering and investigating all listed parameters in Table 4.1 will have a complexity of analysis due to the sensitivity of the system specifically in response to changes in the material concentrations and temperatures. For example, the CuCl_2 particle diameter is one of the factors that impact the conversion of CuCl_2 into the products. However, changing this diameter may change the desired product concentration in the hydrolysis reactor. The total effect of this conversion change may not lead to a significant change in the exergy efficiency and cost of the whole integrated cycle. In addition, assessing the effects of particle diameter in the Aspen Plus simulator software

needs user-defined modules. For this reason, the main influencing design parameters on the system performance in terms of efficiency and cost are selected as outlined in Table 4.2. Integrated Cu-Cl thermochemical water decomposition cycle initial and design parameters [20]. The primary assumptions and property methods for system modeling and development are summarized below:

- The integrated Cu-Cl cycle operates under steady-state conditions.
- The reference environmental conditions are considered as 25°C and atmospheric pressure.
- Aspen Plus data and literature are used to obtain the solid and electrolyte thermophysical and thermochemical properties [20, 24, 71, 91, 93] .
- The Peng-Robinson (Peng-Rob) model for the gaseous phase, Universal Quasichemical (UNIQUAC) model for the aqueous phase and Solid for solid materials are used as the property methods to analyze the system.
- The energy and exergy flows are described on a per mole basis of the produced hydrogen.

In the Aspen Plus simulation tool, an R-Plug reactor is employed for the hydrolysis and thermolysis reactors. This is compatible with the kinetic parameters of the reaction and consequently yields more reliable results that are consistent with empirical data from the past literature. In this respect, the kinetic parameters of the hydrolysis reaction are derived from Refs. [3, 27, 102, 109, 112, 113] . For the Thermolysis reactor, some empirical parameters are employed from Refs. [114- 117]. Finally, the kinetic characteristics for the electrochemical cell are addressed in [24, 39, 92, 94] . Since Aspen Plus software did not provide the electrochemical interactions, the HCl/CuCl(aq) electrolyzer is modeled through the Equation Engineering Software (EES). More detailed descriptions, model development and model verification for the hydrolysis thermochemical reaction and electrolyzer electrochemical reaction were presented previously [20, 23-25] and [133].

The equations of mass conservation, first and second laws of thermodynamic have been used to evaluate thermodynamic performance of the integrated Cu-Cl cycle and all of its components. Under steady-state conditions, the general mass, energy and exergy balance correlations for each component can be written as below.

$$\sum \dot{m}_{in} - \sum \dot{m}_{out} = 0 \quad (4.1)$$

$$\dot{Q} - \dot{W} + \sum \dot{m}_{in} h_{in} - \sum \dot{m}_{out} h_{out} = 0 \quad (4.2)$$

$$Ex^{\dot{Q}} - Ex^{\dot{W}} + \sum \dot{m}_{in} ex_{in} + \sum \dot{m}_{out} ex_{out} - \dot{E}D = 0 \quad (4.3)$$

Here $\dot{E}D$ refers to the exergy destruction rate and $Ex^{\dot{Q}}$ denotes the exergy content associated with the heat transfer rate and can be obtained as follows.

$$Ex^{\dot{Q}} = \left(1 - \frac{T_0}{T_b}\right) \dot{Q} \quad (4.4)$$

The quantitative exergy analysis of the cation exchange membrane electrolyzer unit, the hydrolysis and thermolysis reactors can be conducted in conjunction with the electrochemical and thermochemical modeling, respectively. In this regard, chemical exergy consideration plays a key element to achieve a reliable thermodynamic modeling. Hence, a general formulation for the specific chemical exergy can be written as [134], [135].

$$ex_{ch} = \sum x_j ex_{ch}^0 + RT_0 \sum x_j \ln(x_j) \quad (4.5)$$

where x_j refers the mole fraction of constituent j in the flow and R is the universal gas constant in kJ/molK. As well as, ex_{ch}^0 denotes the standard specific chemical exergy of the constituent j in kJ/mol. The standard specific chemical exergy, standard Gibbs free energy of formation, standard enthalpy of formation and standard entropy of formation and other properties correlations for Cu_2OCl_2 , $CuCl$ and $CuCl_2$ species in the integrated Cu-Cl cycle are tabulated in Table 4.3. The specific chemical exergy correlations for the anolyte interacted with the cation exchange membrane electrolyzer are employed based on Gibbs energy minimization approach in Refs [20, 71, 95, 142-145]. The chemical exergy determination for H_2 can be also gained from the JANAF Table [138]. Also, based on past experimental data [19, 36] at which the electrochemical over-potential was incorporated into the decomposition potential prediction, the average electrical energy consumption at the $CuCl/HCl$ (aq) electrolyzer is taken as 111 kJ/mol H_2 . Besides, Figure 4.3 shows the detailed scheme of the recycling process of anolyte at the Cu-Cl cycle.

Table 4.1. Typical variable ranges in the Cu-Cl thermochemical cycle.

Variable	Lower limit	Upper limit	Units
Hydrolysis Reactor			
Total pressure of reactor	100	110	kPa
Mole fraction of steam in gaseous mixture	0.5	0.9	-
Hot side temperature	350	450	°C
Cold side temperature	200	250	°C
Volumetric flow rate of CuCl ₂ (aq)	100	450	ml/min
Steam/CuCl ₂ ratio	7	23	-
Steam velocity	0.1	0.6	m/s
Particle diameter	100	350	µm
Furnace length	1.0	1.5	m
Furnace tube diameter	Particle diameter × 3	Particle diameter × 6	-
Thermolysis Reactor			
Pressure	100	110	kPa
Hot side temperature	480	580	°C
Surface convection coefficient	0.5	4	W/m ² K
Electrochemical reactor			
Pressure	100	110	kPa
Temperature	25	85	°C
Anolyte supplied into electro-chemical unit	0.5 × mass flow rate of oxidized anolyte	2 × mass flow rate of oxidized anolyte	mol/s
Concentration of HCl (proton constant)	6		mol
Cell potential	0.4	0.9	V
Membrane thickness	500	200	µm
Current density	0	10,0000	A/m ²
Dehydration Unit			
Pressure	100	120	kPa
Temperature of gas bulk flow	100	160	°C
Temperature of droplet surface	100	160	°C
Mean droplet diameter	20	140	µm
Volumetric flow rate of CuCl ₂ (aq)	100	450	ml/min
Pressure Swing Distillation Unit			
Low pressure side pressure	100	130	kPa
High pressure side pressure	300	500	kPa
Low pressure side temperature	100	120	°C
High pressure side temperature	120	160	°C
HCl feed molar concentration at low pressure side	0.08	0.18	-
HCl feed molar concentration at High pressure side	0.11	0.22	-
Reflux ratio	0.4	1.6	-

Table 4.2. Integrated Cu-Cl thermochemical water decomposition cycle initial and design parameters [20]

Parameter	Value	Unit
Hydrolysis reactor operating temperature	410	°C
Hydrolysis reactor operating pressure	1	bar
Thermolysis reactor (Cu ₂ OCl ₂ decomposition reactor) operating temperature	520	°C
Thermolysis reactor (Cu ₂ OCl ₂ decomposition reactor) operating pressure	1	bar
Coppers chloride electrolyzer operating temperature	45	°C
Coppers chloride electrolyzer operating pressure	1	bar
Coppers chloride electrolyzer electrical unit energy consumption	111	kJ/mol H ₂
H ₂ O supplied to the electrolysis reactor (instead describe)	20	mol
Dryer operating temperature	130	°C
Dryer operating pressure	1	bar
ADA operating temperature	105	°C
ADA operating pressure	1	bar
Dry unit operating temperature	110	°C
Dry unit operating pressure	1	bar
Separation unit operating temperature	65	°C
Separation unit operating pressure	1	bar
CuCl ₂ concentrator operating temperature	115	°C
CuCl ₂ concentrator operating pressure	1	bar
PSDU operating temperature	115	°C
PSDU operating pressure (low pressure side (LPS) and high pressure side (HPS))	LPS=1 HPS=4	bar
RO operating temperature	35	°C
RO electrical unit energy consumption	8.5	kJ/ kg water
Quench operating temperature	425	°C
Quench operating pressure	1	bar

Table 4.3. The material properties and correlations applied in Aspen Plus simulation model of proposed integrated Cu-Cl cycle [20, 71, 144, 145].

Copper oxychloride (Cu₂OCl₂, Melanothallite)						
Parameter	Value or correlation*					
Molecule formation	$\Delta_f H^\circ = -384.65 \pm 2.5 \text{ kJ/mol}$; $\Delta_f S^\circ = 154.352 \text{ J/molK}$; $\Delta_f G^\circ = -369.7 \text{ kJ/mol}$; $\log k_f = 64.75$; $\text{ex}_{\text{ch}} = 21.08 \text{ kJ/mol}$; $c_p^\circ = 116.77 \text{ kJ/kmol.K}$; $T_o = 298.15 \text{ K}$ and $P_o = 1 \text{ atm}$					
$c_p, \text{ kJ/kmolK}$	$a + bT + cT^2 + dT^3$; $a = 53.7166572$; $b = 0.334033497$; $c = -5.22127940 \times 10^{-4}$; $d = 2.99950910 \times 10^{-7}$					
$s, \text{ J/molK}$	$a + b \ln(T) + cT + dT^2 + eT^3$; $a = 154.352$; $b = 53.7166572$; $c = 0.334033497$; $d = -0.2610639700 \times 10^{-3}$					
$\text{ex}, \text{ J/mol}$	$a + bT + cT^2 + dT^3 + eT^4 + f \ln(T)$; $a = 0.358948789 \times 10^5$; $b = -45.87542993$; $c = 0.2448529712$; $d = -0.2038527680 \times 10^{-3}$; $e = 1.3589 \times 10^5$; $f = -16015.62134$					
Cuprous chloride (CuCl, Nantokite)						
Parameter	Value or correlation*					
Melting point	Reported value at 436°C					
Normal boiling point	Boiling starts when the temperature is 1221.85°C					
Vapor pressure	The vapor pressure at the triple point is 10.19 Pa					
	T (K)	732.15	816.15	948.15	1,187.15	1,750.15
	P (Pa)	10	100	1,000	10,000	100,000
Molecule formation	$\Delta_f H^\circ = -136.816 \text{ kJ/mol}$; $\Delta_f S^\circ = 87.446 \text{ J/molK}$; $\Delta_f G^\circ = -199.44 \text{ kJ/mol}$; $\log k_f = 21.02$; $\text{ex}_{\text{ch}} = 75.0 \text{ kJ/mol}$; $c_p^\circ = 53.34 \text{ kJ/kmol.K}$; $T_o = 298.15 \text{ K}$ and $P_o = 1 \text{ atm}$					
$c_p, \text{ kJ/kmolK}$	T=298-683 K	$a + bT + cT^{-2}$; $a = 51.087$; $b = 17.656 \times 10^{-3}$; $c = 268 \times 10^3$				
$s, \text{ J/molK}$	T=298-683 K	$a + b \ln(T) + cT + dT^{-2}$; $a = -210.3986829$; $b = 51.087$; $c = 0.017656$; $d = 1.34 \times 10^5$				
$\text{ex}, \text{ J/mol}$	T=298-683 K	$a + bT + cT^2 + dT^{-1} + eT^{-2} + f \ln(T)$; $a = 191,327.176$; $b = 45.823$; $c = 0.008828$; $d = 268,000$; $e = 3.9952 \times 10^7$; $f = -15,231.589$				
Cupric chloride (CuCl₂, Tolbachite)						
Parameter	Value or correlation*					
Melting point	Reported value at 498°C					
Normal boiling point	Boiling starts when the temperature is 993°C					
Decomposition	Melting is accompanied by decomposition in Cu ₂ Cl ₂ at 993°C					
Molecule formation	$\Delta_f H^\circ = -218.0 \text{ kJ/mol}$; $\Delta_f S^\circ = 108.07 \text{ J/molK}$; $\Delta_f G^\circ = -173.826 \text{ kJ/mol}$; $\log k_f = 30.453$; $\text{ex}_{\text{ch}} = 82.474 \text{ kJ/mol}$; $c_p^\circ = 71.88 \text{ kJ/kmolK}$; $T_o = 298.15 \text{ K}$ and $P_o = 1 \text{ atm}$					
$c_p, \text{ kJ/kmolK}$	T=298-675 K, crystal I	$a + bT + cT^2 + dT^3 + eT^4 + fT^5$, $a = -16.3596145$; $b = 0.750699416$; $c = -2.56737967 \times 10^{-3}$; $d = 4.62107127 \times 10^{-6}$; $e = -4.34415987 \times 10^{-9}$; $f = 1.57231698 \times 10^{-12}$				
	675-871 K, crystal II	82.4				
For the liquid phase, Aspen Plus library has the required data						

s, J/molK	T=298-675 K, crystal I	$a + bT + cT^2 + dT^3 + eT^4 + fT^5 + g\ln(T)$; $a = 58.38957705$, $b = 0.750699416$; $c = -1.283689835 \times 10^{-3}$; $d = 1.54035709 \times 10^{-6}$; $e = -1.061039968 \times 10^{-9}$; $f = 3.14463396 \times 10^{-13}$; $g = -16.3596145$
	T=675-871 K, crystal II	$172.2201546 + 82.4 \ln(T/675)$
	For the liquid phase, Aspen Plus library has the required data	
ex, J/mol	$a + bT + cT^2 + d \ln(T)$	
	T=298-675 K	$a = 1.850096 \times 10^5$; $b = 68.091341$; $c = 0.69649 \times 10^{-2}$; $d = -21,667.1954$
	T=675-871 K	$a = 1.978071674$; $b = 82.4$; $c = 1.835569 \times 10^{-9}$; $d = -24,567.55627$
	T=871-1,130.75 K	$a = 2.278675157$; $b = 100$; $c = -6.751777 \times 10^{-9}$; $d = -29815.02$
T=871-1,130.75 K		$a = 2.278675157$; $b = 100$; $c = -6.751777 \times 10^{-9}$; $d = -29815.02$

The exergy destruction rate and the energy and exergy efficiencies of the proposed integrated Cu-Cl cycle and its components are obtained by applying the corresponding conservation of mass, energy and exergy equations. The exergy efficiency and exergy destruction formulations for various units of the proposed system are provided in Table 4.4. Since it has been assumed that there is no heat loss from thermal devices, the energy efficiency of the heat exchanger units would be 100%, so, the energy efficiency of system components are not addressed. Finally, in order to evaluate the performance of whole integrated Cu-Cl cycle for hydrogen production purpose under the specific design and initial operating condition, the overall energy and exergy efficiencies of the system can be defined as

$$\eta_{\text{Cu-Cl}} = \frac{\dot{m}_{\text{H}_2} \text{LHV}_{\text{H}_2}}{\dot{Q}_{\text{net,in}} + \dot{W}_e} \quad (4.6)$$

$$\Psi_{\text{Cu-Cl}} = \frac{\dot{m}_{\text{H}_2} \text{ex}_{\text{H}_2}}{\dot{\text{Ex}}_{\dot{Q}_{\text{net,in}}} + \dot{W}_e} \quad (4.7)$$

where \dot{W}_e refers to the electrical energy consumed by the electrolytic cell (excluding the pumps) considered based on literature [91], and $\dot{Q}_{\text{net,in}}$ denotes the summation of all heat duties consumed at apparatuses as.

$$\dot{Q}_{\text{net,in}} = (\dot{Q}_{\text{ADA}} + \dot{Q}_{\text{Dry}} + \dot{Q}_{\text{PSDU}} + \dot{Q}_{\text{CuCl}_2\text{CON}} + \dot{Q}_{\text{Dryer}} + \dot{Q}_{\text{Pre-H}} + \dot{Q}_{\text{in}}) \quad (4.8)$$

Here, \dot{Q}_{Pre-H} and \dot{Q}_{in} refer to the heat required for preheating the reactants in the hydrolysis and Cu_2OCl_2 solid decomposition reactors and the heat supplied for those reactions, respectively, since the hydrolysis and thermolysis reactions are endothermic.

Table 4.4. Exergy efficiency and exergy destruction rate definition for the proposed integrated Cu-Cl cycle components.

Device	Exergy efficiency	Exergy destruction rate
Hydrolysis reactor	$\psi_{Hyd} = \frac{\dot{m}_{S6}ex_{S6} + \dot{m}_{S7}ex_{S7}}{\dot{m}_{S4}ex_{S4} + \dot{m}_{S5}ex_{S5} + \dot{E}x_{\dot{Q}_{Hyd}} + \dot{E}x_{\dot{Q}_{B3}} + \dot{E}x_{\dot{Q}_{B40}} + \dot{E}x_{\dot{Q}_{B4}}}$	$\dot{E}D_{Hyd} = (\dot{m}_{S4}ex_{S4} + \dot{m}_{S5}ex_{S5} + \dot{E}x_{\dot{Q}_{Hyd}} + \dot{E}x_{\dot{Q}_{B3}} + \dot{E}x_{\dot{Q}_{B40}} + \dot{E}x_{\dot{Q}_{B4}}) - (\dot{m}_{S6}ex_{S6} + \dot{m}_{S7}ex_{S7})$
Thermolysis (Cu_2OCl_2 decomposition reactor)	$\psi_{Th} = \frac{\dot{m}_{S10}ex_{S10} + \dot{m}_{S11}ex_{S11}}{\dot{m}_{S6}ex_{S8} + \dot{E}x_{\dot{Q}_{Therm}} + \dot{E}x_{\dot{Q}_{B5}} + \dot{E}x_{\dot{Q}_{B7}}}$	$\dot{E}D_{Th} = \dot{m}_{S6}ex_{S8} + \dot{E}x_{\dot{Q}_{Therm}} + \dot{E}x_{\dot{Q}_{B5}} + \dot{E}x_{\dot{Q}_{B7}} - (\dot{m}_{S10}ex_{S10} + \dot{m}_{S11}ex_{S11})$
Electrolyser	$\psi_{Elec} = \frac{\dot{m}_{S16}ex_{S16}}{\dot{W}_e + \dot{m}_{S73}ex_{S73} + \dot{m}_{S48}ex_{S48} + \dot{m}_{S27}ex_{S27}}$	$\dot{E}D_{Elec} = \dot{W}_e + \dot{m}_{S73}ex_{S73} + \dot{m}_{S48}ex_{S48} + \dot{m}_{S27}ex_{S27} - (\dot{m}_{S10}ex_{S10} + \dot{m}_{S11}ex_{S11})$
Dryer	$\psi_{Dryer} = \frac{\dot{m}_{S21}ex_{S21} + \dot{m}_{S20}ex_{S20}}{\dot{E}x_{\dot{Q}_{Dryer}} + \dot{m}_{S19}ex_{S19}}$	$\dot{E}x_{d,B14} = \dot{E}x_{\dot{Q}_{Dryer}} + \dot{m}_{S19}ex_{S19} - (\dot{m}_{S21}ex_{S21} + \dot{m}_{S20}ex_{S20})$
H_2 separator (liquid gas separator (LGS))	$\psi_{LGS} = \frac{\dot{m}_{S34}ex_{S34} + \dot{m}_{S53}ex_{S53}}{\dot{m}_{S16}ex_{S16} + \dot{E}x_{\dot{Q}_{LGS}}}$	$\dot{E}D_{LGS} = (\dot{m}_{S16}ex_{S16} + \dot{E}x_{\dot{Q}_{LGS}}) - (\dot{m}_{S34}ex_{S34} + \dot{m}_{S53}ex_{S53})$
Atmospheric distillation unit of Anolyte (ADA)	$\psi_{ADA} = \frac{\dot{m}_{S61}ex_{S61} + \dot{m}_{S58}ex_{S58}}{\dot{m}_{S53}ex_{S53} + \dot{E}x_{\dot{Q}_{B12}} + \dot{E}x_{\dot{Q}_{ADA}}}$	$\dot{E}D_{ADA} = (\dot{m}_{S53}ex_{S53} + \dot{E}x_{\dot{Q}_{B12}} + \dot{E}x_{\dot{Q}_{ADA}}) - (\dot{m}_{S61}ex_{S61} + \dot{m}_{S58}ex_{S58})$
Dry unit of anolyte	$\psi_{Dry} = \frac{\dot{m}_{S62}ex_{S62} + \dot{m}_{S64}ex_{S64}}{\dot{m}_{S61}ex_{S61} + \dot{E}x_{\dot{Q}_{B13}} + \dot{E}x_{\dot{Q}_{DRY}}}$	$\dot{E}D_{DRY} = (\dot{m}_{S61}ex_{S61} + \dot{E}x_{\dot{Q}_{B13}} + \dot{E}x_{\dot{Q}_{DRY}}) - (\dot{m}_{S62}ex_{S62} + \dot{m}_{S64}ex_{S64})$
Separation unit (SEPUNIT)	$\psi_{SEPUNIT} = \frac{\dot{m}_{S18}ex_{S18} + \dot{m}_{S54}ex_{S54}}{\dot{m}_{S64}ex_{S64} + \dot{m}_{S38}ex_{S38} + \dot{E}x_{\dot{Q}_{B14}} + \dot{E}x_{\dot{Q}_{SEP}}}$	$\dot{E}x_{d,B15B5} = (\dot{m}_{S64}ex_{S64} + \dot{m}_{S38}ex_{S38} + \dot{E}x_{\dot{Q}_{B14}} + \dot{E}x_{\dot{Q}_{SEP}}) - (\dot{m}_{S18}ex_{S18} + \dot{m}_{S54}ex_{S54})$
$CuCl_2$ Concentrator ($CuCl_2$ CONC)	$\psi_{B16B2} = \frac{\dot{m}_{S23}ex_{S23} + \dot{m}_{S24}ex_{S24}}{\dot{m}_{S54}ex_{S54} + \dot{E}x_{\dot{Q}_{B8}} + \dot{E}x_{\dot{Q}_{CuCl2con}}}$	$\dot{E}x_{d,B16B2} = (\dot{m}_{S54}ex_{S54} + \dot{E}x_{\dot{Q}_{B8}} + \dot{E}x_{\dot{Q}_{CuCl2con}}) - (\dot{m}_{S23}ex_{S23} + \dot{m}_{S24}ex_{S24})$
PSDU (Pressure swing distillation unit)	$\psi_{PSDU} = \frac{\dot{m}_{S48}ex_{S48} + \dot{m}_{S51}ex_{S51}}{\dot{m}_{S35}ex_{S35} + \dot{E}x_{\dot{Q}_{B31}} + \dot{E}x_{\dot{Q}_{PSDU}}}$	$\dot{E}D_{PSDU} = (\dot{m}_{S35}ex_{S35} + \dot{E}x_{\dot{Q}_{B31}} + \dot{E}x_{\dot{Q}_{PSDU}}) - (\dot{m}_{S48}ex_{S48} + \dot{m}_{S51}ex_{S51})$
RO (Reverse osmosis)	$\psi_{RO} = \frac{\dot{m}_{S50}ex_{S50} + \dot{m}_{S38}ex_{S38}}{\dot{W}_{RO} + \dot{m}_{S54}ex_{S54} + \dot{m}_{S54}ex_{S54} + \dot{E}x_{\dot{Q}_{B31}}}$	$\dot{E}D_{RO} = \dot{m}_{S54}ex_{S54} + \dot{m}_{S54}ex_{S54} + \dot{E}x_{\dot{Q}_{B31}} + \dot{W}_{RO} - (\dot{m}_{S50}ex_{S50} + \dot{m}_{S38}ex_{S38})$

4.2. Hydrolysis Reaction Analysis

In the hydrolysis reaction, the ideal condition (product yield based on the stoichiometry) does not account for the excess steam, undesirable side reactions such as CuCl_2 decomposition into CuCl (s), unreacted materials and effects of the variations of the reactor operating condition on the amount of products.

4.2.1. Thermodynamic modeling of Hydrolysis Reaction

With an increase of reactor temperature, the chemical exergy content in the reactants remains nearly constant while the kinetic parameters and the enthalpy of the species change significantly. Examining the effects of reaction operating parameters on the exergetic efficiency with respect to the ideal stoichiometry condition may lead to the wrong interpretation for assessing the reactor performance. Hence, it is required to study the real reaction conditions, in which the operating parameters change the kinetic characteristics of the chemical reaction and consequently the desirable products. This section will assess the hydrolysis reaction exergetically to analyze the entropy generation of CuCl_2 decomposition and to evaluate the hydrolysis reactor performance under the real operating condition.

The hydrolysis reactor is modeled with Aspen Plus including the primary side reaction of CuCl_2 decomposition into cuprous chloride and chlorine gas. The other probable side reactions (such as oxidation of CuCl_2 into CuO) are not considered in this study. The oxidation of CuCl_2 to CuO in an argon atmosphere, is highly unlikely and a negligible amount of the byproduct increases the complexity of the simulation. Reaction kinetic parameters are used from past experimental studies and then adopted in the simulation. Since Aspen Plus does not account for the chemical exergy of species, the stream properties from Aspen Plus are transferred into Excel and EES software for the parametric studies. Results from the predictive models will be presented and discussed.

The hydrolysis reaction is modeled in a process simulation package, Aspen Plus, as shown in Figure 4.4. The simulation of Cu_2OCl_2 decomposition hydrolysis is performed at thermodynamic equilibrium under a specific operating condition and flow rates. In the Aspen Plus V10, a solid model is used to acquire thermodynamic properties of species interactions in the system, while in the previous software version they were inserted manually into the software database. An R-Plug reactor is employed for the hydrolysis reactor. Unlike the R-Stoic and R-Gibbs reactors, R-Plug reveals consistent outcomes since

this block is compatible with the kinetic parameters of the reaction and consequently yields more reliable results that are consistent with empirical data from the literature [27], [98], [105]. No Argon gas and no Nitrogen gas (as the steam carrier and pressure regulator) are assumed in the simulation. A uniform temperature profile alongside the reactor is assumed.

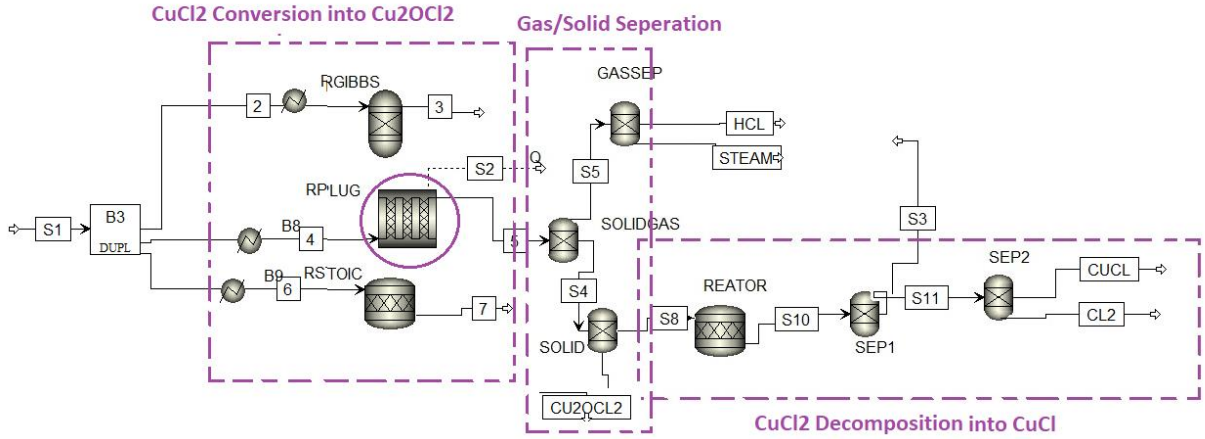


Figure 4.4. Aspen Plus flowsheet of hydrolysis reaction including CuCl_2 conversion into Cu_2OCl_2 , gas/solid product separation and CuCl_2 decomposition into CuCl and Cl_2 .

The specific exergy of each reactant or product species includes the kinetic (k), potential (φ) thermal $((T - T_0)s)$, strain $((P - P_0)v)$ and chemical exergy. In the hydrolysis reaction, the main changes in the exergy content of the reactor are associated with the chemical exergy change of components. The general equation for the exergy can be written as [139], [140]:

$$ex = k + \Psi + (T - T_0)s - (P - P_0)v + \sum_i(\mu_i - \mu_{i0})x_i \quad (4.9)$$

The rate of specific exergy change for moving fluid through the domain can be expressed in terms of the total substantial derivatives as follows [139], [140],

$$\frac{Dex}{Dt} = \frac{DK}{Dt} + \frac{D\Psi}{Dt} + \frac{D((T-T_0)S)}{Dt} - \frac{D((P-P_0)v)}{Dt} + \frac{D(\sum_i(\mu_i - \mu_{i0})x_i)}{Dt} \quad (4.10)$$

The detailed expression of each term in the above equation can be found in [132] and [140].

Here in the CuCl_2 decomposition reaction, the kinetic, potential and strain exergy terms are assumed to be negligible. It is assumed that changes in the aforementioned exergy components are small compared to the chemical and thermal parts of exergy.

Figure 4.5 shows a schematic of a control mass for the exergy analysis model from $t=t$ and $t=t+dt$ corresponding to a solid particle radius of $R(t)$ and $R(t+dt)$, respectively, in the hydrolysis chemical reaction. The control mass exergy balance over the reaction duration with the time interval of dt can be expressed as:

$$Ex_{CM}(t + dt) - Ex_{CM}(t) = \left(1 - \frac{T_0}{T_g}\right) \delta Q_{CM} - (\delta W_{CM} - P_0 dV_{CM}) - \delta Ex_d - \delta Ex_{loss} \quad (4.11)$$

Here $Ex_{CM}(t + dt) - Ex_{CM}(t)$ is the exergy change in a control mass from t until $t+dt$. The terms on the right hand side express the exergy contributions to this exergy change. The first term, $\left(1 - \frac{T_0}{T_g}\right) \delta Q_{CM}$, is the exergy change due to heat transfer between a control mass and its surroundings. The second term $(\delta W_{CM} - P_0 dV_{CM})$ reveals the exergy contribution for the work interactions of a control mass and the surroundings where δW_{CM} denotes the work absorbed or done by the system and $P_0 dV_{CM}$ expresses the work for changing the control mass volume. Also δEx_d and δEx_{loss} express the exergy destruction exergy loss in the control mass, respectively. The exergy change for the hydrolysis chemical reaction can be written as:

$$Ex_f - Ex_i = \left(1 - \frac{T_0}{T_{Hyd}}\right) Q_{Hyd} + \left(1 - \frac{T_0}{T_{PH}}\right) Q_{PH} - Ex_D - Ex_{loss} \quad (4.12)$$

where Ex_f refers to the final exergy content of the reactor (corresponding to the exergy content of desired products of Cu_2OCl_2 and HCl) and Ex_i denotes the initial exergy content of the reactor (corresponding to the exergy content of reactants, CuCl_2 and H_2O). The first and second terms on the right side refer to the exergy change due to the heat of hydrolysis reaction and preheating of the reactants up until the reactor temperature, respectively. Also, Ex_D represents the exergy destruction as a function of entropy generation ($Ex_D = T_0 S_{gen}$) due to the mass, heat and chemical reaction. In the CuCl_2 decomposition reactor, since some undesirable reactions occur and lead to undesirable solid products such as CuCl , this yields a loss of exergy of the system. Several undesirable by-products are formed in the

hydrolysis reaction. In this paper, Ex_{loss} accounts for the exergy content of CuCl (physical and chemical exergy) as the primary undesired solid product. The reaction performance can be defined as the ratio of reaction heating rate at the stoichiometry and real conditions. Based on Refs. [26], [105], the hydrolysis reaction test duration is assumed to be 60 minutes. The parameters in the exergy equations are then converted to rate-based factors.

4.2.2. Hydrodynamic Model of the Hydrolysis Unit

Developing a hydrolysis reactor with a high conversion ratio, low steam consumption, and no side products is a challenging engineering problem. In this study with a new configuration for the hydrolysis reactor, hydrodynamic modeling is required to investigate the interaction of the fluid dynamic parameters like drag coefficient, buoyancy, gravity and drag forces, and terminal velocity when studying the reactor performance. This section will use correlations to determine the hydrodynamic parameters that will be used in the mass transport phenomena with respect to the conversion of reactants at a specific process condition.

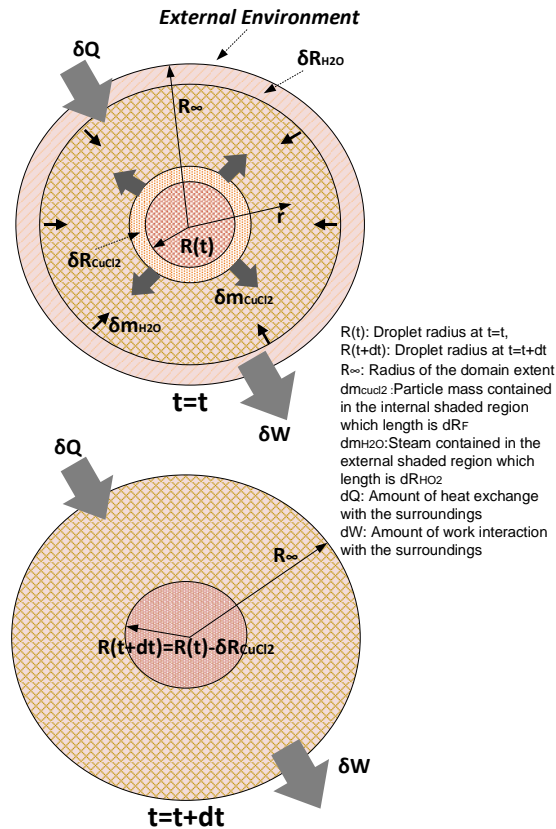
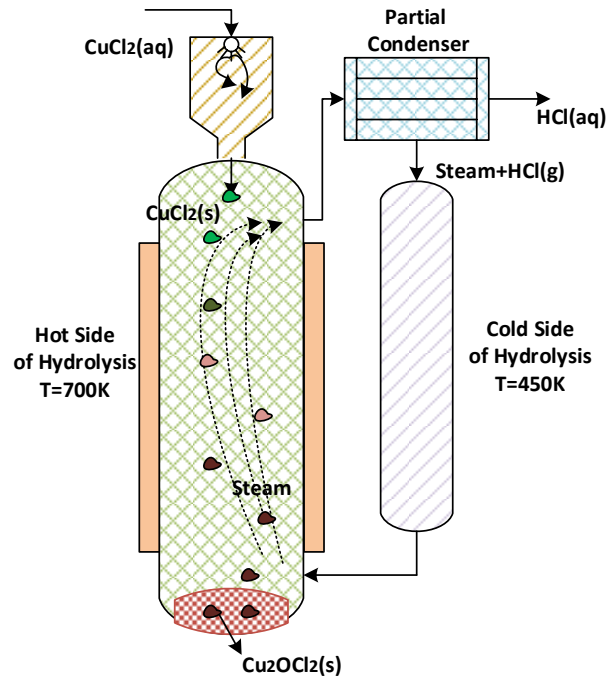
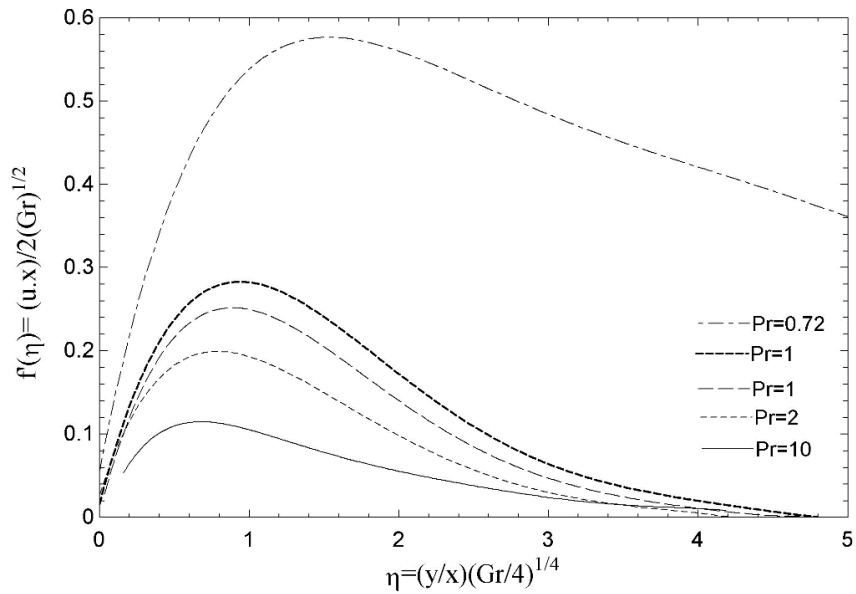


Figure 4.5. Schematic of a control mass with radius of $R(t)$ at time $t= t$ and radius of $R(t + dt)$ at $t+dt$.



(a)



(b)

Figure 4.6 (a). Schematic diagram representing the cupric chloride hydrolysis reactor, (b) Flow velocity distributions estimated in the boundary layer over an isothermal vertical surface [141] and [142]

Figure 4.6 (a) shows a conceptual illustration for the natural-convection driven/falling particle-based hydrolysis reactor at UOIT. Also, a detailed schematic view of the hydrolysis reactor was provided in Figure 3.6. The driving force for the flow of gaseous species occurs from the natural convection mechanism. In this hydrolysis reactor, the falling particle principle is applied for introducing solid copper chloride rather than scattering them in the spray method. A fine distribution of flow within the reactor is expected. The non-ideal flow distribution is not dominant at the reactor. The steam velocity in the hydrolysis unit is a function of hot and cold side temperatures (T_H and T_C), steam partial pressure in the gaseous mixture (P_{st}), height (L) and cross-sectional area of the vertical furnace (A_F). A uniform temperature is assumed for the hot side and cold side of the reactor. For the specific furnace design characteristics, and laminar conditions, the non-dimensional parameters can be determined as functions of the Rayleigh number (Ra) and Grashof number (Gr) as follows [149-151]:

$$Gr_x = \frac{g\beta x^3(T_H - T_C)}{v^2} \quad (4.13)$$

$$Ra = Gr_x Pr \quad (4.14)$$

$$f'(\eta) = \frac{v_{st}x}{2v(Gr_x)^{0.5}} \quad (4.15)$$

$$\eta = \frac{y}{x} \left(\frac{Gr_x}{4}\right)^{1/4} \quad (4.16)$$

where $f'(\eta)$ and η denote the dimensionless stream function and similarity variable, respectively. Sample profiles of flow velocity distributions in the boundary layer over an isothermal vertical surface (shown in Figure 3.6 (b)) are available in Refs. [141] and [142]. The coefficient of thermal expansion β is assumed constant. For a solid particle falling through a fluid, the maximum attainable velocity is called the terminal velocity. The particle is moving at its terminal velocity when the summation of upward drag and buoyancy forces are equal to the downward gravity force. At this state, the particle has zero acceleration, as the net force on the particle is zero. The derivation for the terminal velocity is important for the reactant residence time estimation and it is obtained from mathematical expressions as follows [152- 154]:

$$F_B + F_D = F_G \quad (4.17)$$

$$F_B = \rho_g V_s g \quad (4.18)$$

$$F_D = \frac{1}{2} \rho_g A_S C_D v_{tr}^2 \quad (4.19)$$

$$C_D = \frac{24}{Re} (1 + 0.173 Re^{0.657}) + \left(\frac{0.413}{(1 + 16300 Re^{-1.09})} \right) \quad (4.20)$$

$$F_G = \rho_s V_s g \quad (4.21)$$

where V_s , ρ_g , ρ_s and A_S refer to the particle volume, gas density, solid density and particle cross-sectional area, respectively. The equivalent height of the furnace (x_{tr}) where the particle starts to move at its constant terminal velocity can be obtained from the initial velocity (v_{int}), time take for the particle to attain the terminal velocity (t_{int}) and particle acceleration (a_{par}) as follows [154-156]:

$$F_B + F_{D,int} - F_G = m_{par} a_{par} \quad (4.22)$$

$$F_{D,int} = \frac{1}{2} \rho_g A_S C_D v_{int}^2 \quad (4.23)$$

$$v_{int} = \frac{\dot{V}_{CuCl_2(aq)}}{A_F} \quad (4.24)$$

$$a_{par} = \frac{(v_{int} - v_{tr})}{t_{int}} \quad (4.25)$$

$$x_{tr} = x_0 + v_{int} t_{int} + \frac{1}{2} a_{par} t_{int}^2 \quad (4.26)$$

Here, the residence time of solid cupric chloride particles in the vertical furnace can be calculated as:

$$t_{res} = \frac{(L - x_{tr})}{v_{tr}} + t_{int} \quad (4.27)$$

4.2.3. Shrinking Core Model for the Hydrolysis Reaction

In the hydrolysis reactor, the general non-catalytic gas-solid reaction (NCGSR) occurs and this reaction can be defined as follows:



The shrinking core kinetic model (SCM) is adapted to predict the solid cupric chloride particle conversion in the hydrolysis reaction. The conversion of solid particles depends on

the residence time of particles and the rate of reaction. In SCM, the fluid (A) and the solid (B) react to form products C and D, where C is fluid and D is solid. The reaction product D is called ash and it is porous. Therefore, it can be assumed that in terms of physical properties, B is similar to D, so after the reaction, the complete physical structure and entire particle size remain the same. As shown in Figure 4.7, for the full conversion of particles, the reaction proceeds through the particle from the outer surface. Also, Figure 4.8 displays the diffusion mechanism through the ash layer. During the process, a shrinking unreacted core is formed. But the radius of the particle remains the same providing no corruption of the ash layer [146]. In SCM, five primary steps occur during the reaction.

- 1) Diffusion proceeds through the gas film: diffusion of reactant A from the bulk phase to the surface of the particle.
- 2) Diffusion proceeds through the ash layer: diffusion of reactant A from the ash surface to the unreacted core surface.
- 3) Reaction on the surface: reaction of reactant A with the solid on the unreacted core surface to form C and ash.
- 4) Diffusion proceeds through the ash back: diffusion of the gaseous product C from the unreacted core surface through the ash back to the surface of the solid.
- 5) Diffusion proceeds through the gas film back: diffusion of the product C from the ash surface through the gas film back to the bulk gas.

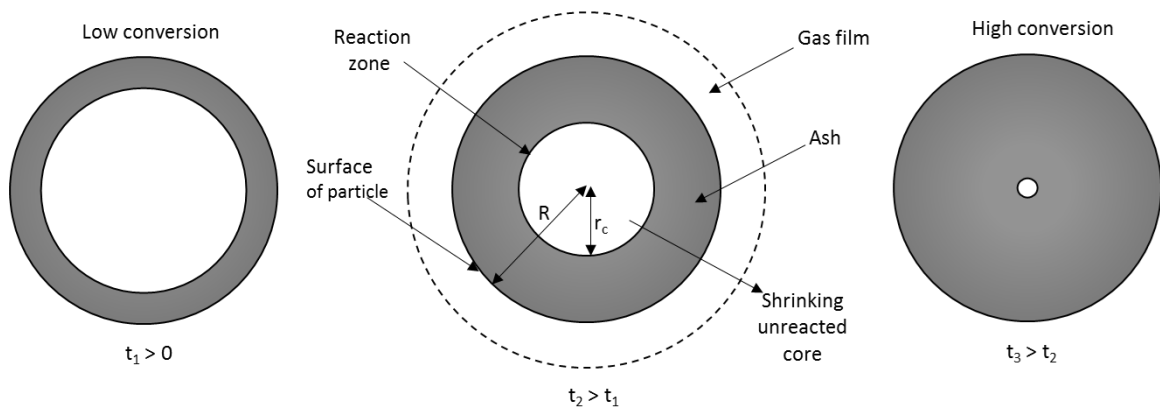


Figure 4.7. Representation of reacting particle with time

In some situations, some steps of this reaction are not present. In addition, the resistance of different steps usually shifts from others [147]. In such cases, the step with higher

resistance will control the particle conversion. The rate of the diffusion across the gas film is low when compared to the other steps because the flow rate of steam is constant around the cupric chloride particle [108].

For gas–solid systems, the rate-controlling steps are steps 2 and 3, and the conversion equations are analyzed in the following manner. For gas-solid systems, by a factor of about 10^3 , the flow rate of reactant A toward the unreacted core is faster than the shrinkage of the unreacted core, which is approximately the proportion of solid density to gas. Therefore, it is reasonable to assume that at any time in the ash layer, the concentration gradient of A to the unreacted core is stationary.

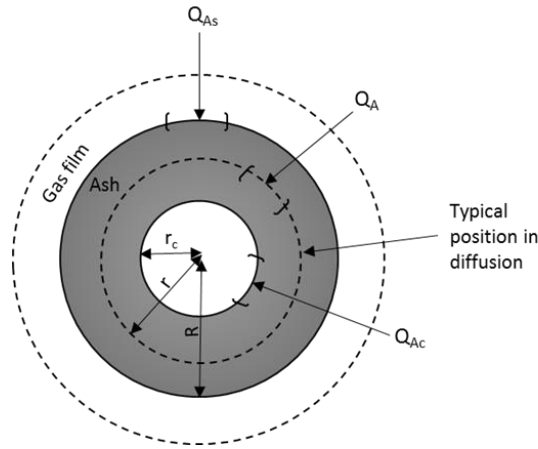


Figure 4.8. Reacting particle representation when rate-controlling resistance is diffusion through the ash layer

When rate-controlling resistance step is diffusion through the ash layer, conversion expression of CuCl_2 particle with time can be written as below [147].

$$\frac{t}{\tau_g} = 1 - 3(1 - X_{\text{CuCl}_2})^{\frac{2}{3}} + 2(1 - X_{\text{CuCl}_2}) \quad (4.29)$$

Here τ_g is the time required for the full conversion of CuCl_2 particle and calculated by

$$\tau_g = \frac{\rho_{\text{CuCl}_2} R_{\text{CuCl}_2}^2}{6bD_e C_{\text{H}_2\text{O}}} \quad (4.30)$$

where R_{CuCl_2} indicates the particle size. Lowering in particle size improved the reactivity of the samples. In Daggupati et al. [108] the particle size was studied over a range of $100\mu\text{m}$ and $500\mu\text{m}$, while in more recent literature [148] the particle size was smaller (20nm - 50nm) using tungsten carbide balls for several hours under an inert atmosphere of high purity argon. The authors addressed that the creation of ball-milled solid particles enhances

significantly the reaction kinetic parameters of the hydrolysis reaction. In the hydrolysis reactor at CERL, a burette is used to control the flow of $\text{CuCl}_2(\text{aq})$ and consequently roughly control the particle size. However, the precise particle controlling process requires additional components as presented before. The parameter D_e is the effective diffusivity of reactant A in the ash layer. It is usually determined by the experiment for a given chemical reaction. For cupric chloride hydrolysis reaction, it is reported in the literature [26, 27, 112] as $4.5 \times 10^{-6} \text{m}^2 \text{s}^{-1}$. The parameter ρ_{CuCl_2} is the cupric chloride molar density and $C_{\text{H}_2\text{O}}$ is the concentration of steam which is specified based on the ideal gas correlation depending on the steam partial pressure and the mean hydrolysis temperature. Here, it is assumed that per 2 moles of CuCl_2 interacted with 14 moles of the excess steam.

Step 3 includes a chemical reaction. The rate of reaction is commensurate to the existing surface of the unreacted core when the reaction is not affected by the existence of any ash layer. If rate-controlling resistance step is a chemical reaction, the following expression shows the conversion of CuCl_2 particle with time as below [147].

$$\frac{t}{\tau_r} = 1 - (1 - X_{\text{CuCl}_2})^{\frac{1}{3}} \quad (4.31)$$

where τ_r is the time required for full conversion of the solid particle by reaction control and can be written as follow [147]

$$\tau_r = \frac{\rho_{\text{CuCl}_2} R_{\text{CuCl}_2}}{b k'' C_{\text{H}_2\text{O}}} \quad (4.32)$$

Here k'' is the first-order reaction rate constant of the surface reaction. It is a measure of intrinsic reaction rate at a unit molar concentration of all reactants and it is assumed to obey the Arrhenius law as follows [27, 112]

$$k'' = \left(\frac{\mathcal{K}T}{h_p}\right) e^{-\Delta G^*/RT} \quad (4.33)$$

where \mathcal{K} and h_p denote the Boltzmann's and Plank's constants. ΔG^* can be expressed as the Gibbs free energy difference between the transition state and reactants (known as activation energy) which is determined by the hydrolysis reaction experiment done by the past studies literature [27, 112].

To analyze the controlling step, diffusion through the ash layer resistance to the chemical reaction resistance ratio is taken as below:

$$\delta^2 = \frac{\tau_g}{\tau_r} \quad (4.34)$$

Dominant resistance of conversion of solid can be found by the value of δ^2 . If $\delta^2 \leq 1$ the chemical reaction is dominant and controls the reaction, If $\delta^2 > 10$, diffusion through the ash layer is dominant and controls the reaction. Intermediate value shows that the reaction is controlled by both ash layer diffusion and chemical reaction [149].

4.3. CuCl/HCl(aq) Electrolyzer Formulation

In order to analyze the CuCl/HCl(aq) electrolyzer stack, the individual unit cells are modeled to determine the equilibrium concentration of species and estimate the equilibrium cell decomposition potential. Since the anolyte included CuCl dissolved in the HCl(aq), it forms complex speciation that is modeled in Engineering Equation Software (EES). Then the kinetic equations are employed to predict the work lost from ohmic, mass and charge transfer irreversible processes when the stack is operating under potential. Through the hydrodynamic analysis and a finite element analysis utilizing Comsol software, the reactant flow distribution through the stack, and consequently, cell-to-cell voltage spread and average voltage efficiency of the stack, are then obtained.

4.3.1. Electrochemical Formulation

Speciation denotes the anolyte composition in terms of different ionic and neutral concentrations at thermodynamic equilibrium in the electrochemistry model. Equilibrium of the half-reaction occurs when the variation in the Gibbs energy of the system is zero. This means that the forward oxidation and backward reduction are sufficiently fast and equal to maintain a specific level of Gibbs energy. At equilibrium, the electrochemical potential of any ion is identical for both phases (electrolyte (i) and solid salt (j)). For a multi-component system, the chemical potential is related to the Gibbs energy as follows [150] and [151]:

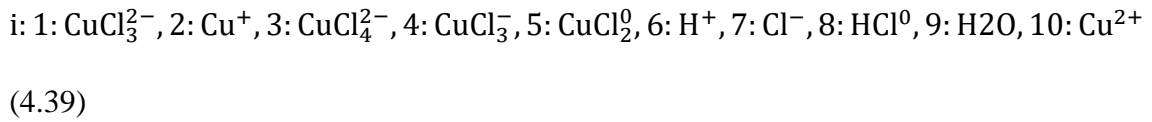
$$G = \sum_j \sum_i \mu_i n_i \quad (4.35)$$

With the assumption of reversibility for the equilibrium study, the hydrogen evolution reaction (HER) is designated for the cathode half-reaction. Depending on the concentrations of the anolyte components (HCl(aq) and CuCl), different species can appear in the anolyte. Different anodic half-reactions would have existed. In this study, 2 molal CuCl (mol/(kg solvent)) and 10 molal HCl(aq) are considered as the solution

concentrations. The following anodic half-reactions (designated as reactions I, II and III, respectively) are obtained [87], [92].



There are different speciation models for the CuCl/HCl(aq) solution in past literature [152], [153] and [154]. Based on these past studies, the most probable species are:



Besides the above reactions, the other stage converts back the copper (II) chloride to the copper (I) chloride [91]. The analysis of this reverse reaction and side processes like the solid copper formation are out of the scope of this study. For determining the equilibrium concentration of species under the specific temperature, pressure and concentration, the Gibbs energy minimization method is used. This can be performed through a Lagrange multiplier method or a minimization algorithm by implementing the governing equations (to be used in this study).

4.3.2. Gibbs Free Energy Minimization (GEM)

For the electrochemical system, the speciation model is used for the phase equilibrium estimation of the anolyte through a thermodynamic model of the electrolytic cell. The standard thermodynamic properties of all species are specified either by the SUPCRT92 database or data reported in past studies [91- 96]. The standard reference state is a temperature of 25°C, pressure of 1 bar, and unit concentration of the solution (1 mol/l). Based on Ref. [87] the conversion extent is assumed as 5%. Since the anolyte in the CuCl/HCl(aq) electrolyzer forms a complex non-ideal aqueous solution for its high ionic strength, the activity coefficient should be taken into account to achieve a reliable thermodynamic result. In past literature, the speciation data are available for the specific range of anolyte concentration, temperature, and pressure. However, to cover the relevant conditions in the present study, the Gibbs free energy (or Gibbs function) minimization

method is used with the stoichiometry and electric charge constraints to determine the equilibrium concentration of all probable species.

In the phase equilibrium modeling, a traditional local optimization method is difficult due to the existence of local minimum points, the existence of trivial solutions, a wide range of decision variables, and a discontinuous objective function in some regions. These points make the optimization problems highly non-linear, non-convex and with many decision variables. Therefore, an alternative efficient and reliable global minimization is employed. The Law of Mass Action is used for the chemical equilibrium problem. The Gibbs energy function is directly minimized by using the optimization capabilities developed in EES software. Another alternative approach is the Lagrange Method of Undetermined Multipliers.

The activity of each species (α_i) should be considered in thermodynamic properties consideration. The specific molar thermodynamic properties at non-ideal conditions can be expressed as [87]

$$\bar{h}_i = \bar{h}_i^0 - RT^2 \frac{\partial(\ln\alpha_i)}{\partial T} \quad (4.40)$$

$$\bar{g}_i = \bar{g}_i^0 - RT\ln(\alpha_i) \quad (4.41)$$

$$\bar{s}_i = \frac{\bar{h}_i - \bar{g}_i}{T} \quad (4.42)$$

$$\alpha_i = \alpha_i(T, P, b_1, \dots, b_{10}) = b_i^{\nu} \gamma_i^{\nu} \quad (4.43)$$

where b and ν are the species molality and stoichiometry coefficient, respectively. Also, γ denotes the activity coefficient of species representing a deviation from the ideal condition ($\alpha_i = 1$) and shows the i th component interaction with other ions in the electrolyte solution. Several empirical correlations have been reported for activity coefficients based on the solution concentration. In this thesis, a concentrated electrolyte is employed. The following Debye-Huckel equation is used for the activity coefficient [87, 91, 92].

$$\log \gamma_s = Cl_e - \log \left(1 + \frac{\sum b_i}{b_{H_2O}} \right) - \frac{A_{DH}|z_a||z_c|I_e^{0.5}}{1 + B_{DH}aI_e^{0.5}} \quad (4.44)$$

$$I_e = 0.5 \sum b_i z_i^2 \quad (4.46)$$

where I_e refers to the ionic strength of electrolyte and b_{H_2O} is the molality of water (moles of water per kg of solvent (water) which is equal to 55.56 mol/kg). Also, A_{DH} and B_{DH} are the Debye-Huckel constants, $1.172 (\text{kg/mol})^{0.5}$ and $0.328 (\text{kg/mol})^{0.5}$, respectively, and \bar{a} is the average ionic radius equal to 4.5 Å. The empirical parameter C is assumed to be 0.1438. For neutral species (like HCl^0), the third term of the above equation is zero and C becomes C_s , the Setchenow coefficient. For temperatures between 20-30°C, it was calculated by Balashov et al. [152] as 0.21. For HCl ions, Ref. [87] is taken as one of the sources to estimate the mean activity coefficient for proton (H^+) and chlorine species (Cl^-) as follows:

$$\gamma_{s,6 \text{ and } 7} = 14.78 - 3.93257I_e + 0.351429I_e^2 \quad (4.47)$$

In order to perform a successful minimization of the Gibbs function, parameters of the Cu(II) molar fraction (ξ) are expressed as:

$$\xi = \frac{\sum_{i=1}^5 b_i}{c_{\text{cu}}} \times 100 \quad (4.48)$$

$$b_6 + b_8 = b_{\text{H}} \quad (4.49)$$

$$(\sum_{i=1}^5 b_i) + b_{10} = b_{\text{cu}} \quad (4.50)$$

$$3b_1 + 4b_3 + 3b_4 + 2b_5 + b_7 + b_8 = b_{\text{cl}} \quad (4.51)$$

$$-2b_1 + b_2 - 2b_3 - b_4 + b_6 - b_7 + 2b_{10} = 0 \quad (4.52)$$

Therefore, the Gibbs energy will have 16 variables, i.e., T , P , b_1, \dots, b_{10} , ξ , b_{H} , b_{cu} and b_{cl} and then by applying the constraints, the degrees of freedom for minimization becomes 10 as b_1, \dots, b_{10} . The Gibbs energy function is minimized based on a Genetic Algorithm method in the EES software.

With the equilibrium concentration values from the Gibbs free energy minimization method, the equilibrium potential for any redox half-reaction ($E_{D,r}$), containing the anodic and cathodic sides, can be evaluated through the Nernst equation as [39]:

$$E_{D,r} = \frac{\bar{\Delta}_r g}{nF} \quad (4.53)$$

$$E_{D,cell} = E_{D,cathode} - (-E_{D,anode}) \quad (4.54)$$

where n is the number of electrons (ideally, each 2 moles of electrons yield one mole of hydrogen) in the half-reaction and F denotes the Faraday's constant (96,485 C/mol). The standard potential of the hydrogen reaction at the cathode side is zero ($E^{\circ} = 0$ V) [39].

4.3.3. Kinetic Study of Electrochemical Cell

Based on Kirochhoff's law, the total current passing through the cells and cell subsections (anode, cathode and membrane) should be identical. The potential drop is different at the positive electrodes, negative electrodes, and membranes inside the stack. To examine the electrolyzer under non-equilibrium and non-ideal conditions, the kinetic equations are employed. Kinetic analysis shows the electrolytic system behavior and presents the overpotential irreversibilities resulting from the electron transfer and hydrogen evolution process. The activation overpotential for electron transfer and mass transfer at the half-cell redox reactions, ohmic overpotential, and consequently the stack/cell voltage efficiency, can then be obtained. The total voltage required for operating the electrolyzer can be written as [39], [92]:

$$E_{cell} = -(|E_{OCP,cell}| + |\eta_{anode}| + |\eta_{cathode}| + |\eta_{ohmic}|) \quad (4.55)$$

For a single unit of the electrode, the mass transfer and charge transfer contribute to the total activation overpotential as

$$\eta_{Electrode} = \eta_{mt} + \eta_{ct} \quad (4.56)$$

Moreover, for the anode electrode, the forward reaction is anodic and backward reaction is cathodic, while for the cathode, the forward reaction is cathodic and the backward reaction is anodic. So the net electrode current can be obtained as

$$i_{Electrode} = i_{anode} + i_{cathode} \quad (4.57)$$

By considering the general relation between the electrode current and current density ($j_{electrode} = i_{electrode}/A_{electrode}$), since no catalyst is used in the electrolyzer, the active surface area for the anode and cathode electrode are the same as the cell surface area (A). The anodic current and cathodic currents at each electrode can be estimated by the Bulter-

Volmer correlation which incorporates the exchange current density of the electrode (j_0), limiting current density (j_{lim}), and transfer coefficient (α) as follows [39]:

$$j_{cathode} = (e^{\frac{\alpha_{a,c} \eta_c F}{RT}} - e^{-\frac{\alpha_{c,c} \eta_c F}{RT}}) / (\frac{1}{j_{0,c}} + \frac{e^{\frac{\alpha_{a,c} \eta_c F}{RT}}}{j_{lim,a,c}} - \frac{e^{-\frac{\alpha_{c,c} \eta_c F}{RT}}}{j_{lim,c,c}}) \quad (4.58)$$

$$j_{anode} = (e^{\frac{(1+\alpha_{c,a}) \eta_a F}{RT}} - e^{-\frac{\alpha_{c,a} \eta_a F}{RT}}) / (\frac{1}{j_{0,a}} + \frac{e^{\frac{(1-\alpha_{c,a}) \eta_a F}{RT}}}{j_{lim,a,a}} - \frac{e^{-\frac{\alpha_{c,a} \eta_a F}{RT}}}{j_{lim,c,a}}) \quad (4.59)$$

The transfer coefficient (α) is the same as the symmetry coefficient since a single-step redox reaction as the anode half-reaction exists. For the cathodic side, the exchange current density is $j_{0,cathode} = 1.3 \text{ mA/cm}^2$. For the anode side, the exchange current density can be obtained as [39, 89]:

$$j_{0,anode} = F k_{0,a} (c_{CuCl}^{1-\alpha} c_{CuCl_2}^{\alpha}) \quad (4.60)$$

where c_{CuCl} and c_{CuCl_2} denote the reductant and oxidant concentration on the molar concentration scale (molarity in mol/L) of the half-cell reaction at the anode, respectively (based on the works in Refs. [89] and [90]). This parameter approximates the reactant concentration at the electrodes which are smaller than the average of the channel for the reactant flow through the MEA sites. The concentration reduction needs to be proportional to the flux, which is proportional to the current density. To study the effect of temperature on the transfer coefficient of the anode, the Tafel correlation is applied. For the anode side, the average anode half-reaction rate constant in the Tafel equation is used for $k_{0, anode}$. The exchange current density for the cathode is used from Ref. [90] as there is no k_0 available data to the authors' knowledge. For the hydrogen evolution reaction in a concentrated acidic catholyte [89] and [90],

$$k_{0,anode} = \Lambda \exp\left(\frac{-\eta_a}{RT}\right) \quad (4.61)$$

Here, Λ is a constant value representing a pre-exponential factor. Assuming zero current leakage, the same current provided by the anode would be received into the cathode,

$$i_{cathode} = i_{anode} \quad (4.62)$$

The ohmic overpotential indicates the proton exchange membrane resistance to the transport of hydrogen ions which is a function of the membrane temperature, humidification and membrane thickness. The general expression for the ohmic resistance can be written as

$$\eta_{ohmic} = R_{PEM} \cdot i_{cell} \quad (4.63)$$

Here, i_{cell} is the current of a unit cell. R_{PEM} refers to the membrane resistance (function of membrane thickness) for a Nafion 117 membrane with a thickness of 105 μm at each MEA as follows [92]:

$$|i_{cell}| = |i_{anode}| \quad (4.64)$$

$$R_{PEM} = \int_0^L \frac{dx}{\sigma[\lambda(x)]} \quad (4.65)$$

Here, the membrane conductivity, $\sigma(x)$, can be specified based on an empirical correlation incorporating the water content in the Nafion 117 PEM, $\lambda(x)$, by crossing the thickness of the membrane (x changes from 0 to L). Table 4.5 tabulates the activation and ohmic overpotential parameters for the $\text{CuCl}/\text{HCl}(\text{aq})$ electrolyzer (23).

$$\sigma[\lambda(x)] = [0.5139\lambda(x) - 0.326\exp[1268(\frac{1}{303} - \frac{1}{T})]] \quad (4.66)$$

The water content through Nafion 117 proton exchange membrane can be calculated in terms of the water content values at anode-membrane (λ_{anode}) and membrane-cathode ($\lambda_{cathode}$) interfaces.

$$\lambda(x) = \frac{\lambda_{anode} - \lambda_{cathode}}{L} x + \lambda_{cathode} \quad (4.67)$$

Table 4.5. Parameters for kinetic study of $\text{CuCl}/\text{HCl}(\text{aq})$ electrolyzer [39, 88, 89]

Parameter	Anode	Cathode
$k_0, \mu\text{mol}/\text{s}$	210	NA
$j_{0,electrode}, \text{A}/\text{cm}^2$	0.387	1.3×10^{-3}
α	0.43	2
$j_{lim,anode}, \text{A}/\text{cm}^2$	1.2	1.0913
$j_{lim,cathode}, \text{A}/\text{cm}^2$	-1.2	-1.128
λ	14	10

4.4.4. Hydrodynamic Model of CuCl/HCl(aq) Electrolyzer Stack

The internal design of the stack is one of the important aspects of the electrolyzer modeling since it directly affects the anolyte and catholyte flow distribution through the MEAs and consequently influences the required voltage spread across the stack. A uniform anolyte and catholyte spread along the stack prevents the gas and solid accumulation and the formation of hot spots especially at elevated current densities which may damage the stack. An optimized geometry leads to a homogenous spread of anolyte and catholyte flows.

A flow distribution model of anolyte and catholyte flow through the stack cells is simulated by a finite element method in Comsol. Figure 4.9(a) shows a stack block containing 10 MEAs with an active area of 140 mm × 140 mm and 4 mm thickness of each cell, in addition to the current density, potentials and model parameters for each MEA. Figure 4.9 (b) illustrates the anolyte and catholyte flow pattern configurations in the bipolar plates of the stack. The anolyte feed port is located at the top left and the outlet port is located at the opposite side at the bottom. The catholyte feed port and the outlet port are placed in the bottom left and top right, respectively. All flow passages in the bipolar module form an X-shape configuration which provides a proper spread of mass inside of each unit cell. The mass and momentum conservation equations are the two primary governing equations which are solved for the moving fluid in the unit cells and manifolds [155].

$$\frac{\partial(\rho u)}{\partial x} + \frac{1}{A} \oint_{\partial A} \dot{m} dl = 0 \quad (4.68)$$

$$\frac{\partial(\frac{\rho u^2}{2})}{\partial x} + \frac{1}{A} \oint_{\partial A} \dot{m} u dl + \frac{\partial(P)}{\partial x} = \frac{f \rho u^2}{2D_h} \quad (4.69)$$

Since the HCl/CuCl(aq) electrolyzer is fed by the liquid flows (dissolved copper(I) chloride and aqueous hydrochloric acid) and the produced hydrogen is the only gaseous phase component, the pressure drop in the stack is much less than the regular water electrolyzer unit with hydrogen and oxygen gases. The second term in the above mass equation represents the mass flux from spreading or re-combination at the header junctions and also mass exchange through the channels. The term on the right-hand side of the above momentum equation represents the friction loss including the Darcy friction factor (f) changing from cell-to-cell channels and headers. With the assumption of a uniform

condition in each channel or header, the second term of the above momentum equation becomes [155]:

$$\phi_{\partial A} \dot{m} u \, dl = \frac{MQ^2}{C\Delta x} \quad (4.70)$$

where Q, M, and C represent the molar flow rate (mol/s), molar mass (kg/mol) and volumetric concentration (mol/m³), respectively.

A finite element analysis using Comsol software was used to predict the velocity and pressure fields for laminar flow. In the boundary condition specifications, no-slip conditions were set at the wall. Since the dimensions of the porous media were nearly 1/10 of the channel, the effects of the porous media on the flow field were not considered in this study. In addition, the physical properties of the copper(I) chloride dissolved in aqueous hydrochloric acid aqueous copper(II) chloride was based on past studies [20] and [156].

The stack performance ratio is the ratio of the produced hydrogen rate to the anolyte flow rate supplied into the stack. The performance ratio reveals how the non-uniform mass spread among the cells affects the produced hydrogen in each MEA. In the CuCl/HCl(aq) electrolyzer, no catholyte is consumed, so the performance ratio is defined only for the anolyte. The stack performance ratio and cell-to-cell performance ratio variation can be expressed as the following equations, respectively [45]:

$$\mathcal{L}_{a,stack} = \frac{i.A.M.N_{cell}}{\dot{N}_{anodeZF}} \quad (4.71)$$

$$S_{\mathcal{F}} = (\mathcal{L}_{cell,max} - \mathcal{L}_{cell,min}) / ((1/N_{cell}) \sum_1^{N_{cell}} \mathcal{L}_{cell}); (\mathcal{L}_{cell} = \frac{i.A.M}{\dot{N}_{cellZF}}) \quad (4.72)$$

The performance of a cell/stack can be evaluated in terms of the cell voltage efficiency and average stack voltage efficiency. The cell voltage efficiency is used to assess the electrolyzer cell performance through the definition of the reversible decomposition potential (obtained by the Nernst equation) and the actual total required voltage to operate the electrochemical process.

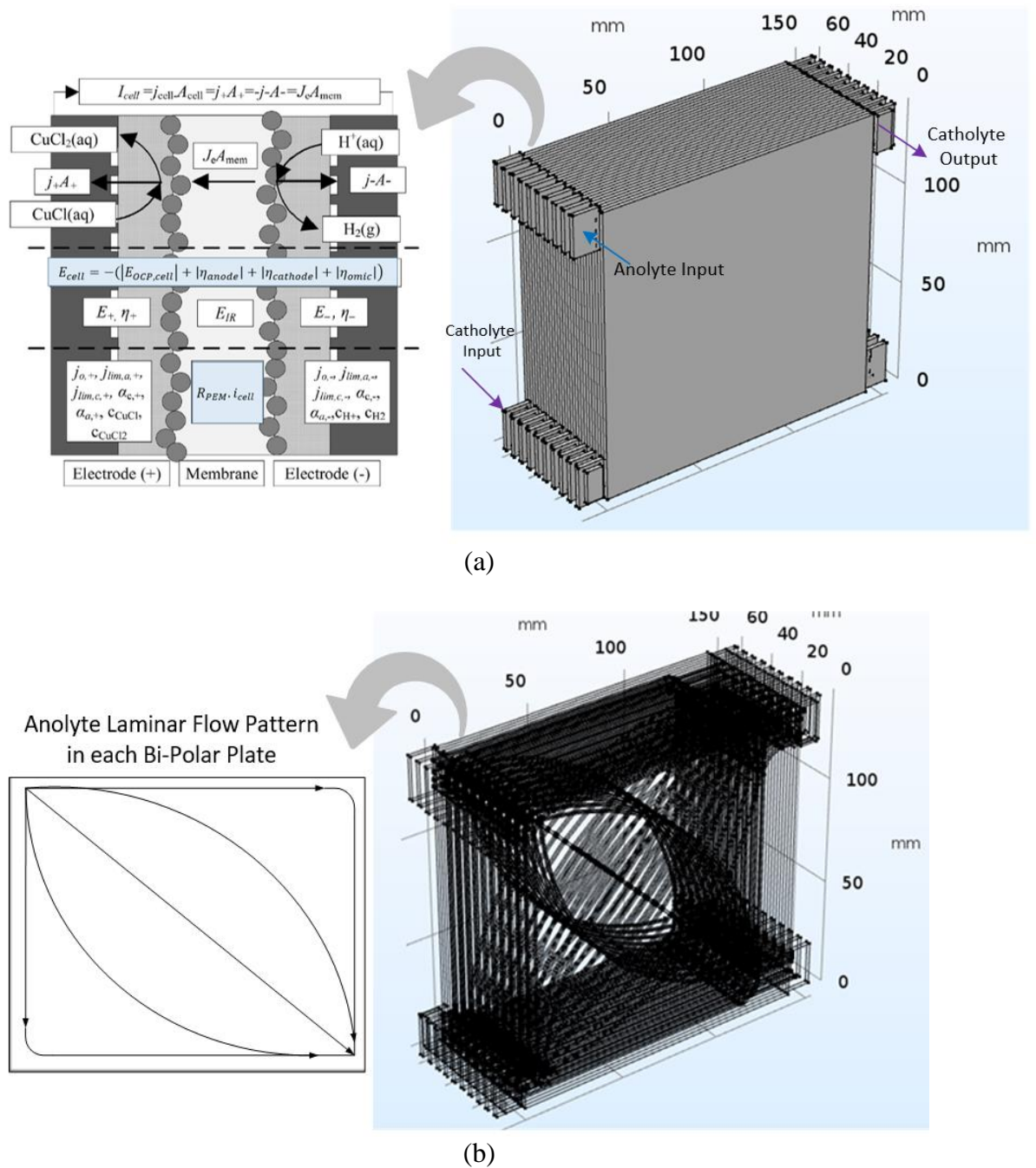


Figure 4.9. (a) Schematic of the CuCl/HCl(aq) electrolyzer stack containing 10 MEAs (left side modified from Hall et al. (19)) and (b) anolyte and catholyte flow patterns in the bipolar modules of manifolds.

Moreover, since there is a non-uniform voltage distribution among the unit cells of the stack for the homogenous flow spread, an average voltage efficiency is used for the stack performance. The voltage efficiency of the unit cell and the average voltage efficiency of the stack can be expressed as [45] and [87].

$$\varepsilon_{cell} = \frac{E_{rev,cell}}{E_{Cell}} \quad (4.73)$$

$$\varepsilon_{ave,stack} = \frac{E_{rev,ave\ stack}}{E_{ave\ stack}} \quad (4.74)$$

4.4. Pressure Swing Distillation Analysis

In this section the thermodynamic, heat and mass transfer studies of pressure swing distillation unit is performed to investigate the separation process of HCl-H₂O binary azeotropic mixture and estimate the height of columns.

4.4.1. Thermodynamic Model of PSDU

In this section, a thermodynamic simulation of PSD of HCl (aq) has been performed in Aspen Plus to identify the temperature and composition profile through the distillation column and to determine the effect of operating parameters on the system's performance. The dynamic behavior of the pressure swing distillation (PSD) process for the separation of HCl from water is derived based on the overall and component mass and energy balance equations. It is assumed that at each tray there is ideal uniform liquid and vapor mixture leaving the stage at the thermal equilibrium. In addition to the negligible pressure drop, the vapor-liquid equilibrium (VLE) is reached in each column's tray [157].

In this respect, the mass and energy conservation at the internal trays, re-oiler and condenser of the PSD apparatus is illustrated in Figure 4.10. Columns are divided into the rectification, stripping, feed, re-boiler and condenser sections with N trays including the condenser and re-boiler, as well. In each section of the columns, stages are counted from the top to the bottom. At the rectification section, the down-flowing liquid is contacting with the rising vapor to remove more volatile component in the feed mixture. At the stripping section, by the rising vapor down flowing liquid is stripped of the more volatile component. Feed enters the column and is collected at the bottom in the re-boiler.

According to Figure 4.10, the mass balance equation of the rectification section for both low and high pressure columns can be expressed as follows:

$$\frac{dm_i}{dt} = \dot{m}_{L_{i-1}} + \dot{m}_{V_{i+1}} - \dot{m}_{L_i} - \dot{m}_{V_1} \quad (4.75)$$

From the above formulations, to obtain the mass balance, the liquid and vapor phases in and out of stage “i” are considered. In the liquid and vapor flows, the component mass balance based on the more volatile component can be determined as:

$$\frac{d(m_i x_i)}{dt} = \dot{m}_{L_{i-1}} x_{i-1} + \dot{m}_{V_{i+1}} y_{i+1} - \dot{m}_{L_i} x_i - \dot{m}_{V_i} y_i \quad (4.76)$$

In the above equation, x denotes the mole fraction of the more volatile liquid component and y refers to the mole fraction of the more volatile vapor component.

The energy balance is formulated based on the enthalpies of the liquid and vapor flows. The energy equation for the rectification section for both high and low pressure sides can be written as follows [157] and [158]:

$$\frac{d(m_i h_i)}{dt} = \dot{m}_{L_{i-1}} h_{L_{i-1}} + \dot{m}_{V_{i+1}} h_{V_{i+1}} - \dot{m}_{L_i} h_{L_i} - \dot{m}_{V_i} h_{V_i} + \dot{Q}_{heat} \quad (4.77)$$

Here, \dot{Q} is the heat required to drive the system. In the low pressure side, electric-thermal tapes are used to supply heat and for the high pressure columns, DURATHERM450 thermal oil is circulating as the heating medium. The thermal properties of DURATHERM450 are shown in Table 4.6. For both high and low pressure sides, the feed section mass balance equation and energy balance equations are formulated by using the same approach as the rectification section. So, the overall and component mass balance equations are given as

$$\frac{dm_i}{dt} = \dot{m}_{L_{i-1}} + \dot{m}_{V_{i+1}} - \dot{m}_{L_i} - \dot{m}_{V_i} + \dot{m}_F \quad (4.78)$$

$$\frac{d(m_i x_i)}{dt} = \dot{m}_{L_{i-1}} x_{i-1} + \dot{m}_{V_{i+1}} y_{i+1} - \dot{m}_{L_i} x_i - \dot{m}_{V_i} y_i + \dot{m}_F x_F \quad (4.79)$$

The energy equation of the feed stage in the high and low pressure columns is formulated as follows:

$$\frac{d(m_i h_i)}{dt} = \dot{m}_{L_{i-1}} h_{L_{i-1}} + \dot{m}_{V_{i+1}} h_{V_{i+1}} - \dot{m}_{L_i} h_{L_i} - \dot{m}_{V_i} h_{V_i} + \dot{m}_F h_F + \dot{Q}_{heat} \quad (4.80)$$

The re-boiler mass balance and energy balance equations for high and low pressure columns can be obtained as:

$$\frac{dm_N}{dt} = \dot{m}_{L_{N-1}} - \dot{m}_{V_N} - \dot{m}_B \quad (4.81)$$

$$\frac{d(m_N x_N)}{dt} = \dot{m}_{L_{N-1}} x_{N-1} - \dot{m}_{V_N} y_N - \dot{m}_B x_B \quad (4.82)$$

$$\frac{d(m_N h_N)}{dt} = \dot{m}_{L_{N-1}} h_{L_{N-1}} - \dot{m}_{V_N} h_{V_N} - \dot{m}_B h_B + \dot{Q}_{Reboiler} \quad (4.83)$$

For the condenser stage, the total condensation is taken into account. Which indicates that the entering vapor is completely condensed. Thus, the overall and component mass balance equations at the reflux condenser sections equations are presented as follows

$$\frac{dm_1}{dt} = \dot{m}_{V_2} - \dot{m}_{L_1} - \dot{m}_D \quad (4.84)$$

$$\frac{d(m_1 x_1)}{dt} = \dot{m}_{V_2} y_2 - \dot{m}_{L_1} x_1 - \dot{m}_D x_D \quad (4.85)$$

The energy equation for the steam condenser in the low pressure side and the HCl (aq) condenser in the high pressure side can be expressed as:

$$\frac{d(m_1 h_1)}{dt} = \dot{m}_{V_2} h_{V_2} - \dot{m}_{L_1} h_{L_1} - \dot{m}_D h_D + \dot{Q}_{cond} \quad (4.86)$$

With respect to Figure 4.10, the condensation part is comprised of the reflux condenser where the vapor is partially condensed through the natural convection, and the condenser section where the liquid phase distillate product is obtained. It should be noted that the system operates under steady-state conditions and the ratio of the reflux flow to total produced vapor (known as the slope of the operating line) is defined based on reflux ratio (RR) as:

$$slope = \frac{\dot{m}_{L_1}}{(\dot{m}_D + \dot{m}_{L_1})} = \frac{RR}{RR+1} \quad (4.87)$$

Table 4.6. DURATHERM450 thermal properties [159]

$T_{oil,in} (^{\circ}C)$	180
$C_p (kJ/kg.K)$	2.52
$Density, \rho (kg/m^3)$	758.94
$viscosity, \mu (kg/m.s)$	1.045×10^{-3}
$Thermal\ conductivity, \lambda (W/m.K)$	0.133

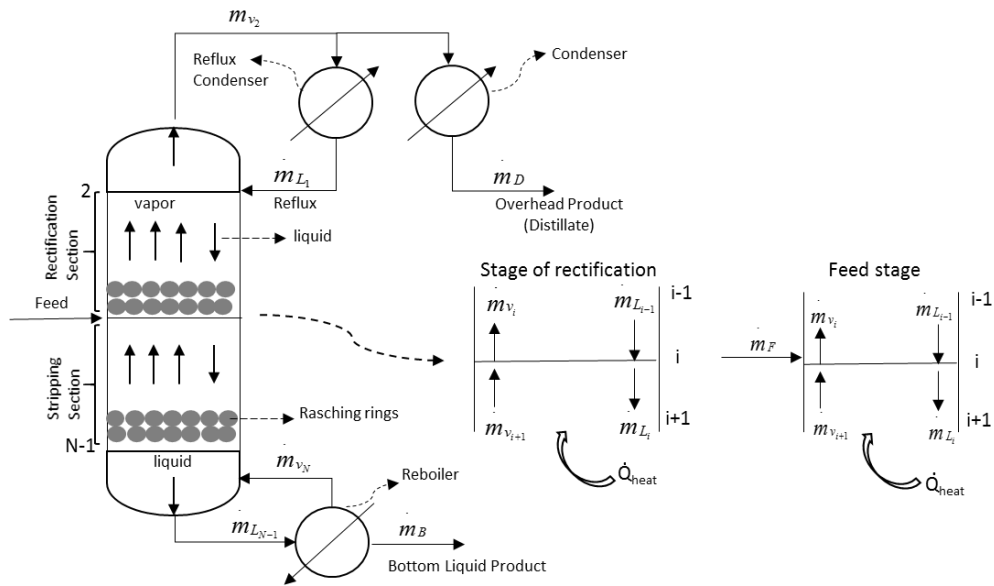


Figure 4.10. Detailed schematic of streams at the column's trays, re-boiler and reflux condenser

4.4.2. Packing Column Height of PSDU

The height of the packed column can be determined through the mass transfer and heat transfer analyses. The McCabe-Thiele as a well-known and practical method has been utilized in mass transfer mechanisms to determine the practical number of trays in each column. Furthermore, the heat transfer analysis through the length of the column has been conducted to specify the heat transfer coefficient and accordingly the heat transfer area. Finally, the values of distillation column height resulted from both analysis are compared with each other.

4.4.3. Mass Transfer Model of PSDU

A mathematical-graphical method for determining the number of physical trays needed for a given separation of a binary mixture of A and B has been developed by McCabe and Thiele [160]. The method uses material balances around certain parts of the tower, which yield operating lines, and x-y equilibrium curves of the system. Vertical lines are drawn on an x-y plot with a plot showing vapor concentration (y) as a function of the liquid concentration (x) corresponding to the concentrations of the feed (x_f), bottom (x_b) and distillate (x_d) products. A "staircase" is drawn between the vapor-liquid equilibrium (VLE)

curve and the operating lines (rectifying line, stripping line). The number of theoretical trays is equal to the number of the horizontal steps on the staircase [129]. For this case study of an HCl-water negative azeotrope (maximum boiling) distillation process, the specific calculations based on the mass transfer and energy balance equations are carried out. This paper uses tabulated data of the HCl- water binary mixture to determine the VLE curve on the x-y plot. The method then plots vertical lines corresponding to the concentrations of the bottom (x_b), feed (x_f), and distillate (x_d). Finally, it plots the operating lines and the q-line, where q represents the mole fraction of liquid in the feed. The slope of the q line is $q/(q - 1)$. In this paper, feed is a saturated liquid. It has no vapor, thus $q=1$ and the slope of the q line is infinite which means the line is vertical [160]. The physical number of trays can be determined as:

$$N = (\textit{Theoretical number of trays} - 1 (\textit{Reboiler tray}) - 1 (\textit{condenser tray}) / \eta_{\textit{Tray}} \quad (4.88)$$

The number of trays is always an integer number. Using an empirical method, the height of the packed column can be determined by the following equation [129]:

$$z = N.HETP \quad (4.89)$$

where HETP refers to the height of an equivalent theoretical plate. The concept of HETP describes the height of a column which is needed to reach the same separation known as the number of physical trays as defined earlier. It indicates the height of passes required to achieve a desirable distillate composition, which conserves the mass balance for vapor-liquid equilibrium per component in the mixture. HETP is a complicated relation between the specifics of the separation undertaken and the physical properties of the fluids.

There are various reasons which cause a difference between the theoretical number of trays and the actual tray's performance such as insufficient mixing and constant time. By the tray efficiency definition, the performance of a tray can be measured. There are other alternative similar definitions such as the overall tray efficiency, Baur Efficiency and Murphree Vapor efficiency, which each measure distinct performance issues. The optimum feed location can be specified from the ratio of the equilibrium stage divided by the tray's efficiency. In this study, an amount of 40% is assumed for the overall tray efficiency [161].

4.4.4. Heat Transfer Model of PSDU

Accurate prediction of the heat transfer rate, as well as the column height, have importance in the packing column design. In this section, for the tubular high pressure separation heat exchanger, a detailed heat transfer model for the boiling and condensing phases has been applied to analyze the packing height column. In the tube-in-tube heat exchanger, DURATHERM450 is used as the heat transfer medium which flows between the tubes. The inner diameters of the tubes are 0.375 in. and 1 in. with a thickness of 0.625 in. In the following sections, for each dominant region at the boiling process consisting of pool boiling, falling film evaporation, mist region and partial condensation, the precise correlations are presented.

In the PSD system, with respect to Figure 4.11, two low pressure columns are heated by the electric-thermal tape wrapped outside of the glassy column surface. In the high pressure side, at the tube-in-tube configuration, the internal tube containing DURATHERM450 thermal oil heats three distillation columns. As shown in Figure 4.11, for both high and low pressure sides, there are four main heat transfer zones involving the pool boiling, falling film evaporation, a mist region and a partial condensation area. From the heat transfer mechanism equations, the heat transfer coefficient for each section and consequently a desired length for the distillation columns can be obtained. The correlations are derived from the past studies as for the pool boiling region literature [141] and [162], the falling film evaporation region [7] and [163], the mist region [141, 143, 164], and the condensation inside the tube and free convection [7, 143, 165]. The boiling in this region exhibits the combined effects of convection and pool boiling. For the heat transfer coefficient in a horizontal tube, Bromely (1950) introduced an empirical constant of 0.62 to predict the heat transfer coefficient in the pool region. The results are also valid for a vertical tube. So, the heat transfer coefficient for a tube with a diameter D can be expressed as [141]:

$$h_{PB} = 0.62 \left[\frac{\rho_G (\rho_L - \rho_G) g \cdot h'_{LG} \lambda_G^3}{D \mu_G (T_w - T_{sat})} \right] \quad (4.90)$$

where the subscripts L and G refer to liquid and gas, respectively. The vapor properties are evaluated at the film temperature $((T_{sat} + \Delta T)/2)$ and the liquid properties are given at the

saturation temperature (T_{sat}). Furthermore, the latent heat is modified for the sensible heating of the vapor as follows [141]:

$$h'_{LG} = h_{fg} \left[1 + 0.34 \left(\frac{c_{pG}(T_w - T_{sat})}{h_{fg}} \right) \right] \quad (4.91)$$

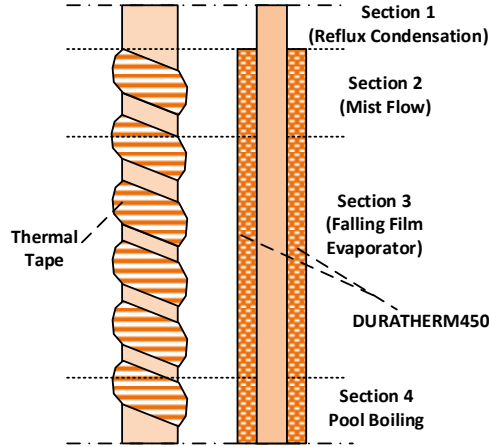


Figure 4.11. Column heating materials; electric thermal tube for the low pressure side (left column) and DURATHERM450 thermal oil for the high pressure side (right column) and their relative heat transfer sections

Various empirical correlations have been developed to predict the heat transfer coefficient of the falling film evaporation region. A significant difference between these equations occurs in the high pressure distillation column due to the dependence on the specific operating conditions [7]. In this paper, the correlation of Fujita et al [163] is written as follows:

$$\overline{Nu}_{FFE} = \left(Re_r^{\frac{2}{3}} + 0.008 Re_r^{0.3} Pr^{0.25} \right)^{\frac{1}{2}} \quad (4.92)$$

$$h_{FFE} = \frac{Nu \lambda}{(v_f^2/g)^{\frac{1}{3}}} \quad (4.93)$$

where v_f is the kinematic viscosity with

$$v_f = \frac{\mu_{FFE}}{\rho_{FFE}} \quad (4.94)$$

The heat transfer model in the mist flow region includes non-equilibrium effects on the vapor quality and local temperature. Models often do not consider these effects. Groeneveld (1973) adopted the Dittus-Boelter equation for single-phase turbulent convection and added another multiplying factor (Y) to approach the non-equilibrium

effects [141] and [143]. These correlations can be used for flows in horizontal and vertical tubes as follows:

$$Nu_{MF} = \frac{h_{MF}D}{\lambda_G} = 0.0327Re_{MF}^{0.901}Pr_{MF}^{1.32}Y^{-1.5} \quad (4.95)$$

$$Y = 1 - 0.1\left[\left(\frac{\rho_L}{\rho_G} - 1\right)(1 - x)\right]^{0.4} \quad (4.96)$$

The velocity is assumed to be the homogeneous velocity obtained by

$$u_H = \frac{\dot{m}}{\rho_H} = \dot{m}\left(\frac{x}{\rho_G} + \frac{1-x}{\rho_L}\right) \quad (4.97)$$

where x is the equilibrium vapor quality and all of the properties are evaluated at the saturation temperature. Moreover, the Reynolds number for the homogeneous vapor can be expressed as

$$Re_{MF} = \frac{\dot{m}D_i}{\mu_G}\left[x + \frac{\rho_G}{\rho_L}(1 - x)\right] \quad (4.98)$$

As mentioned earlier, in the inner tube, there is a small local temperature difference along the tube and the vapor produced in the boiling phase undergoes a partial condensation process. This should be taken into account for the prediction. Hence, the heat transfer correlation for condensation inside the tube can be expressed as follows [164], [165]:

$$h_{cond} = 0.555 \frac{\lambda_l}{D} \left[\frac{\rho_l g (\rho_l - \rho_G) D^3 h_{fg}}{\lambda_l \mu_l (T_{sat} - T_w)} \right]^{0.25} \quad (4.99)$$

where λ is the thermal conductivity and h_{fg} is the enthalpy of vaporization.

With respect to Fig. 4, at the reflux condenser, there is a non-isolated part which yields partial vapor condensation at the top through free convection with air when generating the reflux condensed stream (\dot{m}_l). The heat transfer characteristics of the free convection are determined by [143]:

$$Nu_{FC} = 0.68 + \frac{0.67Ra_L^{0.25}}{\left[1 + \left(\frac{0.492}{Pr}\right)^{1.6}\right]^{\frac{4}{9}}} = \frac{h_{FC}L}{k} \quad (4.100)$$

where Gr is the Grashof number given by

$$Gr = \frac{g\beta(T - T_\infty)L^3}{\nu^2} \quad (4.101)$$

where β is the thermal expansion coefficient obtained based on the fluid type.

By calculating the heat transfer coefficient of the boiling and condensation process for each column section, the height of the column for each section (L_i) can be obtained by

$$L_i = \frac{\dot{Q}_i}{U\Delta T_{LMTD}(\pi D)} \quad (4.102)$$

Here, the overall heat transfer coefficient for the boiling phase (U_B) and condensation phase (U_C) can be expressed as

$$U_{Boiling} = \frac{1}{\frac{1}{h_i A_i} + \frac{1}{h_o A_o} + \frac{\ln(\frac{D_o}{D_i})}{2\pi\lambda L}} \quad (4.103)$$

$$U_{Cond} = \frac{1}{\frac{1}{h_{FC} A_o} + \frac{\ln(\frac{D_o}{D_i})}{2\pi\lambda L} + \frac{1}{h_{cond} A_i}} \quad (4.104)$$

where h_i refers to the heat transfer coefficient of the inside flow stream (HCl-H₂O mixture). Also, h_o refers to the heat transfer coefficient of DURATHERM450 flowing between two tubes which is given by the modified Ginilinski correlation [143] and [162]:

$$h_o = \frac{Nu_o \lambda}{D} \quad (4.105)$$

$$Nu_o = \frac{(\frac{f}{8})(Re-1000)Pr}{1+12.7(\frac{f}{8})^{0.5}(Pr^{\frac{2}{3}}-1)} \quad (4.106)$$

where f is the friction factor obtained by:

$$f = (0.79 \ln Re - 1.64)^{-2} \quad (4.107)$$

4.5. Exergoeconomic Study of Integrated Cu-Cl Cycle

This section aims to develop an exergoeconomic analysis of this lab-scale experimental cycle to gain further insight into the economic viability of the cycle and reduce the produced hydrogen costs. The cost rate corresponding to each energy flow (either material or energy stream) is estimated from the cost balance equation and auxiliary equations to reveal the cost formation processes and unit exergy cost of the product. A relationship between the cost of destroyed exergy and capital cost of each component is defined to determine the component cost-effectiveness subject to its cost of irreversibilities.

In the exergoeconomic method, the scientific (primarily thermodynamics) and economic principles (primarily cost accounting) are combined to reveal optimum designs which cannot be achieved through conventional thermodynamic and cost studies alone [166] and [167]. Additionally, a scale-up study will be carried out to evaluate the cost of the Cu-Cl cycle in a larger scale of 1000 kg/day of hydrogen production capacity. In an

exergoeconomic approach, it is critical to identify the dependence of exergoeconomic parameters with the component type (compressor, chemical reactor, heat exchanger, or pump). The class of particular component determines that the specific evaluating parameter is desirable or undesirable. Also, changing a specific design or operating parameter of one component potentially affects other components which can be recognized by simulating the examined system.

An estimated unit price of experimental components in the lab-scale Cu-Cl cycle is provided in Table 4.7. Also, the cost of cycle subsystems comprising a hydrolysis reactor, thermolysis reactor, electrolyzer, quench cell, PSDU, ADA, dry unit, CuCl_2 concentrator, $\text{CuCl}/\text{CuCl}_2$ separator, RO and condensers are tabulated in Table 4.8. The concentrated CuCl_2 mixture dropping from the burette is removed from the CuCl_2 in the dryer unit at a temperature of 120°C . The hydrolysis reactor comprises a quartz tube (47 in length and the outer diameter of 1.5 in) in a tubular vertical furnace equipped with hot rasching rings/wires to maintain the reaction temperature at 420°C . K-type thermocouples are placed at different zones of the reactor and connected to the multi-zone temperature controller.

The thermolysis reactor is enclosed with the high temperature rasching rings/wires and well-isolated. The electrolyzer stack consists of 10 membrane electrode assemblies (MEA). The Nafion-117 membrane with an active area of 0.49 cm^2 and titanium/ platinum gas diffusion layer are used in the stack. The MEAs inside the stack contains titanium foil bipolar plates equipped with grooves or channels for supplying electrolytes (anolyte and catholyte) through the cell. The PSDU is comprised of two quartz columns (each 1 inch glass cylinder of 5 ft height) at the low pressure side, and at the high pressure side, three carbon steel tubes (each 7 ft tall) with the inner PTFE tubes in which the hot DURATHERM™ 450 oil is circulating to heat up the columns. The other components in the PSDU include an Alihin condenser, reservoirs, hot plates, pressure pump for pressurized $\text{HCl}(\text{aq})$ (masterflex), liquid throttling valve, pressure regulator for $\text{HCl}(\text{g})$, water chiller, and water.

Table 4.7. List of material costs (\$ CAD) within the lab-scale experimental Cu-Cl cycle.

Component	Cost per unit
Multi-zone temperature controller	\$225 per unit
Chemical resistance tube for piping	\$16.82 per ft
Quartz glass (L:1m, ID: 0.025m)	\$73.5 per unit
Bottle reservoir (2 liters)	\$182.47 per unit
Reflux condenser (Alihin condenser)	\$24.2 per unit
Burette clear glass with PTFE key stopcock	\$25
Submersible pump (for anolyte/catholyte buffer vessel in thermal bath)	\$170
Average price of laboratory glassware material (beaker, Erlenmeyer flask)	\$30
Electrolyzer pump (mesterflex peristaltic)	\$762
Pressure regulation with helium	\$23.62
Hot plate with temperature controller	\$214
Thermal oil heater (NESLAB RTE140)	\$2,300
Pump for anolyte dissolution set-up (mesterflex peristaltic)	\$762
Gear motor (for screw conveyer and surface brushing for dryer)	\$51.5
Electromagnetic valve actuated by N ₂ float switch	\$39
Argon flow meter	\$58
Thermal bath tub (heated from underneath)	\$680
Pressure regulator for HCl (g)	\$45
Pressure pump for pressurized HCl(aq) in distillation (masterflex)	\$2129.05
Liquid throttling valve	\$23.9
Pressurized liquid level regulator	\$161
Water chiller (NESLAB ULT-80)	\$8,345
Glacier bay Reverse Osmosis water	\$173.78
Pressurized vessel (bride vessel)	\$55
Electrolyzer stack (10MEA, active area 50cm ²)	\$3,200
Including: Nafion 177 membrane (Titanium/Paltinium)	\$2,000
Carbon steel tube (high pressure side of PSDU)	\$540 per ton
Heating tape Omegalux STH051-080 (600W, 1.2m)	\$140
Thermocouple	\$21
Copper chloride	\$36.9
Cuprous chloride	\$55.6
Duratherm Oil 450	\$36.9
Hydrochloric acid (2.5L, 12M)	\$23.34 per unit
Others (adhesive, insulation, etc.)	\$65

Table 4.8. Cost of experimental units (\$ CAD) in the lab-scale integrated Cu-Cl cycle

Operation Unit	Estimated Capital Cost
Hydrolysis reactor	Quartz glass, insulation, copper thermal wire, 4 thermocouples, multi-zone temperature controller, construction, \$710
Thermolysis reactor	Quartz erlenmeyer (500 ml), insulation, copper thermal wire, temperature controller = \$252
Electrolyzer stack (10MEA, active area 50cm ²)	\$17,000
Dryer unit	Burette clear glass with PTFE key, thermal tape, \$165
PSDU	2 Quartz glass, 3 galon Duratherm oil, 2 Alihin condenser, 3 reservoirs, hot plate, thermal oil heater (NESLAB RTE140), pressure pump for pressurized HCl(aq) in distillation (masterflex), liquid throttling valve, pressurized liquid level regulator, pressure regulator for HCl (g), water chiller, 2 erlenmeyer, glacier bay reverse osmosis, pressurized vessel (bride vessel), 16 thermocouples, 4 heating tape Omegalux, tubing (including carbon, chemical resistance and PTFE), \$13,376.4
Quench	2 Alihin condenser, beaker, \$680.4
ADA	5 reflux condenser, HCl (aq) condenser, hot plate, oil heated DURM boiler (two-neck re-boiler boiling flask 500 ml), \$394.2
Dry Unit	Surface brushing set-up for dryer (Gear-motor), 2 reflux condensers, 2 thermal tape, \$380
Separator Unit	Gear-motor for CuCl(s) screw conveyer, 2 valves, beaker/ erlenmeyer, \$131.5
CuCl ₂ concentrator	Thermal oil beaker (Berzelius 2L insulated), two-neck re-boiler boiling flask 500ml, thermal tape, \$203
Dryer	Burette clear glass with PTFE key stopcock, thermal tape, \$165

If the processes for refining oxidized anolyte, including the ADA, dry unit, CuCl₂ concentrator, CuCl/CuCl₂ separator and PSDU inside the electrochemical unit, the highest capital cost belongs to the electrochemical unit. The PSDU and electrolyzer stack are the primary contributors for the equipment in the electrochemical unit which correspond to 44% and 35% of the total cost, respectively.

4.5.1. SPECO Formulation

The principles of the exergoeconomic methodology will be applied to the experimental lab-scale Cu-Cl cycle. The exergy steams and the fuel and product definitions should be well-

defined. Through the exergy costing, the cost rates of each stream are determined based on the associated exergy rate and unit cost. So at a steady-state condition, to evaluate the cost rate of each stream, the cost balance is applied for each component (k) in terms of the product cost rate (\dot{C}_p) and fuel cost rate (\dot{C}_F) as follows [166].

$$\underbrace{\sum_e (c_e \cdot \dot{E}x_e)_k + c_{w,k} \dot{E}x_{w,k}}_{\dot{C}_p} = \underbrace{c_{q,k} \dot{E}x_{q,k} + \sum_i (c_i \cdot \dot{E}x_i)_k}_{\dot{C}_F} + \underbrace{\dot{Z}_k}_{\dot{Z}} \quad (4.108)$$

Here c is the cost per unit of exergy (\$/kJ) and $\dot{E}x$ is the associated exergy transfer rate. $\dot{E}x_q$ and $\dot{E}x_w$ are exergy rates associated with the heat and workflows. In the economic analysis, annualized values are used for the component's cost because they undergo a change over their economic life. The parameter \dot{Z}_k is the component related cost including the life cycle phases of construction, operation, maintenance and disposal. The capital and operating costs are the most significant contributors to \dot{Z} . The expression for \dot{Z} that can be written as follows [56] and [134]:

$$\dot{Z}_k = CRF \cdot F_m \cdot \frac{\varphi \cdot Z_k}{\tau} \quad (4.109)$$

where F_m refers to material factor (assumed as 1.06 [134]), φ is the maintenance factor generally taken as 1.06 and τ is the annual time of system operation in hours (considered as 2,500 hrs). The unit price of electricity and thermal energy used in the cost analysis is 0.06\$/kWh and 0.02\$/kWh, respectively. The parameter Z_m indicates the capital investment (\$) of component k.

The CRF is the capital recovery factor which depends on the equipment lifetime in years (n) and interest rate (i) as follows:

$$CRF = \frac{i(i+1)^n}{(i+1)^n - 1} \quad (4.110)$$

The cost rate of destroyed exergy within each component k can be expressed as follows:

$$\dot{C}_D = c_f \dot{E}x_D \quad (4.111)$$

where $\dot{E}x_D$ indicates the exergy destruction rate of a component. The unit cost rate of c_f shows the average unit cost of fuel that can be obtained based on the summation of the fuel cost rate in accordance with the purpose of the component ($\dot{C}_{F,k}$) and its corresponding exergy flow rate ($\dot{E}x_{F,k}$) [165] and [168].

$$c_{f,k} = \frac{\dot{C}_{F,k}}{\dot{E}x_{F,k}} \quad (4.112)$$

The total cost rate of a component (\dot{C}_{Total}) is a critical parameter in the SPECO methodology. It can be defined as the sum of cost rates associated with the destroyed exergy (\dot{C}_D) and final capital, operating and maintenance cost rates (\dot{Z}_k):

$$\dot{C}_{Total} = \dot{C}_D + \dot{Z}_k \quad (4.113)$$

In the exergoeconomic approach, the variables of \dot{C}_D and \dot{Z} represent the importance of each component in the system optimization. However, a criterion is needed to measure the component cost-effectiveness. For this respect, the exergoeconomic factor (f) is defined which evaluates the component effectiveness in terms of cost [165] and [168]:

$$f = \frac{\dot{Z}_k}{\dot{C}_{Total}} = \frac{\dot{Z}_k}{\dot{Z}_k + \dot{C}_D} \quad (4.114)$$

When applying the cost balance equation for component k (equation 1), there is usually more than one inlet and outlet stream. So the number of cost balance equations is less than the unknown cost parameters. Here, auxiliary equations as the F and P rules are developed based on the auxiliary thermodynamic equations. Based on the F rule, all of the exergy values entering the control volume, plus all decremented inlet and outlet exergy flows and all of the exergy flows that are not associated with the purpose of the component are considered as being equal to the fuel. In the same way, the summation of all outlet exergy values plus all incremental inlet and outlet exergy flows are in accordance with the purpose of the component.

Figure 4.12 demonstrates the fuel, product, auxiliary costing and productive structure for a component that covers all possible situations (except those in which the stream chemical composition changes) that might occur in the application of the SPECO methodology [166]. In the case of thermochemical/electrochemical reactions in which the

chemical composition of the stream changes, an application of F and P rules appear in complex expressions.

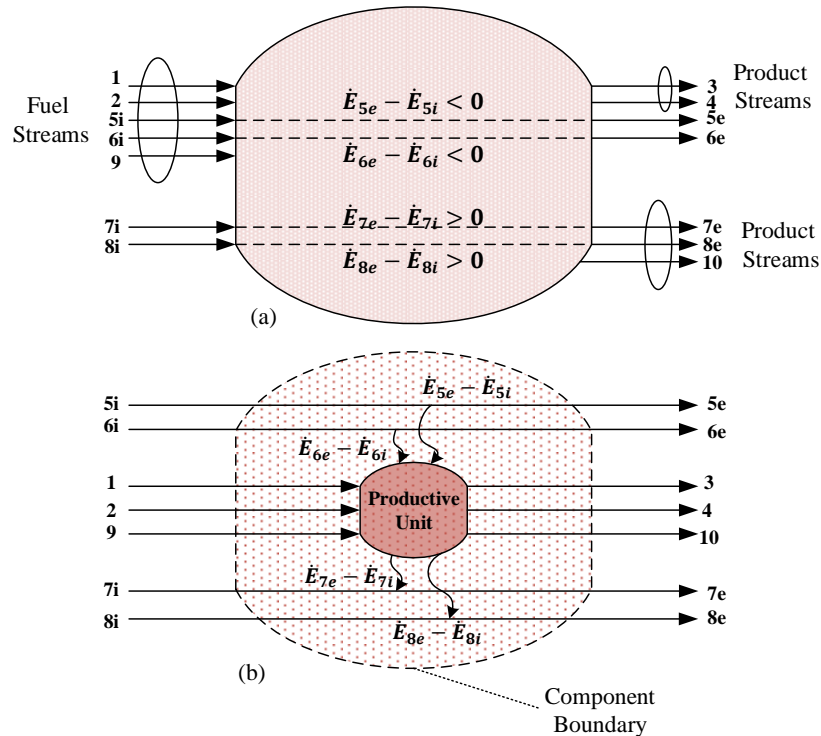


Figure 4.12. (a) Schematic diagram of an energy system representing fuel, products and (b) the structure shown in (a) where all streams are exergy flows.

In the SPECO method, the components are ranked based on the descending order of cost importance (represented as $\dot{Z} + \dot{C}_D$). The exergoeconomic factor (f) is employed in the analysis to reveal the major cost source from either the capital cost or costs of destroyed exergy. The high value of f suggests that it would be more cost-effective to decrease the capital cost for component k even though it may decrease the component efficiency. The low value of f suggests improving the efficiency of a component through the incremental capital cost. The destroyed exergy and increase of exergy loss occurs in the sub-processes without reducing either capital cost or fuel cost. In the case of the large exergy destruction or exergy loss and consequently relatively low exergy efficiency, some consideration should be taken to improve the component exergy efficiency.

Table 4.9. Cost balance equation (CBE) and auxiliary F and P rules for the system components

Component	CBE	Fuel and product expressions
Hydrolysis reactor	$\dot{C}_{QB40} + \dot{C}_{QB3} + \dot{C}_{QHyd} + \dot{Z}_{Hyd}$ $= (\dot{C}_7 + \dot{C}_6) - (\dot{C}_4 + \dot{C}_5)$	$c_6 = c_7$
Thermolysis reactor	$\dot{C}_{QB5} + \dot{C}_{QThrm} + \dot{Z}_{Thrm} = (\dot{C}_{10} + \dot{C}_{11}) - \dot{C}_6$	$c_{10} = c_{11}$
Quench cell	$\dot{C}_{QQuench} + \dot{Z}_{Quench} = (\dot{C}_{10} + \dot{C}_{13})$	-
Electrochemical unit (EU)	$\dot{C}_{WEU} + \dot{C}_{QEU} + \dot{Z}_{EU}$ $= (\dot{C}_{19} + \dot{C}_{34})$ $- (\dot{C}_{10} + \dot{C}_7 + \dot{C}_{57})$ $\dot{C}_{WEU} = \dot{C}_{W_{Elect}} + \dot{C}_{W_{RO}}$ $\dot{C}_{QEU} = (\dot{C}_{Q_{ADA}} + \dot{C}_{Q_{Dry}} + \dot{C}_{Q_{Sepu}} + \dot{C}_{Q_{Conc}}$ $+ \dot{C}_{Q_{PSDU}} + \dot{C}_{Q_{SC}}) - (\dot{C}_{Q_{HClCon1}}$ $+ \dot{C}_{Q_{HClCon2}} + \dot{C}_{Q_{HClCon3}}$ $+ \dot{C}_{Q_{StCon1}} + \dot{C}_{Q_{StCon2}})$	$c_{19} = c_{34}$ $c_{57} = 0$
ADA	$\dot{C}_{QB12} + \dot{Z}_{ADA} = (\dot{C}_{61} + \dot{C}_{58}) - \dot{C}_{53}$	$c_{61} = c_{58}$
Separation unit	$\dot{C}_{38} + \dot{Z}_{Sepu} = (\dot{C}_{54} + \dot{C}_{18}) - \dot{C}_{72}$	$c_{18} = c_{54}$
CuCl ₂ concentrator	$\dot{C}_{QB8} + \dot{Z}_{Conc} = (\dot{C}_{23} + \dot{C}_{24}) - \dot{C}_{54}$	$c_{23} = c_{24}$
Dryer	$\dot{C}_{QDryer} + \dot{Z}_{Dryer} = (\dot{C}_{20} + \dot{C}_{21}) - \dot{C}_{19}$	$c_{21} = c_{19}$
PSDU	$\dot{C}_{QPSDU} + \dot{Z}_{PSDU} = (\dot{C}_{48} + \dot{C}_{51}) - \dot{C}_{35}$	$c_{48} = c_{51}$
DEC	$\dot{Z}_{PSDU} + (\dot{C}_{14} + \dot{C}_{18}) = \dot{C}_{27}$	-
RO	$\dot{C}_{WRO} + \dot{Z}_{RO} = (\dot{C}_{38} + \dot{C}_{Brine}) - \dot{C}_{57}$	$c_{Brine} = 0$

For evaluating the exergy flow rates, the integrated lab-scale Cu-Cl cycle is simulated in the Aspen Plus software. The thermochemical and thermo-physical properties of species were available in the software database library and also can be found in past literature [1], [31–33]. Table 4.2 shows the design input parameters in the cycle simulation. The exergy destruction rate and exergy efficiency definitions for all components of the lab-scale Cu-Cl cycle were provided in Table 4.4.

The cost balance equation (CBE) based on $\dot{C}_F + \dot{Z} = \dot{C}_P$ and the auxiliary equations (from F and P rules) are written for each component and provided in Table 4.9.

4.5.2. Scale-up Analysis

A scale-up analysis predicts the cost of a large scale facility of an industrial Cu-Cl cycle with 1000 kg/day of hydrogen production capacity. The Hydrogen Analysis (H2A)

production model developed by the U.S. DOE Hydrogen and Fuel Cells Program [169] was employed for the scale-up cost assessment. In this methodology, the technical and economic features of a system producing hydrogen are analyzed. The minimum level cost of produced hydrogen and the after-tax internal rate of return from this production are obtained from a return model that uses a standard discount cash flow rate. In the analysis, the year 2020 is considered as the start time. The most similar available model in H2A is used for this study with some modifications and simplifications.

To update the purchased cost of equipment in the hydrogen plant to the current year and deflate dollars from the target year to the reference year, the chemical engineering plant cost index (CEPI) and consumer price inflator (CPI) approaches are applied, respectively, in the present study. In the scale-up cost assessment, the operating cost capacity factor is assumed as 85%. The plant design capacity is considered 1000 kg/day of hydrogen production and the yearly hydrogen production plant output is 364,963.5 kg/year. An inflation tool is used to adjust the basis year cost in 2009 to 2019 dollars [170].

In Table 4.10 the financial parameters in the cost study are provided. The total land required (in Canada, Ontario) for the scaled-up Cu-Cl cycle plant is estimated based on the proportion of the experimental lab-scale Cu-Cl cycle capacity (100 g/day H₂) and the scaled up cycle with 1000 kg/day H₂. The large-scale (scale-up) of the integrated Cu-Cl cycle is shown in Figure 4.13.

The overall full cost of hydrogen production includes labor costs, waste disposal, general expenses, utilities, raw materials, maintenance expenses and taxes. Among those costs, the utilities cost (mostly electricity) contributes the largest portion. The following calculated prices are associated with the production of hydrogen and do not account for storage processes and transportation to the final destination.

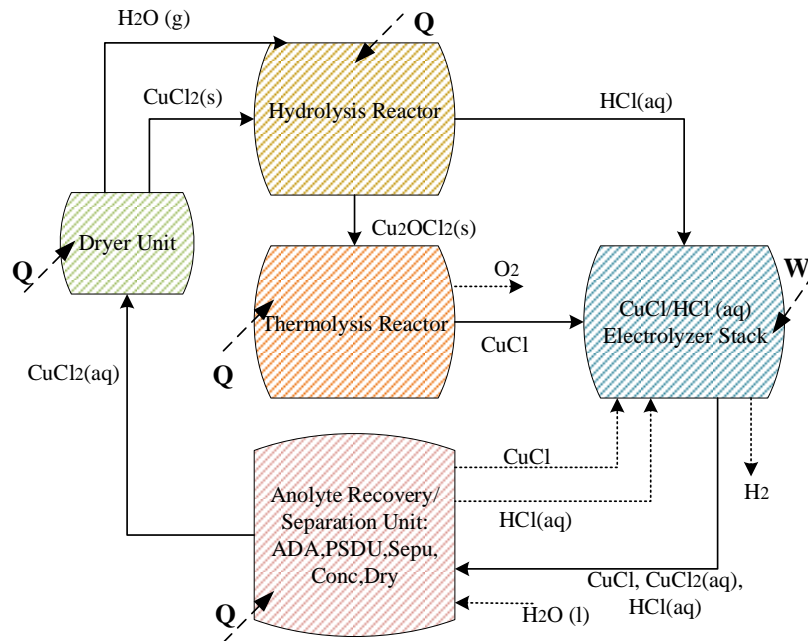


Figure 4.13. Schematic of large-scale thermochemical Cu-Cl cycle for hydrogen production

Table 4.10. Economic factors in the cost analysis

Parameter	Value
Reference year	2009
Start-up year	2020
Basis year	2009
Length of construction period (years)	2
% of capital spent in first year of construction	20%
% of capital spent in second year of construction	80%
Start-up time (years)	0.4
Total plant life (years)	40
Analysis period (years)	40
Depreciation schedule length (years)	20
Decommissioning costs (% of depreciable capital investment)	10%
Salvage value (% of total capital investment)	5%
Inflation rate (%)	1%
Engineering, design, and up-front permitting costs	7.5% of the direct capital cost
Process contingency cost	10% of the direct capital cost
Industrial electricity average prices (\$/kWh)	0.06

4.6. Optimization Study

This section aims to optimize an experimental lab-scale integrated Cu-Cl cycle at the UOIT in terms of exergy efficiency and operational costs of the produced hydrogen. To perform a multi-objective study, the system is simulated in Aspen Plus and EES software. Then, a sensitivity analysis is conducted based on the main influential design operating parameters including the steam to copper molar ratio, hydrolysis temperature, thermolysis temperature, low pressure side of a pressure swing distillation unit (PSDU) temperature, HCl/CuCl (aq) electrolyzer temperature and an average temperature of anolyte recovery separation units. The Aspen Plus and EES results are classified and then the matrix of input design parameters and corresponding exergy efficiency and operational costs of produced hydrogen are introduced in an Artificial Neural Network in Matlab to generate a relationship between the decision variables and objective functions. Finally, through the multi-objective GA-based optimization algorithm, the function is optimized based on exergy efficiency maximization and operational cost minimization for the produced hydrogen. The results of this study will be useful for the performance assessment of lab-scale integrated Cu-Cl cycle by accounting for the actual implementation to achieve more efficient system performance.

The Pareto selection-based methods are common multi-objective evolutionary algorithms. They are relatively efficient in finding a representative set of Pareto optimal solutions. No prior knowledge of the problem is required. Moreover, the methods are independent of the Pareto front form. Generally, Pareto selection-based methods take advantage of a dominance relation between the individuals of the population to determine their respective fitness [171].

An important part of an optimization problem is the determination of decision variables that characterize the suitable design options. There are many parameters which affect the value of the objective function. These parameters (decision variables) should be selected wisely to improve the process of finding the optimal design and also to reduce the optimization time. There are some criteria for the selection of decision variables. These involve the relevant factors that affect the objective functions and system performance. An important optimization parameter involves constraints. The constraints in a given design

problem arise due to limitations on the ranges of the physical variables, conservation principles which must be satisfied and other limitations. The restrictions on the variables may arise due to space, equipment, time and materials that are used. This condition gives rise to an equation that must be satisfied by the relevant design variables, thus restricting the values that may be employed in the search for an optimum. Similarly, energy balance considerations are important in thermal systems and may limit the range of temperatures, heat fluxes, and dimensions that may be used. Several constraints are often considered during modeling and simulation because the governing equations are based on conservation principles. In this way, the objective function considers these constraints. In such cases, only the additional limitations that define the boundaries of the design domain remain to be considered.

The lab-scale integrated Cu-Cl cycle performance is considered in terms of the exergy efficiency and cost analysis. As mentioned earlier, the system analysis is based on a unit mole basis of produced hydrogen, so the hydrogen yield is not considered in the group of measured parameters. The primary reason that the exergy efficiency and cost are chosen as objective functions is to ensure that the resources are most effectively utilized. The input parameters to the cycle include the steam to copper chloride ratio (St/Cu), and temperatures of the hydrolysis reactor, thermolysis reactor, pressure swing distillation unit, anolyte recovery separators and electrolyzer unit. The integrated cycle is simulated in EES and Aspen Plus software. Then the parameter sensitivity analysis is performed. The variations of the St/Cu ratio and reactor temperature effects on the cost, energy and exergy efficiencies become inputs for the optimization study. Table 4.2 shows the primary parameters of the optimized system, while Table 4.11 shows the acceptable ranges for the decision variables (system input parameters).

In order to connect the input and output parameters and introduce them to the Matlab software for optimization purposes, a relation between the decision variables (St/Cu and temperature of the reactors) and objective functions (cost and energy and exergy efficiencies) is required. This is achieved by an Artificial Neural Network in Matlab. The total number of points in Aspen Plus including each increment of the St/Cu and reactor temperatures and the corresponding changes in the cost, energy and exergy efficiencies are

transferred into the ANN as matrices. After finding the generated function from ANN, which shows the relationship between the decision variables and objective function, the multi-objective optimization is performed based on a Genetic Algorithm (GA) to optimize the function. Figure 4.14 represents an illustrative scheme of the multi-objective optimization steps for the integrated Cu-Cl cycle. The parameters and properties of the ANN and the GA to optimize the lab-scale integrated Cu-Cl cycle are tabulated in Table 4.11.

Table 4.11. Properties and parameters of the NN and GA to optimize the lab-scale integrated Cu-Cl cycle

Parameter	Range/ Value
Artificial Neural Network	
Percent of data used for training	70%
Percent of data used for testing	15%
Percent of data used for validation	15%
Training method	Bayesian regularization
Simulating software	Matlab
Genetic Algorithm	
Optimization principle	Pareto optimum points
Simulating software	Matlab
Lower and upper limits of input parameters	
Steam to copper chloride molar ratio (St/Cu)	10-30
Hydrolysis reaction temperature	350°C-450°C
Thermolysis reaction temperature	480°C-580°C
LP PSDU	100°C-130°C
HCl/CuCl (aq) Electrolyzer stack temperature	30°C-80°C
Average temperature of anolyte recovery separation units	100°C-150°C
Objective Functions	
Overall exergy efficiency	%
Operational cost of produced hydrogen	\$

a) Artificial Neural Network (ANN)

In order to link the Aspen Plus model and the GA optimization, the ANN is used as the connector tool. Extracting the relationship between the input and output parameters analytically from the process simulator software with numerous streams and components would be complex. Besides the regression model, another alternative is simulating the deep learning in a human brain to find the best function connecting the variables and objectives. This is known by machine learning methods, and an Artificial Neural Network (ANN). In the ANN, the typically analog and nonlinear computational structure is simulated by

neurons. In this work, a two-layer feed-forward model with linear output neurons and sigmoid hidden neurons is applied to find the function relating the system inputs and objectives. The main reason that this model is selected is that, at the condition of consistent data and enough neurons in the hidden layer, the multi-dimensional mapping cases can be fitted well.

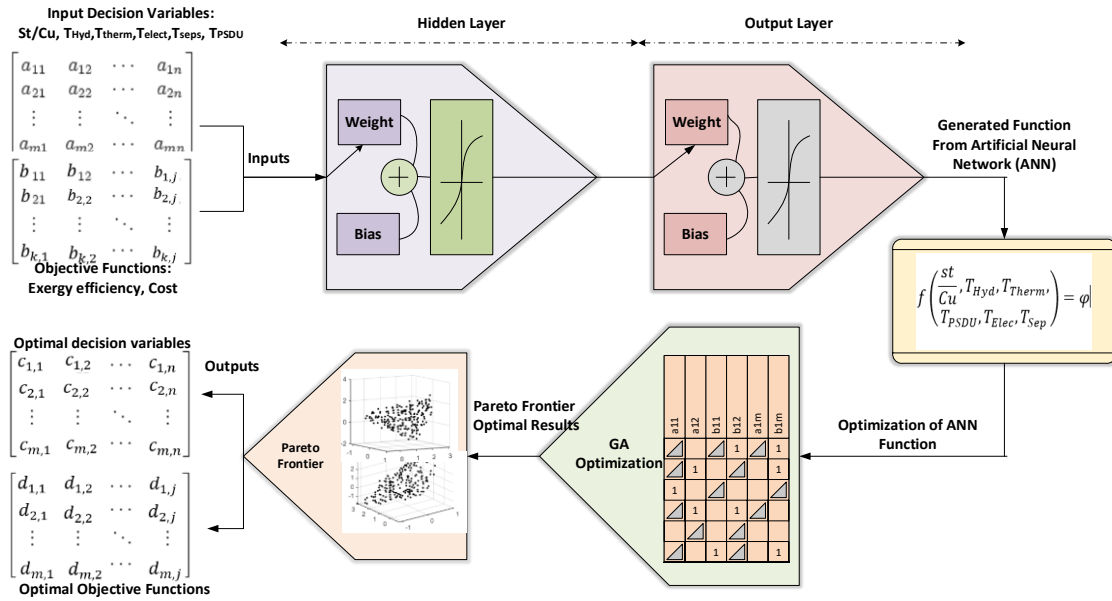


Figure 4.14. Schematic diagram of the Artificial Neural Network to analyze relationships between the inputs and outputs of the lab-scale integrated Cu-Cl cycle.

Two sets of 6×12 and 2×12 matrices which contain the inputs (St/Cu and temperature of reactors) and objective outputs (cost and exergetic efficiency) were generated in the Aspen Plus simulator and introduced to the ANN to be trained. A Bayesian Regulation training method is employed which provides higher accuracy for the system. The quality of ANN performance to generate the relationship between the inputs and objective outputs is specified by the number of hidden layers. An optimized number of hidden layers leads to the best match of a created function by ANN with the inputs and outputs that can be obtained through trial and error. Finally, the generated function is optimized by a GA multi-objective optimization to achieve the optimum operating condition of the Cu-Cl cycle. Figure 4.14 illustrates the schematic diagram of the ANN.

b) Genetic Algorithm Model

The genetic algorithm derives from the natural evolutionary concept wherein there is more opportunity for strong individuals to pass along genes (solutions) to offspring and consequently turn into a dominant member of the population. In this method, the chromosome (or individual) with the specific set of genes acts as the solution vector, and the collection of chromosomes (known as the population) is randomly initialized. From the present sets, the GA algorithm employs two functions of crossover and mutation to create new chromosomes. In the crossover, new offspring (or chromosomes) are created from the combination of parents (two individuals) [172]. Based on the fitness priority, the parents are selected from the current population and considered as a fitter. Then the good genes are inherited by the offspring. The genes of competent individuals happen more frequently through the population by iterations of the crossover operator which finally leads to convergence to the optimum solution [172], [173].

The diversity at the gene level appears through the mutation in which the rate of mutation is the contingency of changes in the gene property that avoids falling into the local minimum or maximum point to reach the global solution. In each optimization step, by a random selection of individuals from the existing population and employing them as parents to create the next generation, the population of individual solutions is continuously changing and evolving until the optimum solution is obtained. The GA algorithm is used for multi-objective optimization by recognizing multiple points; called Pareto optimum points which represent the optimum value of the objectives. Once the Pareto optimality allocations evolve, no objective can be improved without making other objectives worse.

Here for the lab-scale integrated Cu-Cl cycle, the GA is applied to optimize the function generated by ANN which establishes a connection between the input variables (St/Cu molar ratio and the temperature of reactors) and objectives (cost, energy and exergy efficiencies) as follows.

$$(\Psi, cost) = f\left(\frac{St}{Cu}, T_{Hyd}, T_{Trm}, T_{PSDU}, T_{Elect}, T_{Seps}\right) \quad (4.115)$$

The objectives of the GA optimization are to maximize the exergy efficiency and minimize the operational cost for producing hydrogen. The optimization boundaries are listed in Table 4.11.

Chapter 5 . Results and Discussion

In this chapter, the model results of the integrated lab-scale Cu-Cl cycle are presented and discussed. With respect to the model in section 4.2.1, a verification approach is presented for the hydrolysis reaction. The initial input design parameters are provided in Table 5.1. The thermo-physical properties of chemical components of CuCl_2 , Cu_2OCl_2 , CuCl , H_2O and HCl are obtained from the Aspen Plus tool. The power law kinetic expression is applied to incorporate the kinetic parameters from past experimental studies for the hydrolysis reaction [26, 27, 105], and used for the model verification as shown in Figure 5.1. Also, Table 5.2 tabulates the chemical species properties at the specific reactor design condition. According to Table 5.2, the negative values for the molar enthalpy and molar entropy are shown due to the arbitrarily chosen reference state by the Aspen Plus simulator software.

5.1. Lab-scale Integrated Cu-Cl Cycle Simulation Results

The thermodynamic analysis results for the lab-scale integrated Cu-Cl cycle built in CERL at UOIT, are obtained with Aspen Plus simulation package to reveal the properties of species in streams. The composition, temperature, pressure, specific molar enthalpy, specific molar entropy and specific molar exergy of each state point have been identified and provided in Table 5.3. In Table 5.3, the obtained negative values associated with the molar enthalpy and molar entropy is due to the arbitrarily chosen reference state by the Aspen Plus simulator software, however, it has no effect on the accuracy of the energy and exergy balance equations. Moreover, the total hydrogen production rate from the system, temperature, pressure, energy efficiency, exergy efficiency and total exergy destruction of the whole cycle are reported in Table 5.4.

Table 5.1. Hydrolysis reaction design parameters used for verification purpose.

Parameter	Value
CuCl_2 (aq) molar flow rate	1,800 kmol/hr
Dryer temperature (CuCl_2 (aq) inlet temperature into the hydrolysis reactor)	120°C
Dryer pressure	1 bar
Reactor pressure	1 bar
Reactor temperature	400°C
Steam to copper ratio	17
Hydrolysis stoichiometry reaction : $2\text{CuCl}_2(s) + \text{H}_2\text{O}(g) \rightarrow \text{Cu}_2\text{OCl}_2(s) + 2\text{HCl}(g)$ Copper chlorine decomposition side reaction: $2\text{CuCl}_2(s) \rightarrow 2\text{CuCl}(s) + \text{Cl}_2(g)$	

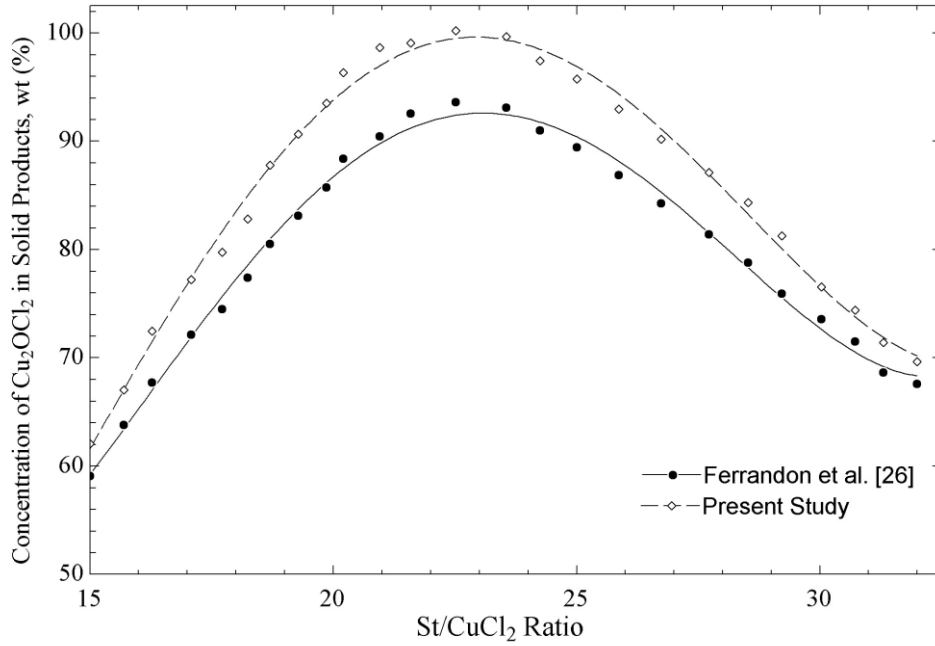


Figure 5.1. Concentration of Cu_2OCl_2 in the solid products as a function of steam to copper chloride ratio and comparison with Ref. [26]

Table 5.2. Thermo-physical properties of the chemical species in the copper chloride (CuCl_2) decomposition reactor ($T_{\text{dryer}}=125^\circ\text{C}$; reactor pressure of 1 atm; $\text{Ar}/\text{N}_2=0$).

Species	Cu_2OCl_2	HCl	CuCl_2	H_2O	CuCl
Phase	Solid Phase	Vapor Phase	Solid Phase	Vapor Phase	Solid Phase
Temperature, $^\circ\text{C}$	125	125	125	125	125
Chemical exergy, kJ/mol	21.10	84.5	82.10	9.5	76.2
Molar Enthalpy, kJ/mol	-372.43	-89.39	-198.50	-238.43	-133.02
Mass Enthalpy, kJ/kg	-1740.33	-2451.81	-1476.37	-13234.90	-1343.7
Molar Entropy, kJ/mol-K	-1.25	0.02	-0.13	-0.03	-0.04
Mass Entropy, kJ/kg-K	-5.85	0.51	-0.94	-1.91	-0.43
Molar Density, kmol/cum	37.02	0.03	25.58	0.03	41.80
Mass Density, kg/m^3	7921.41	1.10	3439.94	0.54	4137.95
Enthalpy Flow, kW	-2069.03	-496.63	-1102.78	-1324.62	-739.03
Heat capacity (kJ/kmol.K)	45.75	29.17	74.55	34.18	52.02

The lower energy and exergy efficiencies of the overall integrated Cu-Cl cycle compared to the literature [8], [174], [175] are mainly attributed to the fact that in those studies a considerable portion of required input energy supplied from recovering heat at the internal or external segments.

Table 5.3. Initial input and assessed thermodynamic properties of the integrated Cu-Cl cycle's state points

	Species	Temperature (°C)	Molar Enthalpy (kJ/mol)	Molar Entropy (kJ/kmolK)	Mole Flows (mol/s)	Molar physical exergy (kJ/mol)	Molar chemical exergy (kJ/mol)
S1	HCl/ H ₂ O	106	-200	-17.15	0.113	0.244	27.5
S2	CuCl ₂	400	-190	-86.43	0.025	10.204	82.1
S3	Cu ₂ OCl ₂ / HCl/ H ₂ O 0.1/0.2/0.68	400	-210	6.07	0.118	10.522	25.468
S4	H ₂ O	125	-240	-34.52	0.092	9.023	9.5
S5	CuCl ₂	125	-210	-126.91	0.025	1.016	82.1
S6	Cu ₂ OCl ₂	410	-340	52.327	0.0125	17.248	21.08
S7	HCl/ H ₂ O 0.23/0.77	410	-190	0.56	0.105	9.722	26.75
S8	Cu ₂ OCl ₂	520	-320	76.11	0.0125	27.663	21.08
S9	CuCl/ O ₂ 0.8/0.2	520	46.28	99.77	0.0313	34.064	61.754
S10	CuCl	520	53.80	116873.2	0.025	40.861	76.2
S11	O ₂	520	15.93	31.00	0.006	6.693	3.97
S12	CuCl ₂ / H ₂ O 0.1/0.9	110	-240	-44.36	0.276	0.285	16.76
S13	CuCl	436	-120	-10.130	0.025	8.796	76.2
S14	CuCl	45	-140	-54.48	0.025	0.031	76.2
S15	HCl/ H ₂ O 0.23/0.77	50	-240	-112.34	0.105	0.124	26.75
S16	CuCl ₂ / CuCl/ HCl/ H ₂ O/ H ₂ 0.398/0.081 6/0.0816 /0.2383/0.1 99	40	-160	-78.22	0.106	0.025	95.0179
S17	CuCl/ HCl/ H ₂ O 0.4/0.4/0.2	58.69494	-140	-34.10	0.752	0.005	66.18
S18	CuCl	40.2464	-140	-55.22	0.048	0.018	76.2
S19	CuCl ₂ / H ₂ O 0.22/0.78	121	-230	-54.58	0.118	7.280	25.472
S20	CuCl ₂	125	-210	-126.91	0.025	1.016	82.1
S21	H ₂ O	125	-240	-34.52	0.0927	9.023	9.5
S23	H ₂ O	110	-240	-35.83	0.158	8.901	9.5
S24	CuCl ₂ / H ₂ O 0.22/0.78	110	-230	-55.78	0.118	7.171	25.472
S25	H ₂ O	45	-280	-158.27	0.158	0.003	9.5
S27	CuCl	43.40489	-140	-54.73	0.030	0.002	76.2
S34	H ₂	40	0.43	1.52	0.0125	-0.022	236.02
S35	HCl/ H ₂ O 0.247/0.752	50	-230	-110.57	0.113	0.125	28.0155
S38	H ₂ O	30	-290	-161.89	0.25	0.005	9.5

S43	H ₂ O	567	-370	30.06	14.769	16.742	9.5
S44	H ₂ O	559.9159	-370	29.63	14.769	16.505	9.5
S46	H ₂ O	558.1557	-370	29.51	1.4769	16.446	9.5
S48	HCl/ H ₂ O 0.8/0.2	120	-120	12.73	0.034	0.772	47
S50	NaCl/ H ₂ O	30	-340	84.14	0.020	0.667	10.46
S51	H ₂ O	120	-240	-34.95	0.079	8.981	9.5
S52	H ₂ O	38	-280	-159.94	0.079	0.024	9.5
S53	CuCl ₂ / CuCl/ HCl/ H ₂ O 0.5/0.1/0.1/ 0.3	40	-180	-91.50	0.093	0.024	59.97
S54	CuCl ₂ / H ₂ O 0.1/0.9	40.2	-280	-158.05	0.276	0.032	16.76
S55	H ₂ O	30	-280	-161.89	0.25	0.005	9.5
S56	NaCl	30	-380	84.14	0.020	0.668	14.2
S57	HCl/H ₂ O 0.19/0.81	30	-290	-141.47	0.27	0.054	10.46
S58	HCl/ H ₂ O 0.19/0.81	104	-210	-22.45	0.011	6.118	23.75
S61	CuCl ₂ / CuCl/ HCl/ H ₂ O 0.64/0.13/0. 078/0.15	104	-160	-68.01	0.082	0.945	70.466
S62	HCl/ H ₂ O 0.36/0.64	107	-180	-11.27	0.008	4.177	36.5
S64	CuCl ₂ / CuCl/ H ₂ O 0.81/0.166/ 0.02	107	-160	-74.00	0.074	0.625	79.3402
S65	H ₂ O	400	-230	-15.87	0.092	13.264	9.5
S70	CuCl ₂ / CuCl/ HCl/ H ₂ O 0.5/0.1/0.1/ 0.3	104	-170	-62.63	0.093	1.545	59.97
S71	CuCl ₂ / CuCl/HCl/ H ₂ O 0.64/0.13/0. 078/0.15	107	-160	-67.56	0.082	0.981	70.466
S72	CuCl ₂ / CuCl/ H ₂ O 0.81/0.16/0. 019	85	-160	-78.40	0.074	0.310	78.883
S73	HCl/ H ₂ O 0.19/0.81	45		-124.12	0.011	0.072	23.75
S74	HCl/ H ₂ O 0.36/0.63	50		-88.55	0.008	0.138	36.405

It should be mentioned that the copper chloride decomposition side reaction within the hydrolysis reactor is not considered in the simulation of the whole lab-scale integrated Cu-Cl cycle.

The unit thermal energy supplied to the elements is depicted in Figure 5.2. As can be observed, the maximum amount of unit thermal energy per mole of the produced hydrogen is associated with the CuCl₂ concentrator unit. This is primarily owing to the separation of CuCl constituent from CuCl₂ which requires a considerable amount of water to dissolve CuCl₂ (as noted before, CuCl does not dissolve in the water). Each 2 moles of CuCl₂ needs at least 20 moles of water to be completely dissolved. However, CuCl is separated from CuCl₂, the other process would be necessary to remove this added water from the CuCl₂ component. This stage would be happened at CuCl₂ concentrator unit by vaporizing the excess water from the aqueous phase consuming a remarkable amount of thermal energy. The more water removed from the mixture, the more concentrated CuCl₂ would be obtained.

Table 5.4. Overall hydrogen production rate, temperature, pressure, energy and exergy efficiencies and exergy destruction of the proposed integrated four-step Cu-Cl cycle.

Parameter	Value	Unit
Overall hydrogen production rate	1.25×10^{-2}	mol/s
Pressure of produced hydrogen	1	bar
Temperature of produced hydrogen	45	°C
Overall energy efficiency of proposed integrated Cu-Cl cycle	35.9	%
Overall exergy efficiency of proposed integrated Cu-Cl cycle	33.6	%
Total exergy destruction rate of integrated Cu-Cl cycle	6300	W

According to Figure 5.2, the second place for unit thermal energy consumption belongs to the Cu₂OCl₂ decomposition reactor (thermolysis) for maintaining the endothermic reaction at a high temperature of 520°C. Also, a remarkable heat is released from the quench cell because of the solidification phase change process of high temperature CuCl by dropping into the cooling water bath which makes the quench cell as the third place in terms of unit thermal heat. After the CuCl₂ concentrator, thermolysis and quench cell; the hydrolysis, PSDU and dryer are leading in terms of unit thermal energy per mole of produced hydrogen at the integrated Cu-Cl cycle. Furthermore, Figure 5.3 reveals the unit exergy per produced hydrogen at different units of integrated Cu-Cl cycle. As can be

interpreted from both Figure 5.2 and Figure 5.3, thermolysis, hydrolysis, quench cell and CuCl_2 concentrator has the highest unit thermal exergy per mole of produced hydrogen, respectively.

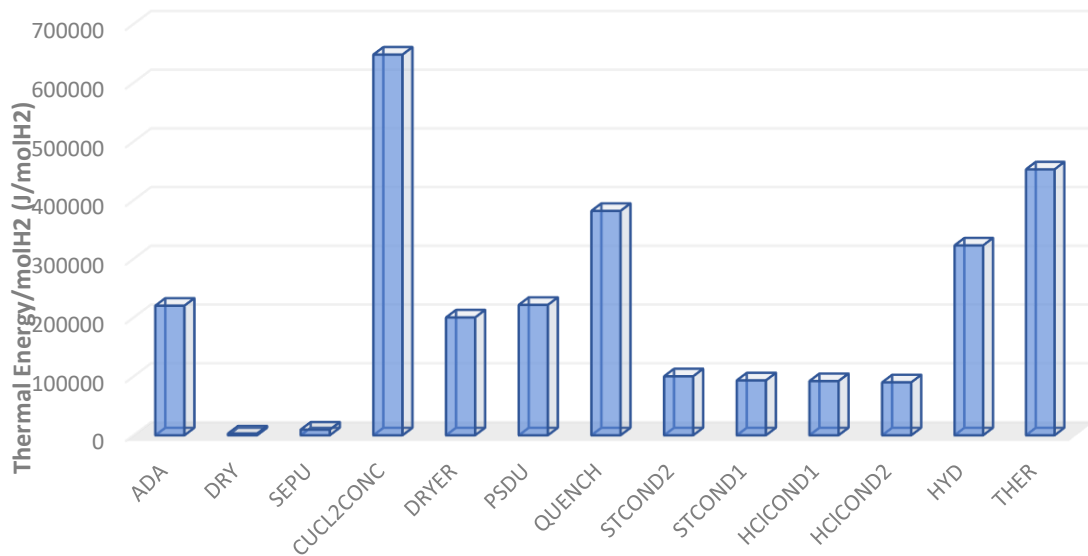


Figure 5.2. Unit thermal energy supplied or released per mole of produced hydrogen at different elements of integrated Cu-Cl cycle

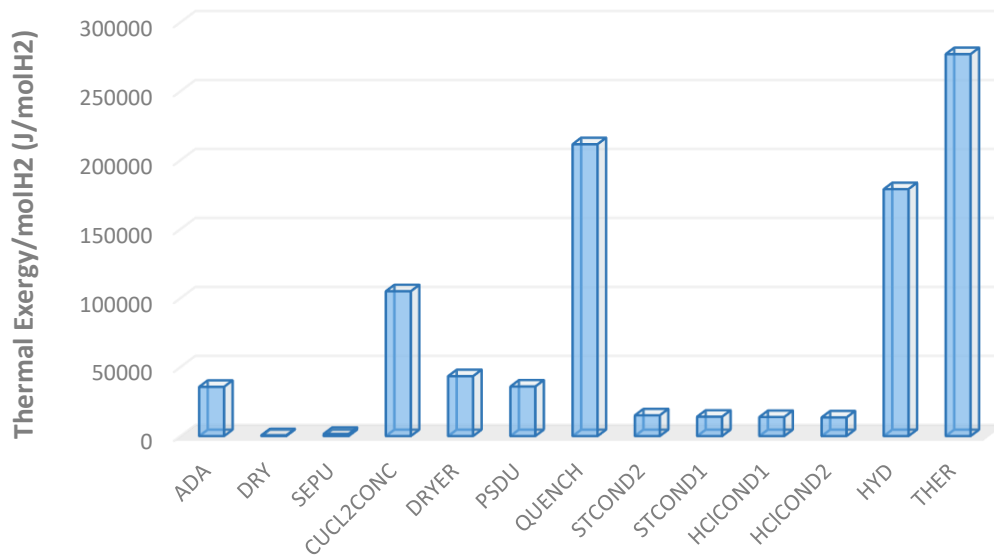


Figure 5.3. Unit exergy rate per mole of produced hydrogen at different integrated Cu-Cl cycle's components

Figure 5.4 represents the exergy efficiency of different elements in the examined Cu-Cl cycle. As can be observed, among the separation modules as ADA, anolyte dryer unit, CuCl₂ concentrator, PSDU and dryer, the separation unit has the lowest exergy efficiency. This is mainly owned to the relatively large water flow rate injected into this unit to accomplish the separation process of CuCl from CuCl₂. While the other separator modules use less equivalent thermal energy for splitting the constituents. Amongst the cooling elements as steam condensers, HCl (aq) condensers and quench cell, since CuCl cools down from 530°C till 420°C and then the phase change solidification process happens at a relatively higher temperature (about 435°C) compared to the steam or HCl (aq) condensation mechanism (temperature below 130°C). So, the higher-quality heat is loosed in the quench cell compared to the steam condensers and HCl (aq) condensers. With respect to Figure 5.4, the exergy efficiency of hydrolysis and thermolysis reactors with their associated pre-heaters are evaluated to be 80.5% and 71.8%, respectively.

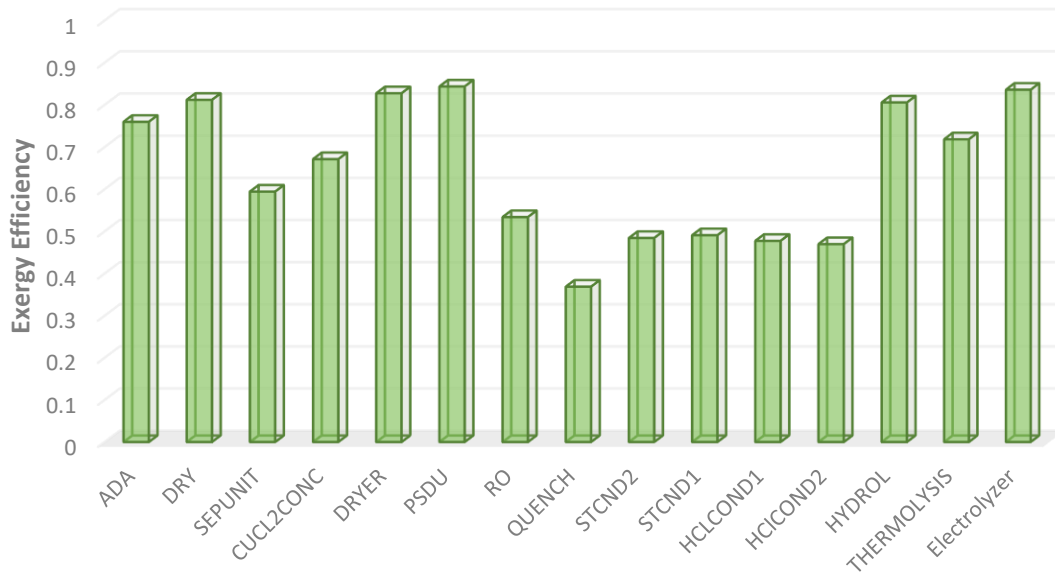


Figure 5.4. Exergy efficiency associated with each of the components of the proposed four-step integrated Cu-Cl cycle

5.2. Sensitivity Analysis Results

The performance of the lab-scale integrated Cu-Cl cycle is evaluated by considering the realistic system operating conditions. In the lab-scale cycle, except for the high pressure

side of the PSDU which operates at a pressure of 4 atm, the rest of the components operate at the atmospheric pressure. The operating temperatures of reactors can be adjusted by a multi-zone controller to achieve the best system performance. In this section, the sensitivity of the system in terms of energy and exergy efficiencies for changing the St/Cu and temperatures of reactors (hydrolysis, thermolysis, PSDU, electrolyzer and anolyte recovery separator units) are presented. The system is simulated in Aspen Plus and EES software by incorporating the kinetics consideration and detailed modeling procedures as provided earlier.

Figure 5.5 shows the effects of the hydrolysis reactor temperature and St/Cu molar ratio on the exergy efficiency of the lab-scale integrated Cu-Cl cycle. The maximum exergy efficiency of the hydrolysis reactor would occur where the excess amount of steam for more conversion of reactants and the operating temperature of CuCl_2 decomposition are most effectively balanced. This leads to create a peak in the exergy efficiency profile as the St/Cu ratio increases thereby reaching the optimal performance condition of the hydrolysis reactor. With the increase of the hydrolysis reaction temperature to 380°C , the copper chloride conversion into cupric chloride increases. With a further increase of reactor temperature (more than 385°C), some portion of CuCl_2 turns into CuCl which is the undesirable product. So the exergy efficiency for the hydrolysis reaction is a maximum at the reactor temperature of 388°C . With the increase of excess steam (increase of St/Cu molar ratio), more conversion of reactants and consequently more copper oxy-decomposition occurs as the desirable product to be obtained.

In Figure 5.5, the maximum reactor performance happens at the steam to copper chloride molar ratio of 20. This indicates that the increase of product yield is not significant enough for a further increase of excess steam (St/Cu ratio more than 20). For the relatively higher reactor operating temperature (above 388°C), the St/Cu ratio of 20 has the higher reactor exergetic performance. With an increase of St/Cu ratio, the maximum exergetic efficiency of the hydrolysis reaction occurs at the lower reactor operating temperature. Neglecting the kinetics consideration may lead to unreliable results because the changes in the amount of product yield are the outcomes of the changes in the reaction kinetic parameters.

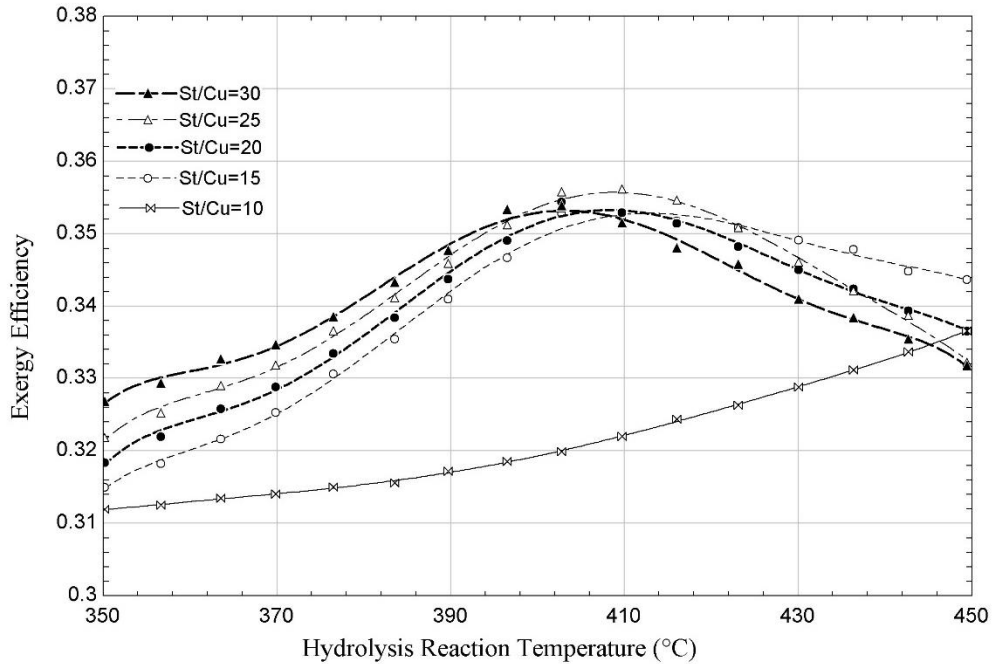


Figure 5.5. Variation of exergy efficiency with the change of hydrolysis reactor temperature at different St/Cu molar ratio

The variations in the exergetic efficiency with the thermolysis reactor temperature and St/Cu molar ratio are depicted in Figure 5.6. Since there is limited information in the literature about the kinetics of the thermolysis reaction, a linear relationship between the temperature and Cu_2OCl_2 decomposition percentage is assumed. With an increase of reactor temperature, more Cu_2OCl_2 decomposes into CuCl and O_2 when neglecting the possible side reactions. According to Figure 5.6, with an increase of reaction rate, both input thermal energy and products increase, thereby indicating a slight increase in the reactor performance with the reaction temperature. Also, the maximum exergy efficiency value corresponds to the St/Cu of 20 due to the higher amount of Cu_2OCl_2 coming from the hydrolysis reactor (at temperature 400°C) and then decomposes at the thermolysis reactor.

Figure 5.7 presents the temperature effects of the low pressure side of PSDU on the exergy efficiency of the Cu-Cl cycle at different St/Cu molar ratios. It can be observed that the total exergy efficiency possesses a maximum value at the distillation unit temperature of 108°C . This occurs since the increase of temperature at the low pressure distillation column generates the superheated steam that cannot be condensed through the partial

condenser. So the operation of the low pressure side more than 108°C will reduce the exergy efficiency for the separation process of HCl from water. At the high pressure side, with an increment of operating temperature, the exergy efficiency increases consistently because of the HCl condensation rather than steam.

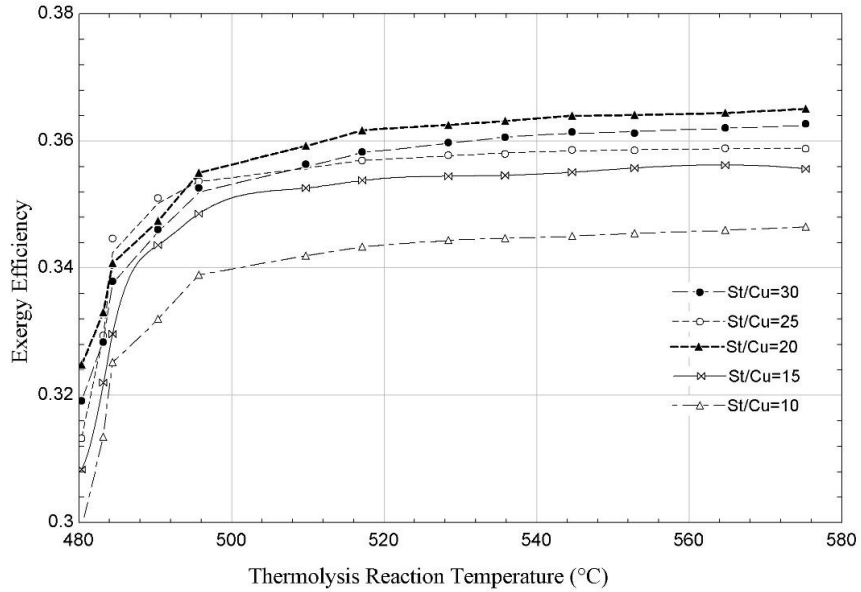


Figure 5.6. Variation of exergy efficiency with the change of thermolysis reactor temperature at different St/Cu molar ratios

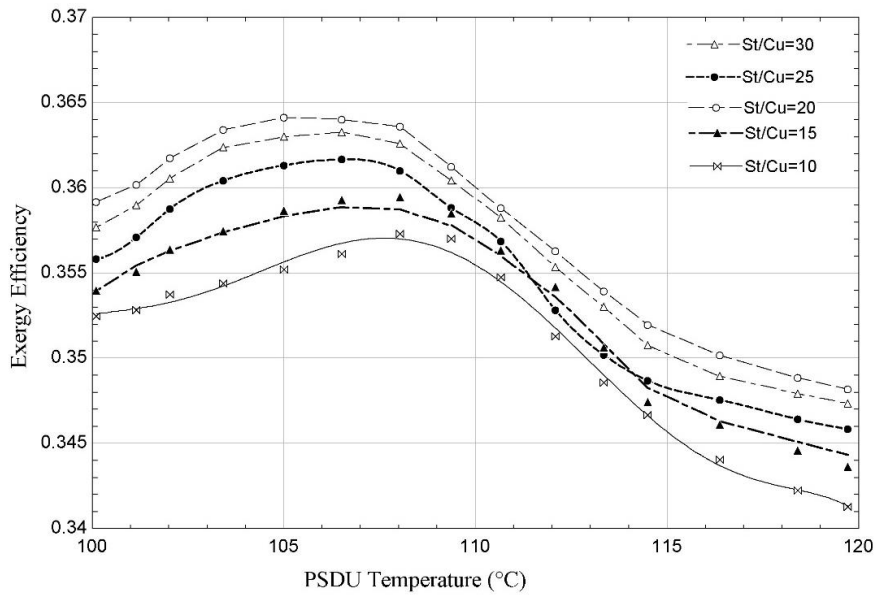


Figure 5.7. Variation of exergy efficiency with changes in the PSDU temperature at different St/Cu molar ratios

Figure 5.8 shows the variations of electrolyzer operating temperature and St/Cu molar ratio of the exergy efficiency of the cycle. It is shown that the increase of anolyte temperature at the electrolyzer leads to significant improvement of the electrochemical parameters resulting in more conversion of Cu^+ to Cu^{++} species and consequently more hydrogen production at the cathode side. So, for a higher electrolyzer temperature (or anolyte temperature), there is higher system performance in terms of exergy efficiency.

The variation of exergy efficiency with the average temperature of the anolyte recovery unit is shown in Figure 5.9. To recycle the oxidized anolyte (consumed anolyte at the electrolyzer), several separators are installed to separate the species (CuCl , CuCl_2 and HCl (aq)) and to recycle them into the cycle. An average temperature of 115°C indicates the optimum temperature in terms of a reasonable compromise between the thermal energy used for separation and product concentration and consequently the higher exergy efficiency.

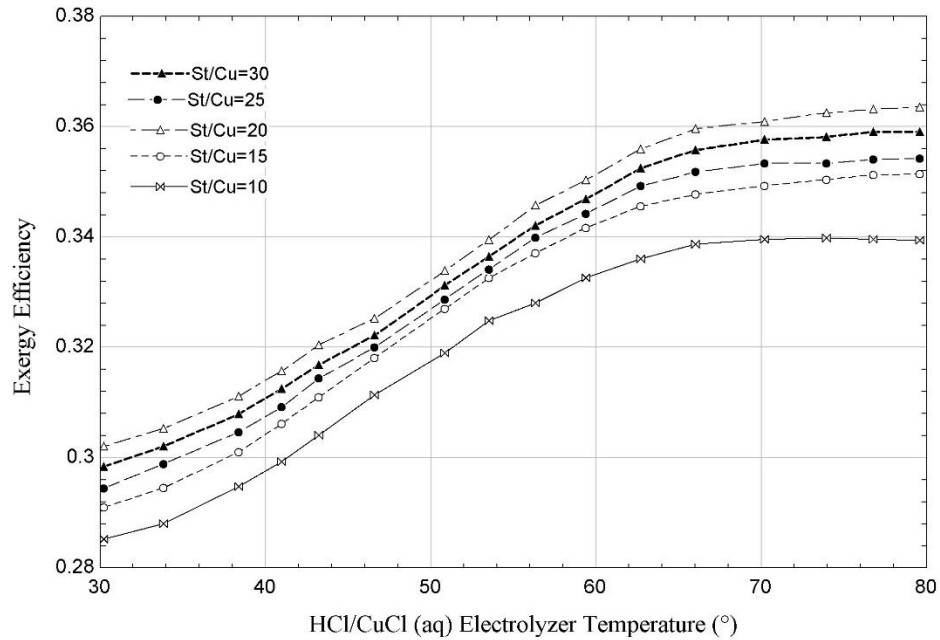


Figure 5.8. Variation of exergy efficiency with changes in the CuCl/HCl (aq) electrolyzer stack temperature at different St/Cu molar ratios

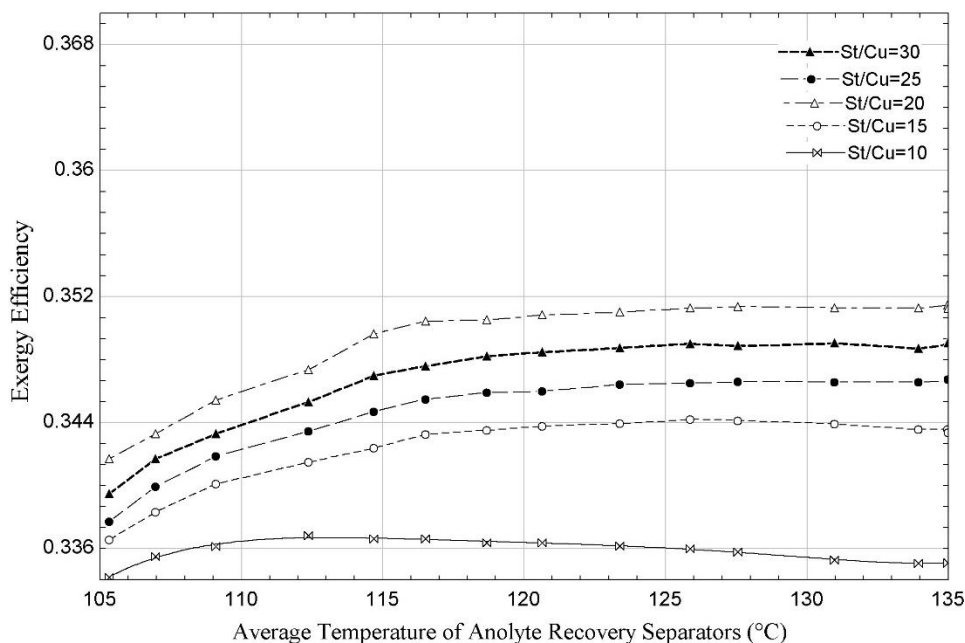
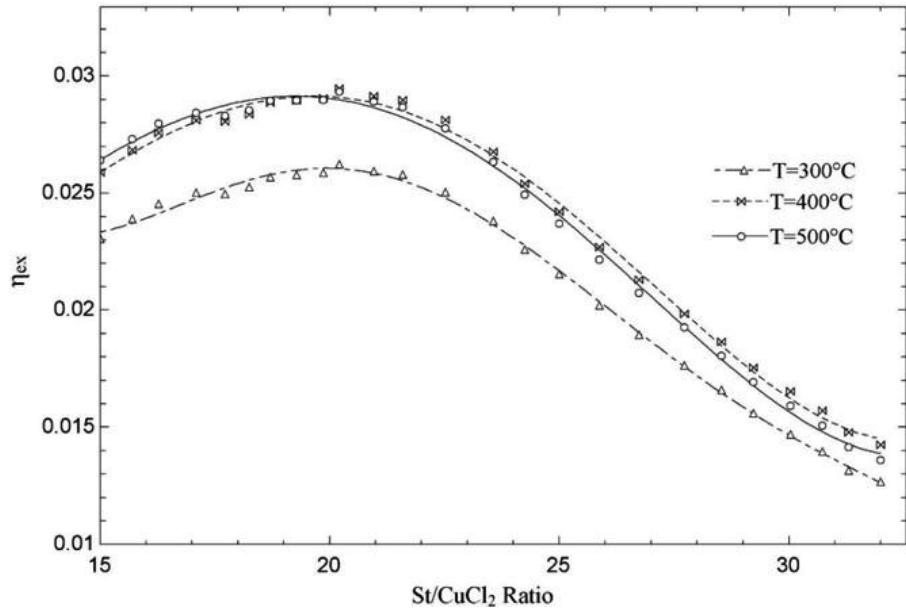


Figure 5.9. Variation of exergy efficiency with changes in the average temperature of the anolyte recovery separators unit at different St/Cu molar ratios

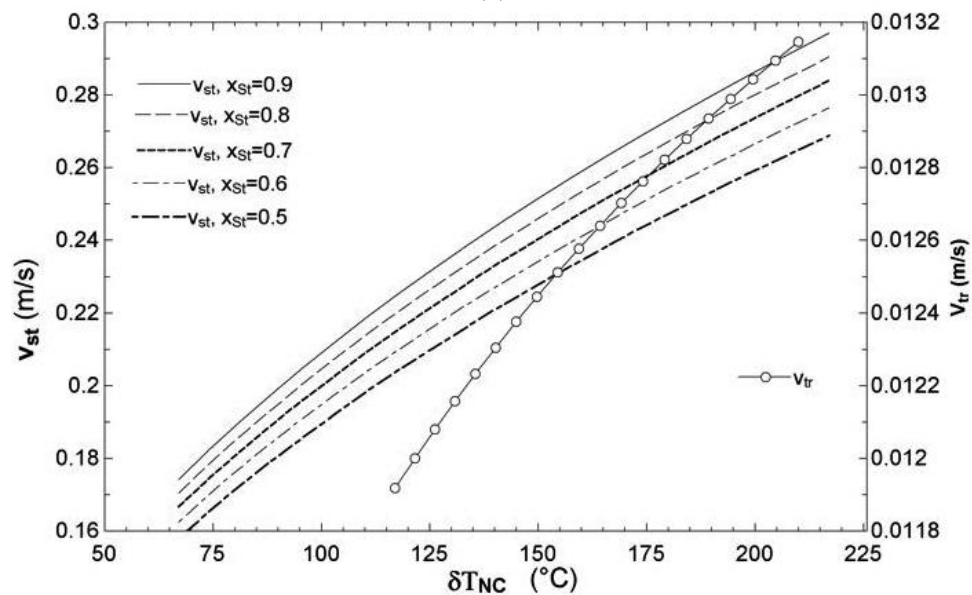
5.3. Hydrolysis Reaction Results

In this section, results will be presented for the new cupric chloride hydrolysis reactor. When introducing excess steam, unreacted CuCl_2 and side reactions are the main contributors to the relatively low exergy efficiency (2.8% shown in Figure 5.10(a)) compared to the stoichiometric ideal condition where the typical exergy efficiency is about 75%. This large difference indicates the importance of analyzing real reaction conditions to provide a more reliable insight when identifying the sources of exergy losses. It can be concluded from Figure 5.10(a) that for the lower amount of excess steam (between 15 and 20) into the reactor, the decomposition of CuCl_2 needs to occur at relatively higher operating temperatures (around 500°C). In other words, when there is more excess steam introduced into the reactor, there is a lower operating temperature needed to achieve the highest exergy efficiency of the reaction.

Also, the reactor behavior is investigated based on hydrodynamic modeling of the natural convection process to predict reactant's residency time. The performance of reactor is examined under the assumption of a limiting kinetic model as shrinking core model.



(a)



(b)

Figure 5.10(a). Exergy efficiency variation with changes in the steam to copper chloride molar ratio at different hydrolysis reaction temperatures, (b) Effect of the temperature gradient between the hot and cold sides of the hydrolysis reactor at different steam concentration ratios.

This model is used for the prediction of the cupric chloride conversion into the products. It is assumed that during the endothermic chemical reaction, there is no decomposition of cupric chloride particles and no reaction of steam with chlorine in the bulk phase. Engineering Equation Solver has been employed to implement the hydrodynamic and

kinetic models of the hydrolysis unit configuration. The required thermodynamic data for the chemical species were taken from the Aspen Plus database and past literature [136, 138 and 156].

Figure 5.10(b) illustrates the influence of temperature gradients between the hot and cold sides on the steam velocity circulating through the loop of the hydrolysis reactor at various vapor fractions of steam in the gaseous mixture ($x_{st}=N_{H_2O}/N_{Total}$). For an average particle size of 200 μ m and aqueous cupric chloride volume flow rate of 200 ml.s⁻¹, a higher temperature difference between the hot and cold sides yields more thermally-driven forces from the natural convection. This results in a higher steam velocity and consequently larger terminal velocity. As mentioned earlier, the effective diffusivity of the gas into a solid is determined based on the experimental data and it increases with temperature and gas velocity. The higher steam velocity leads to more effective diffusion of the steam-gas phase into the cupric chloride reactant particles leading to more conversion of cupric chloride solid particles. Meanwhile, from Figure 5.10(b) with the increase of the steam fraction in the gaseous mixture results in an increase in the pressure difference between two sides of the reactor which leads to a steam velocity increment at the relatively higher steam concentration.

Figure 5.11 shows the effects of cupric chloride particle size on the particle terminal velocity at different hydrolysis reaction temperatures. By enlarging the cupric chloride diameter and the hydrolysis temperature, the drag coefficient and upward drag force decreases and increases respectively, resulting in a higher solid terminal velocity. For a specific furnace length, a larger particle terminal velocity yields less residence time of the reactants in the hydrolysis reactor for preheating and the chemical reaction process.

Figure 5.12 shows the variation of terminal velocity with the volume flow rate of cupric chloride in an aqueous form. In the Cu-Cl cycle dryer unit, the water is extracted from the cupric chloride aqueous mixture (CuCl₂ (aq)) and then the CuCl₂ solid particles and steam are heated to the hydrolysis reaction temperature. The CuCl₂ (aq) volume flow rate depends on the particle size and initial velocity of the reactants. With an increase of the CuCl₂ (aq) volume flow rate, the cupric chloride initial velocity increases significantly, leading to a higher drag force and consequently a higher terminal velocity of the particle. In addition,

the change of hydrolysis hot side temperature results in a lower steam density and consequently more effects of gravity and buoyancy forces (equal to the drag force) leading to a higher solid terminal velocity. Again, a higher terminal velocity indicates a lower reactant residence time for the hydrolysis reaction.

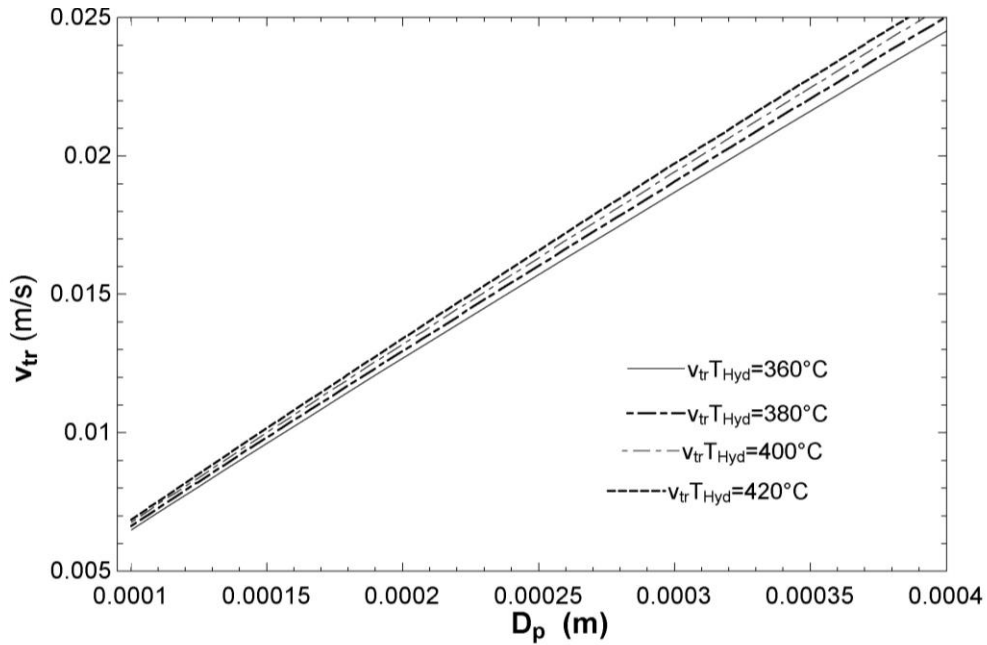


Figure 5.11. Effects of particle size on the terminal velocity of solid particles at different hydrolysis reaction temperatures

Figure 5.13 shows the variation of cupric chloride solid conversion with time as required for complete conversion at different particle sizes for a diffusion-controlled process. From Figure 5.13, a complete conversion of solids for the smaller particles is achieved at the smaller conversion time for the diffusion controlled reaction. Less than one second of time is needed for the complete conversion of cupric chloride particles, indicating an instant conversion of cupric chloride into copper-oxy-chloride without unreacted solid accumulation. On the other hand, the reactant residence time estimated from the terminal velocity (around 91 seconds in Figure 5.11 and Figure 5.12) demonstrates enough time for cupric chloride and steam to be preheated until the hydrolysis reaction is converted into copper-oxy-chloride. Moreover, Figure 5.14 shows the variation of particle conversion with time for different solid diameters for chemical reaction control. Like the diffusion control, the complete conversion of cupric chloride solid particles for the chemical reaction

control occurs over a shorter time for the smaller solid particles. From Figure 5.13 and Figure 5.14 at a larger particle size, the diffusion control time dominates over the chemical reaction control time.

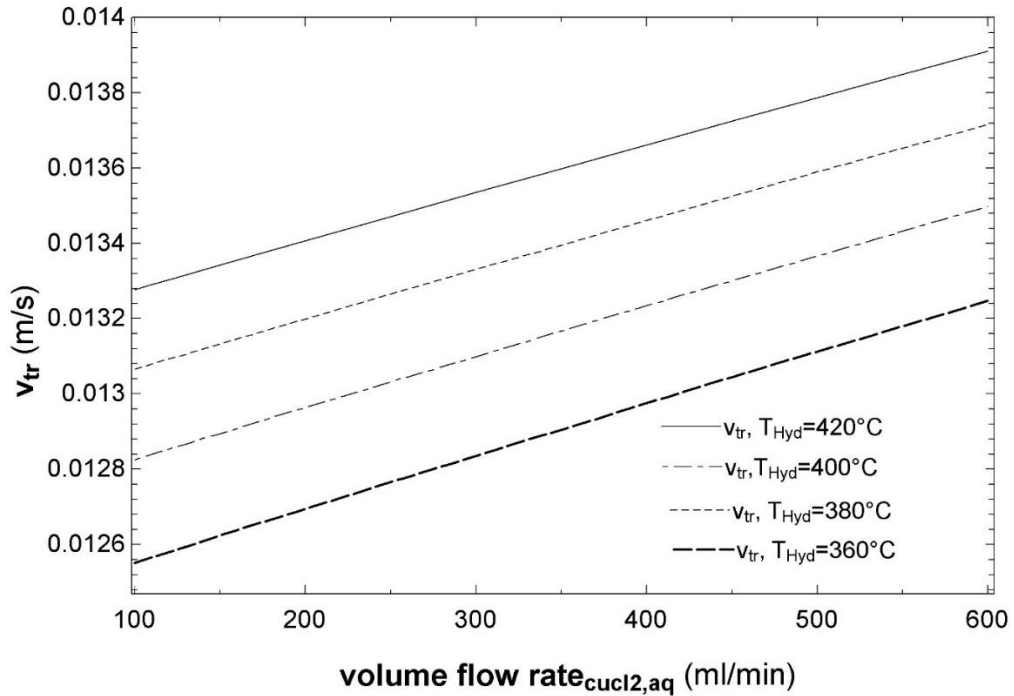


Figure 5.12. Variation of terminal velocity with cupric chloride (aqueous) volumetric flow rate at different hydrolysis temperatures

Figure 5.15(a) and (b) show the variation of cupric chloride particle conversion ratio with time at different hydrolysis temperatures for the diffusion and chemical reaction controlled processes, respectively. With an increase in the hydrolysis temperature, the steam-gaseous phase transport into the cupric chloride solid is augmented which results in a faster rate of solid conversion at the higher temperature levels. From Figure 5.15 (a) and (b) the chemical reaction control time for the complete conversion of solid is smaller than the diffusion control conversion time at different hydrolysis reaction temperatures.

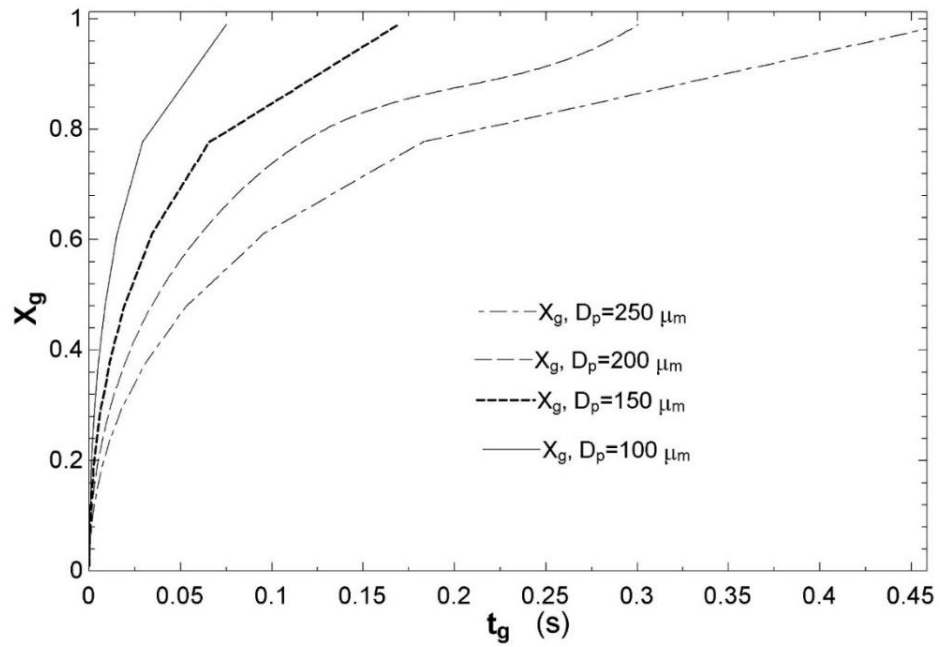


Figure 5.13. Variation of solid conversion with time at different particle sizes for diffusion control

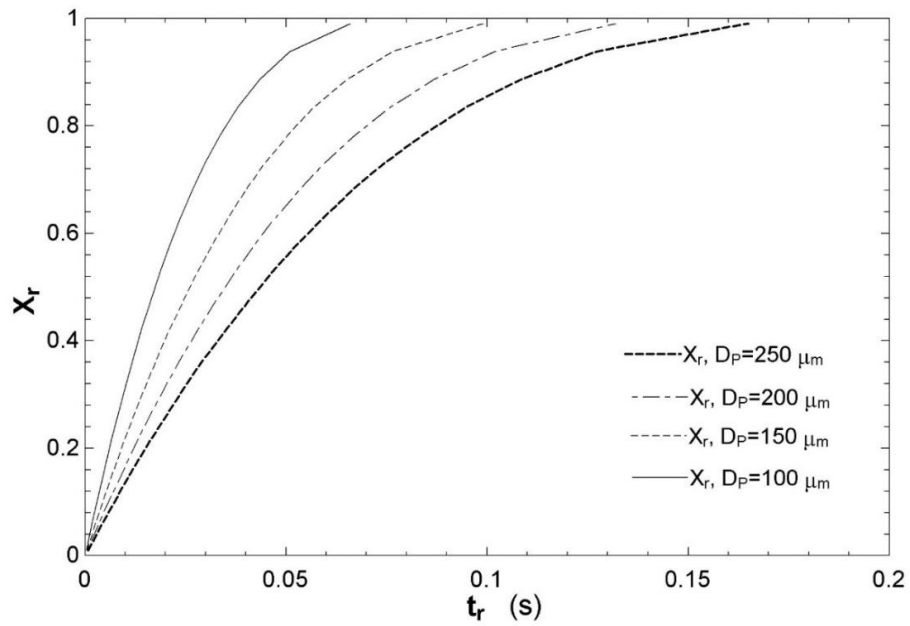
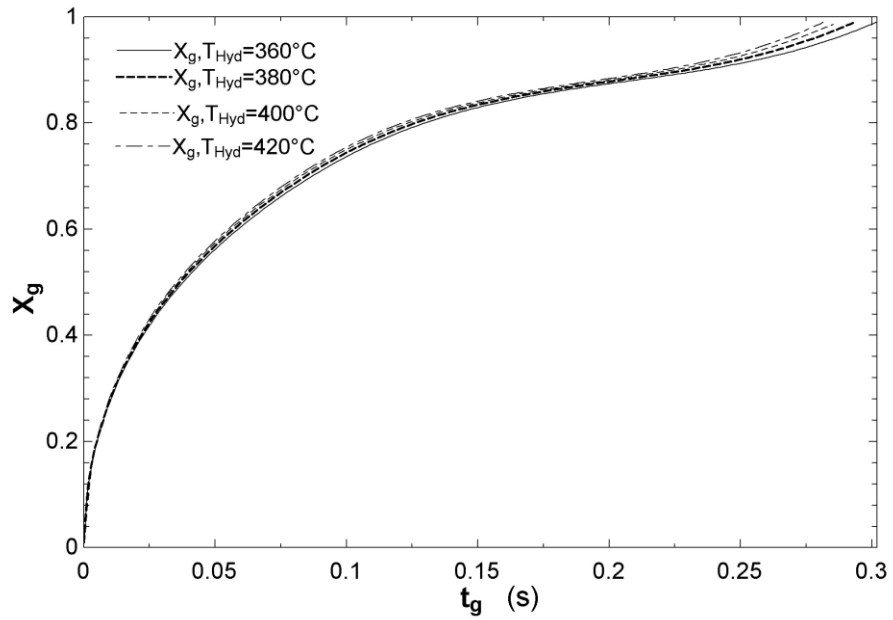
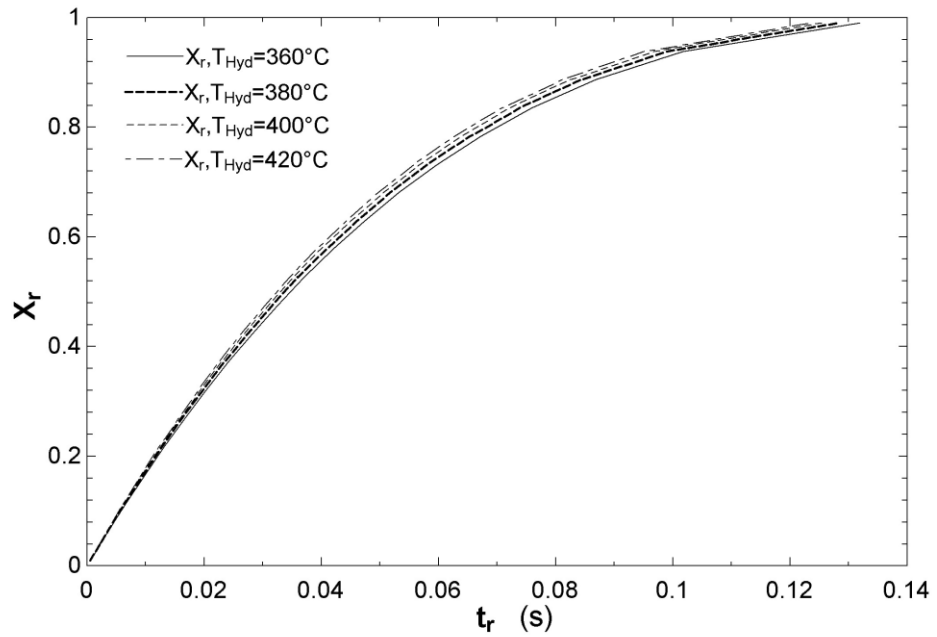


Figure 5.14. Variation of solid conversion with time at different particle sizes in the kinetic control reaction



(a)



(b)

Figure 5.15(a). Variation of solid conversion with time at different hydrolysis temperatures in the diffusion control reaction, (b). Variation of solid conversion with time at different hydrolysis temperatures in the kinetic control reaction

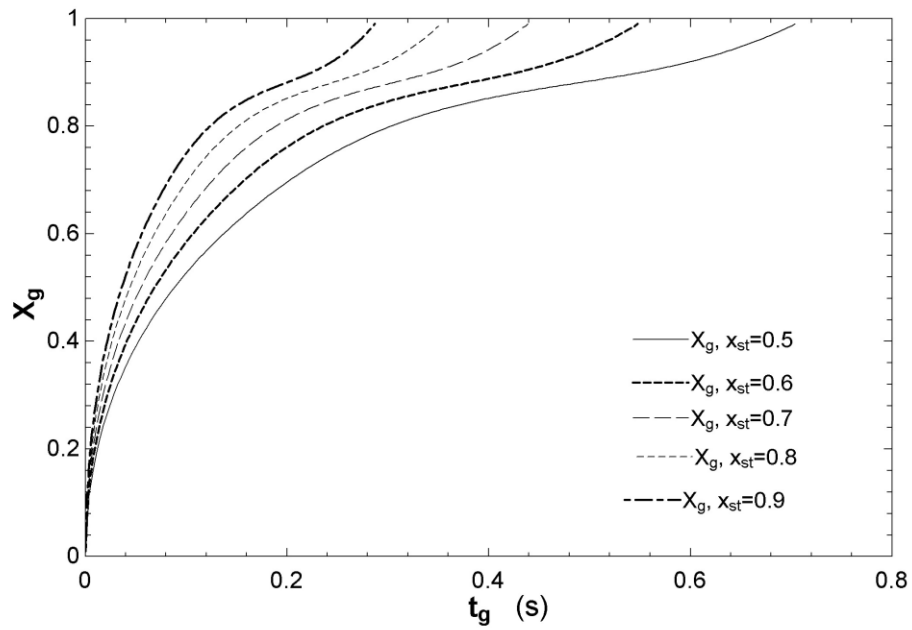


Figure 5.16. Variation of solid conversion with time at different steam/solid fractions in the diffusion-controlled reaction

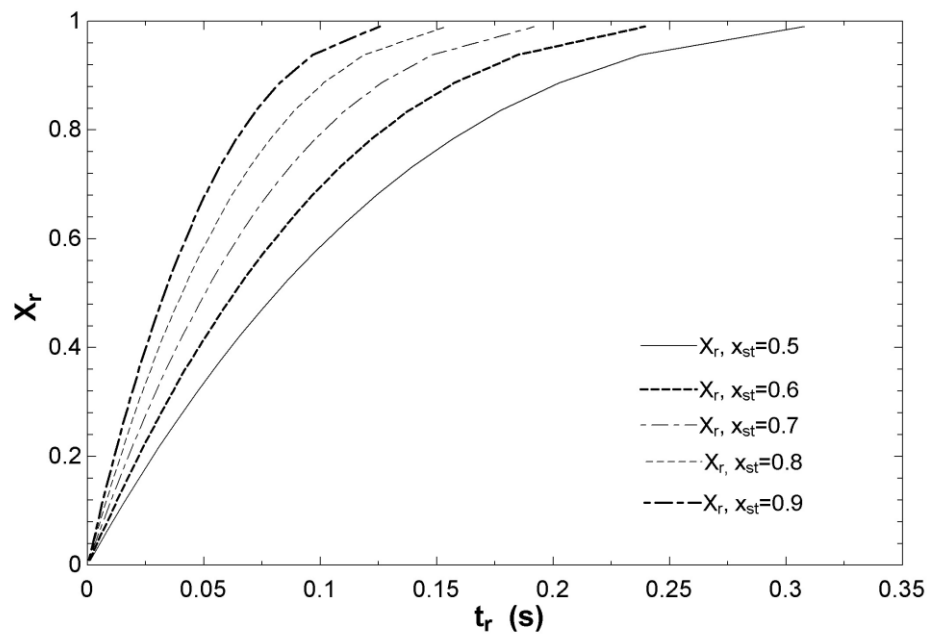


Figure 5.17. Variation of solid conversion with time at different steam/solid fractions in the kinetic controlled reaction

The variation of cupric chloride solid conversion with time at different steam molar fractions for diffusion and chemical reaction controlled processes are illustrated in Figure 5.16 and Figure 5.17, respectively. The solid particle conversion time increases by the steam/solid ratio increment as the steam molarity increases. This demonstrates that lower pressure facilitates the conversion of cupric chloride solid particles into copper-oxy-chloride and hydrochloric gas. Furthermore, the time needed for the complete conversion of cupric chloride solid particles in the diffusion control is dominant over the chemical reaction control at diverse steam/solid ratios.

5.4. CuCl/HCl (aq) Electrolyzer Unit Results

Table 5.5 shows the GEM results for the speciation model of the anolyte in the CuCl/HCl(aq) electrolyzer at the standard temperature and pressure conditions. Moreover, Table 5.6 demonstrates how the thermodynamic properties vary through the cathode and anode-half reactions. From Table 5.5, since $CuCl_3^{2-}$ is significantly higher than Cu^+ , as a result, it is expected that this ion will be the dominating redox contributor on the anode (oxidation of $CuCl_3^{2-}$ into $CuCl_3^-$). This is consistent with what was also found previously. At higher conversions when more potential is applied, the conversion degree lead to the increase of Cu^{++} species concentration, especially $CuCl_3^-$. The effects of non-equilibrium contributions of the overpotential at the anode side at different conversions of CuCl into $CuCl_2$ and corresponding open circuit potentials (E_{OCP}) are shown in Figure 5.18.

The positive overpotential increases with a change of current density under the same initial conditions. With an increase in the conversion extent of CuCl into $CuCl_2$ from 0 to 0.5, the open circuit decomposition potential for a single cell increases. As expected, the total decomposition potential for the electrochemical reaction increases with an increase in the conversion extent of CuCl. However, with an increase of E_{OCP} , a portion of this additional voltage decreases with a reduction of the anodic non-equilibrium overpotential (η_{anode}). Since a negative overpotential does not change with the CuCl to $CuCl_2$ conversion extent, it will be identical for all current densities. As the relations for η_- and E_{IR} are independent of variations in the concentrations of CuCl(aq) and $CuCl_2$ (aq), they are identical for all values of ξ_{CuCl} which are neglected in the comparison.

Table 5.5 . Equilibrium concentrations (mol/l) of anolyte speciation from GEM at standard temperature and pressure conditions (2M CuCl and 10M HCl(aq)) as verified by [91], [92]

ξ_{CuCl}	0%	1%	5%
Species			
CuCl_3^{2-}	1.99	1.98	1.87
Cu^+	5.58×10^{-14}	5.54×10^{-14}	5.58×10^{-14}
CuCl_4^{2-}	1.162×10^{-7}	8.813×10^{-3}	7.02×10^{-2}
CuCl_3^-	1.46×10^{-8}	1.125×10^{-3}	9.01×10^{-3}
CuCl_2^0	4.71×10^{-10}	4.66×10^{-10}	3.14×10^{-4}
H^+	9.99	9.98	9.92
Cl^-	6.0	5.98	5.92
HCl^0	2.37×10^{-4}	2.31×10^{-4}	2.32×10^{-4}
Cu^{++}	2.31×10^{-12}	1.58×10^{-7}	1.31×10^{-6}

Table 5.6 . Variations in thermodynamic properties through the cathode and anode half-reactions for anode conversion degrees of 5% at the standard state (temperature of 25 °C, pressure of 1 atm and concentration of 1 M) as verified by [39][91, 92]

Thermodynamic properties	Anode half-reaction I	Anode half-reaction II	Anode half-reaction III	HER (hydrogen evolution reaction)
$\overline{\Delta g}^0$ (J/mol)	15582.8	55799.7	68926.2	0.000
$\overline{\Delta h}^0$ (J/mol)	-5989.7	2889.1	-21185.2	-11327
$\overline{\Delta s}^0$ (J/mol.K)	-137.69	-243.6	-366.9	0.000
$\overline{\Delta g}$ (J/mol)	50033.6	50251.3	50201.9	0.000
$\overline{\Delta h}$ (J/mol)	19079.3	10336.9	10366.5	65.27
$\overline{\Delta s}$ (J/mol.K)	7.532	-134.6	-131.03	37.9

Figure 5.19 (a) depicts the pressure contours at the MEAs of the stack. Since the CuCl/HCl(aq) electrolyzer is fed by the liquid phase anolyte and catholyte and the only gaseous-phase component is the produced hydrogen, the pressure loss across the stack is relatively small. Consequently, the anolyte and catholyte are expected to spread evenly throughout the stack. Figure 5.19 (b) illustrates the flow velocity at each channel of the bipolar module for series-connected cells inside the electrolyzer stack. The flow distribution profile among the MEAs in the stack is relatively uniform. In each bipolar plate, the flow velocity differs at each channel because of the nature of the fluid motion whereby more fluid flows with a straighter pathway.

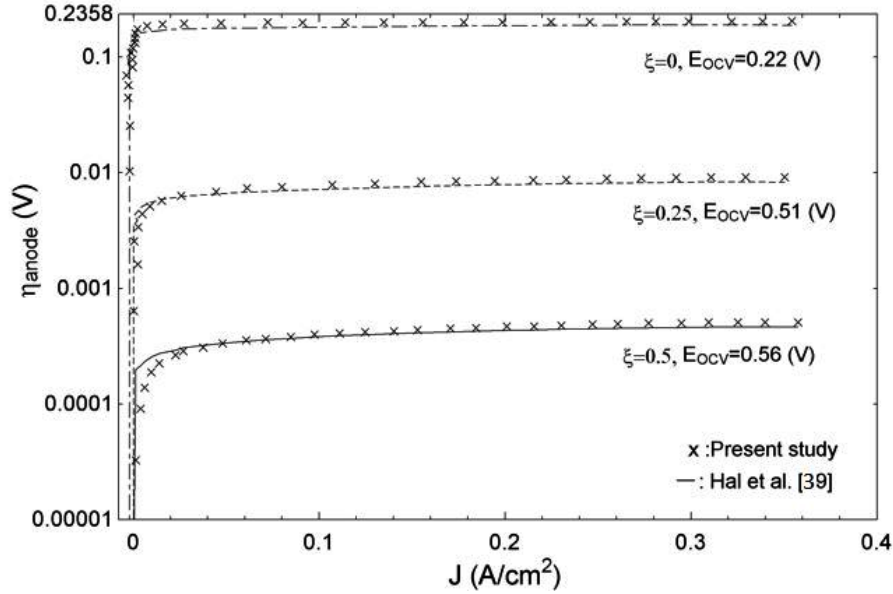
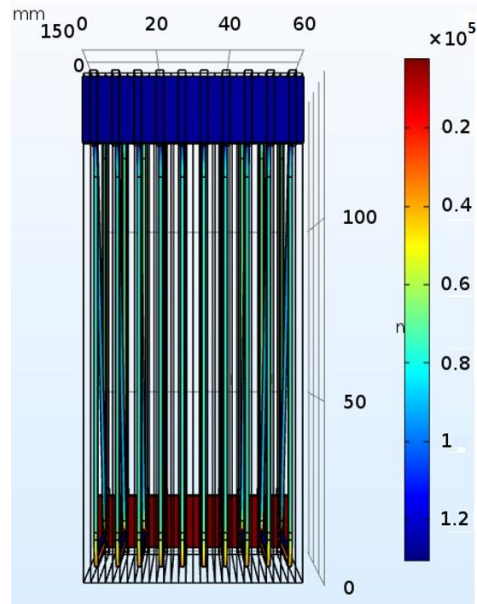
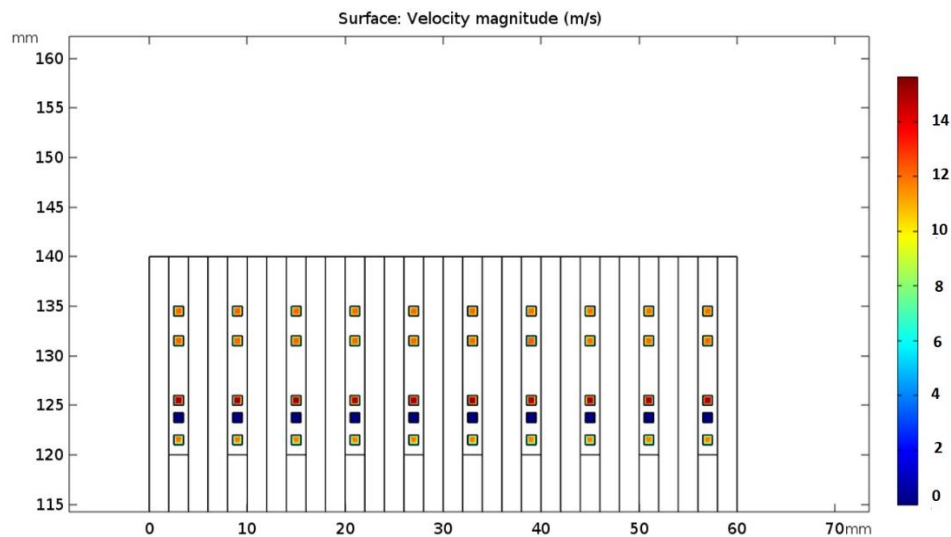


Figure 5.18 . Predicted η_{anode} at a given j_{cell} for $\xi_{CuCl} = 0.0, 0.25$ and 0.5 (compared to Hall et. al. [39])

Figure 5.20 shows the flow distribution among the cells in the electrolyzer stack at 25°C and 1atm. As the stack manifold configuration is a Z-type and the anode and cathode inlet ports are placed at two sides of the stack, the anolyte input port is close to the first unit cell and the catholyte feed port is near the last unit cell. Both anodic and cathodic flow distributions have a tendency to favor the cells that are nearer to the anolyte and catholyte inlet ports, due to the shorter distance of travel. On the other hand, the anolyte flow distribution tends to shift toward the right side. The reduction in the static pressure across the header leads to an increment of pressure drop along with the unit cells. Since the pressure drop is not significant in the copper (II) chloride electrolyzer as the only gaseous-phase component is the produced hydrogen, the Bernoulli effect has less influence on the anodic flow distribution. Thus, the net effect of these two competing effects (shorter distance and the Bernoulli effect), is less anolyte flow at further cells from the anolyte inlet port. From Figure 5.20, the anodic flow distribution exhibits more change compared to the cathodic side because of the reactant species flow rates, anolyte solution properties, and the speciation phenomena. As shown in Figure 5.20, unit cell number 5 receives the minimum electrolyte mass flow rate.



(a)



(b)

Figure 5.19 (a) Pressure distribution profile (Pa) in the MEA modules and (b) flow velocity (m/s) in the bipolar plate channels with identical cross-sectional areas along 10 MEAs series-connected.

The voltage spread along with the unit cells of the CuCl/HCl(aq) electrolyzer stack at different operating temperatures are depicted in Figure 5.21. At a typical temperature of 45°C, the average stack potential (straight line with “x” symbols) is less than the voltage of individual cells which are close to the anolyte/ catholyte feed port, while more than those

which are placed at the middle of the stack. The cell-to-cell potential variation is a result of the non-uniform anolyte/catholyte flow distribution along with the electrolyzer stack. The low cell-to-cell voltage variation and uniform performance are desirable to achieve the maximum stack performance. The majority of the cells inside the electrolyzer stack have a potential less than a single unit cell operating independently, resulting in a higher voltage for the single-cell compared to the average stack potential.

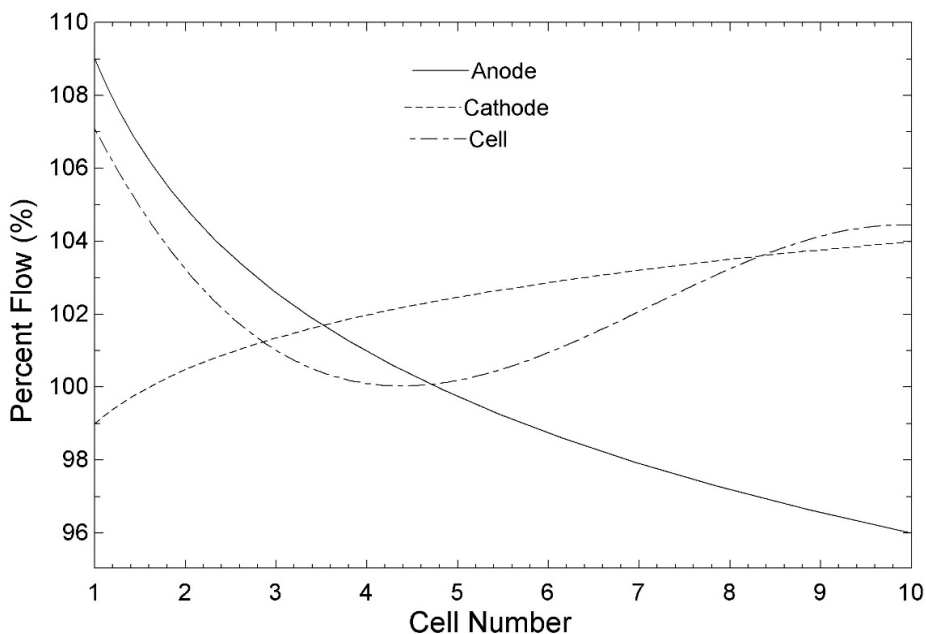


Figure 5.20. Flow distribution percentage at the anodic side, cathodic side and overall cell in the CuCl/HCl(aq) electrolyzer stack at 25°C, conversion extent of 5% and current density of 0.5A/m²

The variation of the anode/cathode flow distribution has a relatively small effect on the ohmic region and kinetic parameters of the polarization curve. From Figure 5.21, with an increase of the electrolyzer stack temperature, a decrease in the charge transfer resistance and ohmic resistance yield an improvement in the kinetic parameters and less required potential at the higher system operating temperature. In Figure 5.21, by raising the stack temperature from 25 °C to 45 °C and 65 °C, the average stack voltage increases from 0.6 V, 0.585 V and 0.545 V, respectively.

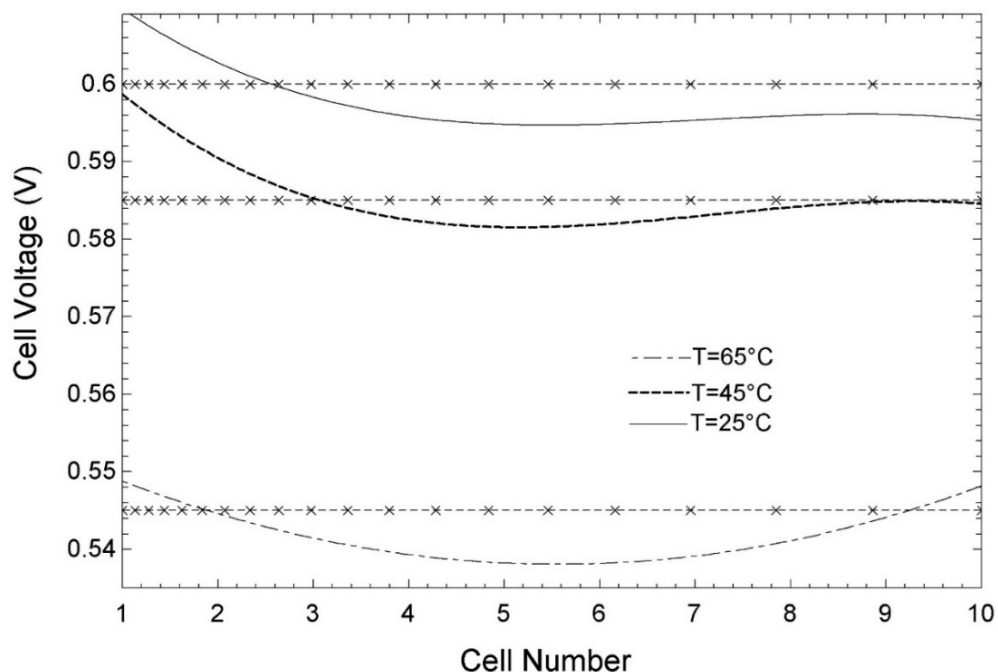


Figure 5.21. Cell-to cell voltage distribution and average stack voltage at different electrolyzer operating temperatures at a conversion extent of 5% and the current density of $0.5\text{A}/\text{m}^2$.

The non-uniform anolyte flow distribution through the cells in the electrolyzer stack leads to cell-to-cell variations of efficiency as shown in Figure 5.22. As described earlier, the performance ratio reveals how the non-uniform mass spread among the cells affects the voltage distribution at the electrolyzer stack and consequently influences the produced hydrogen rate. From Figure 5.22 at a stack operating temperature of $25\text{ }^\circ\text{C}$, 2 M CuCl , and 10 M HCl , for the cell-to-cell performance ratio, the cells which are close to the feed port receive more anolyte compared to those farther from the anolyte inlet port. The increase of consumed anolyte is less than the amount of anolyte feed added to the closer cells. The anode stoichiometry (ratio between the amount of anolyte or catholyte supplied into the stack to the amount which is consumed at the electrolyzer) decreases through the electrolyzer stack moving from the first cell to the last cell. In Figure 5.22, the stack performance ratio of the $\text{CuCl}/\text{HCl}(\text{aq})$ electrolyzer stack is approximately 0.052.

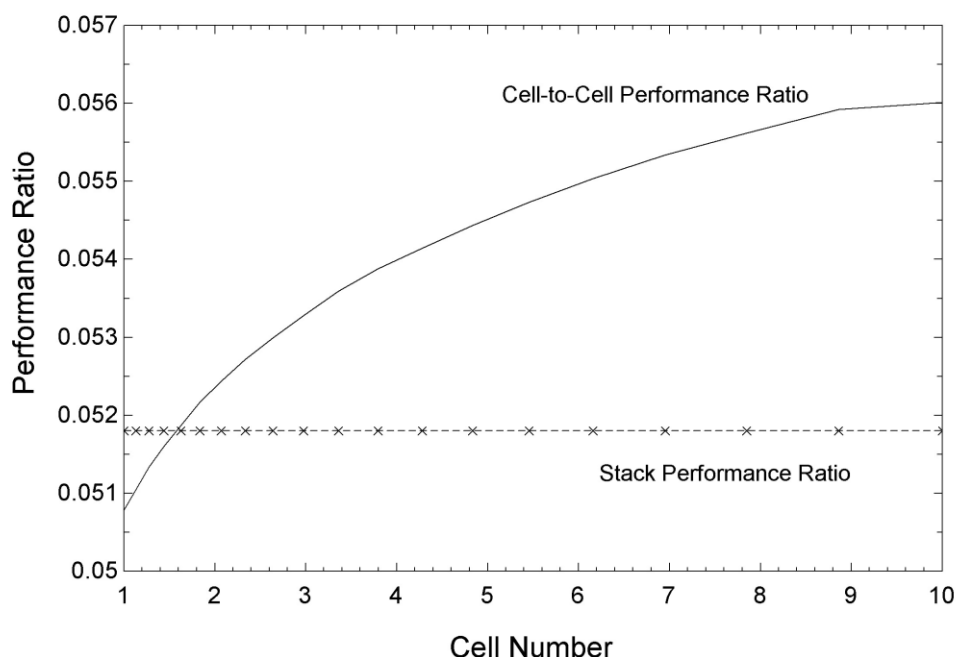


Figure 5.22. Stack and cell-to-cell performance ratio at the initial design operating condition of the CuCl/HCl(aq) electrolyzer unit.

The electrochemical reaction is more affected by the temperature rather than the operating pressure. The polarization curves for the CuCl/ HCl(aq) electrolyzer for a single cell and stack at different operating temperatures are shown in Figure 5.23 and Figure 5.24, respectively. Since the average cell potential in the electrolyzer stack is less than the potential of the single cell, the corresponding average stack potential is smaller than N cells operating independently. In the CuCl/ HCl(aq) electrolyzer stack, the main sources of losses are attributed to the activation overpotential (comprising charge and mass transfer) and ohmic overpotential. However, the magnitude of ohmic overpotential is 10^3 times smaller than the activation overpotential.

In Figure 5.23 and Figure 5.24 at an average stack pressure of 1 bar, with an increase of stack operating temperature, the exchange current density of the anode half-reaction for each unit cell increases significantly, resulting in a decrease at the activation overpotential for each cell and consequently the entire stack. Furthermore, due to the increase in the ionic conductivity, specifically proton species in the CuCl/ HCl(aq) electrolyzer cells, the loss associated with the ohmic overpotential decreases. It can be observed from Figure 5.24 that the best electrolyzer stack performance at high current densities occurs at 65 °C. With a

typical stack current density of 0.5 A/cm^2 and increment of stack temperature from $25 \text{ }^\circ\text{C}$ to $65 \text{ }^\circ\text{C}$, the stack voltage declines from 6.17 V to 5.8 V . From Figure 5.24, the hydrogen production rate from the $\text{CuCl}/\text{HCl}(\text{aq})$ electrolyzer stack at the current density of 0.8 A/cm^2 reaches 165.8 ml/min .

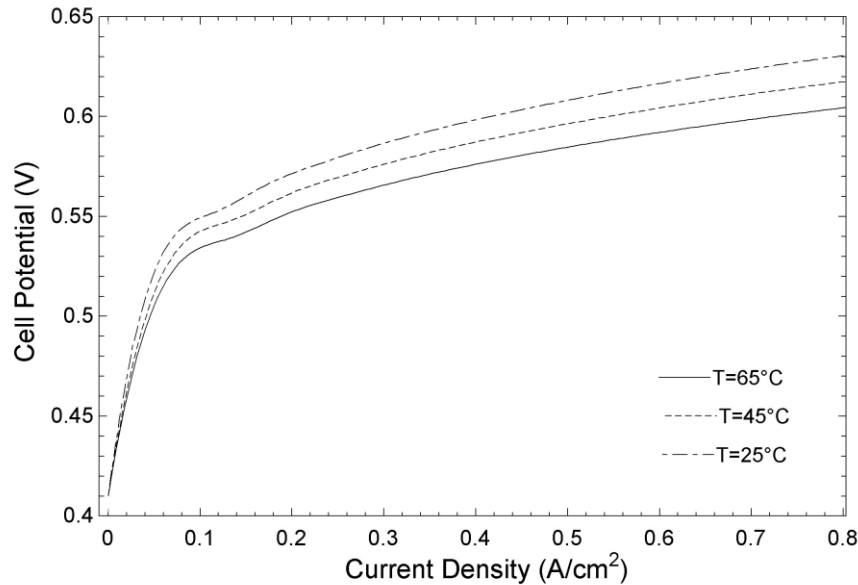


Figure 5.23. Polarization curve for CuCl electrolysis at different operating temperatures for a conversion extent of 5% (2M CuCl and $10\text{M HCl}(\text{aq})$)

As mentioned earlier, in the Cu-Cl electrolyzer stack, additional power is needed for the system to overcome the ohmic, mass transfer and charge transfer resistances as work lost through irreversibilities. The voltage efficiency is often used to evaluate the unit cell performance. The average stack efficiency at different operating conditions like the current density can be obtained from the overpotential curve of the corresponding cell/stack. Figure 5.25 illustrates the voltage efficiency profile of the unit cell and the entire stack for various electrolyzer operating temperatures at a current density of 0.5 A/cm^2 . From Figure 5.25, the cells close to the input anolyte or catholyte port have a higher voltage efficiency than the average stack voltage efficiency, while for the cells in the middle of the stack, less voltage efficiency can be observed. Furthermore, as shown in Figure 5.23 and Figure 5.24, by increasing the stack temperature, the activation and ohmic overpotentials decrease, thereby leading to an improvement of stack voltage efficiency.

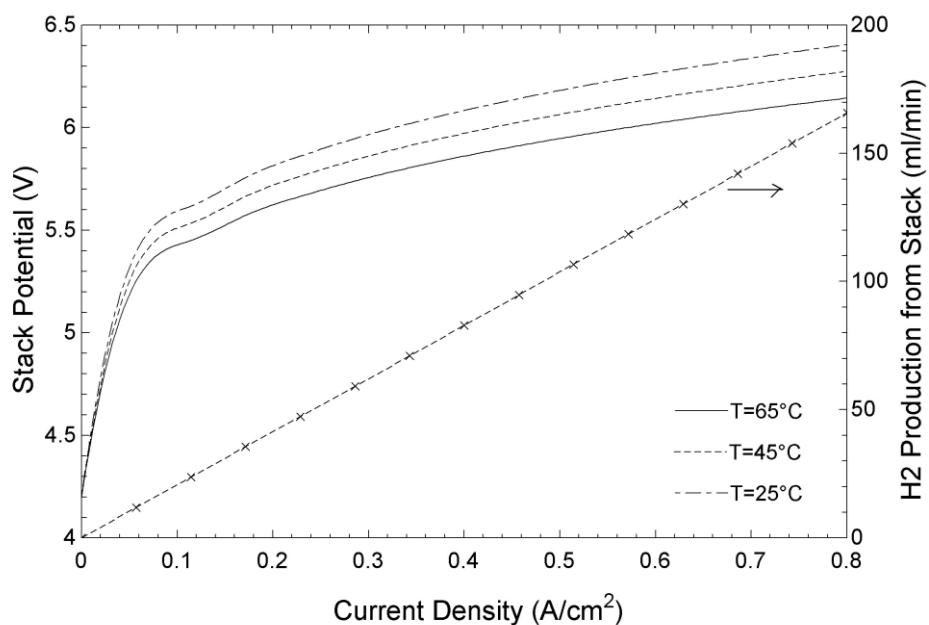


Figure 5.24. Polarization curve for CuCl/HCl(aq) electrolyzer stack at different operating temperatures and variations of hydrogen production rate as a function of current density.

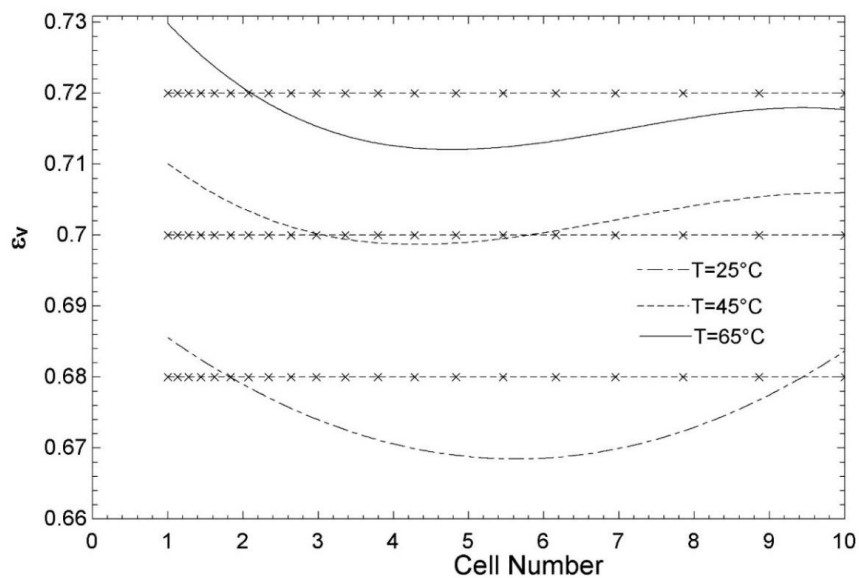


Figure 5.25 .Voltage efficiency of cells and stack (x) at different electrolyzer operating temperatures at conversion extent of 5% and current density of $0.5\text{A}/\text{cm}^2$.

5.5. Pressure Swing Distillation Unit Results

In this section the thermodynamic, heat and mass transfer analysis results are presented and discussed in detail. The results of heat and mass transfer studies are compared together for estimation of packing column height.

5.5.1. Thermodynamic Results of PSDU

To analyze the proposed PSD system, Aspen Plus and EES software have been used in this investigation to predict all thermodynamic and thermal properties of the working fluids. Because of the complex thermodynamic behavior of the HCl-water azeotropic binary mixture, the UNIQRK equation property package and material data has been applied. After modifying the binary coefficients, this package is the only model supported in Aspen Plus which can show azeotropes. However, this model cannot predict the entire HCl (aq) solely and it has limitations to plot phase diagrams of HCl (aq).

A thermodynamic model/models is needed to calculate the binary coefficient and predict the thermodynamic, phase equilibria and calorimetric properties over a wide temperature range (up to 400°C) for the HCl-water binary mixture and over the entire HCl concentration [176]. Therefore, an eNRTL electrolyte model has also been applied to predict the partial pressure of the aqueous solution, K-value, HCl dissociation solution, vapor and liquid enthalpy calculations in trays, and calorimetric properties, with a good agreement with those in the experiment [176]. The azeotropic binary mixture of HCl (aq) thermophysical properties model and correlations used in the Aspen Plus simulation are listed in Table 5.7.

The thermodynamic properties and heat transfer characteristics extracted from the Aspen Plus simulation are tabulated in Table 5.8 and Table 5.9 for the main flows shown in Figure 3.4, including the feed streams (1 and 16), the distillate products (streams 7, 13, 22, 25 and 31) and the bottom streams (4, 10, 19, 28 and 34). With respect to Table 5.8 and Table 5.9, there is a good agreement between the HCl (aq) properties and those in Refs. [129], [161] which proves the accuracy of data from this study.

Table 5.7. Summarize physical constants, empirical equations used in the calculations of saturation pressures, binary interaction parameters and chemical equilibrium constant parameters used in developed HCl(aq) PSD model simulation in Aspen Plus [176]–[178].

DIPPR liquid molar density (ρ_i^L) model parameter for H ₂ O and HCl [39, 40, 41]							
Parameter	C ₁	C ₂	C ₃	C ₄	C ₅	C ₆	C ₇
H ₂ O	17.86	58.61	-95.37	213.89	-141.26	273.16	64.71
HCl	3.34	0.27	324.65	0.32	0	158.97	324.65
$\rho_i^L = C_{1i}/C_{2i}^{1+(1-T/C_{3i})^{C_{4i}}}$ for $C_{6i} \leq T \leq C_{7i}$ for H ₂ O							
$\rho_i^L = C_{1i} + C_{2i}\tau^{0.35} + C_{3i}\tau^{2/3} + C_{4i}\tau + C_{5i}\tau^{4/3}$ for $C_{6i} \leq T \leq C_{7i}$ for HCl							
$\tau = 1 - T/T_c$; v_i^0 is the liquid molar volume of species i; T_c is the critical temperature of species i; linear extrapolation is performed if T goes beyond the temperature bonds.							
DIPPR ideal gas heat capacity model parameter for H ₂ O and HCl [39, 40, 41]							
Parameter	C ₁	C ₂	C ₃	C ₄	C ₅	C ₆	C ₇
H ₂ O	33.363	26790	2610.50	8896	1169	100	2273.15
HCl	29157	9048	2093.80	-107	120	50	1500.00
$C_{p_i}^{ig} = C_{1i} + C_{2i}(\frac{C_{3i}/T}{\sinh(C_{3i}T)})^2 + C_{4i}(\frac{C_{5i}/T}{\sinh(C_{5i}T)})^2$ for $C_{6i} \leq T \leq C_{7i}$							
DIPPR heat of vaporization ($\Delta_{vap}h_i$) model parameters for H ₂ O and HCl [39, 40, 41]							
Parameter	C ₁	C ₂	C ₃	C ₄	C ₅	C ₆	C ₇
H ₂ O	33363	26790	2610.5	8896	1169	100	2273.15
HCl	29157	9048	2093.8	-107	120	50	1500.00
$\Delta_{vap}h_i = C_{1i}(1 - T_{ri})^{C_{2i}+C_{3i}T_{ri}+C_{4i}T_{ri}^2+C_{5i}T_{ri}^3}$ for $C_{6i} \leq T \leq C_{7i}$, $T_{ri} = T/T_{ci}$							
Parameter	A			B		C	
H ₂ O	78.51			31989.4		298.15	
HCl	4.71			3274.0		298.15	
$\varepsilon = A + B(\frac{1}{T} - \frac{1}{C})$ [39, 40]							
eNRTL model parameters (τ_{ij}) for molecule-molecule pairs							
Species i	Species j	a_{ij}	b_{ij}	c_{ij}	d_{ij}	e_{ij}	τ_{ij}
H ₂ O	HCl	2.01	0	-	-	-	2.01
HCl	H ₂ O	0.007±0.347	0	-	-	-	0.007
$\tau_{ij} = a_{ij} + b_{ij}/T$ for molecule-molecule pairs							
Chemical equilibrium constant parameters for unsymmetrical reference state							
Reaction	A	B	LnK at 298.15		ΔG^0_{rxn} (kJ/mol)	ΔH^0_{rxn} (kJ/mol)	
R1	-15.52±0.23	7424.38±69.89	9.38		-23.255	-61.726	
$LnK=A+B/T$, ΔG^0_{rxn} and ΔH^0_{rxn} are the Gibbs free energy of formation and enthalpy of formation of the reaction in the standard temperature of 298.15°C.							
Chemical equilibrium constant parameters for symmetrical reference state							
Reaction	A	B	LnK at 298.15		ΔG^0_{rxn} (kJ/mol)	ΔH^0_{rxn} (kJ/mol)	
R1	-11.74±0.36	4206.11±107.00	2.370		-5.868	-34.969	
$LnK=A+B/T$							

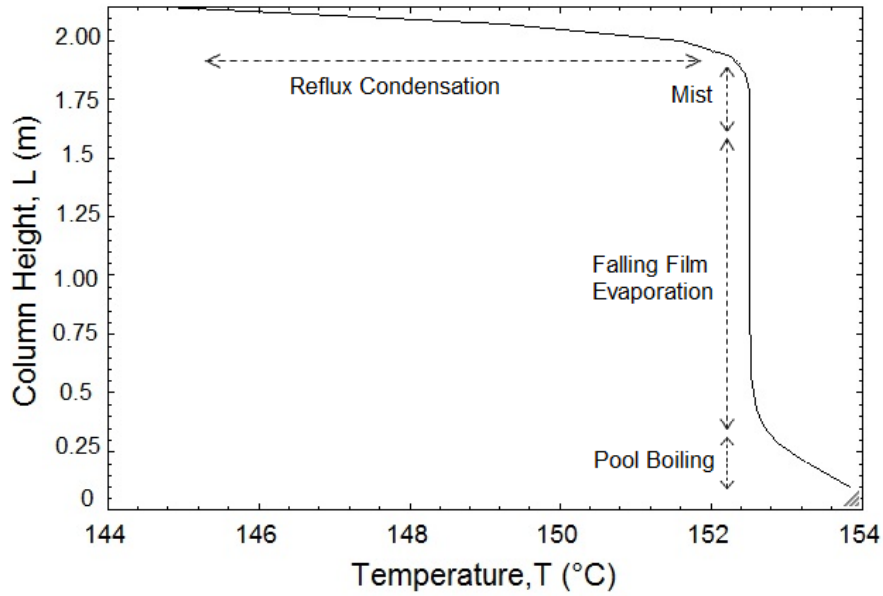
Table 5.8. Aspen Plus data flowsheet for the low pressure side

Stream number	1 (Feed)	4, 10 (Bottom)	7, 13 (Distillate)
Temperature (°C)	35	107.180	103.367
Pressure (bar)	1.013	1.0132	1.013
Molar Fraction	0.106	0.11	0.050
Mole Flowrate (kmol/h)	0.35	0.31	0.04
Specific Enthalpy (kJ/kg)	-13432.5	-13025.5	-14298.50
Viscosity, mixture (cP)	0.583	0.199	0.239
Thermal conductivity (W/m.K)	0.3228	0.260	0.345
Density (kg/m ³)	1004.348	917.423	919.94
Specific heat (kJ/kg-K)	4.390	3.633	4.048
Prandtl number	7.932	2.788	2.802

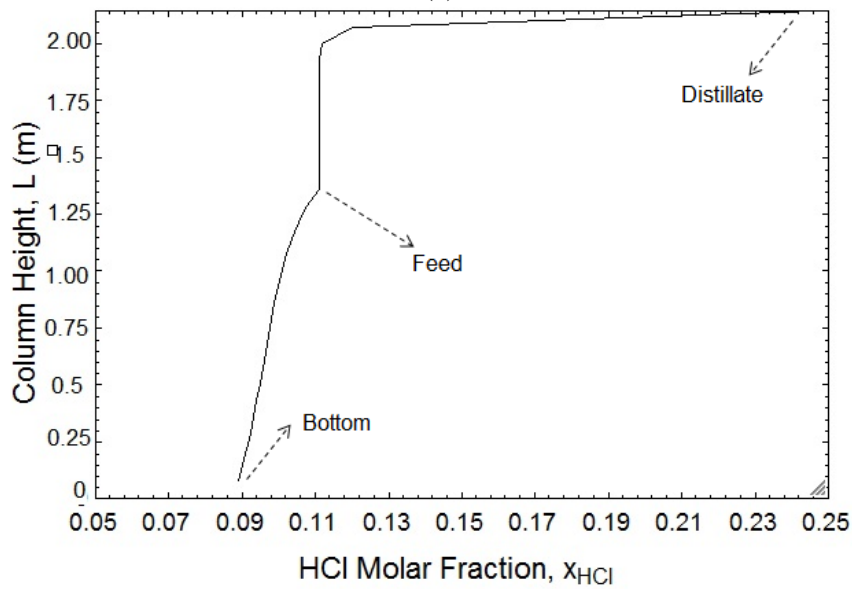
Table 5.9. Aspen Plus data flowsheet for the high pressure side

Stream number	16 (Feed)	19, 28, 34 (Bottom)	22, 25, 31 (Distillate)
Temperature (°C)	50	153.966	144.723
Pressure (bar)	4.053	4.053	4.053
Specific enthalpy (kJ/kg)	-13115.8	-12470.4	-15042.941
Molar fraction	0.11	0.094	0.21
Molar flow rate (kmol/h)	0.3	0.26	0.04
Mass flow rate (kg/h)	6.013	5.284	0.729
Viscosity (cP)	0.432	0.126	0.181
Thermal conductivity (W/mK)	0.261	0.24	0.5
Density (kg/m ³)	988.270	851.106	869.706
Specific heat (kJ/kgK)	4.409	3.712	4.620
Prandtl number	7.303	1.917	1.597

Figure 5.26(a) illustrates the temperature profile and the main heat transfer regions through the high pressure distillation column height. It is shown that the temperature of the distillate product (start point) and the bottom product (end point) are 144.4°C and 154°C, respectively. In Figure 5.26(a), because of the condensation process at the top stages through the reflux condenser (reflux condensation section), a significant temperature drop occurs (from 153°C to 144°C). In addition, at the bottom stages (pool boiling region, re-boiler), where the re-boiler supplies required heat in the column, the temperature rise is more noticeable compared to the temperature increase at the middle stages (mist region and falling film evaporation area).



(a)



(b)

Figure 5.26. (a) Temperature profile and the heat transfer main regions along the high pressure distillation column height. (b) HCl and water molar fraction change along the height of high pressure distillation column.

The variation of HCl (aq) molar concentration along the height of the separation column is depicted in Figure 5.26 (b). As mentioned earlier, breaking the azeotropic point would be possible by the high-pressure separation process of the binary HCl (aq) mixture. By frequent boiling and condensing process from the bottom (first stage) to the top (last stage), the more concentrated HCl obtained at the distillate product. As it shown in Figure 5.26

(b), at the feed stage, HCl-H₂O binary mixture specific feed molar fraction is 0.11 and at the top stage, HCl molar concentration reaches 0.24.

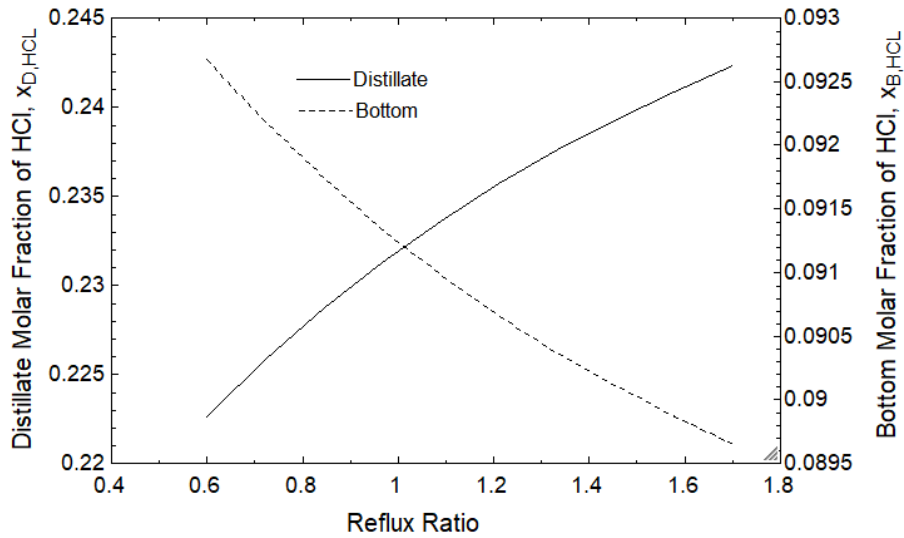


Figure 5.27. Effect of the reflux ratio change on the bottom and distillate molar fraction

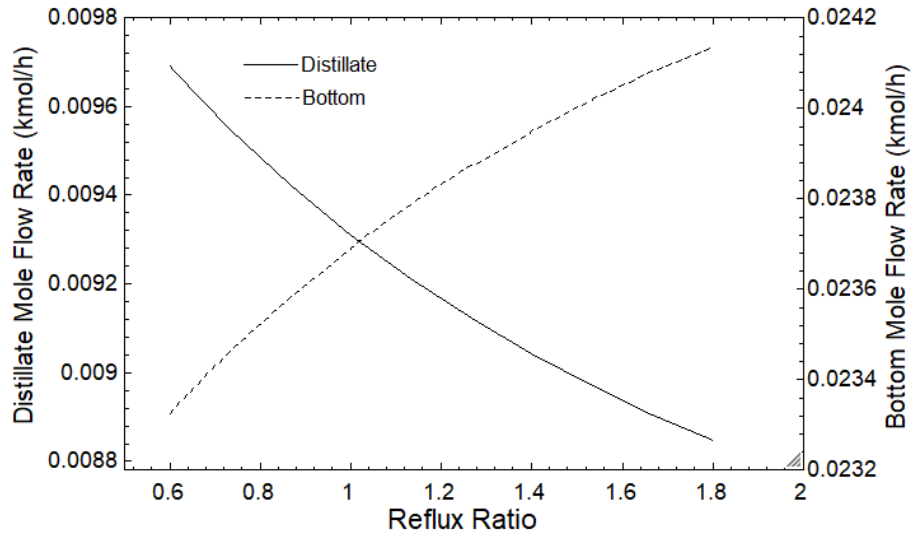


Figure 5.28. Influence of the reflux ratio on the distillate mole flow rate and the bottom mole flow rate

Figure 5.27 demonstrates the effects of the reflux ratio on the molar fraction of HCl at the bottom and distillate products. At the specific operating conditions; the temperature of 50°C, the HCl molar concentration of 0.11 and the molar flow rate of 0.3 kmol/h, it is found that the HCl (aq) molar fraction at the distillate product improves with an increase in the reflux ratio and consequently the weaker mixture in terms of HCl concentration would be existed at the bottom. However, the higher reflux ratio leads to a higher HCl concentration

in the distillate, which is the main objective of the distillation column, with more pure HCl (aq) at the top, there is a lower amount of HCl (aq) (see Figure 5.28). This causes the more final cost for the produced distillate at the top of the distillation column. On the other hand, it is disadvantageous for the low pressure side to be fed by the stream with the lower HCl concentration (bottom product of the high pressure side). So a trade-off between the HCl (aq) concentration and the cost should be considered for achieving the optimum reflux ratio in the system operation.

Figure 5.29 shows the effects of the reflux ratio on the bottom and distillate products temperatures. With an increase in the reflux ratio from 0.6 to 1.8, the distillate temperature decreases from 146.3°C to 136.2°C. The increase in the portion of condensed distillate returning back to the high pressure separation column causes a decrease in the temperature of the distillate product. Therefore, for obtaining a lower temperature distillate product, it is preferable that the separation process operates in a higher range of reflux ratio. Moreover, according to Figure 5.29, a change in the reflux ratio causes a small temperature rise in the bottom product. This would be desirable for the low pressure column in benefiting from the feed (bottom product in the high pressure side) with the higher temperature.

The variation of the bottom molar fraction and distillate molar fraction of HCl with the feed temperature are depicted in Figure 5.30. The increase in the temperature of HCl (aq) feed stream with the specific composition enriches the HCl (aq) concentration in the distillate product and consequently a lower HCl concentration at the bottom product yields. It was found that the temperature of the feed stream does not change the composition of HCl but it increases considerably the molar fraction of HCl at the distillate product. Also, Figure 5.31 shows the increment in the HCl (aq) mole flow rate in the distillate product and the decrease in the HCl (aq) mole flow rate at the bottom with an increase in the feed stream temperature. Thus, an increase in the operating temperature of the low pressure separation column leads to a temperature rise in its bottom product (which is the feed in the high pressure side) and consequently a higher HCl flow rate and concentration at the distillate product.

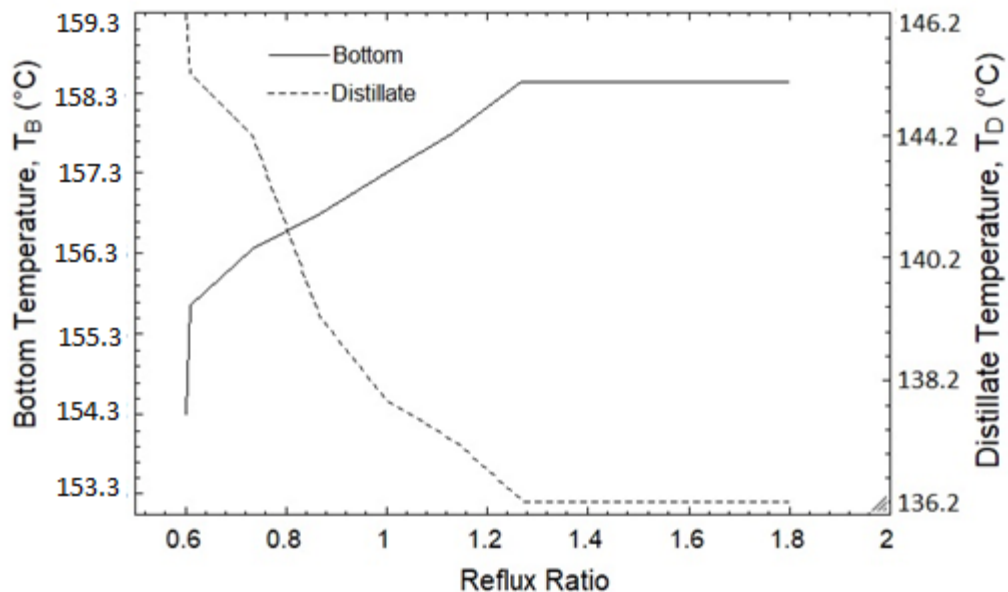


Figure 5.29. Variation of the bottom and distillate temperatures as a function of reflux ratio

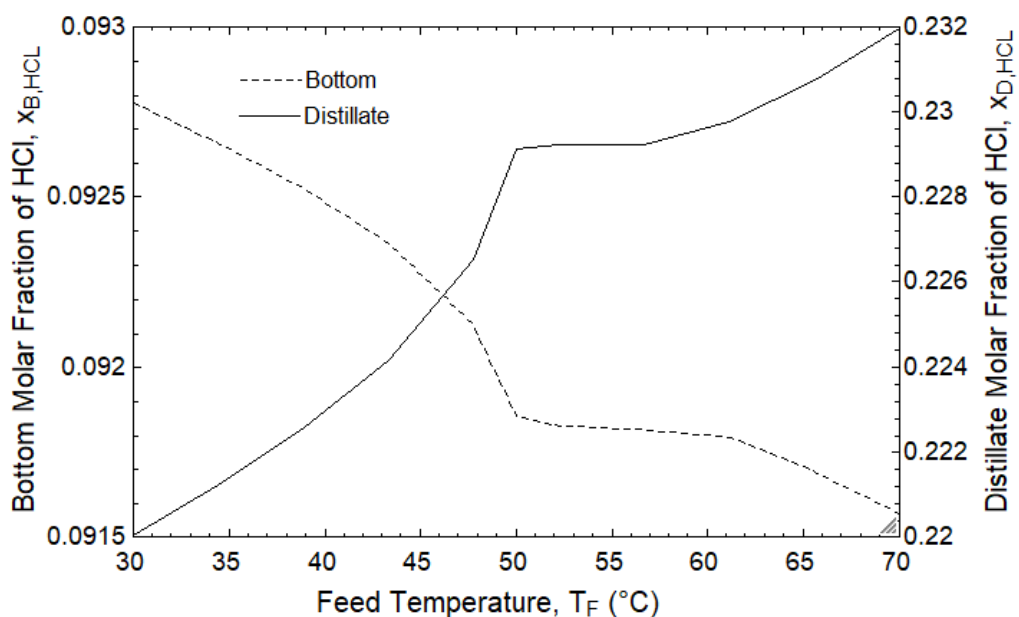


Figure 5.30. Change in the bottom and distillate molar fraction over the feed temperature

The temperature profiles of the high pressure and low pressure distillation column are represented in Figure 5.32 (a) and (b). In Figure 5.32 (a), at the low pressure side, the temperature drops from 107°C at the bottom to 103°C at the top. Whereas, in Figure 5.32 (b) for the high pressure column, from the bottom to the top, the column temperature

declines from 154°C to 144.7°C. As can be seen from both Figure 5.32 (a) and (b), the most significant temperature drop occurs at the reflux condenser sections due to the free convection at the non-isolated part for partial reflux condensation purposes.

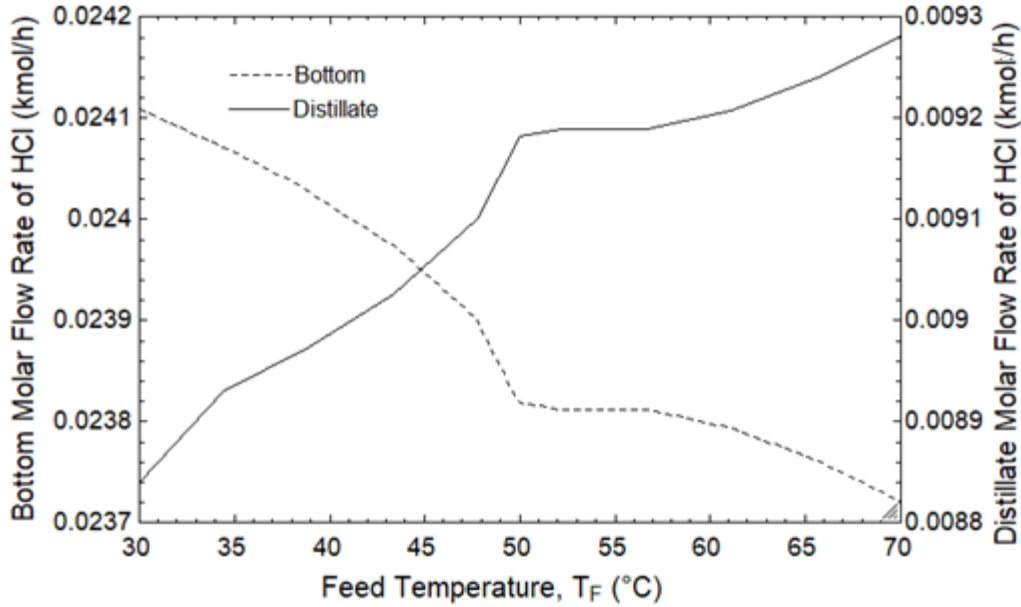
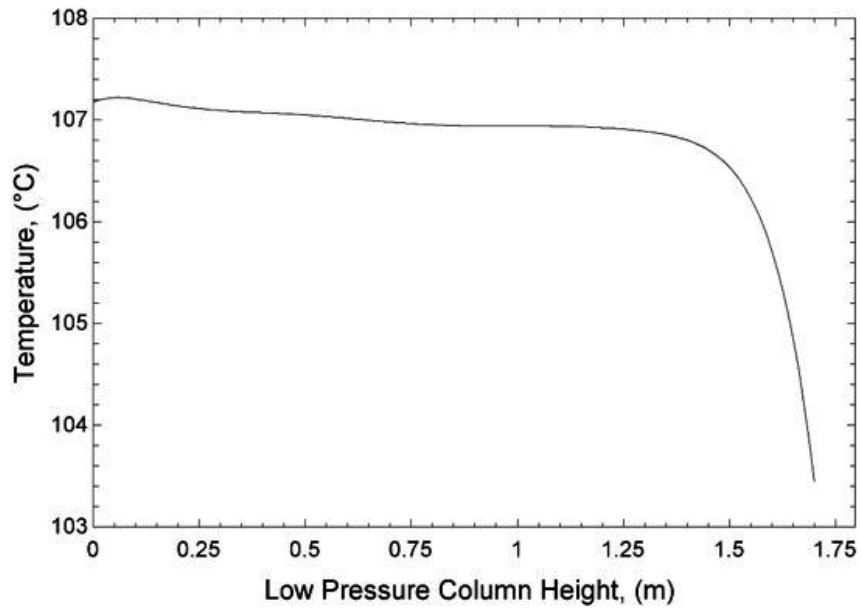


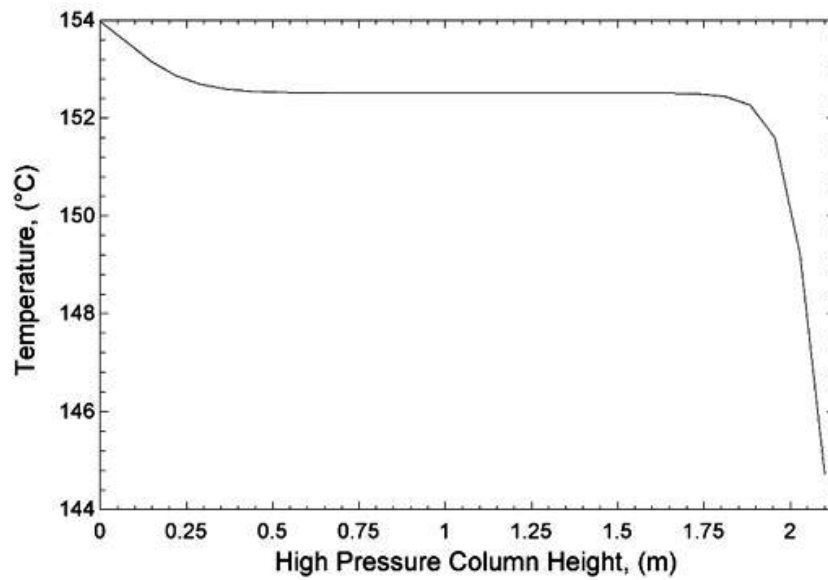
Figure 5.31. Influence of the feed temperature on the bottom and distillate mole flow rates

Figure 5.33 (a) and (b) illustrate the HCl molar concentration at different heights of the distillation column in low and high pressure sides, respectively. As described earlier, the separation process for the HCl- water binary azeotropic mixture can be obtained by pressure changes in the distillation apparatus. This process takes advantage of the fact that the azeotropic concentration point varies with pressure. Moreover, the component's volatility changes by the azeotropic point. With respect to Figure 5.33(a), at the low pressure side with the feed concentration less than the azeotropic point, the bottom product is more concentrated in HCl (aq) compared to the top where almost the pure water exists. In fact, before the azeotropic point, HCl is the component with less volatility. By passing from the azeotropic point at the high pressure side (see Figure 5.33 (b)), the HCl mole fraction in the feed (stream 16) is higher than the relevant azeotropic concentration at 4 atm (high pressure column). Therefore, in the high pressure distillation column, the tendency of the HCl component for vaporization (volatility) is more than water which leads to the

more hydrochloric acid concentration at the top and consequently, the less concentrated HCl at the bottom.

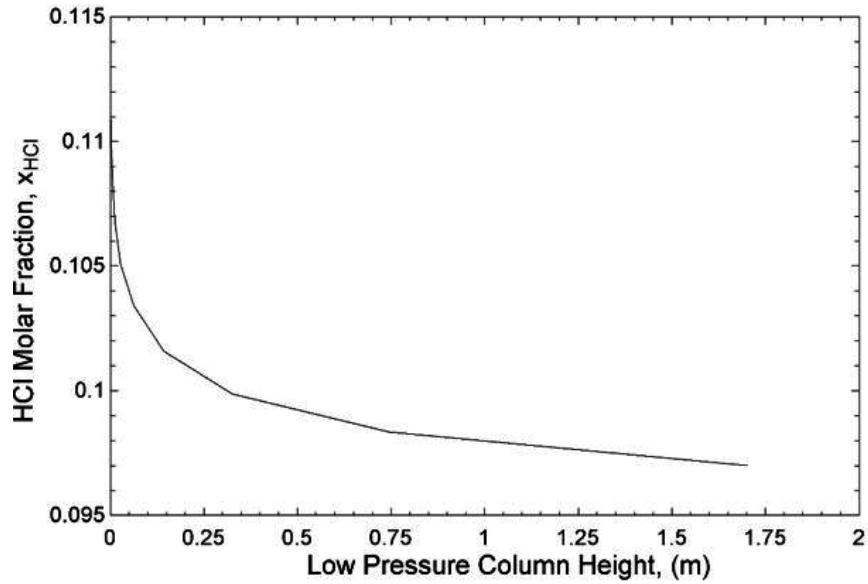


(a)

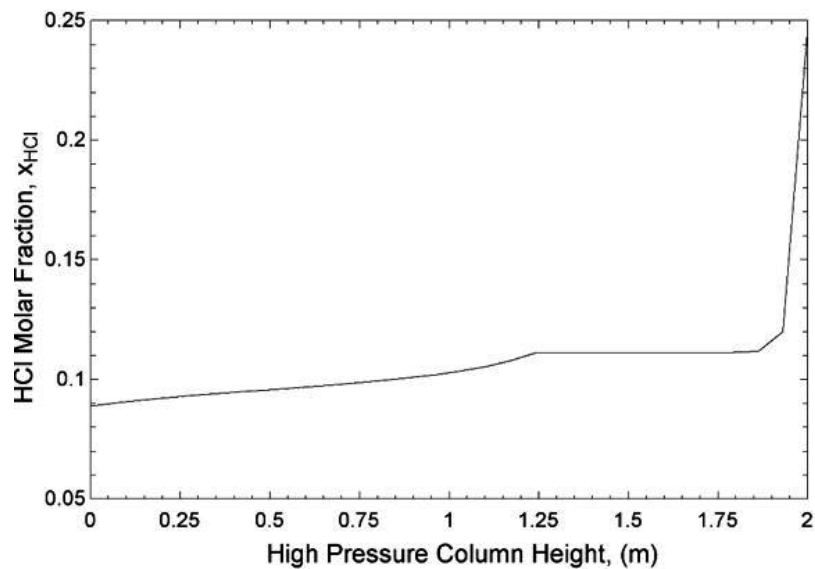


(b)

Figure 5.32. (a) Temperature profile along the low pressure column height from the bottom to top (b) Temperature profile through the high pressure column height from the bottom to top



(a)



(b)

Figure 5.33. (a) Change in the HCl mole fraction from the bottom to the top of the low pressure column (b) change in the HCl mole fraction from the bottom to the top of the high pressure column

In next, the effects of diverse key operating parameters like the temperature, mole flow rate and molar fraction of the low pressure feed stream and the slope of the operating line on the final distillate composition, the re-boiler and condenser heat duties are examined. The minimum allowable composition of feed supplied to the PSD system for the feasible separation process of HCl (aq) is also investigated.

Figure 5.34 shows the degree of HCl (aq) mole fraction at the distillate in the high pressure column against the change in the feed temperature at the low pressure side, as well as the variation of operating line slope. At the specific feed molar composition of 0.1 and the slope of 0.8, with the increase in the temperature of feed injected to the final HCl molar concentration at distillate increases from 0.218 to 0.245. It is shown that at the higher feed temperature coming into the PSD setup, a higher low pressure bottom temperature and eventually a higher HCl concentration and temperature at the high pressure distillate port would be obtained. According to Figure 5.34, in the high pressure side and at the feed temperature of 55°C, by increasing the slope of the operating line from 0.2 to 0.8, the HCl molar fraction of the distillate product increases from 0.324 to 0.245. So regardless of the final cost of HCl (aq) distillate product at the PSD unit, it would be desirable for the high pressure side to benefit from the higher reflux ratio.

Figure 5.35 depicts the effects of feed molar flow rate on the HCl molar concentration of the high pressure distillate at different slopes of operating lines. It is shown that the high pressure distillate mole fraction of HCl increases with the decrease in the low pressure feed molar flow rate and increase in the amount of refluxed condensed flow in the top section. Although operation of the high pressure columns in the higher slope ranges (higher amount of reflux condensed flow) results in a higher concentration of HCl of the distillate product, there would be a less final distillate rate. This leads to a higher cost for the produced HCl (aq) from the separation process. Therefore, a balance between the cost and concentration of distillate should be taken into account for achieving the optimum slope in an actual operation of the setup.

Figure 5.36 (a) illustrates the variation of re-boiler heat duty in both low and high pressure distillation columns as a function of the slope and low pressure feed temperature. For the specific feed component's composition, by the increment in the feed temperature, the low pressure bottom temperature rises which results in a higher feed temperature fed into the high pressure side. For a higher feed temperature in the high pressure column, the less re-boiler heat is required for the separation process. It declines from 6.3kW to 4.8kW for the operation line slope of 0.8 in the high pressure column. On the other hand, as a loop,

the higher bottom temperature in the high pressure column leads to the higher feed temperature in low pressure columns and consequently the less energy consumption.

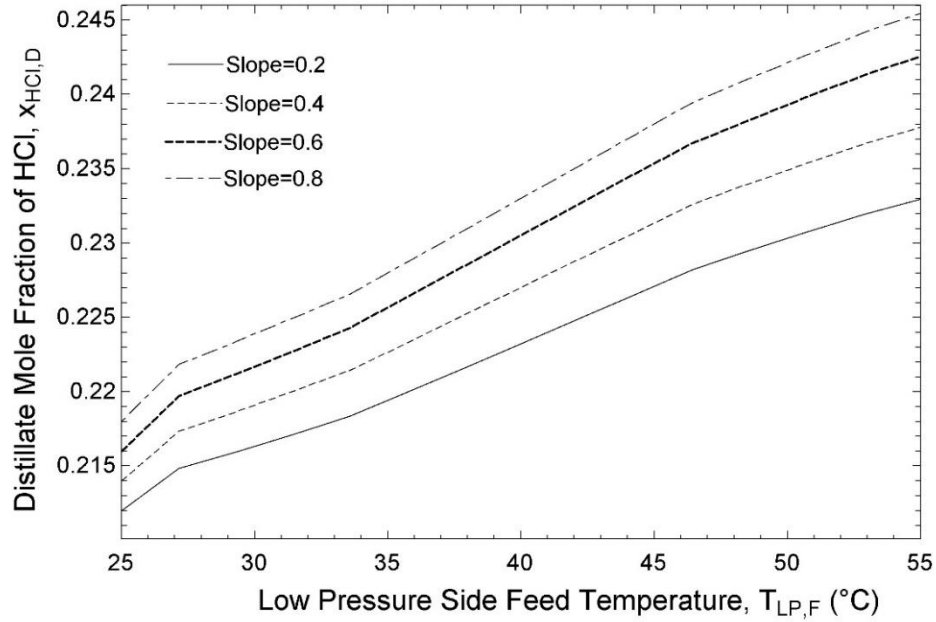


Figure 5.34. Effect of varying low pressure side feed temperature and the slope of operating line on the distillate mole fraction of HCl

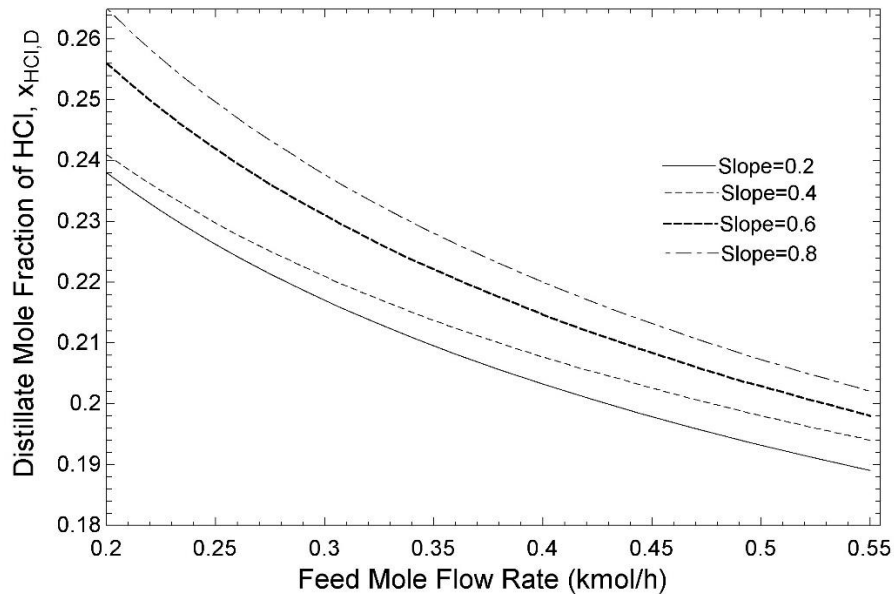
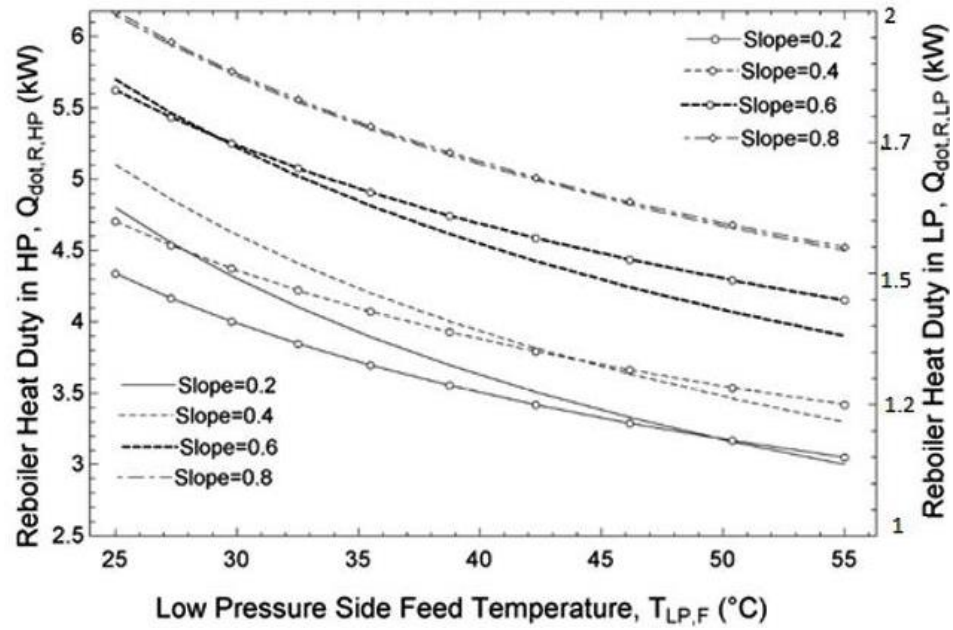
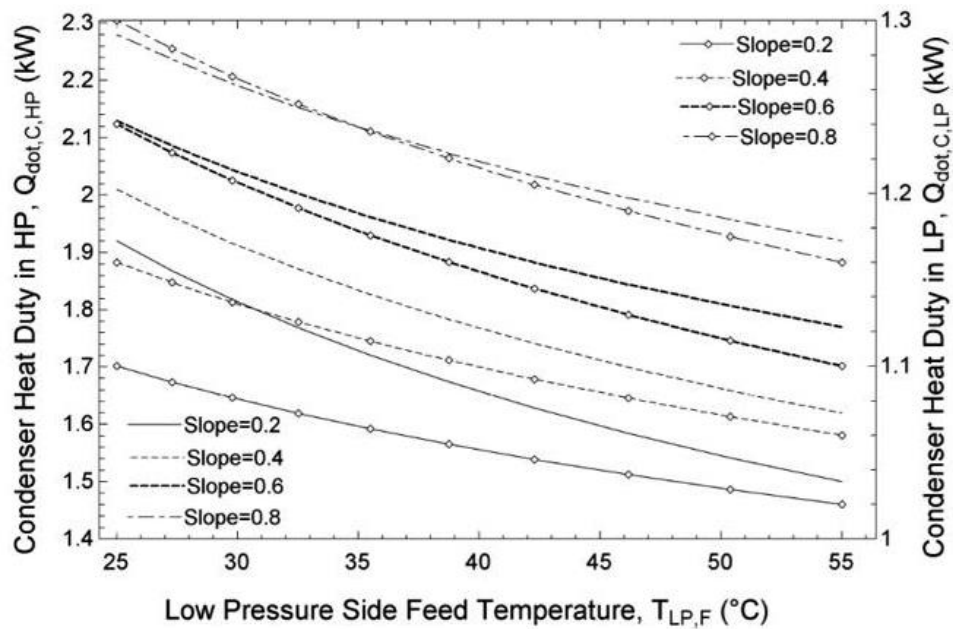


Figure 5.35. Influence of low pressure feed flow rate and the slope of operating line on the distillate HCl molar concentration



(a)



(b)

Figure 5.36 (a). Variations with the low pressure feed temperature and slope for the re-boiler heat duty in high and low pressure columns (b). Variations with the low pressure feed temperature and slope for the condenser heat duty in high and low pressure columns

So, as can be seen in Figure 5.36 (a), the re-boiler heat duty decreases from 3kW to 2.1kW for a slope of 0.8 at the low pressure distillation column.

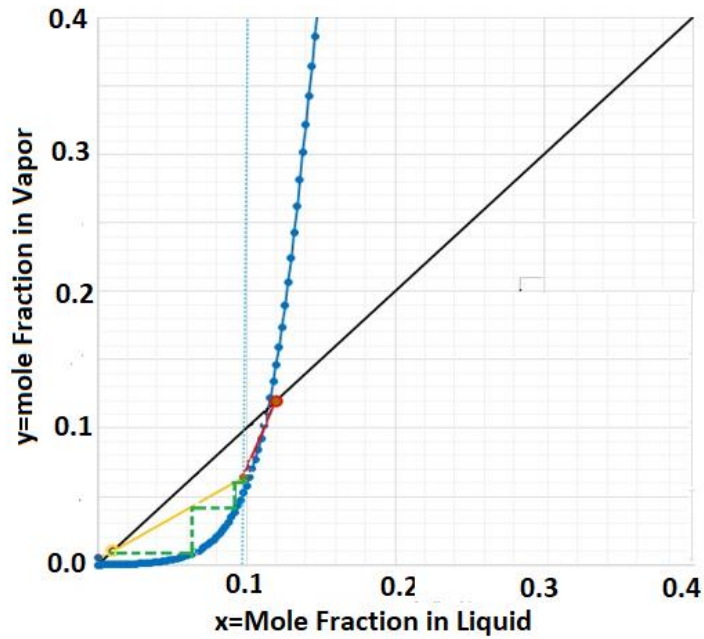
Moreover, according to Figure 5.36 (a), at a constant feed temperature of 35°C, by enlarging the slope from 0.2 to 0.8, the energy supplied for heating three high pressure columns increases from 4kW to 5.5kW (37.5% increment). For two low pressure columns, the re-boiler heat duty rises from 1.26kW to 1.6kW (26.5% increment). Besides, with respect to Figure 5.36 (b), at the same specific feed temperature of 35°C, by an increase of the slope from 0.2 to 0.8, the condensation heat duty for high pressure columns grows from 1.75kW to 2.15kW (22.8% increase). For two low pressure columns, the condenser heat duty rises up from 1.05kW to 1.22kW (16.2% increase). So, it can be concluded that the re-boiler and condensation heat duties in the high pressure side undergo the more change with the variation in the amount of reflux condensed distillate (slope), compared to the low pressure side.

5.5.2. Packing Column Height

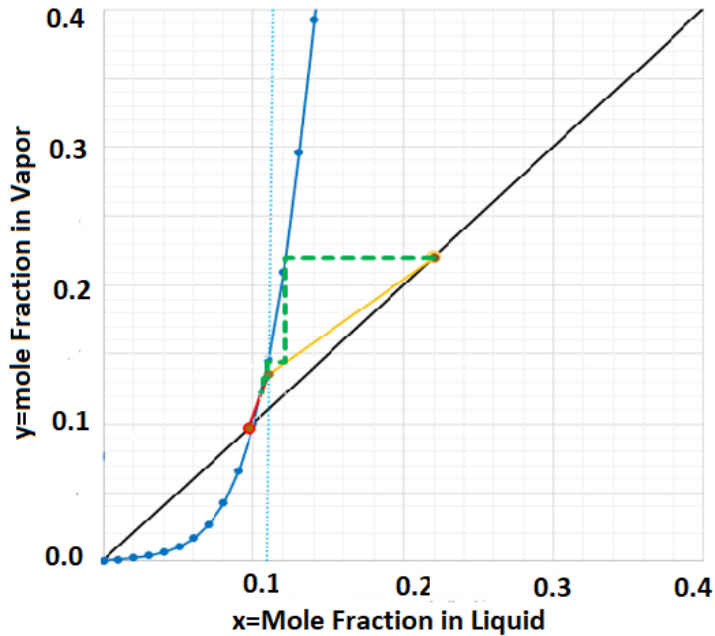
The results from the mass transfer analysis (number of trays specification by McCabe-Thiele method) and the heat transfer analysis (heat transfer coefficient determination) are presented as follows. Based on these results, a practical height for the packing column distillation will be proposed.

The clear McCabe-Thiele graph comprised of VLE curve, operating line, q line, x_f , x_b and x_d lines for the low pressure column (before the azeotropic point) and the high pressure column (after the azeotropic point) are displayed in Figure 5.37 (a) and (b), respectively. It can be interpreted from Figure 5.37 (a) and (b), and equations 14 and 15, for both low pressure and high pressure distillation column the number of trays is evaluated to be 8 and the optimum feed location is in tray number 3. Moreover, among the empirical method correlations for the distillation column height calculation [129], the height equivalent to a theoretical plate (HETP) from Ref. [179] (HETP = 0.229 m) aligns the best match with this case study. Thus, according to equation 15, the net packing height for each distillation column is estimated to be around 1.85 m. As mentioned earlier, in both high and low pressure distillation columns, there are four main heat transfer regions consisting of partial condensation (section 1), mist region (section 2), falling film evaporation (section 3) and pool boiling (section 4). Table 5.10 and Table 5.11 show the results of the heat transfer

mechanism as the heat transfer rate, heat transfer coefficient, and finally the equivalent column length in each heat transfer section.



(a)



(b)

Figure 5.37. (a) McCabe-Thiele graph for the HCl (aq) at 1atm (before azeotropic point) with $q=1$, $x_f=0.1$, $x_b=0.12$ and $x_d=0.001$ (b) McCabe-Thiele graph for the HCl (aq) at 4atm (after azeotropic point) with $q=1$, $x_f=0.12$, $x_b=0.096$ and $x_d=0.22$

As can be observed from Table 5.10 , for the low pressure column, the equivalent packing column height is calculated to be near to 1.7 m (summation of sections 2 to 4). The height of the non-isolated reflux condensation part (section 1) is assessed to be around 0.28 m. Additionally, in Table 5.11 for the high pressure side, the length of each column is around 2 m and the non-isolated condensation part length is about 0.3 m. From Table 5.10 and Table 5.11, when considering the specific constant tube diameter along the column, the heat transfer area in the falling film evaporation region is 2 and 1.5 times larger than the pool boiling and mist regions, respectively.

Regarding the results from the mass transfer and heat transfer models, both analysis predict almost the same value for the packing column height of high pressure and low pressure sides of PSD apparatus.

Table 5.10 . Heat transfer parameters and related height of each section for the low pressure column

Section	\dot{Q} (kW)	T_{tape} (°C)	Re	Pr	h_i (kW/m ² K)	L (m)
1: Partial condensation	0.28	-	133	0.61	0.151	0.277
2: Mist region	0.031	104.84	151	0.96	0.137	0.558
3: Falling film evaporation	0.042	106.83	1282	1.28	0.505	0.792
4: Pool boiling	1.03	107.21	2609	6.69	3.109	0.334

Table 5.11. Heat transfer parameters and related height of each section for the high pressure column

Section	\dot{Q} (kW)	$T_{\text{oil,out}}$ (°C)	Re	Pr	h_i (kW/m ² K)	L (m)
1: Partial condensation	0.51	-	142	0.69	0.163	0.301
2: Mist region	0.055	177.93	171	1.01	0.142	0.611
3: Falling film evaporation	0.057	178.32	1392	1.77	0.561	0.912
4: Pool boiling	1.23	178.61	2887	7.81	3.549	0.468

5.6. Exergoeconomic Study Results

The cost flow rates and specific cost for each stream are obtained by solving the cost balance equations and corresponding auxiliary F and P rules. The cost rate of the produced hydrogen is estimated to be 0.549 \$/h which corresponds to 6.02 \$/kg H₂. This produced hydrogen cost is relatively high compared to the past literature such as values reported by

ANL [7, 39] where the hydrogen cost was 3.5 \$/kg H₂ (using CEPCI, 3.6 \$/kg H₂). The relatively high price of the calculated cost of hydrogen in this study was mainly due to the relatively high-price laboratory facilities and equipment specifically PSDU within the Cu-Cl cycle construction. Equipment costs would be reduced considerably with the enlargement of the plant capacity. Moreover, in the present lab-scale cycle, there is no heat recovery process, however, it can be implemented at larger scales to save significant costs associated with electricity and thermal energy inputs.

The exergy destruction rate in each component of the lab-scale Cu-Cl cycle is shown in Figure 5.38. It can be seen that the highest exergy destruction rate is associated with the hydrolysis reactor, thermolysis reactor, PSDU and steam condenser 2, respectively. The chemical endothermic reactions in the hydrolysis and thermolysis reactors are the main contributors to the destroyed exergy. The two-step distillation process of HCl (aq) (at low and high pressure) and the large temperature gradient are the primary reasons for the irreversibilities of the PSDU. In the steam condenser 2, the large dissipated thermal energy associated with the steam condensation is the main cause of exergy destruction. For the quench cell and CuCl₂ concentrator, the high thermal energy associated with the water vaporization and solidification of CuCl at a relatively high temperature gradient are contributed to the high rate of destructed exergy, respectively. The relatively large flow rate of water supplied into the separation unit causing the main reason for destructing exergy in this module. The CuCl/HCl (aq) electrolyzer stack possesses negligible destroyed exergy compared to the other cycle units.

The cost rate of exergy destruction of components within the Cu-Cl cycle is shown in Figure 5.39. From Figure 5.39, the highest cost rate of exergy destruction belongs to steam condenser 2 (22%), hydrolysis reactor (17%), and thermolysis reactor (15%), respectively. Also, the related cost rate of equipment within the Cu-Cl cycle is shown in Figure 5.40. It can be seen that the electrolyzer stack and the PSDU are the most expensive units within the cycle. In the electrolyzer stack, the titanium/ platinum Nafion-117 membranes are the main contributors to the high price of this component. In the PSDU, the various components to distillate the HCl (aq) solution within a two-step process results in the high price of this unit.

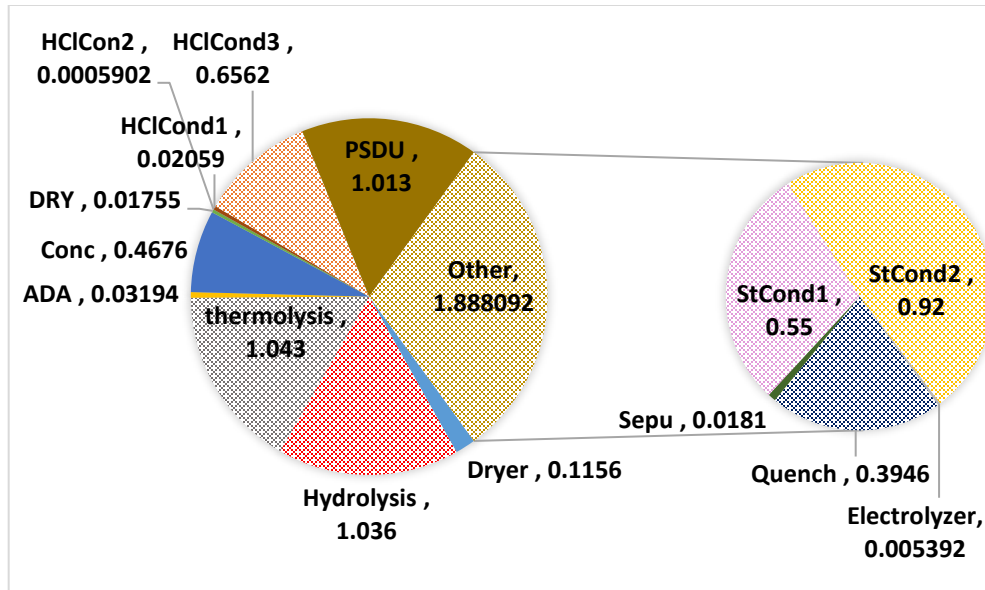


Figure 5.38. Breakdown of exergy destruction rates (kW) in components of the Cu-Cl cycle

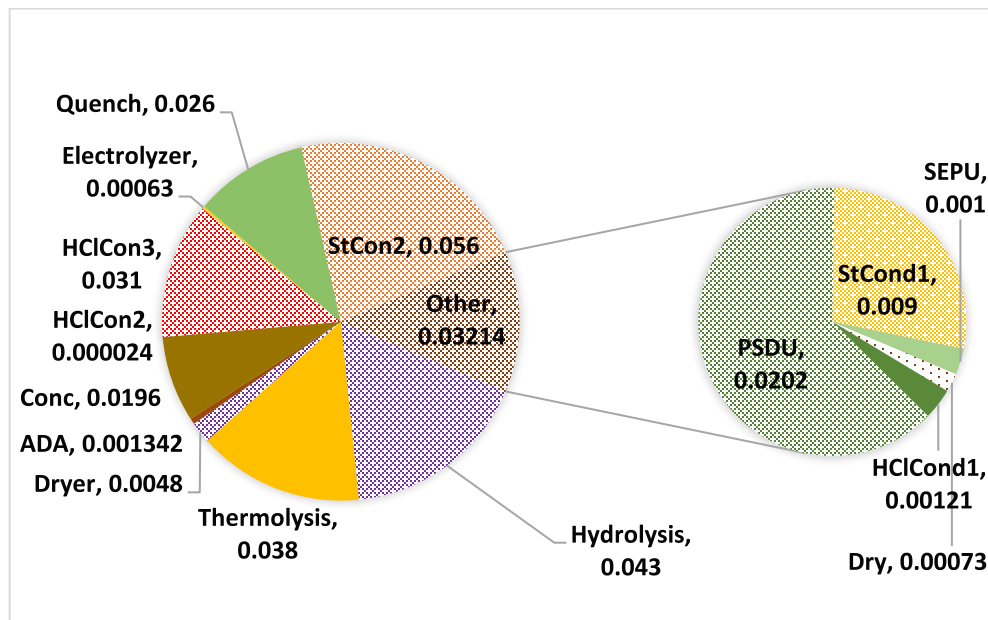


Figure 5.39. Breakdown of cost rates of exergy destruction (\$/h) in the Cu-Cl cycle components

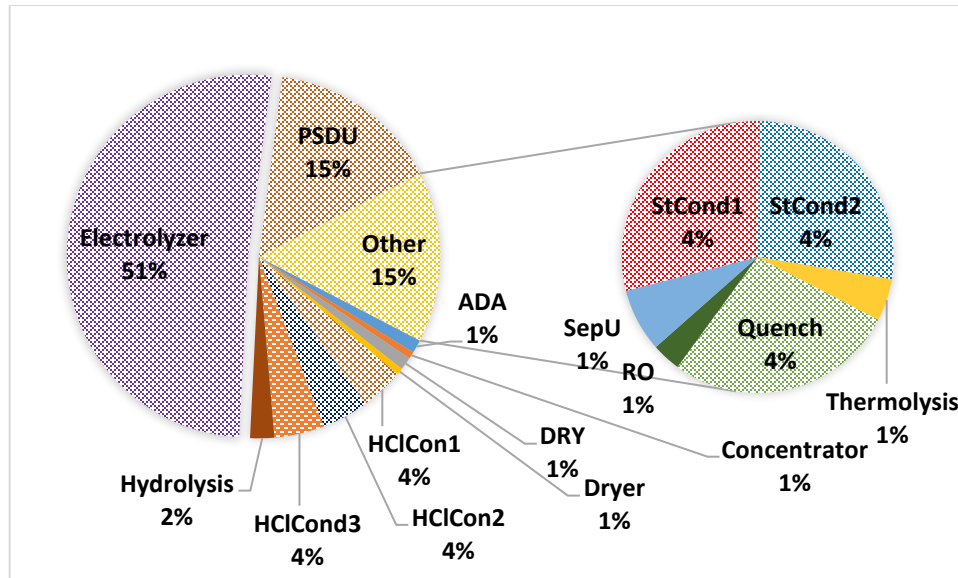


Figure 5.40. Component related cost rates (\$/h) in the lab-scale Cu-Cl cycle

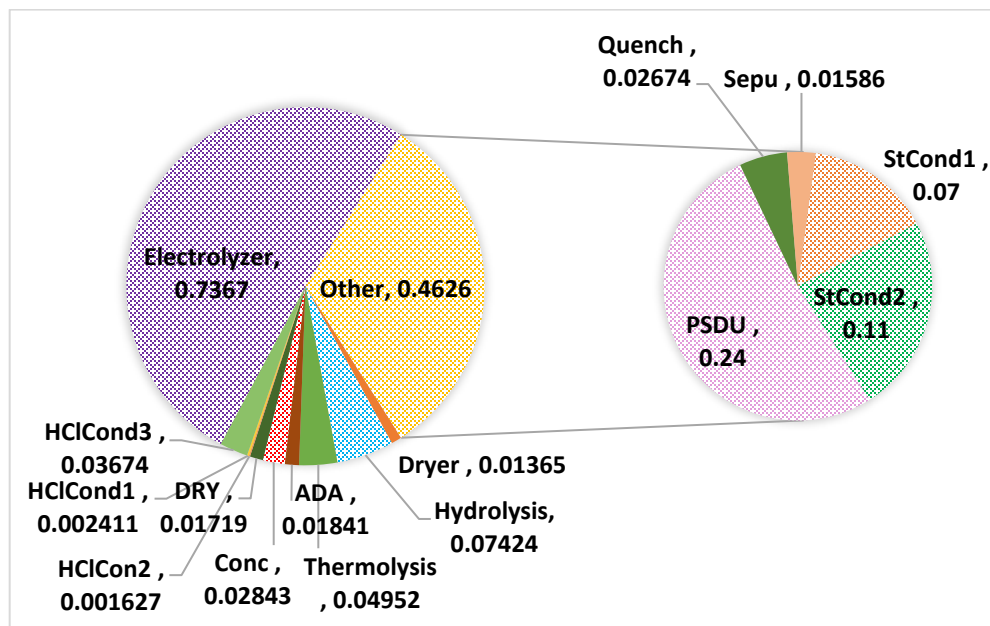


Figure 5.41. Breakdown of total cost rates (\$/h) in the components of the lab-scale integrated Cu-Cl cycle

The cost distribution among destroyed exergy and related cost rates for the Cu-Cl cycle's components are illustrated in Figure 5.41. The highest total cost rate is associated with the electrolyzer stack (51% of the total cost rate of the overall Cu-Cl cycle) and PSDU (17% of total cost rate of the overall Cu-Cl cycle). From Figure 5.39, Figure 5.40, and Figure 5.41, the component related cost rate is dominant over the cost rate of exergy destruction.

Figure 5.42 shows the exergoeconomic factors of components within the Cu-Cl cycle. If the exergoeconomic factor is near 1, the related cost of the component is considerably higher than the cost rate of destroyed exergy at that component. If this factor is near zero, the cost rate of destroyed exergy is dominant over the related cost of the specific component. From Figure 5.42, the relatively high value of the exergoeconomic factor specifically in the electrolyzer and PSDU show that the cost rate associated with the related cost rate of the components is dominant over the destroyed exergy cost rate. Therefore, in order to have a more cost-effective system, it is suggested to reduce the capital investment of equipment in the Cu-Cl cycle at the expense of incremental exergy destruction. However, as mentioned earlier, the relatively high capital cost of cycle components occurs because of the laboratory scale capacity which will decline with an increase in the scale of the cycle.

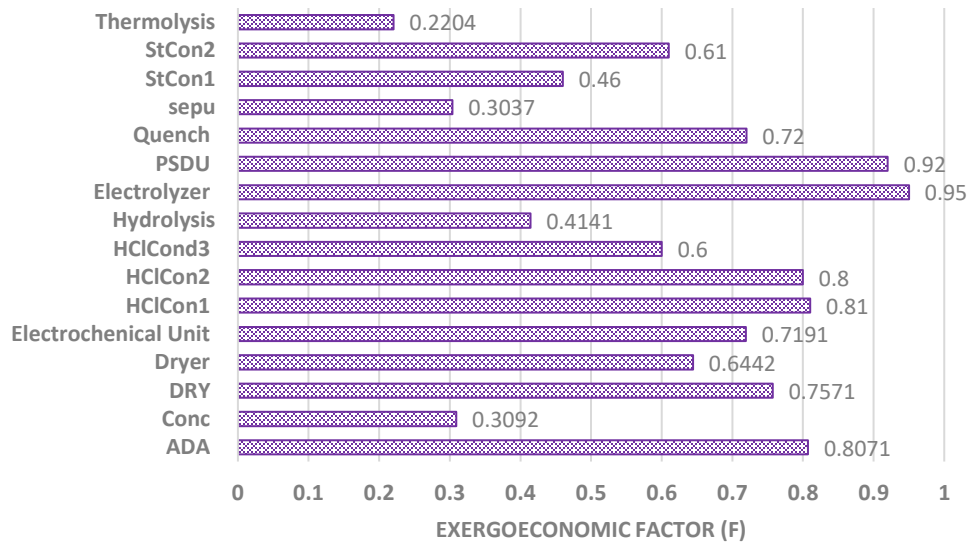


Figure 5.42. Component exergoeconomic factors in the lab-scale Cu-Cl cycle

Since the CuCl/ HCl (aq) electrolyzer stack has the highest capital cost within the lab-scale Cu-Cl cycle, a sensitivity study is conducted for evaluating the effects of the electrolyzer capital cost on the related cost rate, destroyed exergy cost rate and total cost rate of the overall Cu-Cl cycle (see Figure 5.43). The CuCl/ HCl (aq) electrolyzer stack can be built with less quantity of titanium/ platinum catalyst to yield a more economical capital price for the electrolyzer stack. According to Figure 5.43, in the case of investing \$8000

for an electrolyzer stack, the cost rate of exergy destruction decreases to \$0.7/h, the related cost rate reduces to 0.8\$/h, and the total cost rate of the Cu-Cl cycle declines to \$1.48/h.

The interest rate is one of the important factors in the estimation of the cost rate. From Figure 5.44, a higher interest rate negatively affects the cost rate of the cycle. With the rise of interest rate from 5% to 15%, the cost rate of destroyed exergy, related cost rate and total cost rate of the Cu-Cl cycle increases by 18.5%, 25% and 23.3%, respectively. Furthermore, the lifetime of each component of the Cu-Cl cycle can potentially affect the cost rate of the cycle. Different components have different lifetimes depending on the material used in their construction and application. For instance, the membranes in the electrolyzer need to be replaced a maximum of every two years, while the PSDU equipment needs to be replaced over ten years. In the case of a large-scale cycle, the time of replacement can happen over a longer period. For the base case, the lifetime considered in this experimental cycle is ten years which corresponds to the total cost rate of \$2.1/h for the Cu-Cl cycle. With respect to Figure 5.45 with an increase in the lifetime of the Cu-Cl cycle from 5 years to 40 years, the total cost rate of the cycle declines by about 66%.

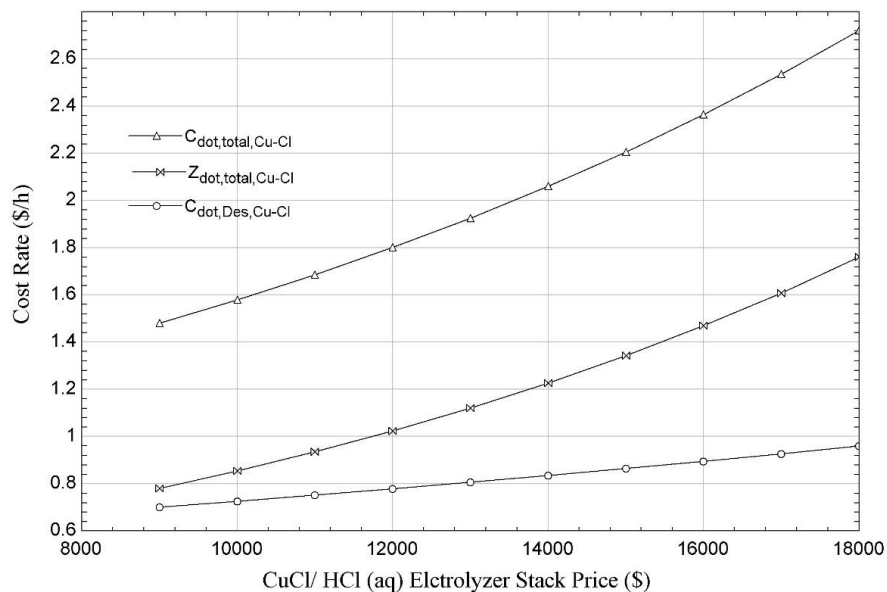


Figure 5.43. Effects of CuCl/HCl (aq) electrolyzer stack capital cost on the cost rates of the overall lab-scale Cu-Cl cycle

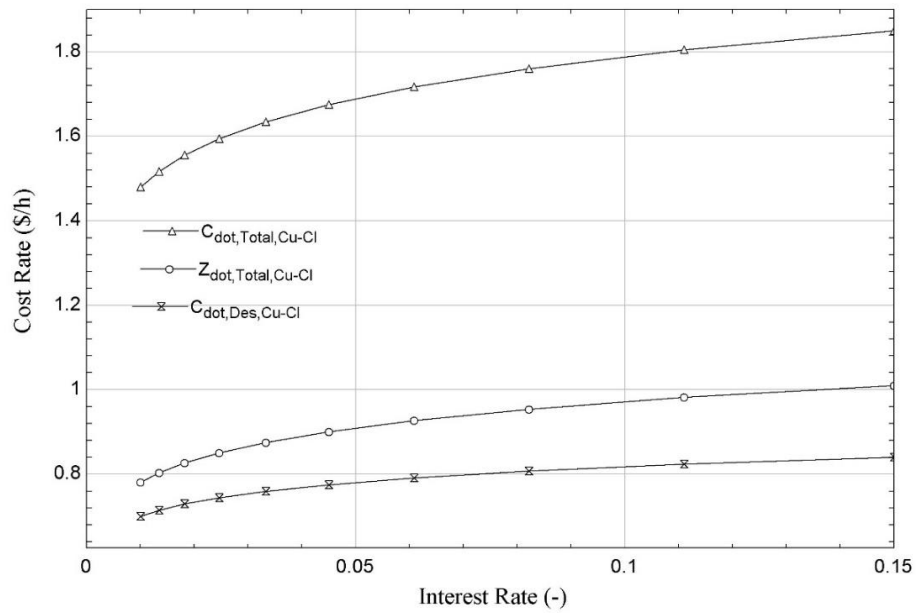


Figure 5.44. Effects of interest rate on the cost rate of the lab-scale Cu-Cl cycle

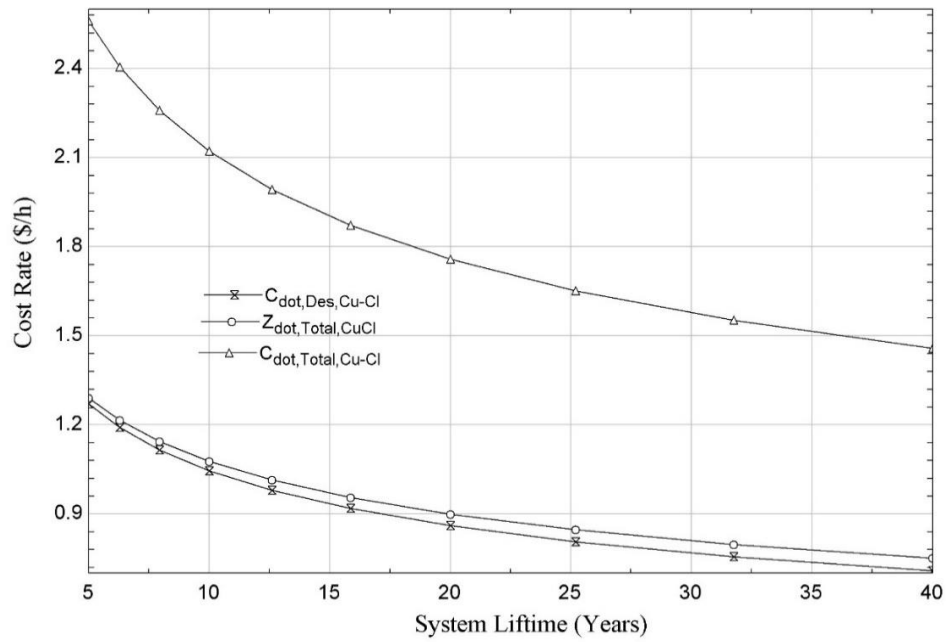


Figure 5.45. Effects of system lifetime (in years) on the cost rates of the lab-scale Cu-Cl cycle

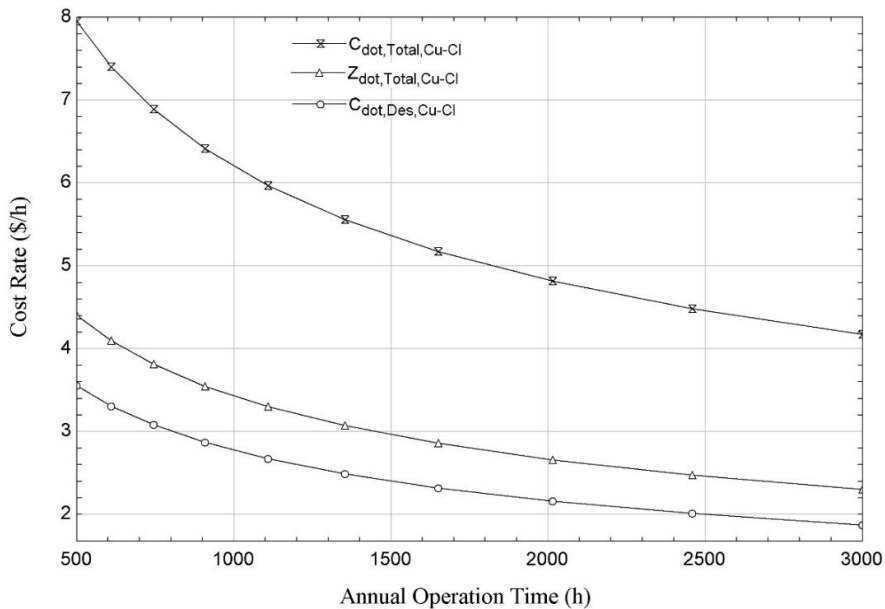


Figure 5.46. Effects of annual operation time (in hours) on the cost rates of the lab-scale Cu-Cl cycle

The annual operation time of the Cu-Cl cycle is another important factor in the cost rate estimation of the cycle, specifically in the case where solar energy is used as the energy source (solar-based systems are significantly affected by solar radiation which contributes to the time of operation). As shown in Figure 5.46, when increasing the annual operation time from 500h to 3000h, the total cost rate of the Cu-Cl cycle declines by around 48%.

5.6.1. Scale-up Study Results

Table 5.12 shows the total capital costs including direct and indirect capital costs of the scaled-up Cu-Cl plant with a capacity of 1000 kg/day of hydrogen production, as obtained from the Hydrogen Analysis (H2A) Production model. The total depreciable capital cost (including direct capital costs) and total non-depreciable capital costs are estimated to be about \$1,229,931 and \$905,530, respectively. Based on the assumptions and limitations taken for the scale-up analysis, for 1,000 kg/day of hydrogen production, the required plant area is 123.55 acres.

Table 5.12. Direct and indirect depreciable capital costs based on Hydrogen Analysis (H2A) Production model [169].

Site Preparation (\$)	157,904
Engineering and design (\$)	499,621
Project contingency (\$)	572,405
Up-front permitting costs (\$)	436,706
Total depreciable capital cost(\$) (including direct capital costs)	1,229,931
Cost of land (\$/acre)	7,329
Land required (acres)	124
Land cost (\$)	905,530
Total non-depreciable capital costs (\$)	905,530
Total capital costs (\$)	2,135,461

Also, the fixed operating costs associated with the Cu-Cl plant are provided in Table 5.13. The scale-up results are obtained with the assumptions of 6% state tax, 35% federal tax and 1% after-tax real rate of return (which accounts for the actual financial benefit of an investment after accounting for inflation and taxes). It is predicted that the repair and maintenance costs are about 4% of the total cost (excluding replacement parts). The component replacement consideration is taken every two-years for replacement of the electrolyzer stack, every ten-years for replacement of hydrolysis/thermolysis and every twenty-year replacement of separation units. In addition, Table 5.14 tabulates the installed costs, reactor foundation, and direct capital costs for a 1000 kg/day Cu-Cl hydrogen production plant using the Hydrogen Analysis (H2A) Production model [169].

Table 5.13. Fixed operating costs of the Cu-Cl plant using a Hydrogen Analysis (H2A) Production model [169]

Fixed Operating Costs (2017)	
Burdened labor cost, including overhead (\$/person-hour)	45.5
Labor cost (\$/year)	24,570
General and administrative expense (\$/year)	4888
Licensing, permits and fees (\$/year)	589
Property tax and insurance rate (% of total capital investment per year in Ontario, Canada)	1.45%
Property taxes and insurance (\$/year)	93,218
Production maintenance and repairs (\$/year)	19,974
Total Fixed Operating Costs (\$)	118,669

Table 5.14. Direct capital costs of units in a 1000 kg/day Cu-Cl cycle plant using a Hydrogen Analysis (H2A) Production model [169].

Major components/system	Installed costs (\$ in 2017)
Make-up water pump	243
Manifold piping	188,684
Collection piping	5,702
Column collection piping	3,362
Final collection piping	657
Condenser	17,432
Programmable logic controller (PLC)	3,349
Control room building	19,567
Control rom wiring panel	3,349
Computer and monitor	1,675
LabVIEW software	4,799
Water level controllers	78,902
Pressure sensors	7,655
Hydrogen area sensors	152,725
Hydrogen flow meter	6,140
Instrument wiring	453
Power wiring	227
Conduit	6,771
Piping installation	8,870
Reactor foundation and erection	724,038
Reactor feed install	213
Gas processing subassembly installation	2,377
Control system installation	85,467
Total Direct Capital Cost	581,187

Figure 5.47 shows a breakdown of processes associated with hydrogen production. The hydrogen cost from the scale-up setup (1000 kg/dayH₂) is estimated to be about \$3.91 /kg H₂ which is considerably less than the value of the lab-scale cycle (\$6.02 /kg H₂). From Figure 5.47, the yearly replacement costs correspond to \$2.01 /kg of produced hydrogen, indicating that with the improvement of stability and durability of the CuCl/HCl (aq) electrolyzer, and PSDU units, a significant decrease in the hydrogen cost would be achieved.

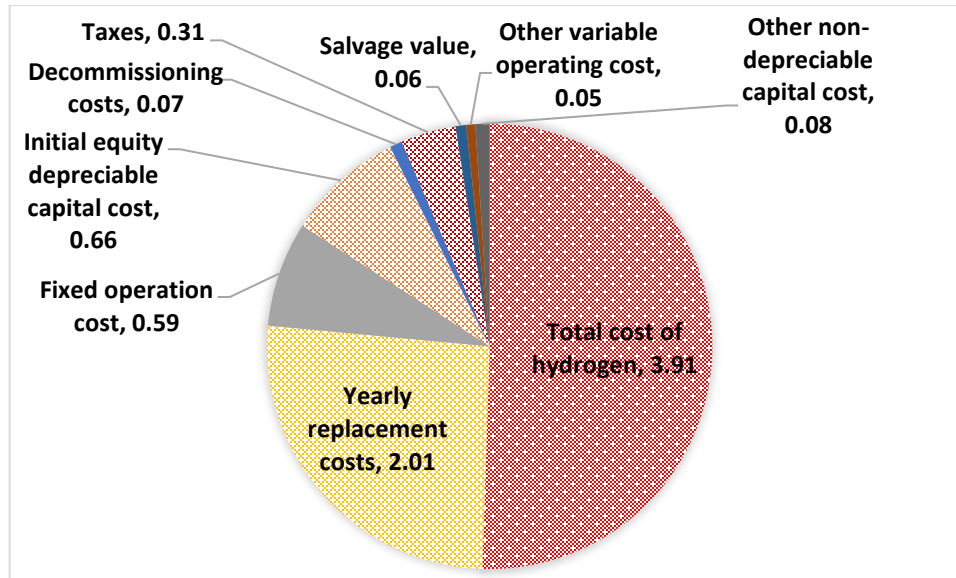


Figure 5.47. Costs of hydrogen and other related costs (\$/kg) in a large-scale Cu-Cl cycle plant with a capacity of 1000 kg/dayH₂.

5.7. Optimization Study Results

One of the ANN performance measures is the mean square error (MSE) which evaluates the average of the squares of the errors or the average squared difference between the estimated value and actual value of the ANN. A low value of the MSE is desired for better performance of the neural network. The other neural network process function is regression in which the R-value (regression presenter factor) near 1.0 indicates a better model prediction for the calculated outputs compared to the actual one, while 0.0 indicates a random relation as predicted by a neural network.

To predict the desired objective values from the input variables, a proper number of hidden layers should be inserted in the neural network procedure steps. This can be achieved by trial and error starting from the minimum number (in this work, 10) to reduce the computational time and cost. A typical trial and error practice is provided in Table 5.15 in which the training samples are presented to the network during training and the network is adjusted according to its error.

Table 5.15. Training results of the ANN-based on Bayesian regularization for different numbers of hidden layers

Number of Hidden Layers	Training mean square method error	Testing mean square method error	Training regression	Testing Regression
75	4.19×10^{-5}	6.024×10^{-3}	0.99045	0.99665
85	9.5×10^{-7}	1.38×10^{-5}	0.99526	1
95	6.55×10^{-7}	1.66×10^{-5}	0.99597	1

The validation samples are used to measure network generalization, and to halt training when generalization stops and improves for the rest of the samples employed for testing that have no effect on training. This provides an independent measure of network performance during and after training. The percentage of training, validation and testing are considered 75%, 15% and 15%, respectively. After several trial and error runs, the best number of hidden layers was found as 85 for the training method of Bayesian Regularization. The ANN model results are shown in Table 5.15. This indicates that an increase of hidden layers to more than 85 shows no significant improvement in the model accuracy while keeping the same training method. The results of the ANN model performance for Bayesian Regularization training with 85 hidden layers is presented in Figure 5.48.

The Matlab function generated by ANN is optimized by the GA method which provides the optimal operating condition for the lab-scale integrated Cu-Cl cycle. As noted earlier, the decision variables are the St/Cu molar ratio and the temperature of the main reactors including hydrolysis, thermolysis, PSDU, electrolyzer, and anolyte recovery separators. The objective functions aim to maximize the exergetic efficiency and minimize operational costs per mole of produced hydrogen.

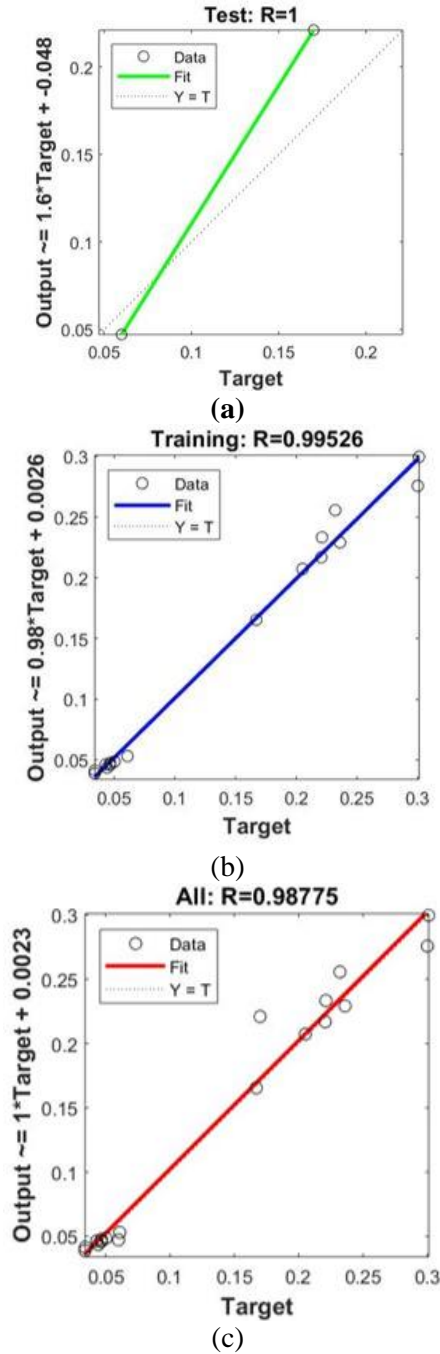


Figure 5.48. Regression plots (a) test (b) training (c) all of models for the supplied data

Figure 5.49 illustrates the Pareto optimum points of over 250 generations for the integrated Cu-Cl cycle with the objective functions of exergy efficiency and operational costs of the produced hydrogen. In the graph, a negative sign is assigned for the exergy efficiency. This occurs since the multi-objective optimization permits only minimization of the objective function. So the exergy efficiency data are turned into positive values and

the graph is replotted. It is shown that the operational costs of produced hydrogen increase slightly as the second law efficiency of the cycle increases to about 35%. With an increase of exergy efficiency from 35% to 36.7%, the operational costs of produced hydrogen grow significantly.

It is shown in Figure 5.49 that the maximum exergy efficiency belongs to point B (36.8%), where the operational hydrogen production cost is around 11.1\$/kmolH₂. The design point B is determined as the optimum point once the exergy efficiency is considered as the single objective function. The minimum operational cost of produced hydrogen occurs at point A (8.8\$/kmolH₂) and can be referred as the optimum value when the objective function is the sole objective function. For the multi-objective optimization, it is required to use the decision making procedure for selecting the final optimum solution from the Pareto frontier optimal solutions. This would be achieved by determining the hypothetical ideal point in Figure 5.49 at which both objective functions are their optimum values, independently. It is impossible that both objective functions possess their optimal value at the same time indicating that the ideal point is not placed on the Pareto frontier optimal solution as shown in Figure 5.49.

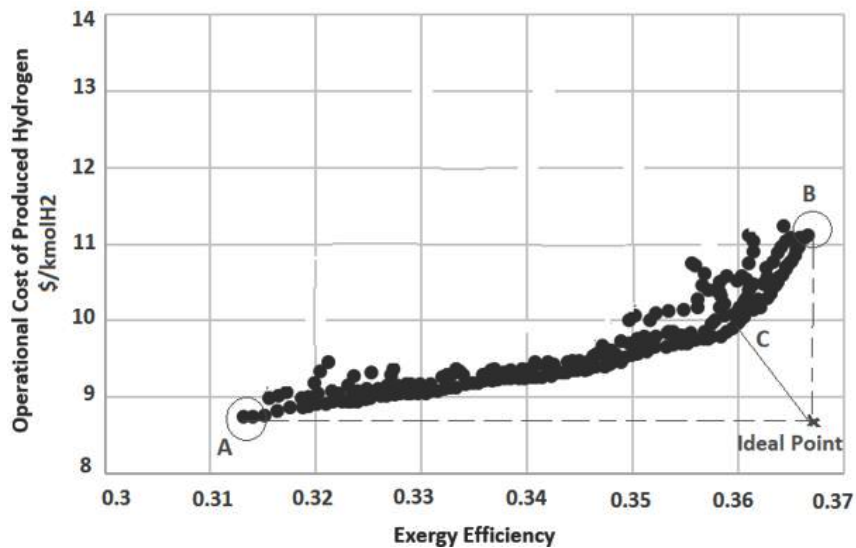


Figure 5.49 . Pareto front from multi-objective optimization results

According to Figure 5.49 the more close a point lies to the ideal point, then the more the optimal solution exists in terms of both objective functions to be obtained (in this case, point C is the closest to the ideal point). This method is reliable when the variation of both

objective functions is almost identical at the optimum area (i.e. a small increase in the exergy efficiency should not result in more enlargement at the operational cost). Based on Figure 5.49 for this case, changes in the value of operational costs of produced hydrogen and exergy efficiency are generally of the same order which verifies that point C is the optimum point in terms of both operational cost of produced hydrogen and exergy efficiency. The optimal values of operational parameters for points A, B, and C and their corresponding operational costs of produced hydrogen and exergy efficiency are tabulated in Table 5.16.

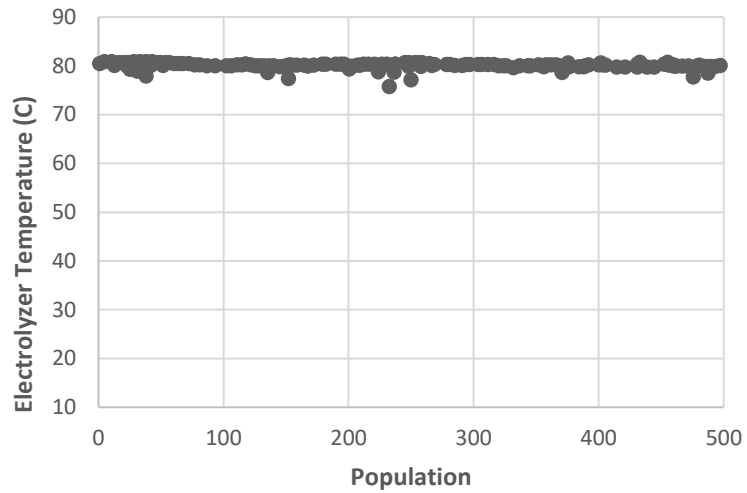
Table 5.16. Design input parameters and objective functions for three different points on the Pareto frontier of Figure 10b

Design input parameters and objective functions	Point A	Point B	Point C
Steam to copper chloride molar ratio (St/Cu)	17	21	19
Hydrolysis reaction temperature	390°C	400°C	390°C
Thermolysis reaction temperature	540°C	580°C	540°C
LP PSDU temperature	108°C	112°C	108°C
HCl/CuCl (aq) electrolyzer temperature	80°C	80°C	80°C
Average temperature of anolyte recovery separation units	115°C	125°C	115°C
Exergy efficiency	0.303	0.368	0.357
Operational cost of produced hydrogen	8.8\$/kmolH ₂	11.1\$/kmolH ₂	9.8\$/kmolH ₂

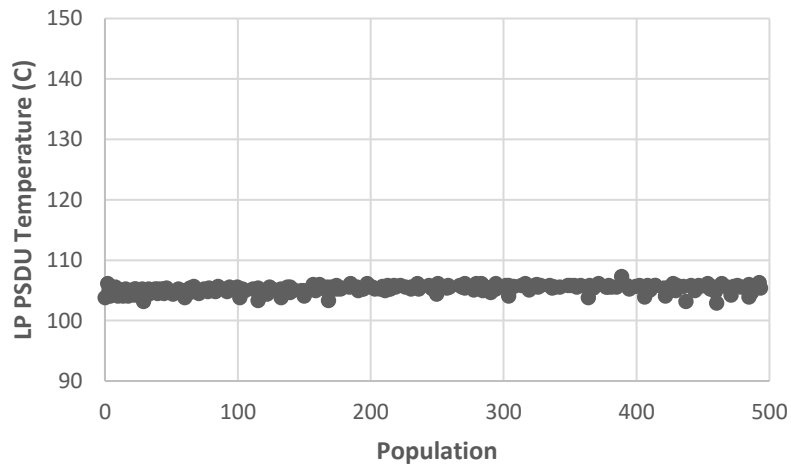
The scattered distribution of optimal input parameters is depicted in Figure 5.50 (a-e) to provide a view of the changes in design parameters based on their upper and lower bounds. Based on the results, it can be concluded that the electrolyzer temperature (Figure 5.50 a) meets its maximum value which indicates that the increase of anolyte temperature results in an improvement in both objective functions and consequently better optimization results. It can be observed from Figure 5.50b that the optimal value for the low pressure side of the PSDU is concentrated at 108°C. This shows the optimum operating temperature for the LP of PSDU in terms of both operating cost of produced hydrogen and exergy efficiency.

Other input design parameters in Figure 5.50(c, d, e and f) include the St/Cu molar ratio, hydrolysis reaction temperature, thermolysis reaction temperature, and average

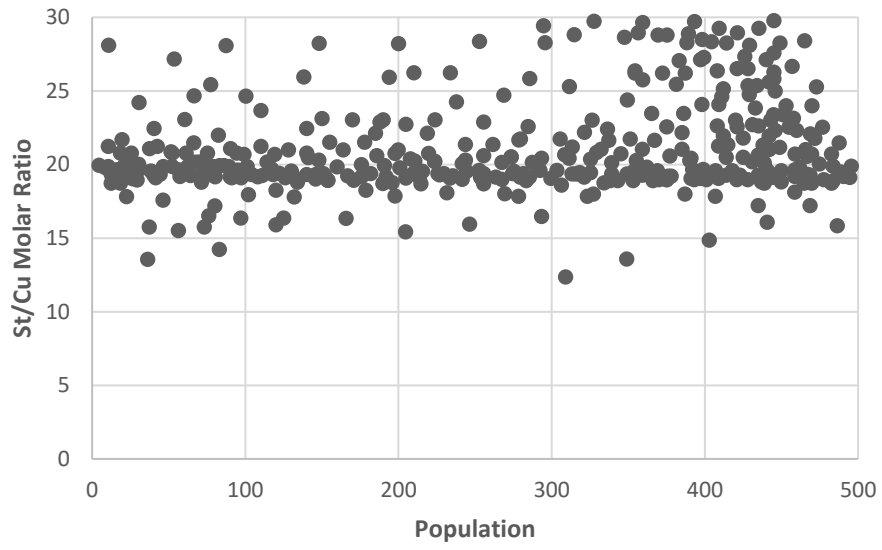
temperature of anolyte recovery separator units. This indicates the significant effects of these design parameters on making a compromise between two objective functions. Furthermore, this suggests that changes in these input decision variables lead to a conflict between the exergy efficiency and operating cost of produced hydrogen over a small range of their changes. In order to investigate this trend and the impact of these parameters on the exergy efficiency and operational cost in the Pareto optimal results, the changes of two objective functions with changes of these design parameters are studied further.



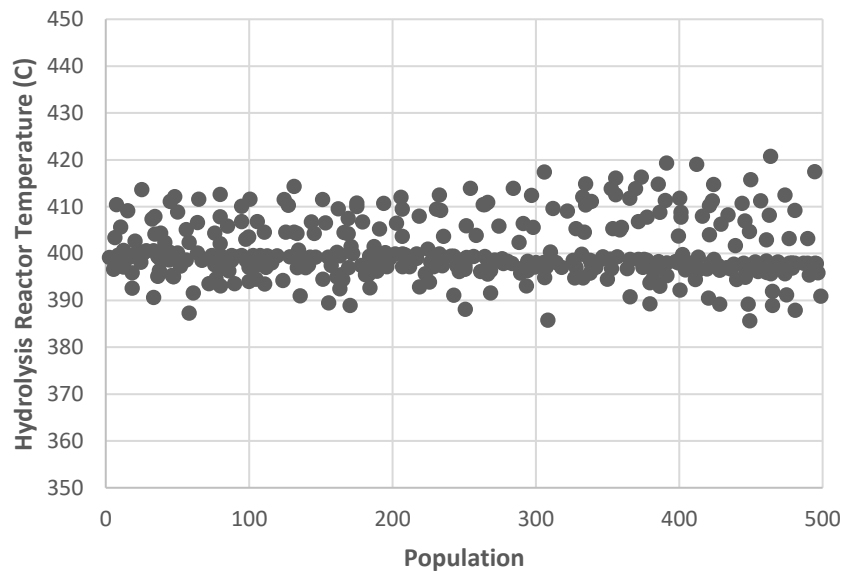
(a)



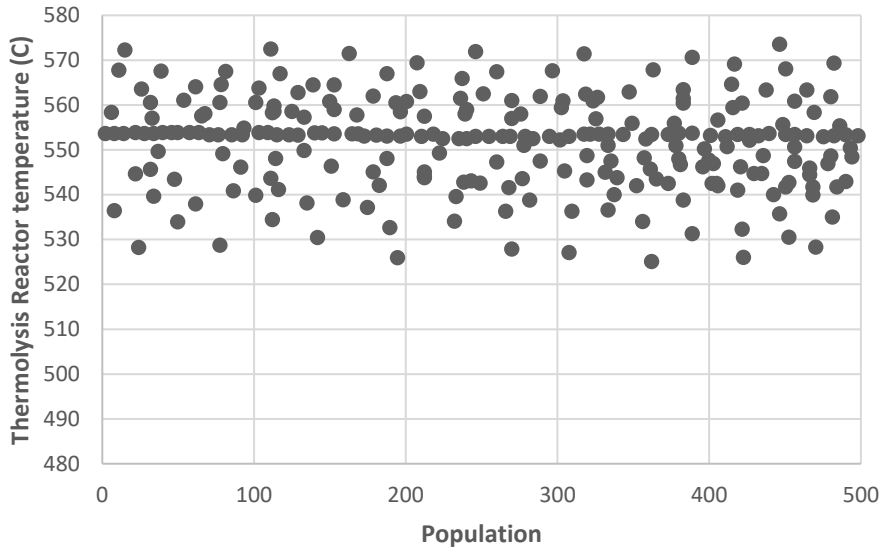
(b)



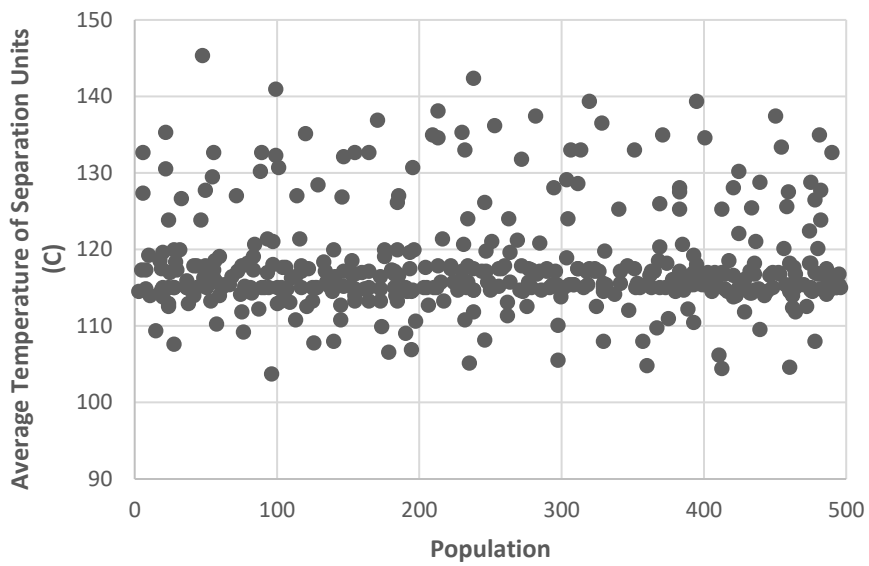
(c)



(d)



(e)



(f)

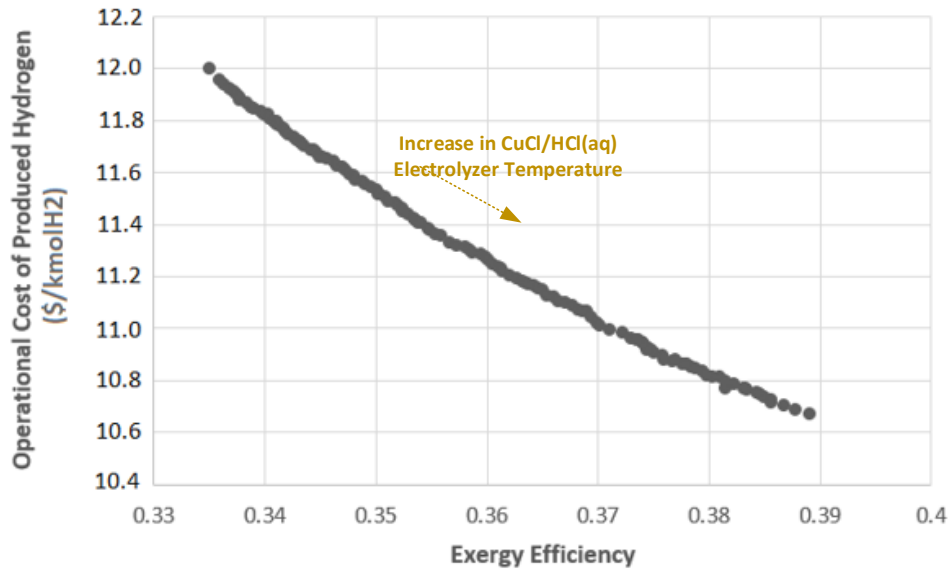
Figure 5.50. Distribution of variables for the Pareto optimal front in Figure 5.49.

The effects of increasing the electrolyzer temperature on the objective functions of exergy efficiency and operational costs of produced hydrogen are illustrated in Figure 5.51a. It can be seen that with the increase of anolyte temperature from the lower bond to the upper bond, the exergy efficiency increases but the operational cost of produced hydrogen declines. This indicates that the operation of the electrolyzer at the higher anolyte

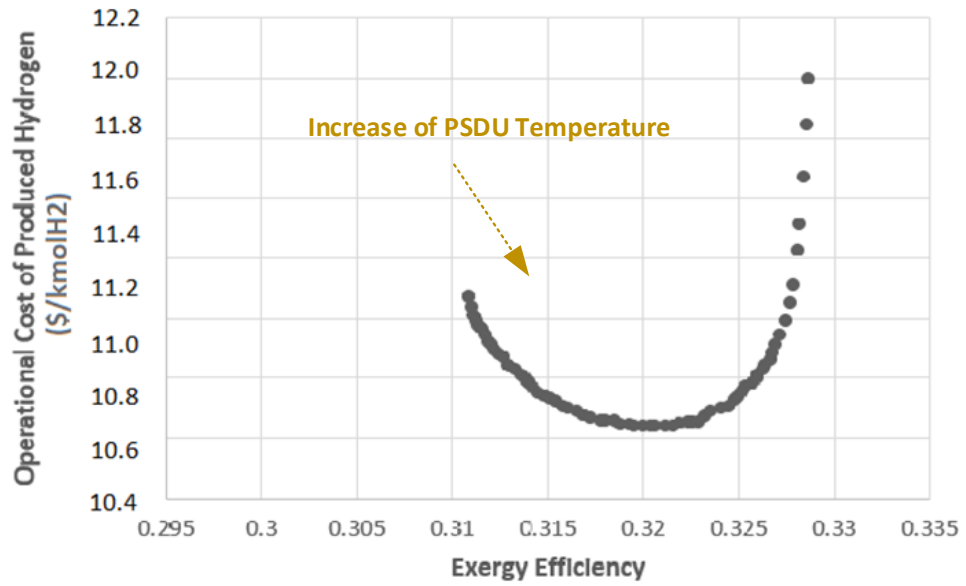
temperatures favors both objective functions. Therefore, the optimal anolyte temperatures in Figure 5.50a are aggregated at the maximum value (upper bound).

The effect of the LP side of PSDU on the exergy efficiency and operational cost of produced hydrogen in the Pareto curve is depicted in Figure 5.51b. As can be observed from Figure 5.51b, with the increase of LP temperature, the exergy efficiency increases, while the operational cost of produced hydrogen decreases at first and then the objective function increases. So it is suggested that with an increment of LP distillation temperature after the saturated vapor (higher than 108°C that is placed in the superheat region), this leads to an increase of supplied heat for this unit (increase of operational cost), while there is no significant improvement in the distillation process. The same trend exists for the sensitivity study of Pareto frontier points for the St/Cu molar ratio (Figure 5.51c), hydrolysis temperature (Figure 5.51d) and an average temperature of anolyte recovery separator units (Figure 5.51 f) indicating the scattered distribution of optimal values for these design parameters.

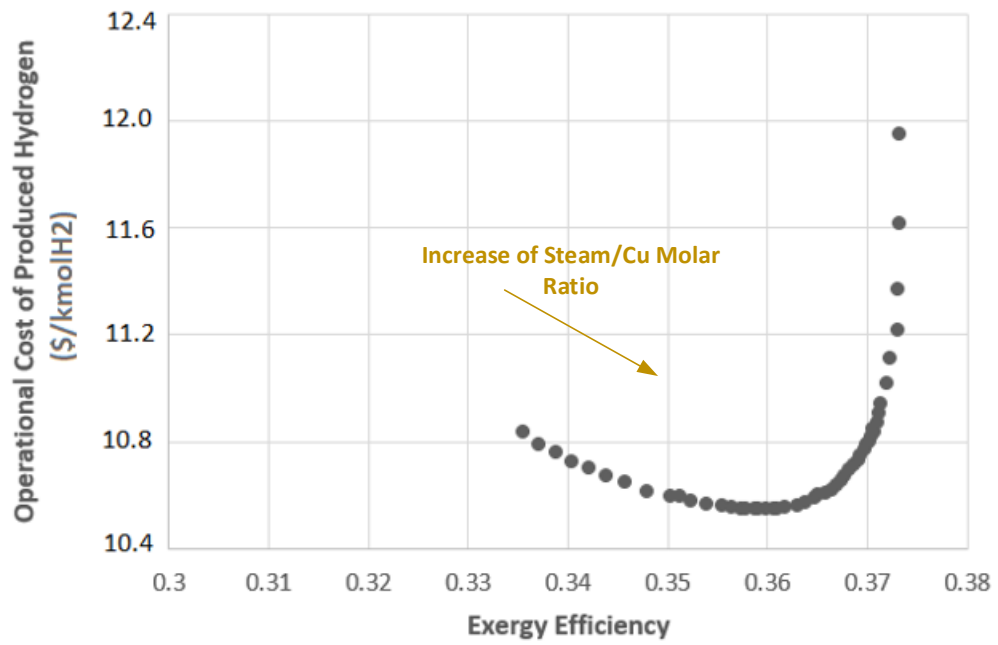
Figure 5.51e presents the changes in the objective function with variations in the thermolysis temperature. With an increase in this reactor temperature from the lower bound to the upper bound, the exergy efficiency increases consistently. The operational costs of produced hydrogen decrease (improvement in both objective functions) and then increase with further increases of thermolysis reactor temperature. Since the region at which both objective functions are in agreement is larger than the region they are in conflict, the reaction temperature is expected to have a scattered distribution. So, the temperature of the thermolysis reaction exhibits a scattered distribution mostly concentrated in the maximum reactor temperature value. This trend is confirmed by Figure 5.50e.



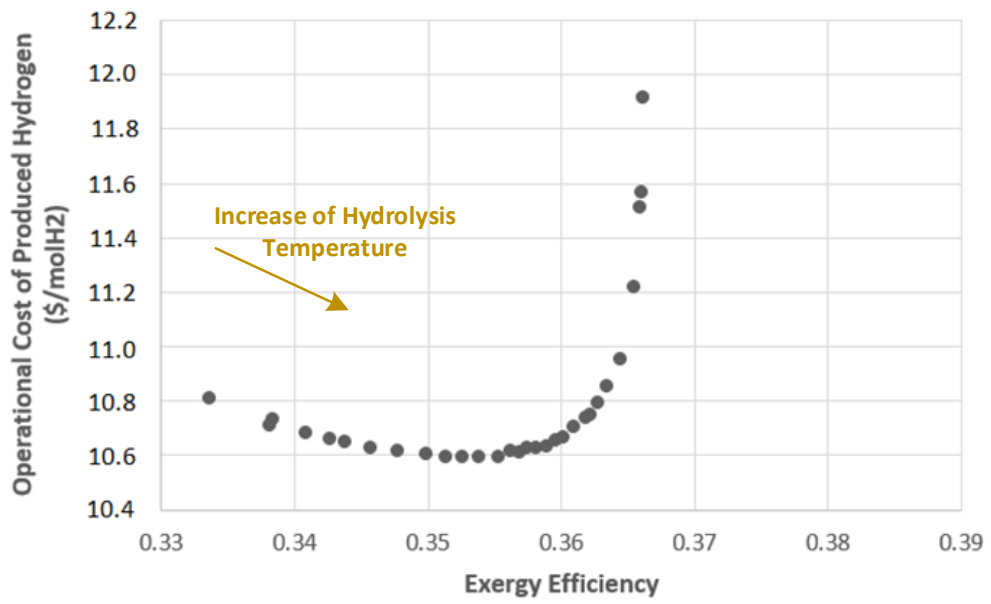
(a)



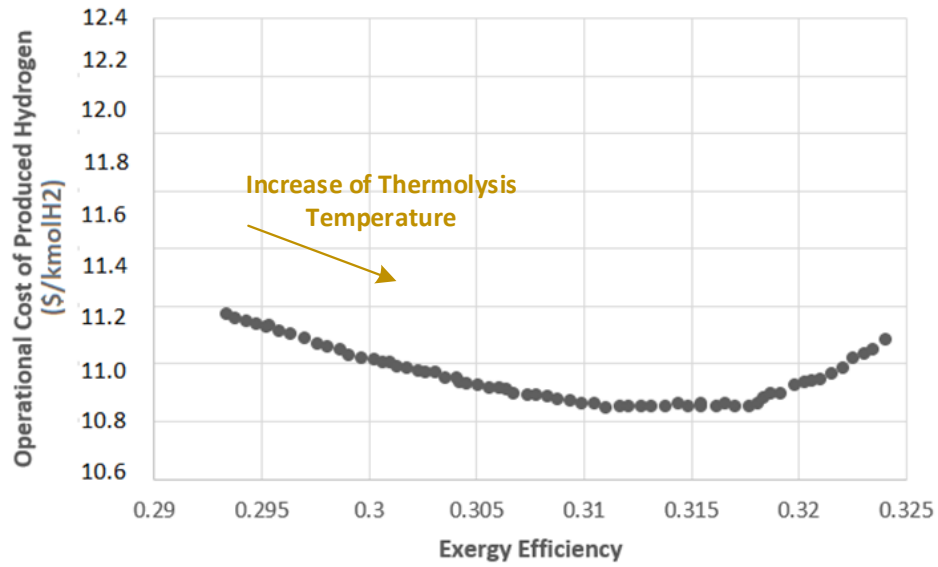
(b)



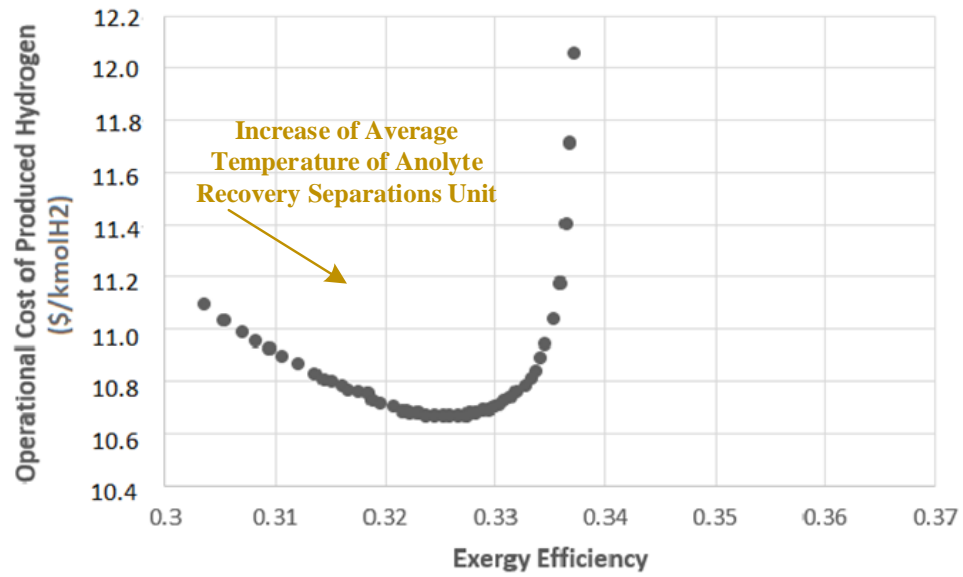
(c)



(d)



(e)



(f)

Figure 5.51. Variation of exergy efficiency with total cost for the optimum design parameters (a) HCl/CuCl (aq) electrolyzer; (b) PSDU; (c) St/Cu molar ratio; (d) hydrolysis temperature; (e) thermolysis temperature; and (f) average temperature of anolyte recovery separations unit

Chapter 6 . Conclusions and Recommendations

This chapter provides the concluding remarks derived from the thesis. Then the recommendation section presents the ideas inferred from the results of this work for further analysis and studies in this research area.

6.1. Conclusions

Hydrogen can be used for cleaner transportation, cleaner energy sources of industrial processes to provide economically promising and energetically efficient solutions. The Cu-Cl cycle offers promising viability for large-scale hydrogen production with nuclear or solar energy. This thesis demonstrates the practical integration of Cu-Cl cycle at UOIT with the capacity of 100 g H₂/day for the first time. The integrated facility is introduced and analyzed to establish the large-scale feasibility of the Cu-Cl cycle. For the GA multi-objective optimization, the neural network with machine learning was employed to connect the Aspen Plus simulation results and optimizations by generating a mathematical function that relates the decision variable (St/Cu molar ratio and temperature of reactors) and objective functions (exergy efficiency and operational cost). Also, through the exergoeconomic approach, the cost of exergy flows and destroyed exergy of each component is analyzed, along with exergoeconomic factors for assessing the cost-effectiveness of each component. The concluding remarks are provided for the overall cycle and its component as follows.

- In the hydrolysis reactor, from the hydrodynamic results, the CuCl₂ terminal velocity increases with an increase of temperature gradient between two sides of the reactor, CuCl₂(aq) volume flow rate, operating temperature, and particle size.
- The SCM results show that the reaction of solid CuCl₂ (size of 200 μm) with superheated steam is controlled by both diffusion through the product layer control and chemical reaction control.
- For the design parameters of the lab-scale reactor, an average reactant residence time is estimated to be around 91s which is adequate to reach the reaction temperature and then fully convert into products.
- In the CuCl/HCl(aq) electrolyzer, from the electrochemical results, with the stack current density of 0.5 A.cm⁻² and increment of stack temperature from 25°C to

65°C, the stack voltage declines from 6.17 V to 5.8 V and the average stack efficiency improves from 68% to 72%.

- The hydrodynamic study of electrolyzer stack showed that the cells close to the input anolyte or catholyte feed port have a higher voltage efficiency than the average stack voltage efficiency. The flow spread through the stack is relatively uniform due to a lower pressure drop for the anolyte and catholyte liquid-phase flow in the electrolyzer compared to the regular water electrolysis which operates with gaseous-phase reactants.
- In the PSDU, the flow stream's thermodynamic flowsheet data extracted from Aspen Plus confirms the feasibility of HCl-water separation up to the azeotropic concentration. The high-pressure distillation system enhances the mole fraction of HCl (aq) from 0.11 up to 0.21 and the increase of reflux ratio and feed temperature assist it to be higher.
- In PSDU, an increment of 76% and 42% for the condensation and re-boiler heat duties with the growth of the reflux ratio indicate the significant impact of this parameter on the high pressure distillation column.
- From both mass transfer analysis (number of trays determination by the McCabe-Thiele method) and heat transfer analysis (heat transfer coefficient specification), the height of the packing column has been determined to be about 2 m and 1.7 m for the high and low pressure distillation columns, respectively.
- From the exergoeconomic results, the relatively high values of the exergoeconomic factor for the CuCl/HCl (aq) electrolyzer (0.95) and PSDU (0.92) show that the cost rate contribution to the related cost of the component is dominant over the cost of the destroyed exergy. It is recommended to reduce the capital investment of this equipment at the expense of increasing the exergy destruction to have a more cost-effective cycle.
- In the case of the annual operation time increment from 500h to 3000h, the total cost rate of the Cu-Cl cycle decreases by about 48%.
- From the MOGA optimization study, the optimal values obtained for the exergy efficiency (35.7%) and operational cost of produced hydrogen (9.8\$/kmolH₂) are associated with the hydrolysis temperature of 380°C, thermolysis temperature of

540°C, PSDU temperature of 108°C, average separation units temperature of 115°C and St/Cu molar ratio of 19.

- The thermolysis temperature exhibits a scattered distribution mostly concentrated around the maximum temperature value (540°C) indicating a conflict between the overall exergy efficiency and operational cost. While, the optimal anolyte temperatures are aggregated at the maximum value (80°C) indicating that the increase of electrolyzer temperature does not result in a conflict between the two objective functions.

6.2. Recommendations

This section presents some ideas found to be worthwhile for study in the future. These suggestions will help researchers for more cycle understanding and predicting the cycle behavior in response to different operating and design conditions. The suggestions are listed as follows:

- Developing a multi-physics model incorporating mass transfer, heat transfer, electrochemistry and flow dynamic, simultaneously to study the CuCl/HCl(aq) electrolyzer behavior under different test conditions. This idea can be attained by developing a comprehensive program in Comsol multi-physics software including the user-defined modules since there is not enough electrochemical data in this software.
- Performing measurements to find out the proper kinetic parameters; for instance, the best formulations using analytical methods for the consumption of cupric chloride particles in a new hydrolysis reactor which operates based on the temperature differences at two sides of the reactor.
- Testing each component within the integrated Cu-Cl cycle experimentally to determine the practical challenges faced during each experiment and modify them, accordingly.
- Conducting a comprehensive experimental study for the whole integrated Cu-Cl cycle to determine the cycle performance in response to different operating conditions.

- Integrating of the large-scale integrated Cu-Cl cycle with the thermal systems specifically nuclear and solar for heat recovery purposes which can improve significantly the cycle's efficiency. One of the practical ways of upgrading the waste heat is to employing heat pumps within the cycle.
- Investigating the designing engineering equipment issues at a larger scale hydrogen production with the Cu-Cl cycle, including the required capacities of feed materials, heat requirements, steam supply, multiphase reactor equipment, thermal management of exothermic reactor, HCl gas absorption tower and operation of a sedimentation vessel for copper separation.
- Analyzing and comparing different kinds of membranes and electrode materials. With the increment of the electrolyzer operating temperature beyond 60°C, this results in a considerable amount of HCl vapor escape from the stack which leads to a lower concentration of HCl acid over a long period of operation. It is recommended to investigate the increase in system pressure to allow the higher temperature operation without having the HCl loss problem.
- Performing an exergo-environmental analysis of the hybrid large-scale Cu-Cl cycle to recognize the location, magnitude, and causes of environmental impacts.
- Proposing other technologies for some components within the Cu-Cl cycle that can provide the same function in a more effective way to increase the system efficiencies.
- Investigating the electrolyzer degradation processes using electrochemical impedance spectroscopy (EIS) and linear sweep voltammetry (LSV).
- Exploring and using other than Pt catalyst on membrane to reduce cost and eliminating copper precipitation.

References

- [1] G. Naterer et al., "Recent Canadian advances in nuclear-based hydrogen production and the thermochemical Cu-Cl cycle," *Int. J. Hydrogen Energy*, vol. 34, no. 7, pp. 2901–2917, Apr. 2009.
- [2] "The Future of Hydrogen," *Futur. Hydrog.*, no. June, 2019.
- [3] V. N. Daggupati, G. F. Naterer, K. S. Gabriel, R. J. Gravelins, and Z. L. Wang, "Solid particle decomposition and hydrolysis reaction kinetics in Cu-Cl thermochemical hydrogen production," *Int. J. Hydrogen Energy*, vol. 35, no. 10, pp. 4877–4882, 2010.
- [4] Z. Wang, G. F. Naterer, and K. Gabriel, "Multiphase reactor scale-up for Cu-Cl thermochemical hydrogen production," *Int. J. Hydrogen Energy*, vol. 33, no. 23, pp. 6934–6946, 2008.
- [5] S. Abanades, P. Charvin, G. Flamant, and P. Neveu, "Screening of water-splitting thermochemical cycles potentially attractive for hydrogen production by concentrated solar energy," *Energy*, vol. 31, no. 14, pp. 2805–2822, 2006.
- [6] "Argonne National Laboratory (ANL)," 2010.
- [7] G. F. Naterer, I. Dincer, and C. Zamfirescu, *Hydrogen Production from Nuclear Energy*. London: Springer London, 2013.
- [8] M. Al-Zareer, I. Dincer, and M. A. Rosen, "Development and assessment of a novel integrated nuclear plant for electricity and hydrogen production," *Energy Convers. Manag.*, vol. 134, pp. 221–234, 2017.
- [9] G. F. Naterer, M. Fowler, J. Cotton, and K. Gabriel, "Synergistic roles of off-peak electrolysis and thermochemical production of hydrogen from nuclear energy in Canada," *Int. J. Hydrogen Energy*, 2008.
- [10] J. D. Holladay, J. Hu, D. L. King, and Y. Wang, "An overview of hydrogen production technologies," *Catalysis Today*. 2009.
- [11] V. N. Balashov, R. S. Schatz, E. Chalkova, N. N. Akinfiyev, M. V. Fedkin, and S. N. Lvov, "CuCl Electrolysis for Hydrogen Production in the Cu-Cl Thermochemical Cycle," *J. Electrochem. Soc.*, vol. 158, no. 3, p. B266, 2011.
- [12] M. F. Orhan, I. Dinçer, and M. A. Rosen, "Efficiency comparison of various design schemes for copper-chlorine (Cu-Cl) hydrogen production processes using Aspen Plus software," *Energy Convers. Manag.*, vol. 63, pp. 70–86, Nov. 2012.
- [13] M. Dokiya and Y. Kotera, "Hybrid cycle with electrolysis using CuCl system," *Int. J. Hydrogen Energy*, vol. 1, no. 2, pp. 117–121, 1976.
- [14] M. A. Lewis and J. G. Masin, "The evaluation of alternative thermochemical cycles - Part II: The down-selection process," *Int. J. Hydrogen Energy*, vol. 34, no. 9, pp. 4125–4135, 2009.
- [15] R. Perret et al., "II . G High-Temperature Thermochemical Processes II . G . 1 High Efficiency Generation of Hydrogen Using Solar Thermochemical Splitting of Water *," pp. 135–140, 2004.
- [16] Z. L. Wang, G. F. Naterer, K. S. Gabriel, R. Gravelins, and V. N. Daggupati, "Comparison of different copper-chlorine thermochemical cycles for hydrogen production," *Int. J. Hydrogen Energy*, vol. 34, no. 8, pp. 3267–3276, 2009.
- [17] F. Information and E. Meeting, "N uclear Production of Hydrogen," no. April 2009, 2010.

- [18] G. F. Naterer et al., "Canada's program on nuclear hydrogen production and the thermochemical Cu-Cl cycle," *Int. J. Hydrogen Energy*, vol. 35, no. 20, pp. 10905–10926, 2010.
- [19] B. W. Mcquillan et al., "HIGH EFFICIENCY GENERATION OF HYDROGEN FUELS USING SOLAR THERMAL-CHEMICAL SPLITTING OF WATER (SOLAR THERMO-CHEMICAL SPLITTING FOR H₂) Solar Thermochemical Hydrogen for the US Department of Energy and F03-STCH2-002 for the University of Nevada," no. December, 2010.
- [20] A. Farsi, C. Zamfirescu, I. Dincer, and G. F. Naterer, "Thermodynamic assessment of a lab-scale experimental copper-chlorine cycle for sustainable hydrogen production," *Int. J. Hydrogen Energy*, vol. 44, no. 33, pp. 17595–17610, 2019.
- [21] "Carty, R H, MAzumder, M M, Schreider, J D, & Pangborn, J B. Thermochemical hydrogen production. Volume 4: Appendix C. Impacts of materials development for thermochemical water-splitting processes. Final report Jan 72-Dec 80 . United States.," vol. 4, p. 80.
- [22] A. Farsi, Ö. Kayhan, C. Zamfirescu, I. Dincer, and G. F. Naterer, "Thermodynamic model of pressure swing distillation for a high pressure process of hydrochloric/water separation and hydrogen production," *Int. J. Hydrogen Energy*, vol. 44, no. 7, pp. 3481–3491, 2019.
- [23] A. Farsi, Ö. Kayhan, C. Zamfirescu, I. Dincer, and G. F. Naterer, "Azeotropic pressure swing distillation of hydrochloric-water for hydrogen production in the Cu-Cl cycle: Thermodynamic and design methods," *Int. J. Hydrogen Energy*, vol. 44, no. 16, pp. 7969–7982, 2019.
- [24] A. Farsi, C. Zamfirescu, I. Dincer, and G. F. Naterer, "Electrochemical Transport in CuCl/HCl(aq) Electrolyzer Cells and Stack of the Cu-Cl Cycle," *J. Electrochem. Soc.*, vol. 167, no. 4, p. 044515, 2020.
- [25] A. Farsi, Ö. Kayhan, C. Zamfirescu, I. Dincer, and G. F. Naterer, "Kinetic and hydrodynamic analyses of chemically reacting gas-particle flow in cupric chloride hydrolysis for the Cu-Cl cycle," *Int. J. Hydrogen Energy*, vol. 44, no. 49, pp. 26783–26793, 2019.
- [26] M. S. Ferrandon, M. A. Lewis, F. Alvarez, and E. Shafirovich, "Hydrolysis of CuCl₂ in the Cu-Cl thermochemical cycle for hydrogen production: Experimental studies using a spray reactor with an ultrasonic atomizer," *Int. J. Hydrogen Energy*, vol. 35, no. 5, pp. 1895–1904, 2010.
- [27] M. S. Ferrandon et al., "Hydrogen production by the Cu-Cl thermochemical cycle: Investigation of the key step of hydrolysing CuCl₂ to Cu₂OCl₂ and HCl using a spray reactor," *Int. J. Hydrogen Energy*, vol. 35, no. 3, pp. 992–1000, 2010.
- [28] L. Croizé et al., "Interest of absorption spectroscopy for the control of industrial processes. Application to H₂ massive production," *Appl. Phys. B Lasers Opt.*, vol. 100, no. 2, pp. 409–415, 2010.
- [29] M. A. Lewis, J. G. Masin, and P. A. O'Hare, "Evaluation of alternative thermochemical cycles, Part I: The methodology," *Int. J. Hydrogen Energy*, vol. 34, no. 9, pp. 4115–4124, 2009.
- [30] R. V. Singh et al., "Investigations on the hydrolysis step of copper-chlorine thermochemical cycle for hydrogen production," *Int. J. Energy Res.*, vol. 44, no. 4, pp. 2845–2863, 2020.

- [31] G. Naterer et al., "Recent Canadian advances in nuclear-based hydrogen production and the thermochemical Cu-Cl cycle," *Int. J. Hydrogen Energy*, vol. 34, no. 7, pp. 2901–2917, 2009.
- [32] S. Ranganathan and E. B. Easton, "Anode electrode materials for use in the Cu-Cl Thermochemical Cycle for the production of hydrogen," vol. 2, pp. 1–6, 2009.
- [33] P. I. M. Lewis, "Electrolyzer Development for the Cu-Cl Thermochemical Cycle," Presentation, pp. 1–30, 2012.
- [34] G. F. Naterer et al., "Clean hydrogen production with the Cu-Cl cycle-Progress of international consortium, II: Simulations, thermochemical data and materials," *Int. J. Hydrogen Energy*, vol. 36, no. 24, pp. 15486–15501, 2011.
- [35] S. Ranganathan and E. B. Easton, "High performance ceramic carbon electrode-based anodes for use in the Cu-Cl thermochemical cycle for hydrogen production," *Int. J. Hydrogen Energy*, 2010.
- [36] G. F. Naterer et al., "Clean hydrogen production with the Cu-Cl cycle-Progress of international consortium, I: Experimental unit operations," *Int. J. Hydrogen Energy*, vol. 36, pp. 15472–15485, 2011.
- [37] E. Agar, K. W. Knehr, D. Chen, M. A. Hickner, and E. C. Kumbur, "Species transport mechanisms governing capacity loss in vanadium flow batteries: Comparing Nafion® and sulfonated Radel membranes," *Electrochim. Acta*, vol. 98, pp. 66–74, 2013.
- [38] S. L. Cobourn and E. B. Easton, "The effect of copper contamination at the cathode of Cu-Cl/HCl electrolyzers," *Int. J. Hydrogen Energy*, vol. 42, no. 47, pp. 28157–28163, 2017.
- [39] D. M. Hall and S. N. Lvov, "Modeling a CuCl(aq)/HCl(aq) Electrolyzer using Thermodynamics and Electrochemical Kinetics," *Electrochim. Acta*, vol. 190, pp. 1167–1174, 2016.
- [40] S. Suppiah et al., "Canadian nuclear hydrogen R & D programme : Development of the medium-temperature Cu-Cl cycle and contributions to the high-temperature sulphur-iodine cycle," pp. 77–87.
- [41] E. Hosgor, T. Kucuk, I. N. Oksal, and D. B. Kaymak, "Design and control of distillation processes for methanol-chloroform separation," *Comput. Chem. Eng.*, 2014.
- [42] K. W. Kim, J. S. Shin, S. H. Kim, S. K. Hong, J. H. Cho, and S. J. Park, "A computational study on the separation of acetonitrile and water azeotropic mixture using pressure swing distillation," *J. Chem. Eng. Japan*, 2013.
- [43] A. M. Fulgueras, D. S. Kim, and J. Cho, "Modeling and optimization study of pressure-swing distillation for the separation process of acetone-methanol mixture with vapor-liquid equilibrium analysis," *J. Chem. Eng. Japan*, 2016.
- [44] W. L. Luyben and I. L. Chien, *Design and Control of Distillation Systems for Separating Azeotropes*. 2010.
- [45] I. Dinçer and C. Zamfirescu, *Sustainable hydrogen production*. Elsevier, 2016.
- [46] M. F. Orhan, I. Dincer, and M. A. Rosen, "Exergy analysis of heat exchangers in the copper-chlorine thermochemical cycle to enhance thermal effectiveness and cycle efficiency," *Int. J. Low-Carbon Technol.*, vol. 6, no. 3, pp. 156–164, 2011.
- [47] M. Al-Zareer, I. Dincer, and M. A. Rosen, "Analysis and assessment of the integrated generation IV gas-cooled fast nuclear reactor and copper-chlorine cycle

- for hydrogen and electricity production,” *Energy Convers. Manag.*, vol. 205, no. July 2019, p. 112387, 2020.
- [48] F. Razi, I. Dincer, and K. Gabriel, “Thermal management of a new integrated copper-chlorine cycle for hydrogen production,” *Energy Convers. Manag.*, vol. 212, no. February, p. 112629, 2020.
- [49] H. Ishaq, I. Dincer, and G. F. Naterer, “New trigeneration system integrated with desalination and industrial waste heat recovery for hydrogen production,” *Appl. Therm. Eng.*, vol. 142, no. July, pp. 767–778, 2018.
- [50] G. F. Naterer, V. N. Daggupati, G. Marin, K. S. Gabriel, and Z. L. Wang, “Thermochemical hydrogen production with a copper-chlorine cycle, II: Flashing and drying of aqueous cupric chloride,” *Int. J. Hydrogen Energy*, 2008.
- [51] S. Ghandehariun, M. A. Rosen, G. F. Naterer, and Z. Wang, “Comparison of molten salt heat recovery options in the Cu-Cl cycle of hydrogen production,” *Int. J. Hydrogen Energy*, vol. 36, no. 17, pp. 11328–11337, 2011.
- [52] O. Jaber, G. F. Naterer, and I. Dincer, “Heat recovery from molten CuCl in the Cu-Cl cycle of hydrogen production,” *Int. J. Hydrogen Energy*, 2010.
- [53] O. Jaber, G. F. Naterer, and I. Dincer, “Convective heat transfer from molten salt droplets in a direct contact heat exchanger,” *Heat Mass Transf. und Stoffuebertragung*, 2010.
- [54] M. F. Orhan, I. Dincer, and G. F. Naterer, “Cost analysis of a thermochemical Cu-Cl pilot plant for nuclear-based hydrogen production,” *Int. J. Hydrogen Energy*, 2008.
- [55] H. Ishaq and I. Dincer, “Design and performance evaluation of a new biomass and solar based combined system with thermochemical hydrogen production,” *Energy Convers. Manag.*, vol. 196, no. March, pp. 395–409, 2019.
- [56] A. Ozbilen, I. Dincer, and M. A. Rosen, “Development of a four-step Cu-Cl cycle for hydrogen production – Part II: Multi-objective optimization,” *Int. J. Hydrogen Energy*, vol. 41, no. 19, pp. 7826–7834, May 2016.
- [57] H. Ozcan and I. Dincer, “Exergoeconomic optimization of a new four-step magnesium-chlorine cycle,” *Int. J. Hydrogen Energy*, 2016.
- [58] M. F. Orhan, I. Dincer, and M. A. Rosen, “An exergy-cost-energy-mass analysis of a hybrid copper-chlorine thermochemical cycle for hydrogen production,” *Int. J. Hydrogen Energy*, vol. 35, no. 10, pp. 4831–4838, 2010.
- [59] M. F. Orhan, I. Dincer, and M. A. Rosen, “Exergoeconomic analysis of a thermochemical copper-chlorine cycle for hydrogen production using specific exergy cost (SPECOC) method,” *Thermochim. Acta*, 2010.
- [60] A. Ozbilen, I. Dincer, and M. A. Rosen, “A comparative life cycle analysis of hydrogen production via thermochemical water splitting using a Cu-Cl cycle,” *Int. J. Hydrogen Energy*, vol. 36, no. 17, pp. 11321–11327, 2011.
- [61] A. Ozbilen, I. Dincer, and M. A. Rosen, “Environmental evaluation of hydrogen production via thermochemical water splitting using the Cu-Cl Cycle: A parametric study,” *Int. J. Hydrogen Energy*, vol. 36, no. 16, pp. 9514–9528, 2011.
- [62] H. Ishihara, H. Kaneko, N. Hasegawa, and Y. Tamaura, “Two-step water splitting process with solid solution of YSZ and Ni-ferrite for solar hydrogen production (ISEC 2005-76151),” in *Journal of Solar Energy Engineering, Transactions of the ASME*, 2008.

- [63] A. Steinfeld, "Solar hydrogen production via a two-step water-splitting thermochemical cycle based on Zn/ZnO redox reactions," *Int. J. Hydrogen Energy*, 2002.
- [64] Y. Bicer and I. Dincer, "Development of a multigeneration system with underground coal gasification integrated to bitumen extraction applications for oil sands," *Energy Convers. Manag.*, vol. 106, pp. 235–248, 2015.
- [65] C. Zamfirescu, I. Dincer, and G. F. Naterer, "Thermophysical properties of copper compounds in copper-chlorine thermochemical water splitting cycles," *Int. J. Hydrogen Energy*, vol. 35, no. 10, pp. 4839–4852, May 2010.
- [66] I. Dincer and G. F. Naterer, "Overview of hydrogen production research in the Clean Energy Research Laboratory (CERL) at UOIT," *Int. J. Hydrogen Energy*, vol. 39, no. 35, pp. 20592–20613, 2014.
- [67] H. Ozcan and I. Dincer, "Performance investigation of magnesium-chloride hybrid thermochemical cycle for hydrogen production," *Int. J. Hydrogen Energy*, vol. 39, pp. 76–85, 2014.
- [68] H. Ozcan and I. Dincer, "Modeling of a new four-step magnesium-chlorine cycle with dry HCl capture for more efficient hydrogen production," *Int. J. Hydrogen Energy*, vol. 41, no. 19, pp. 7792–7801, 2016.
- [69] M. F. Orhan, I. Dincer, and M. A. Rosen, "Energy and exergy assessments of the hydrogen production step of a copper–chlorine thermochemical water splitting cycle driven by nuclear-based heat," *Int. J. Hydrogen Energy*, vol. 33, pp. 6456–6466, 2008.
- [70] A. Ozbilen, I. Dincer, and M. A. Rosen, "Development of a four-step Cu–Cl cycle for hydrogen production – Part I: Exergoeconomic and exergoenvironmental analyses," *Int. J. Hydrogen Energy*, vol. 41, no. 19, pp. 7814–7825, May 2016.
- [71] M. Al-Zareer, I. Dincer, and M. A. Rosen, "Performance analysis of a supercritical water-cooled nuclear reactor integrated with a combined cycle, a Cu–Cl thermochemical cycle and a hydrogen compression system," *Appl. Energy*, vol. 195, pp. 646–658, 2017.
- [72] M. Al-Zareer, I. Dincer, and M. A. Rosen, "Development and analysis of an integrated system with direct splitting of hydrogen sulfide for hydrogen production," *Int. J. Hydrogen Energy*, vol. 41, no. 44, pp. 20036–20062, 2016.
- [73] M. Al-Zareer, I. Dincer, and M. A. Rosen, "Modeling and performance assessment of a new integrated gasification combined cycle with a water gas shift membrane reactor for hydrogen production," *Comput. Chem. Eng.*, vol. 103, pp. 275–292, 2017.
- [74] M. Al-Zareer, I. Dincer, and M. A. Rosen, "Development and assessment of a new solar heliostat field based system using a thermochemical water decomposition cycle integrated with hydrogen compression," *Sol. Energy*, vol. 151, pp. 186–201, 2017.
- [75] F. Khalid, "Development and analysis of a high temperature electrolyser for the Cu–Cl cycle for hydrogen production," p. PhD Thesis, 2017.
- [76] F. Khalid, I. Dincer, and M. A. Rosen, "Thermodynamic viability of a new three step high temperature Cu–Cl cycle for hydrogen production," *Int. J. Hydrogen Energy*, vol. 43, no. 41, pp. 18783–18789, 2018.
- [77] H. Ishaq and A. Science, "Thermal management of the thermochemical Cu–Cl

- cycle linked with industrial processes for hydrogen production,” no. April, 2018.
- [78] H. Ishaq, I. Dincer, and G. F. Naterer, “New trigeneration system integrated with desalination and industrial waste heat recovery for hydrogen production,” *Appl. Therm. Eng.*, vol. 142, no. May, pp. 767–778, 2018.
- [79] M. F. Orhan, I. Dincer, and M. A. Rosen, “Exergoeconomic analysis of a thermochemical copper–chlorine cycle for hydrogen production using specific exergy cost (SPECOC) method,” *Thermochim. Acta*, vol. 497, pp. 60–66, 2010.
- [80] I. Dincer and G. F. Naterer, “Overview of hydrogen production research in the Clean Energy Research Laboratory (CERL) at UOIT,” *Int. J. Hydrogen Energy*, vol. 39, no. 35, pp. 20592–20613, 2014.
- [81] H. Ozcan and I. Dincer, “Energy and exergy analyses of a solar driven Mg-Cl hybrid thermochemical cycle for co-production of power and hydrogen,” *Int. J. Hydrogen Energy*, 2014.
- [82] Z. Wang, G. F. Naterer, and K. Gabriel, “Multiphase reactor scale-up for Cu-Cl thermochemical hydrogen production,” *Int. J. Hydrogen Energy*, vol. 33, no. 23, pp. 6934–6946, Dec. 2008.
- [83] G. F. Naterer, K. Gabriel, Z. L. Wang, V. N. Daggupati, and R. Gravelins, “Thermochemical hydrogen production with a copper-chlorine cycle. I: oxygen release from copper oxychloride decomposition,” *Int. J. Hydrogen Energy*, vol. 33, no. 20, pp. 5439–5450, Oct. 2008.
- [84] G. F. Naterer et al., “Progress of international hydrogen production network for the thermochemical Cu-Cl cycle,” *Int. J. Hydrogen Energy*, vol. 38, no. 2, pp. 740–759, 2013.
- [85] E. Imre, J. Y. Guillemaut, and A. Hilton, “Calibration of nodal and free-moving cameras in dynamic scenes for post-production,” *Proc. - 2011 Int. Conf. 3D Imaging, Model. Process. Vis. Transm. 3DIMPVT 2011*, pp. 260–267, 2011.
- [86] W. Wu, F. T. Hsu, and H. Y. Chen, “Design and energy evaluation of a stand-alone copper-chlorine (Cu-Cl) thermochemical cycle system for trigeneration of electricity, hydrogen, and oxygen,” *Int. J. Energy Res.*, vol. 42, no. 2, pp. 830–842, 2018.
- [87] D. M. Hall, N. N. Akinfiev, E. G. Larow, R. S. Schatz, and S. N. Lvov, “Thermodynamics and Efficiency of a CuCl(aq)/HCl(aq) Electrolyzer,” *Electrochim. Acta*, vol. 143, pp. 70–82, 2014.
- [88] D. M. Hall, R. S. Schatz, E. G. LaRow, and S. N. Lvov, “CuCl/HCl Electrolyzer Kinetics for Hydrogen Production Via Cu-Cl Thermochemical Cycle,” *ECS Trans.*, vol. 58, no. 2, pp. 15–25, 2013.
- [89] D. M. Hall, E. G. LaRow, R. S. Schatz, J. R. Beck, and S. N. Lvov, “Electrochemical Kinetics of CuCl(aq)/HCl(aq) Electrolyzer for Hydrogen Production via a Cu-Cl Thermochemical Cycle,” *J. Electrochem. Soc.*, vol. 162, no. 1, pp. F108–F114, 2015.
- [90] D. M. Hall, J. R. Beck, and S. N. Lvov, “Electrochemical kinetics of the hydrogen reaction on platinum in concentrated HCl(aq),” *Electrochem. commun.*, vol. 57, no. 1, pp. 74–77, 2015.
- [91] C. Zamfirescu, G. F. Naterer, and M. A. Rosen, “Chemical exergy of electrochemical cell anolytes of cupric/cuprous chlorides,” *Int. J. Hydrogen Energy*, vol. 42, no. 16, pp. 10911–10924, 2017.

- [92] R. Soltani, I. Dincer, and M. A. Rosen, "Electrochemical analysis of a HCl(aq)/CuCl(aq) electrolyzer: Equilibrium thermodynamics," *Int. J. Hydrogen Energy*, vol. 41, no. 19, pp. 7835–7847, 2016.
- [93] A. Odukoya and G. F. Naterer, "Electrochemical mass transfer and entropy generation of cuprous chloride electrolysis," *Int. J. Hydrogen Energy*, vol. 36, no. 17, pp. 11345–11352, 2011.
- [94] M. F. Orhan, I. Dincer, and M. A. Rosen, "Thermodynamic analysis of the copper production step in a copper-chlorine cycle for hydrogen production," *Thermochim. Acta*, vol. 480, no. 1–2, pp. 22–29, 2008.
- [95] S. Ranganathan and E. B. Easton, "Ceramic carbon electrode-based anodes for use in the Cu-Cl thermochemical cycle," *Int. J. Hydrogen Energy*, vol. 35, no. 10, pp. 4871–4876, 2010.
- [96] L. Stolberg, H. A. Boniface, S. McMahon, S. Suppiah, and S. York, "Electrolysis of the CuCl/HCl aqueous system for the production of nuclear hydrogen," 2008 Proc. 4th Int. Top. Meet. High Temp. React. Technol. HTR 2008, vol. 2, pp. 491–495, 2009.
- [97] S. Khurana, D. Hall, R. Schatz, and S. N. Lvov, "Diagnosis and Modeling of the CuCl Electrolyzer Using Electrochemical Impedance Spectroscopy," *ECS Trans.*, vol. 53, no. 9, pp. 41–50, 2013.
- [98] M. A. Lewis, M. S. Ferrandon, D. F. Tatterson, and P. Mathias, "Evaluation of alternative thermochemical cycles - Part III further development of the Cu-Cl cycle," *Int. J. Hydrogen Energy*, vol. 34, no. 9, pp. 4136–4145, 2009.
- [99] M. S. Ferrandon, M. A. Lewis, F. Alvarez, and E. Shafirovich, "Hydrolysis of CuCl₂ in the Cu-Cl thermochemical cycle for hydrogen production: Experimental studies using a spray reactor with an ultrasonic atomizer," *Int. J. Hydrogen Energy*, vol. 35, no. 5, pp. 1895–1904, 2010.
- [100] V. N. Daggupati, G. F. Naterer, and I. Dincer, "Convective heat transfer and solid conversion of reacting particles in a copper(II) chloride fluidized bed," *Chem. Eng. Sci.*, vol. 66, no. 3, pp. 460–468, 2011.
- [101] Y. Haseli, I. Dincer, and G. F. Naterer, "Hydrodynamic gas-solid model of cupric chloride particles reacting with superheated steam for thermochemical hydrogen production," *Chem. Eng. Sci.*, vol. 63, no. 18, pp. 4596–4604, 2008.
- [102] Y. Haseli, G. F. Naterer, and I. Dincer, "Fluid-particle mass transport of cupric chloride hydrolysis in a fluidized bed," *Int. J. Heat Mass Transf.*, vol. 52, no. 11–12, pp. 2507–2515, 2009.
- [103] G. F. Naterer, I. Dincer, and C. Zamfirescu, "Thermochemical Water-Splitting Cycles," in *Hydrogen Production from Nuclear Energy*, London: Springer London, 2013, pp. 153–272.
- [104] M. A. Lewis, J. G. Masin, R. B. Vilim, and M. Serban, "Development of the low temperature Cu-Cl thermochemical cycle," in *Proceedings of the American Nuclear Society - International Congress on Advances in Nuclear Power Plants 2005, ICAPP'05*, 2005.
- [105] M. S. Ferrandon et al., "The hybrid Cu-Cl thermochemical cycle. I. Conceptual process design and H₂A cost analysis. II. Limiting the formation of CuCl during hydrolysis," in *NHA Annual Hydrogen Conference*, 2008, no. May, pp. 1–20.
- [106] M. A. Lewis and J. G. Masin, "The evaluation of alternative thermochemical

- cycles - Part II: The down-selection process,” *Int. J. Hydrogen Energy*, vol. 34, no. 9, pp. 4125–4135, 2009.
- [107] K. Pope, V. N. Daggupati, G. F. Naterer, and K. S. Gabriel, “Experimental study of gaseous effluent and solid conversion in a fluidized bed hydrolysis reactor for hydrogen production,” *Int. J. Hydrogen Energy*, vol. 37, no. 21, pp. 16397–16401, 2012.
- [108] V. N. Daggupati, G. F. Naterer, and K. S. Gabriel, “Diffusion of gaseous products through a particle surface layer in a fluidized bed reactor,” *Int. J. Heat Mass Transf.*, vol. 53, no. 11–12, pp. 2449–2458, 2010.
- [109] V. N. Daggupati, G. F. Naterer, K. S. Gabriel, R. J. Gravelins, and Z. L. Wang, “Equilibrium conversion in Cu-Cl cycle multiphase processes of hydrogen production,” *Thermochim. Acta*, vol. 496, no. 1–2, pp. 117–123, 2009.
- [110] G. D. Marin, Z. Wang, G. F. Naterer, and K. Gabriel, “X-ray diffraction study of multiphase reverse reaction with molten CuCl and oxygen,” *Thermochim. Acta*, vol. 524, no. 1–2, pp. 109–116, 2011.
- [111] G. Marin, G. F. Naterer, and K. Gabriel, “Chemically lly Reacting and Particle Laden Multiphase Flow in a Molten olten Salt Vessel , Z Wang University of Ontario Institute of Technology Oshawa , Ontario , Canada 10th AIAA / ASME Joint Thermophysics and Heat Transfer Conference Chicago , Illinois ,” no. July, pp. 1–10, 2010.
- [112] G. D. Marin, Z. Wang, G. F. Naterer, and K. Gabriel, “Byproducts and reaction pathways for integration of the Cu-Cl cycle of hydrogen production,” *Int. J. Hydrogen Energy*, vol. 36, no. 21, pp. 13414–13424, 2011.
- [113] A. Nixon, M. Ferrandon, M. H. Kaye, and L. Trevani, “Thermochemical production of hydrogen: Synthesis, characterization, and decomposition of copper oxychloride,” *J. Therm. Anal. Calorim.*, vol. 110, no. 3, pp. 1095–1105, 2012.
- [114] M. Serban, M. A. Lewis, and J. K. Basco, “Kinetic study of the hydrogen and oxygen production reactions in the copper-chloride thermochemical cycle,” in *2004 AIChE Spring National Meeting, Conference Proceedings, 2004*, pp. 25–9.
- [115] M. Lewis, “Alternative Thermochemical Cycles for Nuclear Hydrogen,” *USDOE Report, USDOE, Washingt. DC, 2005*.
- [116] W. L. Luyben, “Comparison of extractive distillation and pressure-swing distillation for acetone/chloroform separation,” *Comput. Chem. Eng.*, vol. 50, pp. 1–7, 2013.
- [117] I. Rodriguez-Donis, K. Papp, E. Rev, Z. Lelkes, V. Gerbaud, and X. Joulia, “Column configurations of continuous heterogeneous extractive distillation,” *AIChE J.*, vol. 53, pp. 182–1993, 2007.
- [118] S. K. Wasylkiewicz, L. C. Kobylka, and F. J. L. Castillo, “Optimal design of complex azeotropic distillation columns,” in *Chemical Engineering Journal, 2000*, pp. 219–227.
- [119] W. L. Luyben, “Methanol/trimethoxysilane azeotrope separation using pressure-swing distillation,” *Ind. Eng. Chem. Res.*, vol. 53, no. 13, pp. 5590–5597, 2014.
- [120] J. P. Knapp and M. F. Doherty, “A New Pressure-Swing-Distillation Process for Separating Homogeneous Azeotropic Mixtures,” *Ind. Eng. Chem. Res.*, vol. 31, pp. 346–357, 1992.
- [121] J. U. Repke, F. Forner, and A. Klein, “Separation of homogeneous azeotropic

- mixtures by pressure swing distillation - Analysis of the operation performance,” *Chem. Eng. Technol.*, vol. 28, pp. 1151–1157, 2005.
- [122] Y. Wang, Z. Zhang, D. Xu, W. Liu, and Z. Zhu, “Design and control of pressure-swing distillation for azeotropes with different types of boiling behavior at different pressures,” *J. Process Control*, vol. 42, pp. 59–76, 2016.
- [123] Z. Lei, R. Zhou, and Z. Duan, “Process improvement on separating C4 by extractive distillation,” *Chem. Eng. J.*, vol. 85, pp. 379–386, 2002.
- [124] W. L. Luyben, “Control of a multiunit heterogeneous azeotropic distillation process,” *AIChE J.*, vol. 52, pp. 623–637, 2006.
- [125] R. Muñoz, J. B. Montón, M. C. Burguet, and J. de la Torre, “Separation of isobutyl alcohol and isobutyl acetate by extractive distillation and pressure-swing distillation: Simulation and optimization,” *Sep. Purif. Technol.*, vol. 50, pp. 175–183, 2006.
- [126] A. Baharev, L. Kolev, and E. Rév, “Computing multiple steady states in homogeneous azeotropic and ideal two-product distillation,” *AIChE J.*, vol. 57, pp. 1485–1495, 2011.
- [127] Y. Wang, P. Cui, and Z. Zhang, “Heat-integrated pressure-swing-distillation process for separation of tetrahydrofuran/methanol with different feed compositions,” *Ind. Eng. Chem. Res.*, vol. 53, no. 17, pp. 7186–7194, 2014.
- [128] B. Kiran and A. K. Jana, “A hybrid heat integration scheme for bioethanol separation through pressure-swing distillation route,” *Sep. Purif. Technol.*, 2015.
- [129] M. Lescisin, O. A. Jianu, M. A. Rosen, and K. Pope, “Azeotropic distillation of hydrochloric acid in the copper-chlorine cycle for hydrogen production,” 2017 5th IEEE Int. Conf. Smart Energy Grid Eng. SEGE 2017, pp. 322–329, 2017.
- [130] V. N. Daggupati, G. F. Naterer, K. S. Gabriel, R. J. Gravelsins, and Z. L. Wang, “Effects of atomization conditions and flow rates on spray drying for cupric chloride particle formation,” *Int. J. Hydrogen Energy*, vol. 36, pp. 11353–11359, 2011.
- [131] G. F. Naterer et al., “Progress in thermochemical hydrogen production with the copper-chlorine cycle,” *Int. J. Hydrogen Energy*, vol. 40, no. 19, pp. 6283–6295, 2015.
- [132] A. Farsi, I. Dincer, and G. F. Naterer, “Second law analysis of CuCl₂ hydrolysis reaction in the Cu–Cl thermochemical cycle of hydrogen production,” *Energy*, p. 117721, 2020.
- [133] A. Farsi, I. Dincer, and G. F. Naterer, “Second law analysis of CuCl₂ hydrolysis reaction in the Cu–Cl thermochemical cycle of hydrogen production,” *Energy*, vol. 202, p. 117721, 2020.
- [134] A. Bejan, G. Tsatsaronis, and M. J. Moran, *Thermal Design and Optimization*, no. July. 1996.
- [135] A. Farsi and I. Dincer, “Thermodynamic assessment of a hybrid particle-based concentrated solar power plant using fluidized bed heat exchanger,” *Sol. Energy*, vol. 179, pp. 236–248, 2019.
- [136] T. Parry, “Thermodynamics and Magnetism of Cu₂OCl₂,” Brigham Young University - Provo, 2008.
- [137] R. H. Perry, D. W. Green, and J. O. Maloney, *Perry’s Chemical engineers’ handbook*. McGraw-Hill, 1984.

- [138] D. R. Lide, CRC handbook of chemistry and physics: a ready-reference book of chemical and physical data. CRC Press, 2008.
- [139] S. O. Hiwase, A. Datta, and S. K. Som, "Entropy balance and exergy analysis of the process of droplet combustion," *J. Phys. D. Appl. Phys.*, vol. 31, p. 1601, 1998.
- [140] N. Lior, W. Sarmiento-Darkin, and H. S. Al-Sharqawi, "The exergy fields in transport processes: Their calculation and use," in *Energy*, 2006, pp. 553–578.
- [141] A. Bejan and A. D. Kraus, *Heat Transfer Handbook*. 2003.
- [142] N. A. and S. A. C. O. L. R. C. Force, Body, "An analysis of laminar free-convection flow and heat transfer about a flat plate parallel to the direction of the generating body force," 2018.
- [143] F. P. Incropera, D. P. DeWitt, T. L. Bergman, and A. S. Lavine, *Fundamentals of Heat and Mass Transfer*(6th edition). 2007.
- [144] A. Haider and O. Levenspiel, "Drag coefficient and terminal velocity of spherical and nonspherical particles," *Powder Technol.*, vol. 58, pp. 63–70, 1989.
- [145] S. Ito and T. Kajiuichi, "Drag Force On A Sphere Moving in Plastic Fluid," *J. Chem. Eng. Japan*, vol. 2, no. 1, pp. 19–24, 1969.
- [146] P. Dai and E. College, "Modelling Non-Catalytic Gas-Solid Reactions," no. April, 2017.
- [147] O. Levenspiel, *Chemical reaction engineering*, vol. 38, no. 11. 1999.
- [148] R. V Singh and M. R. Pai, "Investigations on the hydrolysis step of copper-chlorine thermochemical cycle for hydrogen production," no. December 2019, pp. 2845–2863, 2020.
- [149] B. L. Dou, J. S. Gao, and X. Z. Sha, "A study on the reaction kinetics of HCl removal from high-temperature coal gas," *Fuel Process. Technol.*, 2001.
- [150] S. N. Lvov, *Introduction to Electrochemical Science and Engineering*. 2014.
- [151] P. Koukkari and R. Pajarre, "Calculation of constrained equilibria by Gibbs energy minimization," *Calphad Comput. Coupling Phase Diagrams Thermochem.*, 2006.
- [152] V. N. Balashov, R. S. Schatz, E. Chalkova, N. N. Akinfiev, M. V. Fedkin, and S. N. Lvov, "CuCl Electrolysis for Hydrogen Production in the Cu–Cl Thermochemical Cycle," *J. Electrochem. Soc.*, 2011.
- [153] D. A. Sverjensky, E. L. Shock, and H. C. Helgeson, "Prediction of the thermodynamic properties of aqueous metal complexes to 1000°C and 5 kb," *Geochim. Cosmochim. Acta*, 1997.
- [154] J. Brugger et al., "An XAS study of the structure and thermodynamics of Cu(I) chloride complexes in brines up to high temperature (400 °C, 600 bar)," *Geochim. Cosmochim. Acta*, 2007.
- [155] P. A. C. Chang, J. St-Pierre, J. Stumper, and B. Wetton, "Flow distribution in proton exchange membrane fuel cell stacks," *J. Power Sources*, vol. 162, no. 1, pp. 340–355, 2006.
- [156] C. Zamfirescu, I. Dincer, and G. F. Naterer, "Thermophysical properties of copper compounds in copper-chlorine thermochemical water splitting cycles," *Int. J. Hydrogen Energy*, vol. 35, no. 10, pp. 4839–4852, 2010.
- [157] J. F. Mulia-Soto and A. Flores-Tlacuahuac, "Modeling, simulation and control of an internally heat integrated pressure-swing distillation process for bioethanol separation," *Comput. Chem. Eng.*, 2011.
- [158] R. Gani, C. A. Ruiz, and I. T. Cameron, "A generalized model for distillation

- columns-I. Model description and applications,” *Comput. Chem. Eng.*, 1986.
- [159] B. Hall, “Sales Receipt,” vol. 0044, no. 05722282, p. 15260, 2012.
- [160] C. J. Geankoplis, “Transport Processes and Unit Operations (Geankoplis).pdf,” Englewood Cliffs. 2003.
- [161] V. Mahindrakar and J. Hahn, “Dynamics and control of benzene hydrogenation via reactive distillation,” *J. Process Control*, 2014.
- [162] G. F. Naterer, *Advanced Heat Transfer*. 2018.
- [163] Y. Fujita and M. Tsutsui, “Experimental investigation of falling film evaporation on horizontal tubes,” *Heat Transf. - Japanese Res.*, 1998.
- [164] İ. Dinçer and C. Zamfirescu, *Drying Phenomena : Theory and Applications*. 2016.
- [165] A. Farsi, S. M. H. Mohammadi, and M. Ameri, “Thermo-economic comparison of three configurations of combined supercritical CO₂ refrigeration and multi-effect desalination systems,” *Appl. Therm. Eng.*, 2017.
- [166] A. Lazzaretto and G. Tsatsaronis, “SPECO: A systematic and general methodology for calculating efficiencies and costs in thermal systems,” *Energy*, vol. 31, no. 8–9, pp. 1257–1289, 2006.
- [167] I. Dincer and M. A. Rosen, *Exergoeconomic Analysis of Thermal Systems*. 2013.
- [168] I. Janghorban Esfahani and C. Yoo, “A highly efficient combined multi-effect evaporation-absorption heat pump and vapor-compression refrigeration part 2: Thermoeconomic and flexibility analysis,” *Energy*, 2014.
- [169] D. Steward and T. Ramsden, “H₂A Production Model , Version 2 User Guide H₂A Production Model , Version 2 User Guide,” *Natl. Renew. Energy Lab.*, no. September, 2008.
- [170] Coinnews, “US Inflation Calculator,” *US Inflation Calculator*, 2016. .
- [171] Y. Bicer, I. Dincer, and M. Aydin, “Maximizing performance of fuel cell using artificial neural network approach for smart grid applications,” *Energy*, 2016.
- [172] J. Hogerwaard, I. Dincer, and G. F. Naterer, “Experimental investigation and optimization of integrated photovoltaic and photoelectrochemical hydrogen generation,” *Energy Convers. Manag.*, 2020.
- [173] W. Zhang, A. Maleki, M. A. Rosen, and J. Liu, “Sizing a stand-alone solar-wind-hydrogen energy system using weather forecasting and a hybrid search optimization algorithm,” *Energy Convers. Manag.*, 2019.
- [174] A. Ozbilen, I. Dincer, and M. A. Rosen, “Development of new heat exchanger network designs for a four-step CuCl cycle for hydrogen production,” 2014.
- [175] M. F. Orhan, I. Dincer, and M. A. Rosen, “Design and simulation of a UOIT copper-chlorine cycle for hydrogen production,” *Int. J. Energy Res.*, vol. 37, no. 10, pp. 1160–1174, Aug. 2013.
- [176] S. H. Saravi, S. Honarparvar, and C. C. Chen, “Thermodynamic modeling of HCl-H₂O binary system with symmetric electrolyte NRTL model,” *J. Chem. Thermodyn.*, 2018.
- [177] A. Plus, A. Properties, A. E. Suite, A. Technology, T. C. Park, and O. Systems, “Aspen Physical Property System 11,” *Engineering*, 2001.
- [178] M. Chase Jr., “Tables, NIST-JANAF Thermochemical,” *J. Phys. Chem. Ref. Data*. p. 1952, 1998.
- [179] M. S. Ray, “Distillation Design, by HZ. Kister, McGraw-Hill, New York, USA (1992). 710 pages. ISBN 0-07-034909-6.” *Dev. Chem. Eng. Miner. Process.*, vol.

- 2, no. 4, pp. 255–256, 2008.
- [180] M. A. Lewis, J. G. Masin, and P. A. O. Hare, “Evaluation of alternative thermochemical cycles , Part I : The methodology,” *Int. J. Hydrogen Energy*, vol. 34, no. 9, pp. 4115–4124, 2009.

Appendix

Copyright Permission

The high similarity of this thesis is mainly due to the 6 published journal papers by the candidate. As a result, some critical information, equations and illustrations which cannot be revised without losing the fundamental essence of the work were maintained. For this reason, permissions were duly obtained from the publishers to include this information in the thesis.

The following are the obtained permissions from the publishers for the reuse of the published work based on this PhD thesis.

1) Elsevier

Article: Submission declaration and verification in the Guide for authors:

“Submission of an article implies that the work described has not been published previously (except in the form of an abstract, a published lecture or academic thesis, see 'Multiple, redundant or concurrent publication' for more information), that it is not under consideration for publication elsewhere, that its publication is approved by all authors and tacitly or explicitly by the responsible authorities where the work was carried out, and that, if accepted, it will not be published elsewhere in the same form, in English or in any other language, including electronically without the written consent of the copyright-holder. To verify originality, your article may be checked by the originality detection service Crossref Similarity Check.”

2) Journal of Electrochemical Society (ECS)

The permission letter is shown in Figure A.1.

June 16, 2020

Re: Permission to Reproduce Published Article in Ph.D. Thesis

Aida Farsi,

This letter is to confirm that you are free to reproduce the published article of your paper, "Electrochemical Transport in CuCl/HCl(aq) Electrolyzer Cells and Stack of the Cu-Cl Cycle", published in the *Journal of The Electrochemical Society* within your Ph.D. Thesis with cost.

Sincerely,



Paul Cooper
Editorial Manager
The Electrochemical Society Journals

Figure A.1. A photograph of permission letter to reproduce published article in Ph.D. thesis